ISSN 1068-3755, Surface Engineering and Applied Electrochemistry, 2010, Vol. 46, No. 2, pp. 87–90. © Allerton Press, Inc., 2010.
Original Russian Text © S.A. Baranov, P.G. Globa, S.P. Yushchenko, A.I. Dikusar, 2010, published in Elektronnaya Obrabotka Materialov, 2010, No. 2, pp. 4–8.

ELECTRICAL PRECISION TREATMENT OF MATERIALS

On the Electrodeposition for Manufacturing of Meso- and Nanomaterials by the Template Synthesis Method at a Variable Diameter of the Template Pores

S. A. Baranov[a, b], P. G. Globa[a], S. P. Yushchenko[a, b], and A. I. Dikusar[a, b]

[a] *Institute of Applied Physics, Academy of Sciences of Moldova, ul. Akademiei 5, Chisinau, MD-2028 Republic of Moldova*
[b] *Shevchenko Pridnestrov'e State University, ul. 25 Oktyabrya 128, Tiraspol, Republic of Moldova*
e-mail: baranov@phys.asm.md

Received December 22, 2009

Abstract—It has been shown that the height of the nanoproduct deposited in the case of electrodeposition under conditions of the template synthesis into pores of variable (in height) diameter becomes a nonlinear function of the passed charge. The results of the experimental research data, which are indicative of the presence of such effects at the electrodeposition of silver and copper into membranes from Al_2O_3, have been presented. The analysis of these results shows that the nonlinearity results from the noncylindricity of the pores only in the layers of the membranes close to the initial electrode surface or when the pores represent the internal surface of a rotation body with a weak dependency of the radius on the pore height.

DOI: 10.3103/S1068375510020018

Electrodeposition, or template synthesis, is one of the methods of manufacturing of meso- and nanomaterials. According to this method, on one of the sides of a template, a conducting layer of metal is deposited and the electrodeposition is performed into the membrane pores with the sizes of the pores determining the dimensions of the obtained nanoproduct [1–3].

Porous aluminum oxide is used as a template [4], along with membranes obtained by ion etching [5] and porous semiconductor structures produced, apart from other methods, by anodic dissolution [6]. If the pores are cylindrical, the deposition rate and the layer's thickness (at a specified quantity of the passed charge) may be calculated following Faraday's law:

$$h = \frac{C}{\rho S}Q, \tag{1}$$

where h is the deposit's height, S designates the area of a cylindrical pore, Q denotes the quantity of electricity applied for obtaining the deposit, and ρ and C are the density and electrochemical equivalent of the given substance. From formula (1), it follows that the rate of the deposition increase ν is constant and depends only on the current density j:

$$\nu = \frac{C}{\rho}j. \tag{2}$$

However, the problem becomes more complex due to the pore size variation in height, when the deposition rate already depends on the electricity quantity in a complicated way and, hence, on the time. These dependencies for the elementary geometry will be derived below.

This paper describes the calculation peculiarities of the rates in Faraday's processes of deposition into real pores with variable geometry.

PECULIARITIES OF THE TEMPLATE DEPOSITION INTO A PORE

If the nanopores are not cylindrical volumes and their diameter varies in proportion to the deposit height, the measured rate of its increase in a nanopore has a more complex dependency than (1) or (2) already by reason of geometry alone.

Below, we shall obtain the dependency of the deposition height and the rate increase for a simple model of a flattened cone.

Let us write Faraday's law as follows:

$$V = \frac{C}{\rho}Q, \tag{3}$$

where V is the deposit's volume (the rest of the designations are identical to (1)).

It is seen from Fig. 1 that, unlike the deposit's increase in the cylinder, in the flattened cone, the variation of the deposit's height h along the coordinate Z also involves a change in the cross section area, which results in the deposition rate varying. According to Faraday's law, the deposition rate for a cylindrical pore must not depend on Z.

The preceding experiments (see, e.g., [7, 8]) show that, in certain cases, the rate appears to be variable at

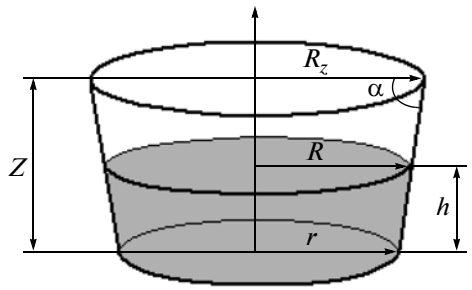

Fig. 1. Diagram of the simplest pore model in the form of a flattened cone.

small quantities of the passed electricity. It was assumed in those papers that the observed dependency was obvious. Upon various activities of the surface areas at the initial moment of time, nonuniform deposition is possible on various areas. However, it is the deposition's maximum thicknesses (the deposition rates) that are found to be fixed at the cross sections of the membranes [7, 8]. With account for that in [7, 8], at Q high values, the deposition rate is already been independent of Z, and the mechanism involving the leveling of the deposition rates at various sites with high Q is not yet clear. Below, it will be shown that the reason for the observed effects lies in the diameter irregularity of the pores in relation to the membrane height.

In addition to the geometry reasons of the deposition rate's decrease, there are electrochemical, kinetic, and other kinds of reasons. It is apparent that the consideration of the geometry factor is necessary at least in the case of a simple model as presented in Fig. 1. Since, in the experiments [7, 8], the rate of the deposition decreased upon the Q increase, one should assume that, at the initial stages of the deposition process, the diameter of the pores was smaller than that at the subsequent stages. If we simulate the pore variation using the model of a flattened cone, then, in the given case, it should be positioned as illustrated in Fig. 1.

METHODS OF CALCULATION IN A FLATTENED CONE MODEL

The volume of a flattened cone filled with the deposit up to the height h is known to be represented (see, e.g., [9, p. 18]) by the following expression:

$$V = \frac{\pi}{3}h(R^2 + rR + r^2), \quad (4)$$

where $R = r + h(R_z - r)/Z$, and R_z is the maximum value of the pore radius (when $h = Z$). It is convenient to introduce a parameter of

$$\tan\alpha = \frac{Z}{R_z - r} = \frac{1}{\cot\alpha},$$

which, by a value order (if $r \sim 10$ nm, $R_z \sim 100$ nm, $Z \sim 10$ μm), equals $\tan\alpha \sim 100$.

The substitution of (4) into (3) gives an algebraic equation of power 3 with respect to the value of h measured in the experiment:

$$h^3 + ah^2 + bh + c = 0, \quad (5)$$

where $a = \dfrac{3r(R_z - r)}{Z} = 3r\cot\alpha,$

$$b = \frac{3r^2(R_z - r)^2}{Z^2} = 3r^2\cot^2\alpha,$$

$$c = \frac{3CQ(R_z - r)^2}{\pi\rho Z^2} = \frac{3CQ}{\pi\rho}\cot^2\alpha.$$

The solution of Eq. (5) is known to be found using Cardano's formula. The standard substitution (see, e.g., [9, p. 8])

$$h = y - r\cot\alpha,$$

leads (5) to a canonical form of the equation. Using the solution for the equation, we get the following formula:

$$h = \left(\frac{3CQ}{\pi\rho}\cot^2\alpha - r^3\cot^3\alpha\right)^{1/3} - r\cot\alpha \sim Q^{1/3}. \quad (6)$$

With sufficient accuracy, one may estimate the rate of the galvanostatic (in the case of a direct current I) increase of the deposition from the expression obtained from (6):

$$\nu = \left(\frac{3CIt}{\pi\rho}\cot^2\alpha - r^3\cot^3\alpha\right)^{-2/3}\frac{CI\cot^2\alpha}{\pi\rho}. \quad (7)$$

It is seen from formula (7) that the rate of the deposition will decrease in time according to a complicated exponential law:

$$\nu \sim t^{-2/3}. \quad (8)$$

Note that, for the deposition into a cylindrical pore, the deposition rate is constant (see (2)); i.e., it does not depend on the time.

METHODS OF CALCULATION FOR MORE COMPLEX MODELS AND THE SIMPLEST GEOMETRICAL THEORY OF SIMILARITY

One of the reasons for the feasible divergences of formula (6) and its results from the experimental data is the alternate angle of the slope of the flattened cone. If we accept this supposition, then it is possible to account for the fact that only at the initial period of the electrodeposition is the rate of the deposit growth a nonlinear function of Q [7,8]. At large thicknesses, the electrodeposition is already performed into the cylindrical pore, which involves the linear dependency of h on Q and the independence of the deposition rate of

the quantity of the passed charge. In these events, the experimental dependency may be intermediate between the dependency of (6) and the linear dependency of h on Q (see (1)) for a cylindrical pore of a constant diameter.

Based on these arguments, one may assume that, in a general form, the dependency of the deposit's height on the passed electricity can be as follows:

$$H \sim q^{1/L}. \quad (9)$$

In this part of the paper, we shall use the dimensionless values of the height and charge, which, unlike the preceding dimensional ones, will be designated as H and q, correspondingly. Whereby, H and q are the simplexes, and the nondimensionalizing is performed by the normalizing using certain standard values of h and Q. The parameter L introduced by us, the value of which is presented in the table (see below), may use any number and thereat characterize the geometrical parameter of the electrodeposition process.

The latter can be demonstrated by trivial argumentation. Suppose the electrodeposition is performed into a pore that is a body of rotation. Let the process be carried out in the galvanostatic mode within the range of negligibly small current densities when the current efficiency tends to 100%. Then, for the body of rotation, from (3), we obtain the expression

$$\int_0^H R^2(H)dH \sim q, \quad (10)$$

where $R(h)$ is the height function of the radius (in our case, it is the deposition height).

From (9) and (10), it follows that

$$R^2(H) \sim \frac{\partial q}{\partial H} \sim H^{L-1}. \quad (11)$$

For the unknown function $R(h)$, the approximation is as follows:

$$R(H) \sim H^{(L-1)/2} \sim H^K, \quad (12)$$

where another important parameter is introduced into (12),

$$K = (L - 1)/2. \quad (13)$$

Thus, using (9), the pore may be presented as a body of rotation with any (power) dependency of the radius on the height, and, in the limiting case, it may transform into a form close to cylindrical. As a purely mathematic example, let us study the event when a pore is a body of rotation whose generatix line is preset by the simplest parabola, i.e., $K = 2$, and the root parabola at $K = 1/2$. The geometrical parameters introduced by us for all these events are presented in the table.

The geometrical parameters for the simplest pores

Pore form	L	K
Cylindrical	1	0
Cone	3	1
Square–parabolic	5	2
Root–parabolic pore	2	1/2

COMPARISON WITH THE EXPERIMENTAL RESULTS

Figure 2 shows the experimental dependencies of h on $\bar{Q}$ in logarithmical coordinates, where $\bar{Q}$ denotes the density of the passed charge. These dependencies are taken from [7, 8], correspondingly, for the electrodeposition of silver from a thiocyanate solution and copper from a pyrophosphate solution into membranes with the average diameter of the pores of 200 nm at a current density of 6 mA/cm^2 (for the electrodeposition of copper [8]).

The experimental results shown in Fig. 2 relate only to the initial stages of the electrodeposition. At high values of $\bar{Q}$, the dependence of the rate on the time fails to be observed. These results make it possible to experimentally obtain the value of $1/L$ from (9), which appeared to equal 0.72 ± 0.02 for the silver electrodeposition [7] and 0.68 ± 0.09 for the copper electrodeposition [8]. Despite the fact that these values were obtained for the dimensional magnitudes, it seems evident that they characterize the value of $1/L$ exactly; i.e., the ratio for the dimensionless parameters is the same, as was confirmed by the relevant numerical estimations.

The dependencies observed experimentally mostly correspond to the situation when the diameter of the

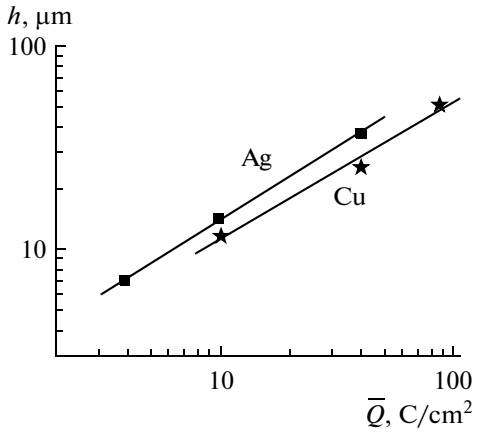

Fig. 2. Dependency of the deposit height of silver [7] and copper [8] into the membranes from the porous Al_2O_3 with an average size of the pores of 200 nm based on the density of the passed charge.

pores varies at the initial moment of time of the deposition with transition to a cylindrical pore at high $\bar{Q}$ (long deposition times). This is vividly demonstrated not only by the absence of the dependency of the deposition rate on the time (see [7, 8]) but also by the $1/L$ value's estimation. For copper, the observed slope (0.68 ± 0.09) appears to be average at various times. At relatively short times, it equals 0.56, and, at longer ones, the dependency is as follows: $h \sim Q^{0.92}$. It is clear that, in the case of silver electrodeposition, the observed dependency appears to be the average value as well at a certain Q interval.

Thus, in the examples described in the present paper, the following experimental dependency is traced:

$$h \sim Q^{2/3}. \quad (14)$$

If we use the experimental values of (14), we shall obtain the following approximation for the unknown function of $R(h)$:

$$R(h) \sim h^{1/4}. \quad (15)$$

Thus, upon the accomplishment of (9), the pore may be presented as a body of rotation with a weak dependency of the radius on the height in the limit transforming into a pore of a form close to cylindrical, which agrees with the described experimental data.

CONCLUSIONS

It is shown that, in the electrodeposition based on the template synthesis into pores of variable (in height) diameter, the height of the manufactured layer of the nanoproduct becomes a nonlinear function of the passed charge. At a cone form of the pores, $h \sim Q^{1/3}$ (h is the layer height, Q is the charge). The previous experimental results [7, 8] show that, at minor values of the passed charge, $h \sim Q^{2/3}$. The obtained results are the outcome of the pore noncylindricity only for the layers of the membranes close to the initial electrode surface or when the pores represent the internal surface of bodies of rotation with a weak dependency of the radius on the pore height ($R \sim h^{1/4}$).

ACKNOWLEDGMENTS

This research was supported within the framework of the state programs of the Republic of Moldova: The Electrophysical and Chemical Surface Processes of Micro- and Nanometric Scales, and Multilayer Nanostructural Materials Obtained by Electrochemical Methods: The Study of the Tribological, Corrosion, and Magnetic Properties. Support was also received from the bilateral Moldavian–Ukrainian project The Effects of the Corrosion Rate of Nanostructures and Nanocomposites during their Electrochemical Manufacturing and Application.

REFERENCES

1. Martin, C.R., Nanomaterials: a Membrane-Based Synthetic Approach, *Science*, 1994, vol. 266, pp. 1961–1965.
2. El-Giar, E.M., Said, R.A., Bridges, G.E., and Thomson, D.J., Localized Electrochemical Deposition of Copper Microstructures, *J. Electrochem. Soc.*, 2000, vol. 147, pp. 586–592.
3. Hulteen, J.C. and Martin, C.R., A General Template–Based Method for the Preparation of Nanomaterials, *J. Mater. Chem.*, 1997, vol. 7, pp. 1075–1089.
4. Furneaux, R.C., Rigby, W.K., and Davidson, A.P., The Formation of Controlled–Porosity Membranes from Anodically Oxidized Aluminum, *Nature*, 1989, vol. 337, pp. 147–149.
5. Schonenberger, C., van der Zande, B.ML, Fokkink, G.J., Henny, M., Schmid, C., Kruger, M., Bachtold, A., Ruber, R., Brik, K., and Staufer, U., Template Synthesis of Nanowires in Porous Polycarbonate Membranes: Electrochemistry and Morphology, *J. Phys. Chem., Ser. B*, 1997, vol. 101, pp. 5407–5505.
6. Tiginyanu, I., Monaico, El., and Monaico, Ed., Ordered Arrays of Metal Nanotubes in Semiconductor Envelope, *Electrochem. Comm.*, 2008, vol. 10, pp. 731–734.
7. Globa, P.G., Sidelnikova, S.P., Dikusar, A.I., Zasavitskii, E.A., and Kantser, V.G., Precision Electrochemical Deposition: Kinetics of Nanopore Filling in Template Synthesis, *Surf. Eng. Appl. Electrochem.*, 2006, vol. 42, no. 3, pp. 1–10.
8. Dikusar, A.I., Globa, P.G., Belevskii, S.S., and Sidelnikova, S.P., On the Limiting Rate of Dimensional Electrodeposition at Meso- and Nanomaterial Manufacturing by Template Synthesis, *Surf. Eng. Appl. Electrochem.*, 2009, vol. 45, no. 3, pp. 171–179.
9. Tsypkin, A.G. and Tsypkin, G.G., *Matematicheskie formuly* (Mathematical Formulas), Moscow: "Nauka", 1985.

ISSN 1068-3755, Surface Engineering and Applied Electrochemistry, 2010, Vol. 46, No. 2, pp. 91–99. © Allerton Press, Inc., 2010.
Original Russian Text © S.S. Belevskii, N.I. Tsyntsaru, A.I. Dikusar, 2010, published in Elektronnaya Obrabotka Materialov, 2010, No. 2, pp. 9–18.

ELECTRICAL SURFACE TREATMENT METHODS

Electrodeposition of Nanocrystalline Co–W Coatings from Citrate Electrolytes under Conditions of Controlled Hydrodynamic: II. The Electrodeposition Rate and Composition of the Coatings

S. S. Belevskii[a], N. I. Tsyntsaru[a], and A. I. Dikusar[a, b]

[a] *Institute of Applied Physics, Academy of Sciences of Moldova, ul. Academiei 5, Chisinau, MD-2028 Republic of Moldova*
[b] *Shevchenko Pridnestrov'e State University, ul. 25 Oktyabrya 128, Tiraspol, Republic of Moldova*
e-mail: dikusar@phys.asm.md

Received June 30, 2009

Abstract—The influence of the ionic mass-transfer effects on the deposition rate, the current efficiency, and the composition and morphology of the coatings has been studied using a rotating cylindrical electrode in a citrate electrolyte containing $CoSO_4$ (0,2 mol/l) and Na_2WO_4 (0.2 mol/l) (pH = 6.8) at the electrodeposition temperature of 60°C. It has been found that the decrease of the electrodeposition potential and the tungsten concentration in the coating with the current efficiency increase upon the Re number growth ($Re \geq 200$) occur only under galvanostatic conditions. At the potentiostatic mode, similar of influence fails to be observed. It is shown that the estimated effects take place due to the electrodeposition through the nonstoichiometric surface coating layer with electronic conductivity, the composition components of which are in electrochemical equilibrium with the components of the solution at the film–solution boundary.

DOI: 10.3103/S106837551002002X

This paper, a continuation of a preceding one [1], deals with the electrodeposition of Co–W coatings from citrate solutions. The principal peculiarities of the manufacturing and properties of such coatings are as follows. Firstly, they occur due to the so-called induced codeposition [2–5]. Despite the fact that the mechanism of the induced codeposition is characterized as "anomalous" [5] and appears to be ill-defined until now, there is a whole group of alloys obtained by this method. In particular, the category of such processes includes the electrodeposition of metals from the iron group with refractory metals (W, Mo, and Re) [2–18]. The second peculiarity of similar coatings is that the materials of this type are nanocrystalline [6, 7, 9–12, 14, 15, 17, 18]. For the Co–W and Fe–W coatings produced from citrate solutions, this is vividly shown by Fig. 1 taken from [18].

Figure 1 also shows that the degree of "nanocrystallinity" largely depends on the tungsten concentration in the coating. The small size of the crystallites is an important factor for achieving certain properties of the coatings, in particular, the anticorrosion [3, 6, 19] and mechanical ones [3, 16, 18, 20, 21].

Finally, a third peculiarity of these coatings is the technology of their production. As is noted in [21], since the electrodeposition of CoW–alloys is based on an ecologically pure electrolyte whose properties may successfully compete with those of the electrolytic chromium ones, such coatings appear to be the best alternatives for the coatings deposited from solutions of hexavalent chromium taking into account the ecological risks resulting from the production technology of the latter.

Concerning the induced codeposition of the iron group metals comprising refractory metals, it was repeatedly noted that the composition of the coatings and hence their properties strongly depend on the hydrodynamic conditions of their manufacturing [4, 5, 22].

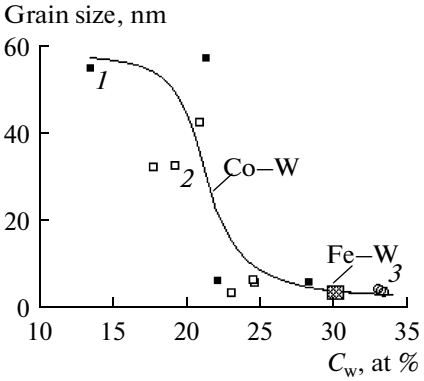

Fig. 1. The influence of the alloy's W content on the grain size in the Co–W and Fe–W electrolytic coatings obtained at a constant current and pH = 6.7 (*1*), a pulse current and pH = 6.7 (*2*), and a pulse direct and current and pH = 8 (*3*) [18].

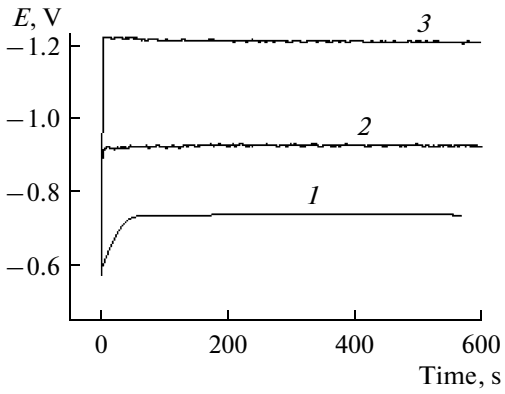

Fig. 2. The dependency of the potential on the time for the various current densities of the electrodeposition at the RCE rotation velocity of 165 rot/min (Re = 600). *1*—0.03; *2*—1.0; *3*—3.0 A/dm^2.

In the present paper, the influence of the hydrodynamic conditions (the ion mass transfer effects) on the electrodeposition rate, the composition, and the morphology of the coatings manufactured from a definite citrate electrolyte used previously in a number of papers [16, 18, 19, 22] is investigated. The estimated regularities are assumed to be important not only for the applied composition of the solution but for other processes in manufacturing the Co–W coatings along with the processes of the induced codeposition of the iron group of metals comprising the refractory metals.

EXPERIMENTAL

Electrolyte Composition and Electrodeposition Modes

The electrolyte of the following composition was used for the manufacturing of the cobalt–tungsten coatings (mol/l): Na_2WO_4—0.2; $CoSO_4$—0.2; $C_6H_8O_7$ (citric acid)—0.04; $Na_3C_6H_5O_7$ (sodium citrate)—0.25; H_3BO_3—0.65 (pH = 6.8). The deposition temperature was 60°C. The electrodeposition was performed onto a rotating cylindrical electrode (RCE), the form and geometric parameters of which were presented in [1]. The (RCE) rotation velocity was varied from 0.3 to 165 rot/min. Under the above temperature, the kinematic viscosity of the solution was 0.72×10^{-2} cm^2/s, making it possible to vary the Re number from 1 (0.3 rot/min) to 600 (165 rot/min). A graphite plate served as the anode.

It is known that the RCE developed turbulent mode with the known ratios that determine the ion mass-transfer rate may be achieved at Re ≥ 200 [23, 24]. Lower rotation rates provided for the uniformity of the deposited layers since the anode was fixed only at one side of the cylinder. As in [1], the influence of the hydrodynamics (on the deposition rate (the current density), the current efficiency, and the coating composition) was registered only at the RCE rotation velocities above 11 rot/min (Re > 40).

The electrodeposition was carried out both under galvanostatic and potentiostatic conditions. In all the events, the potential was measured with regard to a saturated argentum chloride electrode and recounted for the hydrogen scale. The PARSTAT 2273 (Princeton Applied Research) was used as the potentiostat–galvanostat. The electrodeposition was performed on St 3 specimens. Immediately prior to the electrodeposition, the surface was coated by a nickel layer, as is described in [1].

Determination of the Current Efficiency, Composition, and Morphology of the Coatings

The current efficiency was determined by the weight increase of the specimens upon the transmission of a certain quantity of electricity. The value of the passed charge was measured by integrating the current–time curves at the potentiostatic mode or fixing the time at the galvanostatic one. The measured gains in weight varied from ~30 to ~70 mg.

The current efficiency was calculated (irrespective of the alloy composition) using the value of the electrochemical equivalent of the alloy equaling 0.311 mg/C [25]. The morphology of the coatings was studied using scanning electron microscopy (SEM), and the elemental composition of the alloy was determined by EDX analysis (a TESCAN VEGA scanning electron microscope with an EDX analysis supplement). The coating composition, apart from Co and W, incorporated carbon and oxygen (hydrogen fails to be determined by the EDX analysis). The values of the composition of the coatings (presented below) include only the content of the elements (in atomic percents) of the alloy metal fraction (without account for the light elements). The analysis was carried out at three arbitrarily selected points of the RCE surface. The average values together with the standard deviations from the arithmetic mean are presented.

RESULTS AND DISCUSSION

Galvanostatic Electrodeposition. The Influence of the Hydrodynamics on the Process Rate, Current Efficiency, and Composition of the Coatings

Figures 2–4 show the galvanostatic measurement results in the potential–time coordinates at various current densities and a constant velocity of the RCE rotation (Fig. 2), the dependency potential and rotation velocity (number Re) at various current densities (Fig. 3), and the dependence of the current density-potential at various Reynolds numbers (Fig. 4). The values of the potentials and current densities presented in Figs. 3, 4 are relevant to the established magnitudes of the obtained values (see, e.g., Fig. 2).

A number of peculiarities of the obtained dependencies have been observed. The first one suggests that the hydrodynamic effect is involved only at a certain

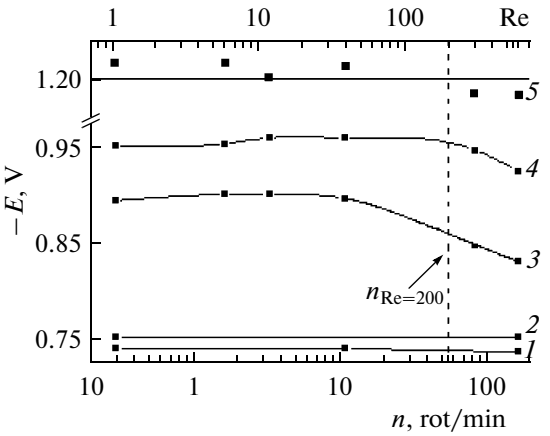

Fig. 3. The dependency of the electrodeposition potential on the RCE rotation velocity (Re) at the various current densities, A/dm^2: 0.03 (*1*); 0.1 (*2*); 0.5 (*3*); 1.0 (*4*); 3.0 (*5*).

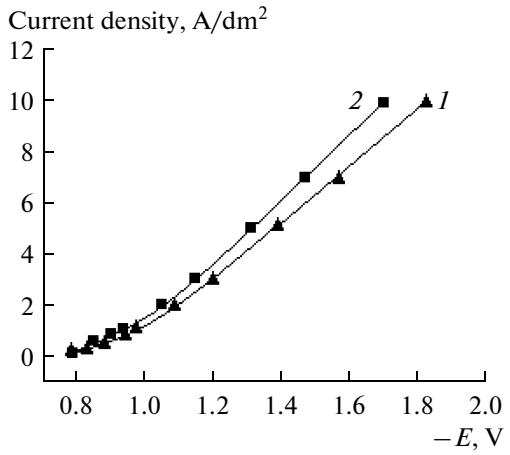

Fig. 4. The polarization curves at the galvanostatic mode and various Re numbers: 40 (*1*); 600 (*2*).

region of the current densities (potentials). At the low current densities (up to 0.5 A/dm^2), this kind of influence fails to occur, just as at the high ones (Fig. 3).

The second one conveys that the hydrodynamic influence may be observed only at sufficiently high Reynolds numbers (at Re > 40 or at the rotation velocities above 11 rot/min). The cause may be that, according to [23, 24], the expression for the limiting current density determined by the rate of the ionic mass transfer to the RCE is as follows:

$$i_{\lim} = 0.079nFC_0\omega(\omega r/\nu)^{-0.3}(\nu/D)^{-0.644}, \qquad (1)$$

where C_0 is the concentration of the electroactive particles, ω denotes the frequency of the cylinder's rotation, ν implies the kinematical viscosity, D designates the diffusion coefficient, F is Faraday's constant, and n stands for the number of the transferred electrons during the electrochemical reaction.

In accordance with (1), the rate of the ionic mass transfer (convective diffusion) is proportional to the cylinder rotation frequency of the power 0.7, and the RCE surface itself is equally available for the mass transfer processes (the absence of variation of the ionic mass transfer rate versus the cylinder's height). However, according to [23], (1) can be performed only at $\mathrm{Re} = \omega r^2/\nu \geq 200$. From the results shown in Fig. 3, one may see that, experimentally, the hydrodynamic influence is observed precisely at the Reynolds numbers above 200 (measurements in the range of 40 < Re < 200 were not performed). At a high enough current density (3 A/dm^2), one may assume that the dependency on the RCE rotation velocity is absent (the mean value of the potential at all the Re numbers being used was -1.20 ± 0.01 V, Fig. 3).

The third peculiarity of the obtained dependencies suggests that, at fairly high current densities (precisely when the hydrodynamic effect occurs), the current density is directly proportional to the potential and, hence, the nonlinearity of Tafel' coordinates is involved (Fig. 4). An identical dependency was detected in [1] upon cobalt deposition from the same solution (but without sodium wolframate).

The presence of such a linear dependency implies that the process rate is determined by the transfer in the surface film with the film conductivity apparently being of the electron type. However, the film composition is defined among other factors by the conditions of the ionic mass transfer in the solution, since the slope of the current density curve and the potential depends on the hydrodynamic conditions (Fig. 4).

Such a hydrodynamic effect is also characteristic for the dependency of the current efficiency on the current density (Fig. 5). At low rates of mixing (up to Re ≤ 40), a similar influence is absent, and the high rotation velocities lead to a substantial enhancement of the current efficiency.

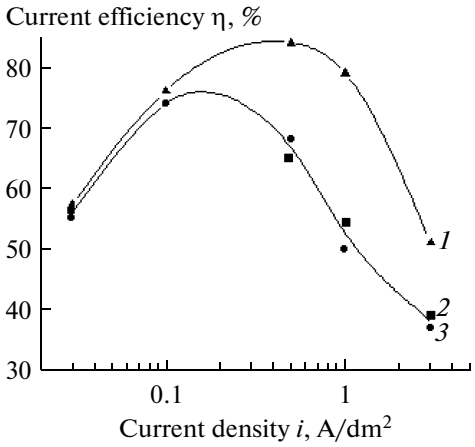

Fig. 5. The dependency of the current efficiency on the current density at various RCE rotation velocities (Re), rot/min: 165 (*1*); 11 (*2*); 0.3 (*3*).

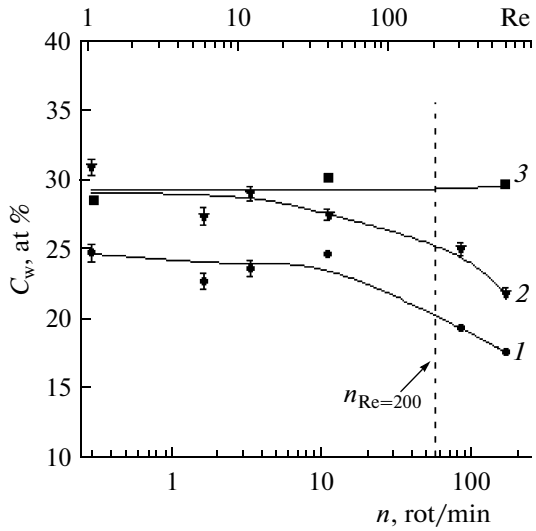

Fig. 6. The influence of the RCE (Re) rotation velocity on the tungsten concentration in the coatings at various current densities, A/dm^2: *1*—0.5; *2*—1.0; *3*—3.0.

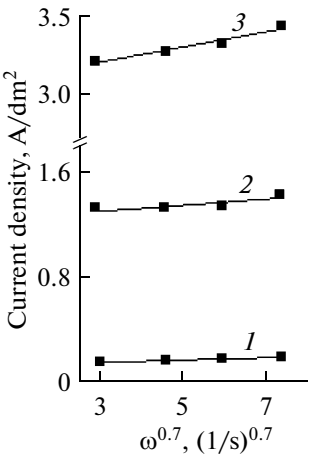

Fig. 7. The influence of the RCE frequency rotation on the electrodeposition current density at the potentials equaling −0.8 (*1*), −1.0 (*2*), and −1.2 (*3*).

The reaction of the hydrogen release is known to be a side reaction at the Co–W coating manufacturing. One can see that its contribution increases upon an increase of the current density (with the electrodeposition potential growth exhibiting a linear dependency on the current density). However, since at certain Re values, due to the hydrodynamics effect, the potential shifts to the region of positive potentials (i.e., it decreases, Fig. 3), this, in turn, involves the current efficiency enhancement due to the decrease of the charge share needed for the hydrogen release reaction. Thus, the hydrodynamics appears to have a dual effect on the electrodeposition rate, increasing its current density along with the current efficiency.

At low current densities, the current efficiency decreases, and the influence of the hydrodynamics is absent (Fig. 5). It is not inconceivable that the latter is caused by the corrosion processes in the region of the potentials close to the stationary potential of the de-energized electrode (the mixed corrosion potential) in the electrodeposition electrolyte.

The potential variation due to the influence of the hydrodynamics leads to the composition modification of the coatings, namely, to a substantial decrease of the tungsten concentration in the metal fraction of the alloy (and, hence, the cobalt share increases) in the coating (Fig. 6). The comparison of the results presented in Figs. 6 and 3 shows that it is the electrode potential value that determines the alloy composition (of the metal constituent). And, when it shifts towards the positive potentials, the cobalt concentration increases (and that of the tungsten decreases). However, for this composition of the solution (and for the temperature), the influence of the potential (the current density) varying has a limit of 30 at % W. The RCE rotation velocity fails to influence the coating composition upon reaching this limit (Fig. 6).

Potentiostatic Deposition.

The influence of the hydrodynamics according to (1) in the presence of the process rate limitations resulted from the ionic mass transfer in the solution, and the current density is proportional to the rotation frequency ω with the power 0.7. This very dependency is observed under the conditions of the potentiostatic deposition at various potentials (Fig. 7). Moreover, it should be noted here that Fig. 7 shows the current density values obtained at ω relevant to the Re numbers above 200. One can also see that the control of the process rates appears to be a diffusion-kinetic one with the current density being predominantly influenced by the electrode potential variation. However, unlike the galvanostatic mode, the potentiostatic deposition (with the same Re numbers at which the potential, current efficiency, and coating composition (Figs. 3, 5, 6) are affected by the hydrodynamics) is not subjected to such an influence. (Fig. 8).

If for the estimation of the role of the hydrodynamic conditions in the coating composition formation the absence of their influence is evident (Fig. 8), then, for the current efficiency, it needs explanation, since a minor dependence still exists (Fig. 8). However, it ranges within the limits of the experimental error. In fact, the mean value of the current efficiency in the range of the Re numbers of 40–600 equals 59 ± 3% (the standard deviation from the arithmetic mean is given as the interval value) at a maximum deviation from the average by 5% (Fig. 8). It is evident that, if such a deviation is regarded as the one falling within the limits of the experimental errors in case of the current effi-

ciency determination under the conditions of the described experiments, then one may state the absence of such influence both on the coating composition and on the current efficiency. For comparison, in the galvanostatic experiment at the current density, say, of 1 A/dm^2 and in the same range of the Re numbers, the current efficiency increases from ~50 to 80% (Fig. 5).

It seems evident that both the coating composition and the current efficiency are predominantly influenced by the electrode potential. And, if it shifts in the positive direction at the RCE rotation velocity, then only in this case is the coating composition modified (in particular, the tungsten and cobalt ratio) along with the current efficiency varying.

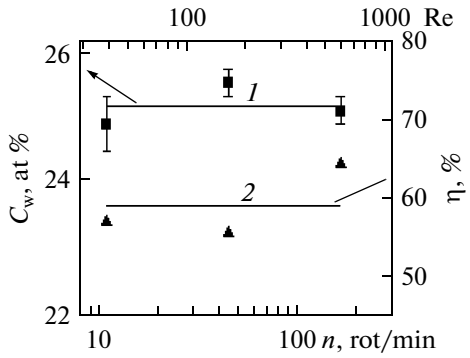

Fig. 8. The influence of the RCE rotation velocity (Re numbers) on the tungsten concentration in the coating (*1*) and the alloy current efficiency (*2*) at the electrodeposition potential of –1.0 V.

The Surface Morphology

Figure 9 shows the electronic images of the surface after the deposition of the coatings at a charge density from 4×10^3 to 6×10^3 C/dm^2. One can see that not only the coating composition but the morphology of its surface is determined by the electrode potential. The morphology of the surface changes (Fig. 9) only when the hydrodynamics influence the potential. It is mostly manifested upon maintaining the constant current density of 0.5 A/dm^2 (Figs. 9a and b). At Re increasing from 40 to 600, the potential at maintaining this current density decreases by ~75 mV (Fig. 2). And, as a consequence, the morphology modifies. At keeping the potential constant and under the galvanostatic conditions at actually the same potential, the surface morphology is identical (Figs. 9c and d). The latter is valid also for the high current density (3 A/dm^2), the potential of which actually fails to be influenced by the hydrodynamics (Fig. 3, Figs. 9e and f). Here, it is worth noting that, at the high current densities, the surface fracture formation occurs due to the coating's internal tension onset.

Kinetics of the Electrodeposition, Composition, and Structure of the Coatings

It follows from Fig. 1 that the degree of the "nanocrystallinity" of the obtained electrolytic deposits depends significantly on the tungsten concentration in the coating and, hence, on the solution composition and the deposition modes, including the hydrodynamic conditions. The analysis of the results presented in the paper asks for an explanation of the following experimental factors as viewed from the unified positions: (a) the linear dependency of the current density on the potential, whose slope is defined by the hydrodynamic conditions; (b) the hydrodynamic influence on the composition, the morphology of the coatings, and the current efficiency under the galvanostatic conditions and the absence of a similar influence under the potentiostatic ones.

The set of these experimental factors may be explained by accepting the hypothesis that the deposition occurs through a nonstoichiometric coating layer with the electron conductivity under the conditions of equilibrium between the anions (cations) of the solution and the coating layer [26, pp. 749–758]. The present hypothesis allows one to explain the linear dependency between the current density and the potential. And the presence of the equilibrium between the cations of the layer and the metal involves the following dependency at the film–electrolyte boundary [26, p. 753],

$$E_{Me} = E^0_{Me} + \frac{RT}{zF}\ln\alpha_{Me^{z+}}, \qquad (2)$$

and at the equilibrium between the anions of the layer and the electrolyte [26, p. 751],

$$E_A = E^0_A - \frac{RT}{mF}\ln\alpha_{A^{m-}}, \qquad (3)$$

where E^0_{Me} and E^0_A are the standard potentials, and $\alpha_{Me} + \alpha_{A^{m-}}$ denote the relevant activities.

Despite the fact that the exact composition of the near-electrode layer is unknown, the presence of the rigid dependencies of the (2) and (3) type resulting from the equilibrium at the film–solution boundary makes it possible to explain why, at keeping the potential constant, the coating composition is exposed to no modifications upon the hydrodynamic conditions variation. And that is precisely because of the fact that, due to the equilibrium, the constant surface concentration of the solution components remains unchanged. At the same time, under the galvanostatic conditions, the surface concentration, for instance, of that of cobalt citrate, may increase and, hence, the potential may decrease and the cobalt concentration increase in the surface film, which appears to be observed in the experiment.

The presence of the nonstoichiometric phase film (see Fig. 10) implies that the coating composition may

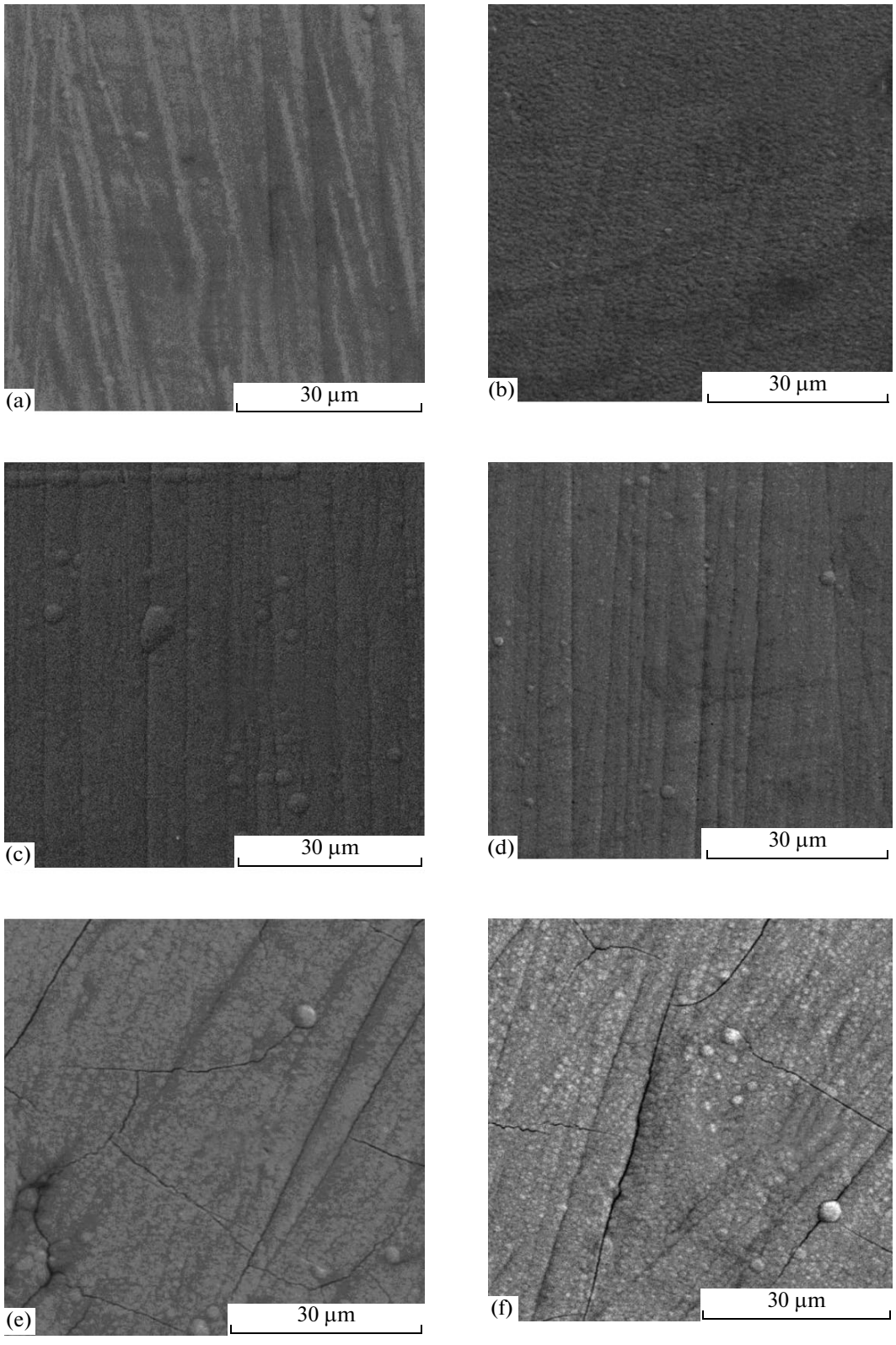

Fig. 9. Electron images of the coating surfaces obtained under the galvanostatic (a, b, c, e, f) and potentiostatic (d) conditions at the current densities, A/dm^2: 0.5 (a, b), 1.0 (c), 3.0 (e,f), at the potential of 1.0 V (d) and the following Re numbers: 40 (a, c, e), 200 (d), 600 (b, f).

comprise not only Co and W but also the components of the electrolyte. Indeed, as the results of the EDX analysis have shown, regardless of the deposition conditions, the overall content of cobalt and tungsten in the coating makes up ~60 at %, and ~40 at % falls on the light elements (C, O, according to [27] using the example of the Fe–W deposits; the coatings may be observed to contain hydrogen as well). And although such a high concentration of the light elements may be doubted, considering the accuracy of their determination by the EDX analysis, the presence of these elements in the film (in the coating) is doubtless.

Presently, there are two groups of papers devoted to the mechanism of the induced codeposition of the metals of the iron group with refractory metals, which make it possible to explain the influence of the hydrodynamic conditions on the alloy composition. The first group [4, 28, 29] (Podlaha-Landolt's mechanism) is based on the assumption that the deposition of the metals follows two ways (reactions a–c):

$$[\mathrm{MeCit}]^- + 2\bar{e} \longrightarrow \mathrm{Me}_{(s)} + \mathrm{Cit}^{3-}, \quad \text{(a)}$$

$$[\mathrm{MeCit}]^- + \mathrm{WO}_4^{2-} + 2\mathrm{H_2O} + 2\bar{e} \longrightarrow [\mathrm{MeCitWO_2}]^-_{ads} + 4\mathrm{OH}^-, \quad \text{(b)}$$

$$[\mathrm{MeCitWO_2}]^-_{ads} + 2\mathrm{H_2O} + 4\bar{e} \longrightarrow \mathrm{W}_{(s)} + [\mathrm{MeCit}]^- + 4\mathrm{OH}^-. \quad \text{(c)}$$

Considering that, simultaneously, the reaction of hydrogen release takes place, it should be written as

$$\mathrm{H_2O} + \bar{e} \longrightarrow \frac{1}{2}\mathrm{H_2} + \mathrm{OH}^-. \quad \text{(d)}$$

Depending on the ratio of the concentrations of the metal components of the iron group and the refraction metal, the reduction of the metal complex of the iron group occurs straightforwardly up to the metal state (reaction (a)) or it appears to be used as a reducer for the refraction metal complex with the formation of the intermediate product of $[\mathrm{MeCitWO_2}]^-_{ads}$ type (reaction (b)). This intermediate reduces afterwards to the metal (reaction (c)). Reaction (a) may be diffusion controllable and the reactions (b–c), kinetic. At other concentration ratios, the opposite variant is possible. It is noteworthy that each of these reactions appears to be electrochemical, and the dependency of its rate on the potential is the Tafel one. An adequate mathematic model [28] allows one to predict the metal ratio in the coating with account for the degree of the surface filling by the intermediate. The kinetic constants used for this purpose are taken from the experimental data. However, according to the inferences of the authors themselves [28], the model-based degrees of the coating filling are found to be abnormally low, which allows one to distrust the model's validity.

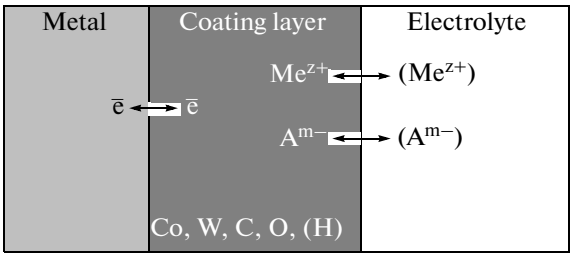

Fig. 10. Phase diagram of the electrode with a coating layer of the electron conductivity for the electrodeposition of the Co–W coatings from the citrate solution.

Nevertheless, qualitatively, the very idea of the two-way electrodeposition (reactions (a–c)) accompanied by the (d) reaction agrees with the experimental results of the present paper provided the (a) reaction is diffusion-controllable and the (b–c) reactions are kinetic. However, considering all these, the present model should be modified with account for the existence of the nonstoichiometric coating surface layer that has the electron conductivity.

The possibility of an advance in the development of the model of the induced electrodeposition on the basis of the fundamental estimation of the composition of the resulting complexes that are the sources of manufacturing the coatings has been described in a number of papers [30–32] generalized in [5]. It has been assumed that a source for manufacturing of the coatings is the intermediate (as applied to the deposition of the W alloy); $[(\mathrm{Me})(\mathrm{HWO_4})(\mathrm{Cit})]^{2-}$ obtained using reaction (e),

$$[(\mathrm{Me})\mathrm{Cit}]^- + [(\mathrm{HWO_4})\mathrm{Cit}]^{4-} \longrightarrow [\mathrm{Me}(\mathrm{HWO_4})(\mathrm{Cit})]^{2-} + \mathrm{Cit}^{3-}, \quad \text{(e)}$$

or even $[(\mathrm{Me})(\mathrm{HWO_4})_2(\mathrm{Cit})]^{3+}$ obtained using reaction (f),

$$[(\mathrm{Me})(\mathrm{HWO_4})(\mathrm{Cit})]^{2-} + [(\mathrm{HWO_4})\mathrm{Cit}]^{4-} \longrightarrow [(\mathrm{Me})(\mathrm{HWO_4})_2(\mathrm{Cit})]^{3-} + \mathrm{Cit}^{3-}, \quad \text{(f)}$$

with the subsequent reduction of this intermediate to the metal state (e.g., in relation to the nickel-tungsten coatings, to NiW, or even to $\mathrm{NiW_2}$).

Thus, unlike [4, 28, 29] the intermediate, it is assumed to be formed in the solution as a result of the chemical reactions, e.g., (e, f). Evidently, depending on the ratio of the concentrations of the components, (a) the intermediate composition may vary or (b) its formation (as a complex with a specific stoichiometry) may be controlled by the convective diffusion of some of the components of the blend. In addition, the present results show that the initially forming intermediate (due to the reactions (b, e, f) or any others) subsequently (during the reduction) is found to be transformed into a phase film with the electron conductiv-

ity (probably of a nonstoichiometric composition) through which the process of the induced codeposition seems to be realized.

The intermediate being transformed into the surface layer with the electron conductivity should not necessarily be considered as a heterocomplex (heteropolycomplex). It is shown in [1] that the linear dependency of the current density on the potential has also been registered during the deposition of Co from a citrate solution of the composition under study. To the composition of the forming complexes (presumably of a polymer nature) should be devoted an independent course of investigations.

CONCLUSIONS

The results of the present investigation showed that the composition of the coatings with Co–W alloys produced from the citrate solutions (and determining the degree of its "nonocrystallinity") is influenced by the hydrodynamic conditions.

The influence of the hydrodynamic conditions on the current density, the current efficiency of the electrodeposition, and the morphology of the coatings is accomplished immediately through the electrode potential variation. Under the potentiostatic conditions, the hydrodynamics influence neither the alloy composition nor the current efficiency.

A hypothesis has been put forward that the induced codeposition occurs through the surface coating layer with the electron conductivity, and the coating composition is determined by the surface concentration of the blend of the components being in electrochemical equilibrium with the components of the coating layer.

ACKNOWLEDGMENTS

The financing of the research was performed in the framework of the State Programs of the Republic of Moldova: Electrophysical and Electrochemical Surface Processes of Micro- and Nanometric Scales; Multilayer Nanostructural Materials Obtained by Electrochemical Methods: The Study of Tribological, Corrosion, and Magnetic Properties; and the Moldavian National Project for Young Research Workers (project no. 09.819.05).

REFERENCES

1. Belevskii, S.S., Yushchenko, S.P., and Dikusar, A.I., Electrodeposition of Nanocrystalline Co–W Coatings from the Citrate Electrolytes under the Controlled Hydrodynamics Conditions. 1. Co Electrodeposition, *Surf. Eng. Appl. Electrochem.*, 2009, vol. 45, no. 6, pp. 446–454.
2. Brenner, F., *Electrodeposition of Alloys*, New York: Academic Press Inc., 1963.
3. Vas'ko, A.T., *Elektrokhimiya molibdena i vol'frama* (Electrochemistry of Molybdenum and Tungsten), Kiev: Naukova Dumka, 1977.
4. Podlaha, E.J., and Landolt, D., Induced Codeposition. I. An Experimental Investigation of Ni–Mo Alloys, *J. Electrochem. Soc.*, 1996, vol. 143, no. 3, pp. 885–892.
5. Eliaz, N., and Gileadi, E., Induced Codeposition of Alloys of Tungsten, Molybdenum and Rhenium with Transition Metals, In *Modern Aspects of Electrochem.*, Springer, New-York: 2008, vol. 42, pp. 183–186.
6. Yao, S., Zhao, H., and Kowaka, M., A New Amorphous Alloy Deposit with High Corrosion Resistance, *Corrosion*, 1996, vol. 52, no. 3, pp. 183–186.
7. Donten, M., and Stojek, Z., Pulse Electroplating of Rich- in Tungsten Thin Films of Amorphous Co–W Alloys, *J. Appl. Electrochem.*, 1996, vol. 26, p. 665.
8. Atanasov, N., Gencheva, K., and Bratoeva, M., Properties of Nickel–Tungsten Alloys Electrodeposited from Sulfamate Electrolytes, *Plating and Surf. Finishing*, 1997, vol. 84, no. 2, pp. 67–71.
9. Donten, M., Bulk and Surface Composition, Amorphous Structure and Thermocrystallization of Electrodeposited Alloys of Tungsten with Iron, Nickel and Cobalt, *J. Solid State Electrochem.*, 1999, vol. 3, pp. 87–96.
10. Cesiulis, H., Baltutiene, A., Donten, M., Donten, L., and Stojek, Z., Increase in Rate of Electrodeposition and in Ni(II) Concentration in the Bath as a Way to Control Grain Size of Amorphous / Nanocrystalline Ni–W Alloys, *J. Solid State Electrochem.*, 2002, vol. 6, pp. 237–244.
11. Ibrahim, M.A.M., El Kerim, S.S., and Moussa, S.O., Electrodeposition of Nanocrystalline Cobalt–Tungsten Alloys from Citrate Electrolyte, *J. Appl. Electrochem.*, 2003, vol. 33, pp. 627–633.
12. Abdel Hamid, Z., Electrodeposition of Cobalt–Tungsten Alloys from Acidic Bath Containing Cationic Surfactants, *Materials Letters*, 2003, vol. 33, p. 2558–2564.
13. Huang, Q., Young, D.P., Chan, J.Y., Jiang, J., and Podlaha, E.J., Electrodeposition of FeCoNiCu/Cu Compositionally Modulated Multilayers, *J. Electrochem. Soc.*, 2002, vol. 149, no. 6, pp. 349–354.
14. Donten, M., Cesiulis, H., and Stojek, Z., Electrodeposition of Amorphous / Nanocrystalline and Crystalline Ni–Mo Alloys from Pyrophosphate Baths, *Electrochimica Acta*, 2005, vol. 50, no. 6, pp. 1405–1412.
15. Santana, R.A.C., Campos, A.R.N., Medeirosv, E.A., Oliveira, A.L.M., Silva, L.M.F., and Prasad, Sh., Studies on Electrodeposition and Corrosion Behavior of a Ni–W–Co Amorphous Alloy, *J. Mater. Science*, 2007, vol. 42, no. 22, pp. 9137–9144.
16. Tsyntsaru, N., Belevsky, S., Dikusar, A., and Celis, J.-P., Tribological Behaviour of Electrodeposited Cobalt-Tungsten Coatings: Dependence on Current Parameters, *Trans. Inst. Metal Finish.*, 2008, vol. 86, pp. 301–307.
17. Tsyntsaru, N., Bobanova, J., Ye, X., Cesiulis, H., Dikusar, A., and Celis, J.-P., Iron–Tungsten Alloys Electrodeposited under Direct Current from Citrate–Ammonia Plating Baths, *Surf. Coating Technology*, 2009, vol. 203, nos. 20–21, pp. 3136–3141.

18. Tsyntsaru, N., Cesiulis, H., Bobanova, J., Croitoru, D., Dikusar, A., and Celis, J.-P., Electrodeposition and Tribological Characterization of Nanostructural Co–W and Fe–W Alloys, In *Proc. Int. Conf. Balttrib., Kaunas, Lithuania* 2009, pp. 259–264.
19. Tsyntsaru, N., Belevskii, S.S., Volodina, G.F., Bersirova, O.N., Yapontseva, Yu.S., Kublanovskii, V.S., and Dikusar, A.I., Composition, Structure and Corrosion Properties of Coatings of CoW Alloys Electrodeposited under Direct Current, *Surf. Eng. Appl. Electrochem.*, 2007, vol. 43, no. 5, p. 312–317.
20. Bobanova, Zh.I., Dikusar, A.I., Cesiulis, H., Celis, J.-P., Tsyntsaru, N.I., and Prosycevas, I., Micromechanical and Tribological Properties of Nanocrystalline Coatings Electrodeposited from Citrate–Ammonia Solutions, *Russian J. Electrochem.*, 2009, vol. 45, no. 8, pp. 895–901.
21. Weston, D.P., Shipway, P.H., Harris, S.J., and Cheng, M.K., Friction and Cobalt–Tungsten Alloy Coatings for Replacement of Electrodeposited Chromium, *Wear*, 2009, vol. 267, pp. 934–943.
22. Silkin, S.A., Belevskii, S.S., Tsyntsaru, N.I., Shul'man, A.I., Shchuplakov, A.N., and Dikusar, A.I., Influence of Long–Term Operation of Electrolytes on the Composition, Morphology, and Stress-Strain Properties of Surfaces Produced at Deposition of Co–W Coatings from Citrate Solutions, *Surf. Eng. Appl. Electrochem.*, 2009, vol. 45, no. 1, pp. 1–12.
23. Eisenberg, M., Tobias, C.W., and Wilke, C.R., Ionic Mass Transfer and Concentration Polarization at Rotating Electrodes, *J. Electrochem. Soc.,* 1954, vol. 101, p. 306.
24. Madore, C., West, A.C., Matlosz, M., and Landolt, D., Design Considerations for a Cylinder Hull Cell with Forced Convection, *Electrochim. Acta,* 1992, vol. 37, no. 1, p. 69.
25. Bobanova, Zh.I., Petrenko, V.I., Silkin, S.A., Yushchenko. S.P., and Yakhova, E.A., Electrodeposition of Amorphous Alloys of Co–W. The Role of Hydrodynamic Conditions, *Elektron. Obrab. Mater.*, 2005, no. 6, pp. 86–91.
26. Fetter, K., *Elektrokhimicheskaya kinetika* (Electrochemical Kinetics), Moscow; Leningrad: Khimiya, 1967.
27. Gamburg, Yu.D. and Zaharov, E.N., The Effect of Hydrogen on Amorfization of Iron–Tungsten Alloys Produced by Electrochemical Synthesis, *Russian J. Electrochem.*, 2008, vol. 44, no. 6, pp. 736–740.
28. Podlaha, E.J. and Landolt, D., Induced Codeposition. II. A Mathematical Model Describing the Electrodeposition of Ni–Mo Alloys, *J. Electrochem. Soc.*, 1996, vol.143, pp. 893–899.
29. Podlaha, E.J. and Landolt, D., Induced Codeposition. III. Molybdenum Alloys with Nickel, Cobalt and Iron, *J. Electrochem. Soc.*, 1997, vol. 144, no. 5, pp. 1672–1680.
30. Younes, O. and Gileadi, E., Electroplating of High Tungsten Content Ni / W Alloys, *Electrochem. Solid–State Lett.*, 2000, vol. 3, no. 2, pp. 543–545.
31. Younes, O., and Gileadi, E., Electroplating of Ni/W Alloys, *J. Electrochem. Soc.*, 2002, vol. 149, no. 2, pp. 100–111.
32. Younes-Metzler, O., Zhu, L., and Gileadi, E., The Anomalous Codeposition of Tungsten in the Presence of Nickel, *Electrochim. Acta*, 2003, vol. 48, no. 18, pp. 2551–2562.

ISSN 1068-3755, Surface Engineering and Applied Electrochemistry, 2010, Vol. 46, No. 2, pp. 100–107. © Allerton Press, Inc., 2010.
Original Russian Text © A.G. Anisovich, I.N. Rumyantseva, P.N. Misuno, V.F. Bevza, V.V. Azharonok, 2010, published in Elektronnaya Obrabotka Materialov, 2010, No. 2, pp. 19–26.

ELECTRICAL SURFACE TREATMENT METHODS

Variation in the Structure and Properties of Cast-Iron Sealing Rings under Magnetic-Pulse Treatment

A. G. Anisovich[a], I. N. Rumyantseva[a], P. N. Misuno[a], V. F. Bevza[b], and V. V. Azharonok[c]

[a]*State Scientific Institution, Physical-Technical Institute, National Academy of Sciences of Belarus, ul. Kuprevicha 10, Minsk, 220141 Republic of Belarus*

e-mail: anna-anisovich@yandex.ru

[b]*State Scientific Institution, Institute of Metal Technology, National Academy of Sciences of Belarus, ul. Byalynitskogo–Biruli 11, Mogilev, 212030 Republic of Belarus*

e-mail: sncl@yandex.ru

[c]*State Scientific Institution, Stepanov Institute of Physics, National Academy of Sciences of Belarus, pr. Nezavisimosti 68, Minsk, 220072 Republic of Belarus*

e-mail: azharonok@imaph.bas-net.by

Received December 1, 2009

Abstract—The variation in the structure and properties of cast-iron sealing rings (content in wt %: 2.8–3.0 Si; 0.4–0.6 Mn; 0.1–0.2 Cr; 0.5–0.6 Ni; 0.7–0.9 Cu; 0.04–0.06 Mg; 2.8–3.0 C) under their exposure to a 5.28-MHz pulsed magnetic field is studied. Variations in the eutectoid morphology, the internal structure of the graphite inclusions, and the size of the free cementite inclusions, which result in the enhancement of the hardness, are observed. The magnetic-pulse treatment of rings induces compression stresses in them. The physicomechanical properties of the rings change periodically upon the variation of the number of treatment cycles. The optimum mode corresponds to two cycles.

DOI: 10.3103/S1068375510020031

INTRODUCTION

One of the important problems in automotive engineering and tractor construction is to enhance the operational life of the components of the cylinder–piston group of the internal combustion engines, in particular, the piston rings. At present, the basic material used for their fabrication is cast iron with a plate-like and spherical shape of the graphite. The short life of the rings is most often attributed to the inadequacy of their structure compared to the requirements of State Standart.

High quality can be obtained by the crucially new technique of casting of piston-ring blanks into a water-cooled mold not involving rods that has been developed at the Institute of Metal Technology of the National Academy of Sciences of Belarus. The technique is based on the principles of freeze casting [1], which allows fabricating cast-iron castings with a compact highly dispersed structure and increased physicomechanical properties in comparison with traditional casting methods. Thus, for example, the relative elongation of the castings obtained by this high-strength spheroidal graphite cast iron (SGCI) of the ferrite class is comparable with the analogous parameter for steel samples and it is 12–15%. These castings are characterized by their high elastic properties, which are preserved under heating up to temperatures of 300–4000°C. As a consequence, the castings with these physicomechanical properties have become commonly used for fabricating piston and sealing rings for various applications; however, the use of them appears to be the most efficient in the production of sealing rings for turbocompressors whose service ability and lifetime depend directly on the rotor seal with its body and bearing. The elastic split ring applied as a sealing element is placed without clearances with an expansion end gap of 0.01–0.05 mm; due to the elastic forces, it must remain motionless as the rotor rotates with a frequency up to 160000 r/min. The specified value of the ring joints in the free condition is usually obtained by their heat fixing. However, it should be noted that a decrease in the ring size causes difficulties in both the obtainment of the castings and the fabrication of the product proper. The latter is attributed, e.g., to the circumstance that the diametral compression force of a ring of SGCI with a diameter of 13 mm must be at the level of the analogous characteristic for the upper compression ring with a diameter of 85 mm of a Mercedes-Benz engine that has a cross sectional area larger than the 13-mm ring by a factor of 4.5 [2].

Therefore, studies focused on finding methods and techniques for the obtaining of the desired structure of the cast-iron castings used in domestic mechanical engineering and the required physicomechanical

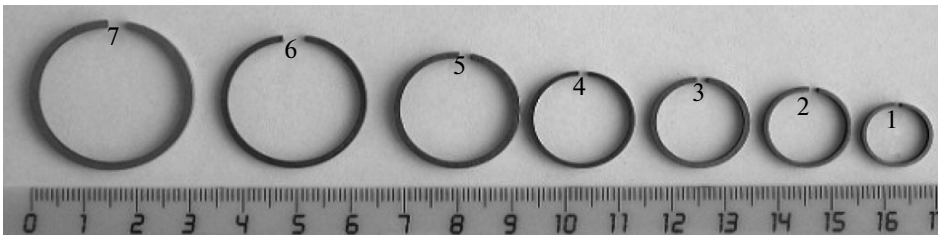

Fig. 1. Sealing rings.

properties of the small-diameter compression rings made of them are of current concern.

The traditional methods of improvement of the structure and properties of cast-iron castings have been studied thoroughly enough for the moment. It is possible to obtain a new complex of their physicomechanical properties only by way of nonconventional impacts on the cast iron, in particular, by magnetic-pulse treatment (MPT). The number of works concerned with the MPT of cast iron is relatively small [3–6]; however, the available data confirm the applicability of this technique for variations in the structure and properties of iron–carbon alloys. Thus, e.g., the authors of [4] studied the effect of a high-frequency magnetic field on the variation in the structure and properties of СЧ-25 vermicular graphite cast iron obtained by the method of continuous-cycle freeze casting. It is found that the structure effects of a high-frequency magnetic impact on cast iron are the healing of surface defects, the dispersion of perlite, a reduction in the ferrite content in the structure due to the ferrite–graphite complex transformation into perlite, the enlargement and variation of the internal structure of the graphite inclusions, and changing the cementite morphology. It is recorded that the observed structural variations of cast iron are accompanied by an increase in the hardness of automotive components of the cylinder–piston group prepared of it.

In this work, we study the possibility to apply a high-frequency magnetic impact to vary the structure and to enhance the elastic properties of sealing rings of SGCI.

EXPERIMENT AND RESEARCH TECHNIQUES

As the experimental samples, we used sealing rings of various diameters being components of turbocompressors (Fig. 1, Table 1). The rings were made of SGCI (Table 2) by freeze casting.

The high-frequency magnetic-pulse treatment (HFMPT) of the rings was carried out using an experimental installation of the Institute of Physics of the National Academy of Sciences of Belarus according to the impact cyclogram given in [7]. A diagram of the samples' arrangement in the operating space of the installation (inductor) is shown in Fig. 2.

The cast-iron structure variations due to the HFMPT were studied by the method of sighting metallography using an MIKRO-200 metallographic complex. The metallographic sample of the cast-iron ring under study was marked and then photographs of it were taken before and after the treatment. The chemical etching of the metallographic samples' surface for the examination of its microstructure was carried out using a 4% solution of nitric acid in ethyl alcohol. The macrostresses were studied by X-ray structure analysis by virtue of a DRON-3M installation in CuK_α radiation in the line of ferrite (110).

The ring resistance to tensile loads was studied using a toolmaker's microscope according to the diagram in Fig. 3. In the course of the measurements, we determined the value of the difference $d - d_0$, where d_0 is the gap between the ring edges in the nonloaded condition; d, at a tensile load with weight m.

RESULTS AND DISCUSSION

In the initial state, the ring material's structure is represented by a perlite matrix (Fig. 4a) with spheroidal inclusions of graphite (Fig. 4b). The HFMPT does not result in a significant change in the graphite distribution in the matrix; however, there are variations in

Table 1. Parameters of the rings

Ring number	Diameter, mm
1	13.0
2	16.1
3	18.0
4	19.3
5	23.0
6	26.0
7	29.6

Table 2. Composition of the cast iron

Element content, wt %							
Fe	Si	Mn	Cr	Ni	Cu	Mg	C
Base	2.8–3.0	0.4–0.6	0.1–0.2	0.5–0.6	0.7–0.9	0.04–0.06	2.8–3.0

Table 3. Spread in the values of the microhardness ΔH_μ

Number of HFMPT cycles	Ring number						
	1	2	3	4	5	6	7
0	1644.0	1098.8	1275.3	1069.3	1644.0	1098.8	1275.3
2	491.5	1903.6	997.9	878.7	491.5	1903.6	997.9
4	1825.8	1273.1	1690.5	1591.4	1825.8	1273.1	1690.5
6	1910.8	1272.4	1270.8	1427.4	1910.8	1272.4	1270.8

the sizes of the free cementite inclusions (Fig. 5) and the eutectoid morphology, which can be seen clearly enough in the rectangular fragment in Fig. 6, which contains a region of the metallographic sample in the neighborhood of the arrow head in Fig. 5.

One of the consequences of the variation in the structure of the perlite component of the cast iron is a decrease in the spread of the values of the microhardness ΔH_μ (Table 3), which is indicative of the increasing uniformity of its structure.

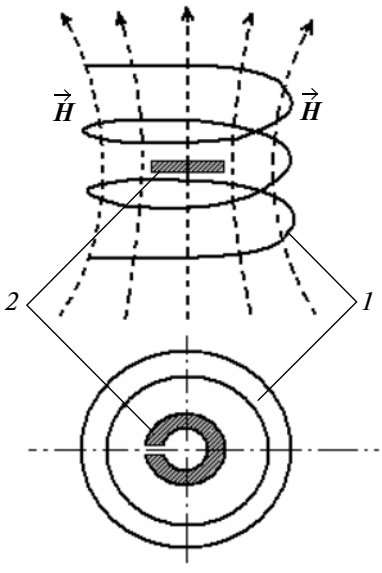

Fig. 2. Diagram of the samples' arrangement in the inductor: *1* is the inductor, *2* is the sample under treatment, and $\vec{H}$ are the magnetic field lines with the intensity H.

As is seen from Table 3, the HFMPT leads to a decrease in the spread in the values to a range of 1000 MPa: after two and six impact cycles for rings number 1, four and six cycles for number 2, two and four cycles for number 3, two and four cycles for number 4, six cycles for number 6, and two and four cycles for number 7.

The observed decrease in the spread of the values of the microhardness is illustrated in a diagram form in Fig. 7.

The variation in the perlite structure and the cementite morphology is connected with the increase in the Rockwell hardness (HRC) of the cast iron

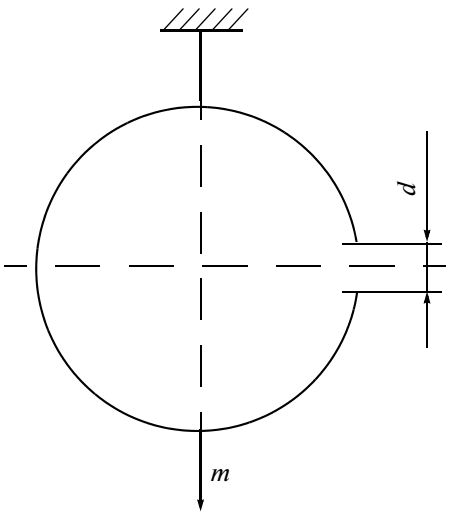

Fig. 3. Diagram of the determination of the rings' resistance to a tensile load with the weight m.

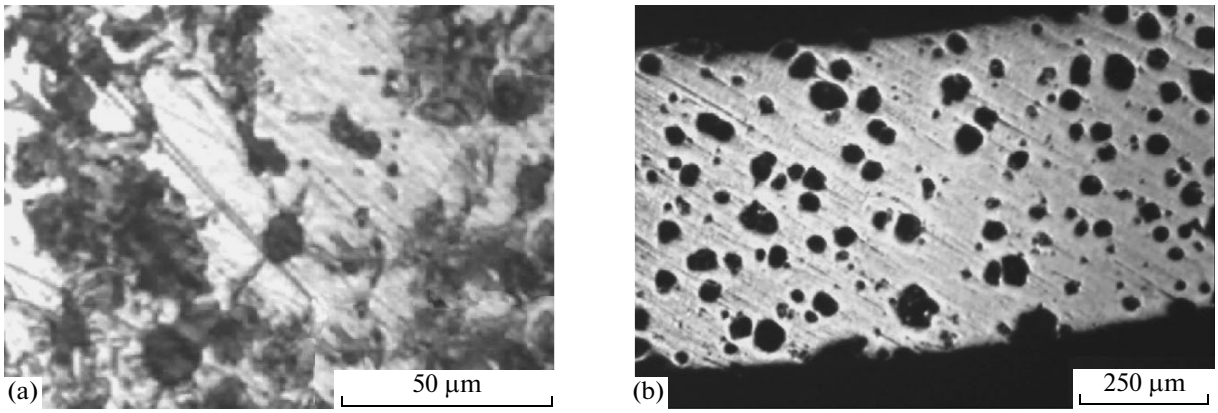

Fig. 4. Structure of the rings in the as-received condition: (a) the perlite matrix and (b) the spheroidal graphite inclusions.

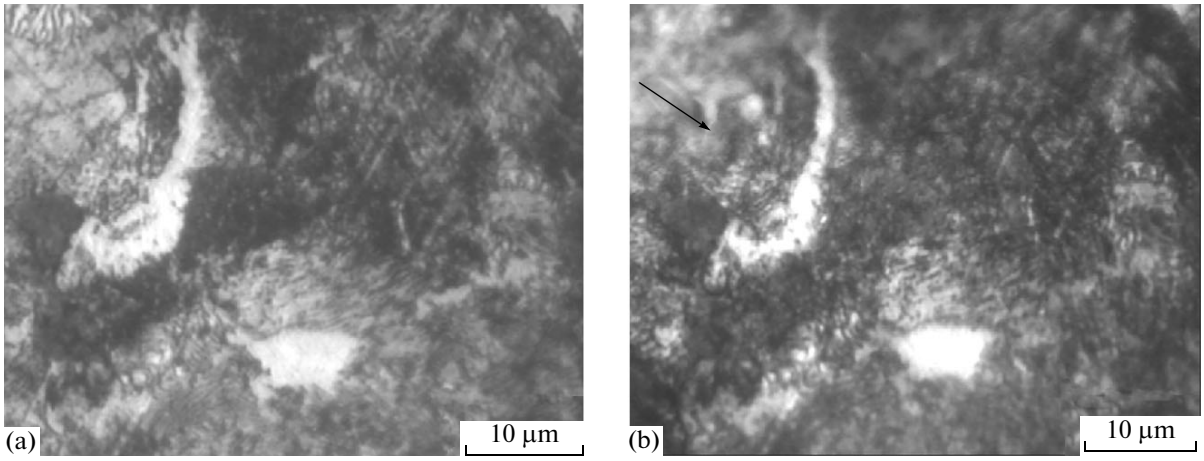

Fig. 5. Variation in the sizes of the free cementite inclusions: (a) the as-received condition and (b) after two cycles of HFMPT.

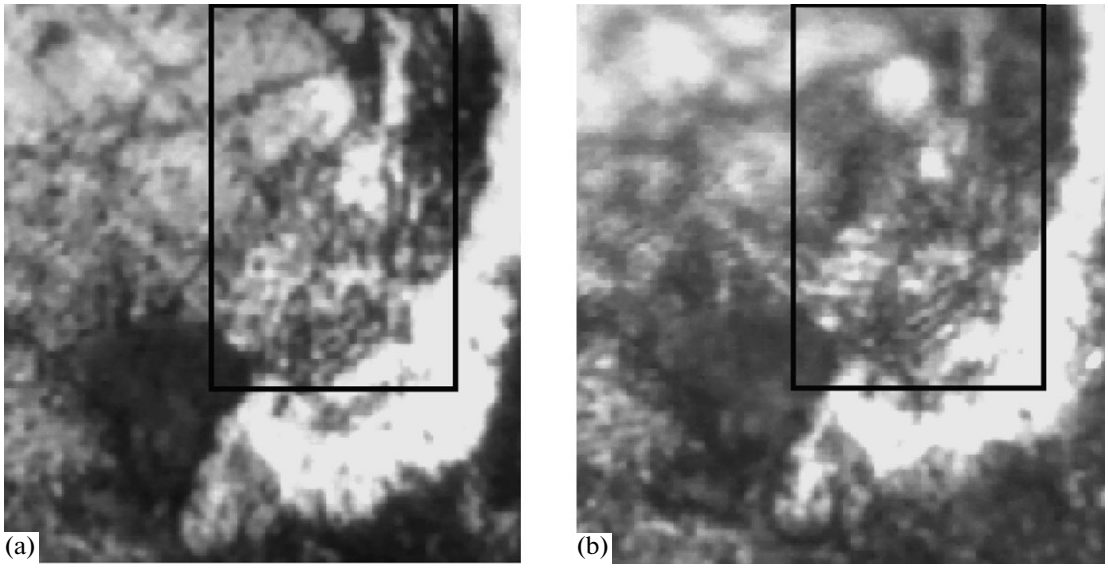

Fig. 6. Variation of the eutectoid structure (enlarged fragment of Fig. 5): (a) the initial state and (b) after two cycles of HFMPT.

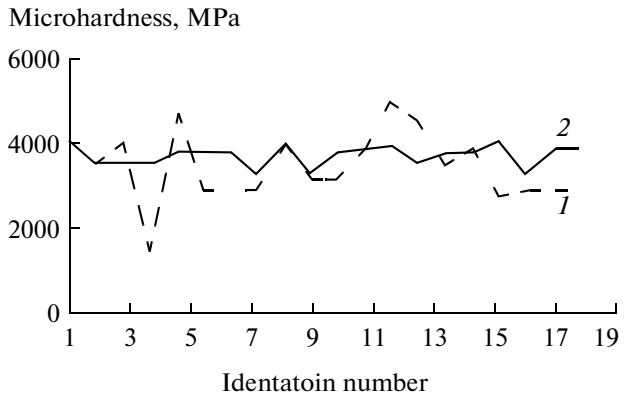

Fig. 7. Microhardness values of ring no. 7 in the initial state and after cycles of HFMPT.

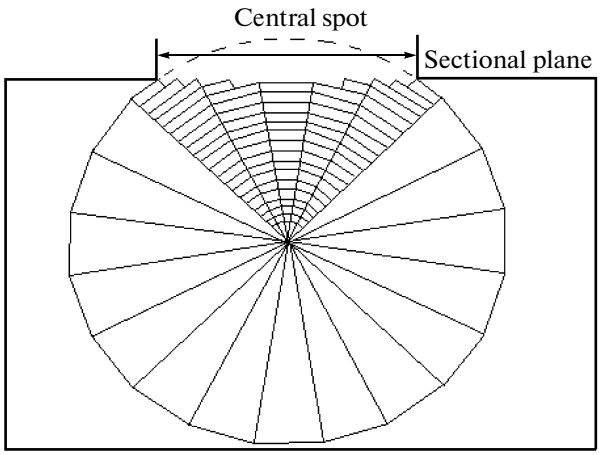

Fig. 8. Diagram of a graphite spherocrystal section according to the metallographic sample's plane.

(Table 4). The most significant increase in the hardness is found in rings numbers 5 and 7. In addition, we can see the influence of the HFMPT on the periodic variation of the HRC values of the rings depending on the number of cycles of their treatment.

A characteristic effect of the HFMPT is the variation in the internal structure of the spheroidal graphite, which is similar to the one found earlier by the authors of [4] for cast iron with platelike graphite.

According to [8], the structure type of the section of spheroidal graphite is determined by the position of the sectional plane with respect to the spherocrystal center (Fig. 8). In addition, there is a "central spot" that is recorded in the event that the sectional plane runs above the crystal center.

Figures 9 (the rectangular fragment) and 10 represent photomicrographs of inclusions of spheroidal graphite. The data show that the HFMPT results in the evolution of the structure of the central part of the inclusion accompanied by an increase in the central spot sizes.

Table 4. Variation in the HRC hardness of the rings as a result of the HFMPT

Ring number	Number of HFMPT cycles			
	0	2	4	6
1	63.600	66.450	53.800	65.950
2	73.100	74.650	73.950	75.200
3	71.850	71.350	70.300	71.800
4	73.625	74.450	73.050	74.700
5	73.900	75.350	74.800	76.450
6	74.300	69.780	72.850	74.950
7	73.450	77.550	76.500	76.150

The morphology of the fringe region of the inclusion varies with the tendency for forming flat facets.

The revealed variations in the structure of the graphite inclusions can be explained by several reasons. Among them, one can find the intensification of the diffusion processes, as well as the possible diffusion of carbon atoms along a flat facet in the central spot and variation in the step structure of the section periphery. The change in the intensity of the interference lines counts in favor of the variation in the carbon structure in a magnetic field [4]. We should also take into account the possible ferromagnetism of the cast-iron graphite both due to the great amount of ferromagnetic inclusions (iron) and due to the variation in the magnetic properties of the graphite in a magnetic field [9].

A variation in the stress state of the ferrite in cast iron can also have an effect on the graphite inclusion type by deforming it similar to the deformation of the diamond indenter of a microhardness gage [8], when concentric rings or polyhedra appear in the section. The results of the X-ray structure analysis show that mainly compression macrostresses take place in the ferrite phase under HFMPT (Table 5). The stress values are the difference between the stresses of the initial and treated samples. In the respective calculations, the stress of the first kind for the initial rings was taken equal to zero.

The stress state variation is connected with the change in the ring's resistance to tensile loads (Table 6). An increase in the compression stress level enhances the load resistance (decreases the inflection $d - d_0$, Table 6).

The variation in the pattern of the stress state of a sample is governed by the nonuniform distribution of the pressures in the sample under HFMPT (Fig. 11).

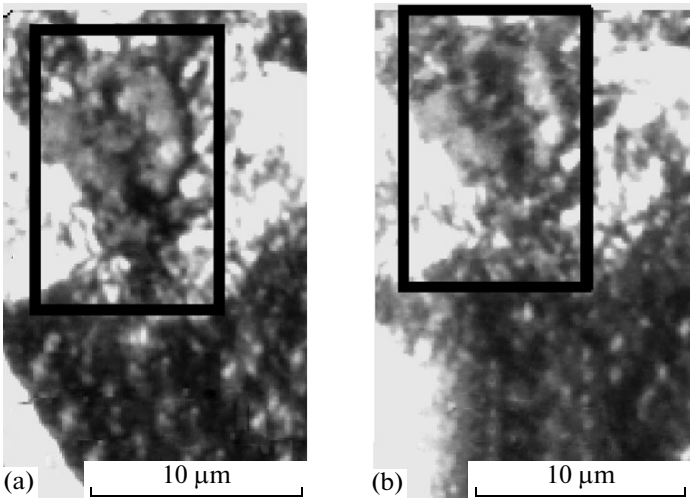

Fig. 9. Structure of a spheroidal graphite inclusion: (a) the as-received condition and (b) after two cycles of HFMPT.

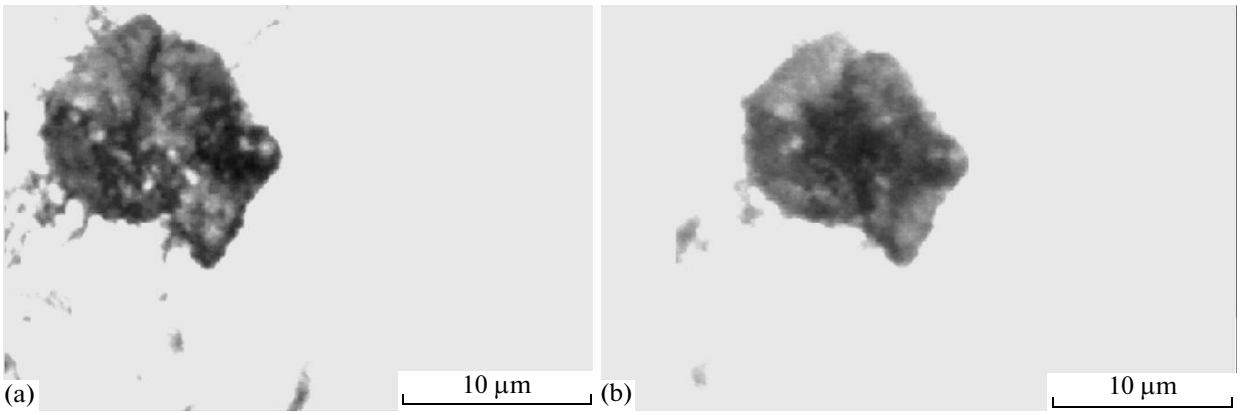

Fig. 10. Variation of the internal structure of a graphite inclusion: (a) the as-received condition and (b) after two cycles of HFMPT.

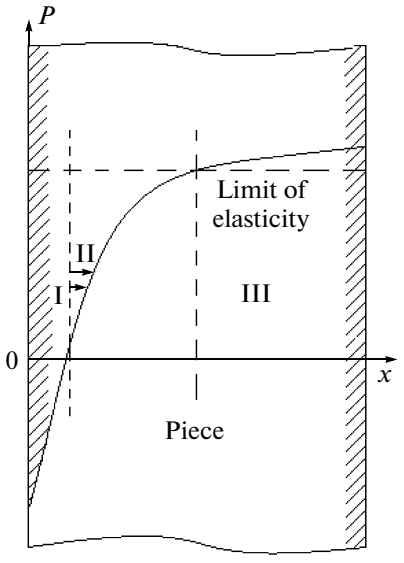

Fig. 11. Distribution of the pressures in a piece under a magnetic-pulse impact: II is the tensile region; I and III are the compression region [10].

Table 5. Variation of the value of the macrostresses in ferrite

Ring number	Δσ, MPa		
	2 HFMPT cycles	4 HFMPT cycles	6 HFMPT cycles
1	–0.692	0.576	1.614
2	–3.694	–3.636	0.462
3	–2.886	0.346	–2.651
4	–0.573	–0.459	–2.236
5	0.231	–0.115	0.519
6	–0.347	–0.116	–0.463
7	0.231	0.578	–0.346

Table 6. Variation in the ring inflection $d - d_0$ depending on the load weight m and the number of HFMPT cycles

Ring number	Load weight m, g	Ring inflection $d - d_0$, mm			
		0 HFMPT cycles	2 HFMPT cycles	4 HFMPT cycles	6 HFMPT cycles
1	150	1.00	2.00	3.25	2.10
2	175	3.75	5.13	4.10	4.25
3	200	3.00	4.75	4.00	2.25
4	225	6.50	12.75	9.80	12.00
5	250	7.00	7.00	6.00	4.80
6	275	11.00	14.25	8.50	11.10
7	300	8.00	4.75	9.50	6.75

According to the data of [10], the tensile and compression regions alternate in the section of a piece treated in a magnetic field. In zone *I*, the pressure has a negative value and, as applied to our case, it is directed towards the inductor and induces variations in the macrostresses that can be recorded by X-ray structure analysis.

CONCLUSIONS

The results of our studies are as follows.

(i) It is found that the HFMPT of SGCI sealing rings leads to variations in the eutectoid morphology, the internal structure of the graphite inclusions, and the sizes of the free cementite inclusions, which results in an enhancement of the ring's hardness.

(ii) It is revealed that the HFMPT of sealing rings induces compression stresses in them, which leads to the enhancement of the rings' hardness.

(iii) It is shown that the physicomechanical properties of the rings resulting from the HFMPT change periodically upon the variation in the number of treatment cycles. The optimum mode corresponds to two cycles.

REFERENCES

1. Bodyaka, A.M., Bevza, V.F., and Galagaev, S.V., Continuous-Cycle Free Casting is an Efficient Technology for Obtaining of High-Quality Preforms, *Lit'e Metall.*, 2005, no. 3 (35), pp. 20–27.

2. Marukovich, E.I., Bevza, V.F., and Grusha, V.P., Realization of the Concept of Wall Crystallization for Obtaining of High-Quality Hollow Cylindrical Preforms of Cast Iron, in *Materialy, tekhnologii i oborudovanie v proizvodstve, ekspluatatsii, remonte i modernizatsii mashin* (Materials, Technologies, and Equipment in Production, Operation, Maintenance, and Modernization of Machines), Novopolotsk, 2007, vol. 1, pp. 33–35.

3. Fokina, E.A., Kaletina, Yu.V., and Schastlivtsev, V.M., Specific Features of the Martensitic Transformation of Deformed Austenite in the 50N26 Alloy upon Cooling and Magnetic Treatment, *Fiz. Met. Metalloved.*, 2006, vol. 101, no. 4, pp. 381–391 [*Phys. Met. Metallogr.* (Engl. Transl.), vol. 101, no. 4, p. 355].
4. Anisovich, A.G., Rumyantseva, I.N., Bevza, V.F., and Azharonok, V.V., Variation in the Structure and Properties of СЧ-25 Cast Iron in a Pulsed Magnetic Field, *Sbornik trudov XV mezhdunarodnoi nauchno-tekhnicheskoi konferentsii "Mashinostroenie i tekhnosfera XXI veka"* (Proc. XV Int. Sci.-Tech. Conf. "Mechanical Engineering and Technosphere of XXI century"), Sevastopol, 2008, vol. 1, pp. 65–68.
5. Poletaev, V. A., Pomel'nokova, A. S., Shipko, M. N., and Vorob'ev, V.F., The Effect of Treatment in a Pulsed Magnetic Field and Corona Discharge on the Strength of Steels, *Metalloved. Term. Obrab. Met.,* 2000, no. 4, pp. 34–37.
6. Gvozdev, A.G., Borodin, I.P., Gvozdeva, L.I., Sushkova, T.V., and Pakhomov, A.A, Study of the Effect of Treatment in a Pulsed Magnetic Field on the Properties of 4Х5МФ1С Steel, *Materialy V Mezhdunarodnoi konferentsii "Prochnost' i razrushenie materialov i konstruktsii"* (Proc. V Int. Conf. on Strength and Damage of Materials and Structures), Orenburg, 2008, vol. 1, pp. 370–373.
7. Anisovich, A.G., Rumyantseva, I.N., Marukovich, E.I., Azharonok, V.V., and Goncharik, S.V., Structural Changes in СЧ-25 cast Iron in an Amplitude-Modulated High-Frequency Electromagnetic Field, *Elektron. Obrab. Mater.*, 2009, no. 2, pp. 47–56 [*Surf. Eng. Appl. Electrochem.* (Engl. Transl.), vol. 45, no. 2, p. 116].
8. Bunin, K.P., Malinochka, Ya.N., and Taran, Yu.N., *Osnovy metallografii chuguna* (Fundamentals of Metallography of Cast Iron), Moscow: Metallurgiya, 1969.
9. Makarova, T.P., Magnetic Properties of Carbon Structures: Review, *Fiz. Tekh. Poluprovodn.*, 2004, vol. 38, no. 4, pp. 641–664.
10. Bron, O.B. and Epechurin, V.P., Distribution of Pressures in a Workpiece under Magnetic-Pulse Treatment, *Kuznechno-Shtampov. Proizvod.*, 1968, no. 5, pp. 26–29.

ISSN 1068-3755, Surface Engineering and Applied Electrochemistry, 2010, Vol. 46, No. 2, pp. 108–114. © Allerton Press, Inc., 2010.
Original Russian Text © N.M. Chigrinova, A.A. Kuleshov, V.V. Nelaev, 2010, published in Elektronnaya Obrabotka Materialov, 2010, No. 2, pp. 27–34.

ELECTRICAL SURFACE TREATMENT METHODS

Microplasmaspark Alloying with Ultrasonic Surface Modifying

N. M. Chigrinova, A. A. Kuleshov, and V. V. Nelaev

Society of the Chemical Industry Institute of Welding and Protective Coatings, National State University Institute of the Metal Powder Industry, ul. Platonova 12B, Minsk, 220005 Republic of Belarus

e-mail: chigrinova@wpc-i.anitex.by

Received December 7, 2009

Abstract—The analysis of the physical processes in microplasmaspark material processing based on the effects of the electrodischarge plasma and mechanical impact with a varying intensity (MPA, MPA + UM, UM + MPA + UM) was carried out. The impossibility of a universal theory's construction describing the peculiarities of the above processes and being grounded on the basic principles of solid state physics was ascertained due to the given analysis. A new integrated approach valid both for the description of each of the described combined processing variants and for their comparative analysis is proposed, and it seems applicable for their parametric optimization. This approach for the physical interpretation of the experimental data set is based on the assumption that, during the transition from one mode of the cathode processing to another (from MPA to MPA + UM and to UM + MPA + UM), the initial structure state of the processed surface (that of the anode) undergoes an integral change that determines the structurization peculiarities at the subsequent alloying. The high correlation of the resilience properties, the resistance forces, the oscillation system's inertance, and the maximum values of the mechanical energy with the resultant properties of the coatings formed at various energies and mechanical impact intensities during the alloying has been noted.

DOI: 10.3103/S1068375510020043

INTRODUCTION

The effect of the electrodischarge plasma energy, along with the mechanical impact of various intensity (MPA and UM), on a material results in the activation of the processed surface, the increase of the internal energy of the material, the acceleration of the interaction processes in the anode–cathode system, the formation (at their vibro-impact contacting) of a thin transitional layer essential for the consequent diffusion saturation, and the creation and sustaining in the contact zones of the surface and bulk waves of the required degree necessary for the relaxation of the remaining tensions [1]. The problem of the MPA and UM parametetric optimization using a model of small vibrations of a system with a limited number of degrees of freedom is solved for the determination of the mechanisms and optimization of the modes of the combined energy effect at various intensities of the ultrasonic processing based on the developed physicomathematical models of the electrode erosion in the process of the microplasmaspark alloying and the calculation of the time of cooling of a droplet of the molten anode material [2].

The results of the experiments on the formation of the strengthened surfaces performed in trivariant microplasmaspark alloying are discussed from the unified theoretical positions [2]:

—Variant 1: Microplasmaspark alloying (MPA) along with a low frequency (~150 Hz) mechanical vibration of the anode. A strengthened surface with a stochastic character of the properties (composition, porosity, initial state) is created as a result.

—Variant 2: Microplasmaspark alloying with the consequent ultrasonic (at a frequency of $f > 20$ kHz) modifying of the cathode surface by means of vibration processing using the anode (MPA + UM). The formation of a surface with a more uniform microstructure, controllable porosity, and roughness with a reduced degree of the internal tensions is predicted.

—Variant 3: Preliminary mechanical vibrational high frequency (>20 kHz) anodic processing of the cathode surface with its subsequent microplasma alloying and ultrasonic modifying (UM + MPA + UM). The layers of a higher quality and regular structure with a reduced degree of internal remaining tensions are expected to be manufactured on a metal substrate with a random structure and hardness at the initial state.

1. THEORETICAL ANALYSIS

As follows from the analysis of the various physical mechanisms that contribute to the strengthened surface formation due to various combinations of the exterior effects (MPA, MPA + UM, UM + MPA + UM), it appears inaccessible to construct a universal theory based on the fundamental principles of the solid state physics that explains and predicts the results of each of the methods for the surface processing based on the MPA process.

In this relation, a new integrated approach valid both for the description of each of the studied variants of alloying and for their comparative analysis and, hence, adequate for their parametrical optimization is offered in [3]. The approach is based on a physical interpretation of the mass-transfer experimental data in the surface processing by the above methods. The nonuniform character modification of time of the value of $\Delta m/\Delta t$ for each of the studied alloying variants evidences for the modification in the course of time of the state of the contacting surfaces of the interacting electrodes due to various physical mechanisms and phenomena including the following:

—modification of the roughnesses of the cathode and anode surfaces, which leads to the timewise modifications of the conditions for the electrospark discharge onset according to Paschen' law [1];

—modification of the hardness of the materials of both electrodes in the near surface layers due to the mechanical hardening phenomenon;

—modification of the microstructure of the near surface areas of both of the electrodes due to their nanostructuring.

Thus, the offered approach for the physical interpretation of the set of the experimental data on the mass-transfer appears to be based on the assumption that, at the transition from one variant of the cathode processing to another (i.e., upon modification of the intensity and frequency of the mechanical impact), the state of the initial structure of the processed surface integrally changes, which in turn effects the subsequent development of the alloying. In terms of the theory of small oscillations of the systems with the final number of degrees of freedom, a set of such states can be interpreted in the form of the influence coefficients in a differential equation that describes the free oscillations of the mechanical systems in [4, 5]. This theory appears valid both for the optimization of the modes of the discussed variants of the microplasmaspark processing and for the prediction of the resulting properties of the surface being formed.

The overall view of the time dependency of the anode mass loss based on the experimental data analysis shows that the set of these results may be generally represented as a solution for the stochastic differential equation of second order. This choice is accounted for by the fact that the class of solutions for the first-order differential equation is too narrow: its solution has the form of an exponentially increasing or decreasing function, which dissatisfies the arguments of the universality of the problem being solved. The differential equation of a higher order appears invalid for attaining a more precise solution due to the arising calculation complexities. In addition, the coefficients of the higher order equations seem to lack an explicit physical content.

The behavior description of the system performing small oscillations is based on the assumption that its free oscillations decrease in real conditions, since its component elements are found to be effected by certain forces of the R_j resistance causing the dissipation of the overall mechanical (kinetic and potential) energy. For a mechanical system with stationary bonds that has a single degree of freedom, the length of the path r travelled by a point of the system is a function of the generalized coordinate q of this system depending on the time t [5]:

$$r = r(q).$$

Hence, the velocity of each system point is

$$\nu = \frac{\partial r}{\partial q} q \left(\overset{def}{=} \frac{dr}{dt} \right).$$

Suppose the force of the R resistance effecting certain i points of the system is proportional to the velocity:

$$R = -\mu\nu,$$

where μ_j is the corresponding coefficient of the proportionality.

In a general form, the summarized force of the resistance is determined as follows:

$$Q_R \overset{def}{=} R\frac{\partial r}{\partial q}.$$

Since

$$\nu = \frac{\partial r}{\partial t} = \frac{\partial r}{\partial q} q,$$

then

$$\frac{\partial \nu}{\partial q} = \frac{\partial r}{\partial q}.$$

Substituting these values into the expression of the generalized force of the resistance, one obtains

$$Q_R = -\mu\nu\frac{\partial \nu}{\partial q} = -\frac{\partial}{\partial q}\left(\frac{\mu\nu^2}{2}\right).$$

Let us introduce the dissipation function (the notion of it was presented by Rayleigh in the classic work of his "The Theory of Sound"), or the scattering function, whose form is identical to that of the expression for the kinetic energy:

$$\Phi = \frac{\mu\nu^2}{2}.$$

Then, the generalized forces of the resistance will be determined according to the following formula:

$$Q_R = -\frac{\partial \Phi}{\partial q}.$$

To write the differential equation of motion of the system with a single degree of freedom, one may use Lagrange's equation [220]:

$$\frac{\partial}{\partial t}\left(\frac{\partial T}{\partial \dot{q}}\right) - \left(\frac{\partial T}{\partial q}\right) = Q_P + Q_R, \quad (1)$$

where $Q_P = -\frac{\partial U}{\partial q}$ are the so called "regaining" forces that tend to bring the system into the equilibrium state, and T and U denote the kinetic and the potential energies of the system, correspondingly.

For the system with a single degree of freedom in the generalized system of coordinates, the expressions for the kinetic T, potential U, and dissipation Φ energies look as follows [4, 5]:

$$T = \frac{1}{2}a\dot{q}^2, \quad U = \frac{1}{2}cq^2, \quad \Phi = \frac{1}{2}b\dot{q}^2,$$

and the relevant generalized "regaining" forces Q_P and the forces of the resistance Q_R are

$$Q_P = -cq; \quad Q_R = -b\dot{q}^2.$$

Substituting these expressions into Lagrange's equation (1), one obtains

$$a\ddot{q} = -cq - b\dot{q}. \quad (2)$$

Let us introduce the designations such as

$$c = k^2/a; \quad b = 2n/a.$$

Then, equation (2) will be as follows:

$$\ddot{q} + \frac{2n}{a}\dot{q} + \frac{k^2}{a}q = 0. \quad (3)$$

Let us consider the general case of motion of the system with a single degree of freedom near the position of equilibrium when the points of the system are affected by the Q_P regaining forces (tending to return the system to the equilibrium state), the Q_R forces of resistance (counteracting the substrate's state modification), and the Q_F perturbing forces (determining the external effect on the system, i.e., of the electric parameters, monitoring the coating process). At $Q_F = 0$, i.e., at equation (3) with the right side being equal to zero, the forced oscillations of the system are absent: in the studied MPSA process, this state is relevant to the anode mass loss at the processing startup only.

Thus, the Lagrange equation for the system in question with account of the perturbing forces is

$$\frac{\partial}{\partial t}\left(\frac{\partial T}{\partial \dot{q}}\right) - \left(\frac{\partial T}{\partial q}\right) = Q_P + Q_R + Q_F.$$

By substituting the values of all of the indicated magnitudes (see Eqs. (1) and (2)) into this equation, one obtains

$$\ddot{q} + \frac{2n}{a}\dot{q} + \frac{k^2}{a}q = \frac{1}{a}Q_F(t). \quad (4)$$

Equation (4) is a generalized differential equation of the forced oscillations of the system with a single degree of freedom.

Considering the right hand side of equation (4) as that describing the Gaussian distribution with independent excesses, one may calculate the k, n, and a coefficients by which the forces of the resilience, resistance, and inertia of the system are brought into agreement. These coefficients are calculated on the basis of the uniform equation (3), which determines the free oscillations of the mechanical system in real conditions in the presence of the resistance forces that induce the mechanical energy dissipation of the system.

2. METHODS OF CALCULATION

The results of the calculations of the a, n, and k coefficients in the medium of the Mathematica software package are presented below along with the application of the experimental data obtained by the MPA methods at the mean voltage values of $U = 96$ V and the current of $I = 0.6$ A, along with the UM mean parameters of $U_{USM} = 125$ V and $I = 0.8$ A for the described variants of the alloying processes: MPA, MPA + UM, and UM + MPA + UM. The input parameters can be written as follows:

MPA:

$$\{\{0.5, 0.0050\}, \{1., 0.0100\}, \{1.5, 0.0115\}, \{2., 0.0045\}, \{2.5, 0.0175\}, \{3., 0.0180\}, \{3.5, 0.0190\}, \{4., 0.0200\}, \{4.5, 0.00205\}, \{5., 0.0215\}. \quad (5)$$

MPA + UM:

$$\{\{0.5, 0.00465\}, \{1., 0.0026\}, \{1.5, 0.0185\}, \{2., 0.00275\}, \{2.5, 0.0027\}, \{3., 0.00225\}, \{3.5, 0.0021\}, \{4., 0.00205\}, \{4.5, 0.00155\}, \{5., 0.0016\}. \quad (6)$$

UM + MPA + UM:

$$\{\{0.5, 0.00022\}, \{1., 0.00012\}, \{1.5, 0.00008\}, \{2., 0.00025\}, \{2.5, 0.00005\}, \{3., 0.00005\}, \{3.5, 0.00022\}, \{4., 0.00024\}, \{4.5, 0.00012\}, \{5., 0.0002\}. \quad (7)$$

The third order interpolation spline $S_3(x)$ is constructed according to the nodes of the interpolation of expressions (5), (6), and (7) while obeying the following:

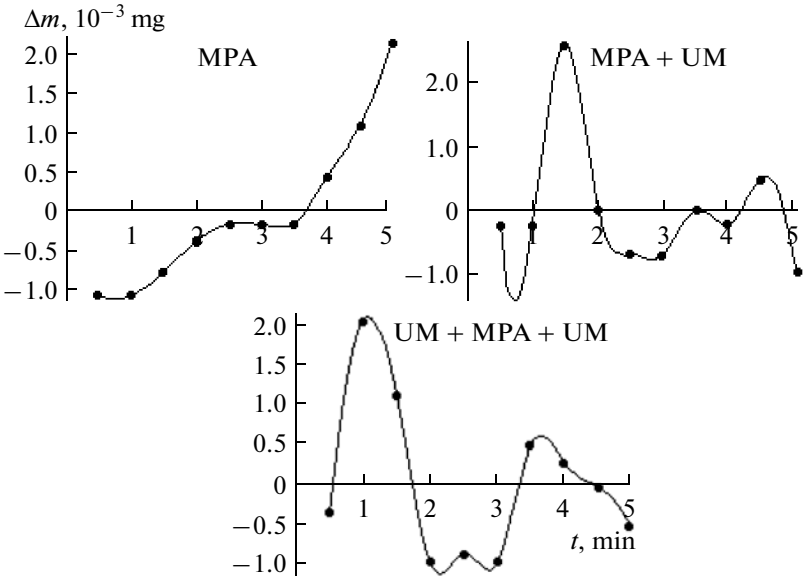

Fig. 1. Interpolation splines of the anode mass loss dependency Δm on the alloying time t.

(1) $S_3(x)$ is assumed to be a third order polynomial in each interval of time $[t_{k-1}, t_k]$, $k = 1, \ldots, 10$ at fixing the anode material mass-transfer;

(2) within the entire time interval of the alloying process under study (from 0.5 to 5 min [0.05, 5.0] $S_3(x)$), there are the continuous derivatives up to the ones of second order inclusively;

(3) $S_3(t_k) = f(t_k)$ are the values of the anode mass loss.

Figures 1 and 2 show the interpolation splines for the MPA, MPA + USM, and UM + MPA + UM processes, respectively.

The constructed splines are used for the recalculation of the quantity of the interpolation nodes (the initial time data is presented with a step of 0.5, and due to the spline interpolation it becomes possible to calculate the values of the anode mass loss at any t, since they are determined in each point of the time interval [0.5, 5.0] relevant to the initial moment of time of the experimental determination of the anode mass loss (0.5 min) and to the final one (5 min)). At the next stage, the calculation of the a, n, and k coefficients of Eq. (3) is produced. For this aim, the numeric integration of Eq. (3) is done for each of the technological variants of the alloying with the initial conditions that

$$y(0.5) = S_3(0.5), \quad y'(0.5) = S_3'(0.5).$$

This operation is performed with specified values of the a, n, and k coefficients until a certain group of the a, n, and k values (selected according to a special rule) attains the most optimal result (from the viewpoint of satisfying Eq. (4)). In this fashion, the a, n, and k coefficients were calculated for the MPA (5), MPA + UM (6), and UM + MPA + UM (7) at the metal substrate alloying in the MPA range of modes: $I = 0.6$ A, $U = 96$ V; UP: $I = 0.5$ A, $U = 85$ V; and UM: $I = 0.8$ A, $U = 125$ V:

$$\{k = 8.98433, n = 0.04965, a = 0.454860\}, \quad (8)$$

$$\{k = 0.00044, n = 1.56958, a = 0.673953\}, \quad (9)$$

$$\{k = 3.67472, n = 0, a = 0.841726\}. \quad (10)$$

The following stage of the described algorithm is the calculations of the right hand side of Eq. (4) according to the methodology of the calculation of the a, n, and k coefficients of uniform equation (3). In the given case, the c_k coefficients in the expansion of the

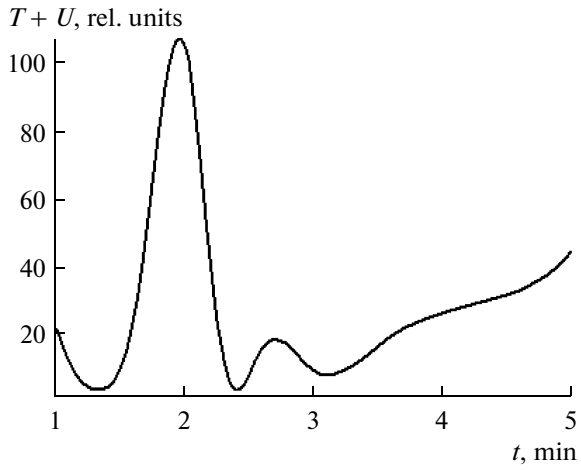

Fig. 2. The alloying time dependency t of the system's overall energy ($T + U$) at MPA in the mode of $I = 0.6$ A; $U = 96$ V.

Table 1. Experimental data of the anode mass loss

Time, min	Electrode Δm mass loss, g		
	MPA	MPA + UM	UM + MPA + UM
0.5	0.0050	0.00465	0.00022
1.0	0.0100	0.0026	0.00012
1.5	0.0115	0.00185	0.00008
2.0	0.0045	0.00275	0.00025
2.5	0.0175	0.0027	0.00005
3.0	0.0180	0.00225	0.00005
3.5	0.0190	0.0021	0.00022
4.0	0.0200	0.00205	0.00024
4.5	0.0205	0.00155	0.00012
5.0	0.0215	0.0016	0.0002

right hand side of the equation are calculated instead of the a, n, and k coefficients:

$$\frac{1}{a}Q_F(x) = \sum_{k=1}^{\infty} c_k J_0\left(\frac{z_k}{10-0.5}(x-0.5)\right), \qquad (11)$$

where $J_0(x)$ is Bessel's function of the first kind and zero order, and z_k denotes the roots of this function.

Let us determine the coefficients c_k confined to the final number of items in the right hand side of (5). The calculated right hand sides of Eq. (11) allow one to solve equation (4) and to predict the evolution of the anode mass loss for the future values of time at longer-term alloying.

Let us now analyze the calculations of the a, n, and k coefficients obtained using the described algorithm for the various variants of the microplasmaspark alloying (Table 1).

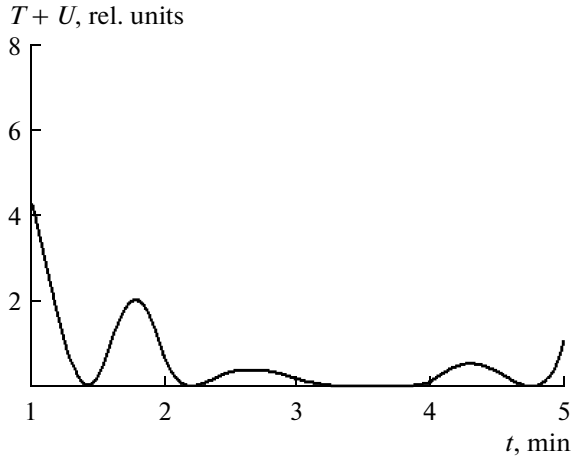

Fig. 3. The alloying time dependency t of the system's overall energy ($T + U$) at MPA + UM in the modes of MPA: $I = 0.6$ A, $U = 96$ V; UM: $I = 0.8$ A, $U = 125$ V.

Table 2. Calculated values of the k, n, and a coefficients and the overall (the kinetic T + the potential U) ($T + U$) energy of the system

Coefficients	Coefficient values		
	MPA	MPA + UM	UM + MPA + UM
k	8.98433	0.00044	3.67472
n	0.04965	0.56958	0
a	0.45486	0.673953	0.841726
$T + U$	110	9	30

Table 1 presents the values of the coefficients k, n, and a calculated within the framework of the offered algorithm of a numeric solution of Lagrange's equation describing the small vibrations of the system and the interpretative state of the anode and cathode contacting surfaces for the same modes of the combined processes under study.

The analysis of the data from Table 2 shows that, in the triple processing of UM + MPA + UM, the k coefficient, which characterizes the system's resilience, is less than the one at the standard MPSA alloying. The decrease of the cathode surface's roughness (due to the preliminary ultrasonic processing) is considered to be responsible for the k coefficient's value reduction in the case of the intensified method, which promotes the elimination of the stochastic character of the created conditions for the spark discharge initiation. The n coefficient determining the system's resistance at the triple alloying, vice versa, appears to be higher, which indicates the more rapid decay of the system's oscillations. In the conventional MPSA, the latter implies the faster transition of the anode mass loss velocity to the stationary mode. A higher coefficient a value characterizing the inertance of the oscillation system suggests a more gradual decline of the stochastic character of the spark discharges at the USM + MPSA + USM due to the increase of the cathode surface's hardness resulting from the preliminary USM.

As follows from expressions (1–3), the state of the anode–cathode simulated model is characterized by its kinetic T and potential U energies along with their sum ($T + U$). Figures 2–4 show the time dependencies of the overall energy of the system under study for each of the alloying variants being compared.

Justification tests of the performed optimization calculations were performed via the experiments on fixing the cathode de-erosion value (Fig. 5) with respect to the microstructure state of the processed surface (Fig. 6) and the thicknesses of the created coatings (Fig. 7) in the surface processing in accordance with the studied variants within the optimal range of the electric modes of the MPA and UM.

One can see the advantages of the triple processing from the figures presented below.

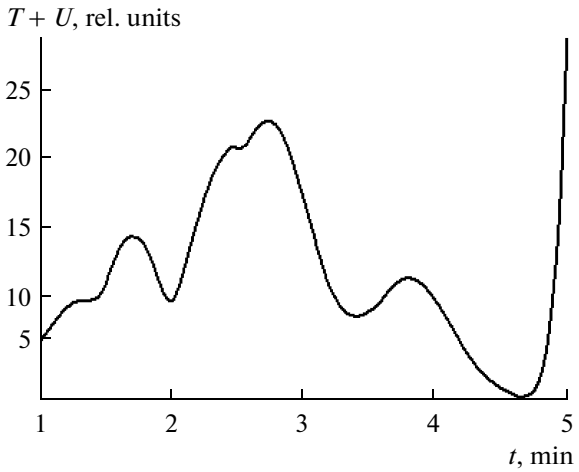

Fig. 4. The alloying time dependency t of the system's overall energy ($T + U$) at UM + MPA + UM in the modes of MPA: $I = 0.6$ A; $U = 96$ V. UM (before): $I = 0.5$ A; $U = 85$ V. UM (after): $I = 0.8$ A; $U = 125$ V.

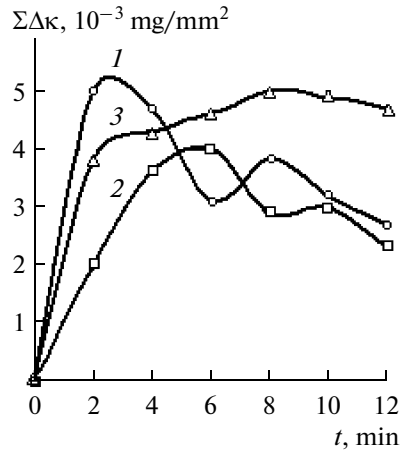

Fig. 5. Influence of the intensity of the energy impact on the cathode de-erosion value at the *P6M5* steel alloying by the electrode from the *BK* in the optimal modes of the combined processing. *1*—MPA; *2*—MPA + UM; *3*—UM + MPA + UM.

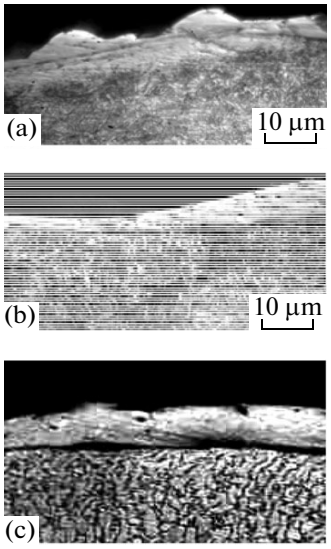

Fig. 6. Microstructure of the coating on the steel *P6M5* after MPA (a), MPA + USM (b), and UM + MPA + UM (c) in the optimal range of the electric modes.

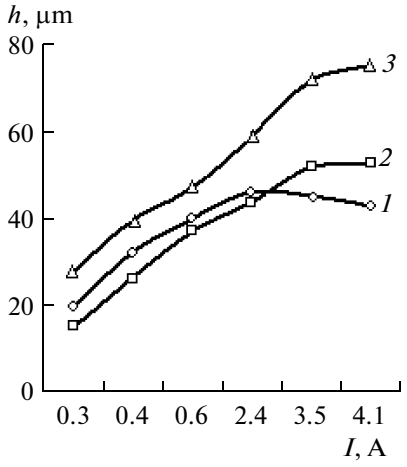

Fig. 7. Effect of the processing method on the thickness of the created coating on the surface of the *P6M5* steel substrate at the strengthening in the optimal range of the electric modes. *1*—MPA; *2*—MPA + UM; *3*—UM + MPA + UM.

CONCLUSIONS

A vivid correlation between the resilience properties, the resistance forces, the inertance of the anode–cathode oscillation system, and also between the maximal values of its mechanical energy and the properties of the coatings developed by the alloying variants under study was noted based on the performed data analysis. The highest resilience of the system (determined by the k coefficient's value) and the minimal resistance to the energy impacts (determined by the n coefficient's value) at the microplasmaspark processing, combined with the high inertance of the anode–cathode system and the maximal overall kinetic energy, can be attained upon processing in the following modes using the following:

—the conventional method of the MPA: $I = 0.3$ A, $U = 45$ V;

—the method of the MPA + UM: $I = 0.4$ A, $U = 67$ V; UM: $I = 0.8$ A, $U = 125$ V;

—the method of the UM + MPA + UM: $I = 2.4$ A, $U = 67$ V; UM (before): $I = 0.5$ A, $U = 85$ V; UM (after): $I = 1.3$ A, $U = 125$ V.

It is only for the calculated modes of the processing that the optimal indices of the developed surface state, the mass-transfer velocity, and the maximal and uni-

form thicknesses of the created coatings are accomplished.

REFERENCES

1. Chigrinova, N.M., Quality Improvement of the Metal Articles by the Microplasmaspark Alloying Method with the Ultrasonic Modification, *Trudy 12-ogo mezhdunarodnogo simposiuma "Tekhnologii. Oborudovanie. Kachestvo"* (Proc. 12th Int. Symposium "Technologies. Equipment. Quality"), Minsk, 2009, pp. 115–117.
2. Chigrinova, N.M., Physical and Mathematical Models of the Microplasmaspark Alloying with the Discrete Ultrasonic Effect, *Trudy mezhdunarodnoi nauchnoi konferentsii "Impul'snye protsessy v mekhanike sploshnykh sred"* (Proc. Int. Sci. Conf. "Pulse Processes in the Mechanics of Solids"), Nikolaev, Inst. Impuls. Prots. i Tekhnologii NAS Ukraine, p. 114–115.
3. Chigrinova, N.M., Concept Elaboration of the Energy Intensification Simulation in the Microplasmaspark Processing in a Gas Medium, *Trudy mezhdunarodnoi konferentsii po kompositsionnym materialam v promyshlennosti* (Proc. Int. Conf. on Ind. Composit. Mater.), Slavpolikom, pp. 124–127.
4. Vladimirov, V.S., *Uravneniya matematicheskoi fiziki* (The Equations of Mathematical Physics), Handbook, Fifth ed., Moscow: Nauka, 1988.
5. Landau, L.D., Lifshits, E.M., *Mekhanika* (Mechanic), Moscow: Nauka, 1988.

ISSN 1068-3755, Surface Engineering and Applied Electrochemistry, 2010, Vol. 46, No. 2, pp. 115–119. © Allerton Press, Inc., 2010.

ELECTRICAL SURFACE TREATMENT METHODS

Comparative Study of the Morphological Degradation in Nickel Thin Films Exposed to H_2S Media and Deposited by Magnetron Sputtering and Electrolytic Process[1]

C. Magaña-Zavala[a], M. E. Angeles-San Martin[b], F. J. Rodríguez-Gómez[c], D. R. Acosta[a], R. Avila-Godoy[d], and A. López-Suárez[a]

[a] *Instituto de Física, Universidad Nacional Autónoma de México, Ap. Postal 20-364, México, D.F. 01000, México*

[b] *División de Estudios de Posgrado e Investigación, Departamento de Polímeros, Institute Tecnológico de Cd. Madero*

[c] *Departamento de Ingeniería Metalúrgica, Facultad de Química, Universidad National Autónoma de México 04510, México D. F., México*

[d] *Universidad de los Andes. Mérida Venezuela*

e-mail: craul@fisica.unam.mx

Received December 7, 2009

Abstract—Nickel thin films with regular configuration and similar thickness were deposited on steel AISI 1018 (UNSG 10180) by two different techniques: magnetron sputtering and electrolytic process. The main aim of this work is to compare the surfaces deposited films made by the two techniques using the scanning electronic microscopy and to identify their morphological differences and imperfections. We evaluate the protective coatings properties when the films are in contact with an acid medium. We also study the thin films coatings by the spectroscopy impedance technique. We obtain that the sputtering deposits present a homogeneous thin film coating that is better than the one obtained by the electrolytic technique. It is expected that the thin film coatings made in this work can protect the steel against corrosion when it is in contact with an acid environment.

DOI: 10.3103/S1068375510020055

1. INTRODUCTION

Corrosion process in H_2S environment has been widely studied [1–3] due to the interest that petrochemical industry have shown to understand the mechanisms involved in corrosion processes The presence of sulphides compounds in pipelines and tanks that are used to store and transport oil and gas has resulted in economical losses to petrochemical industry because corrosion produces failures in pipelines and equipments due to wet cracking. Many works have been focused on the inhibition corrosion mechanisms in the presence of sulphide species, as well as on the development of protective coatings that guarantee the isolation of this aggressive media to the materials used as storage. Petrochemical industry has been used widespread the carbon steel on pressure vessels, pipelines and other equipments; nevertheless, this material and its welded joints are easily attacked by the sulphur atoms during corrosion events.

Metallic coatings can be used as a protective film in sulfurous media because their properties promote the resistance to oxidation [4, 5]. In the present work we study the properties of a passive nickel film deposited on a steel sheet by two different techniques. This nickel film can be used as a protective film for the metallic substrate because the interaction of the electrolytes will occur with the nickel oxide instead of the nickel metal or the steel. The deposition techniques used in this work were the magnetron sputtering and the electrolytic deposit. Magnetron sputtering [6, 7] has been reported in literature as a promising technique in the deposit of metallic thin films, even in large areas, acting as an anticorrosive barrier [8–10].

2. EXPERIMENTAL

Mild carbon steel AISI 1018 (UNSG 10180) sheets ($2 \times 2 \times 0.1$ cm) were used during the study. Samples were exhaustively cleaned, degreased and washed with a commercial detergent. Afterwards they were ultrasonically cleaned using acetone during 10 min. In order to finish the cleaning process, these samples were dried.

Once the steel samples were cleaned, they were coated with nickel using two different techniques in order to obtain different deposit characteristics. The first technique was the electrolytic film deposit, where a typical Watt's bath [11] was employed. The electrolytic solution used during the film deposit was 1.07 M $NiSO_4$, 0.15 M $NiCl_2$ and 2.38 M H_3BO_3; the process

[1] The article is published in the original.

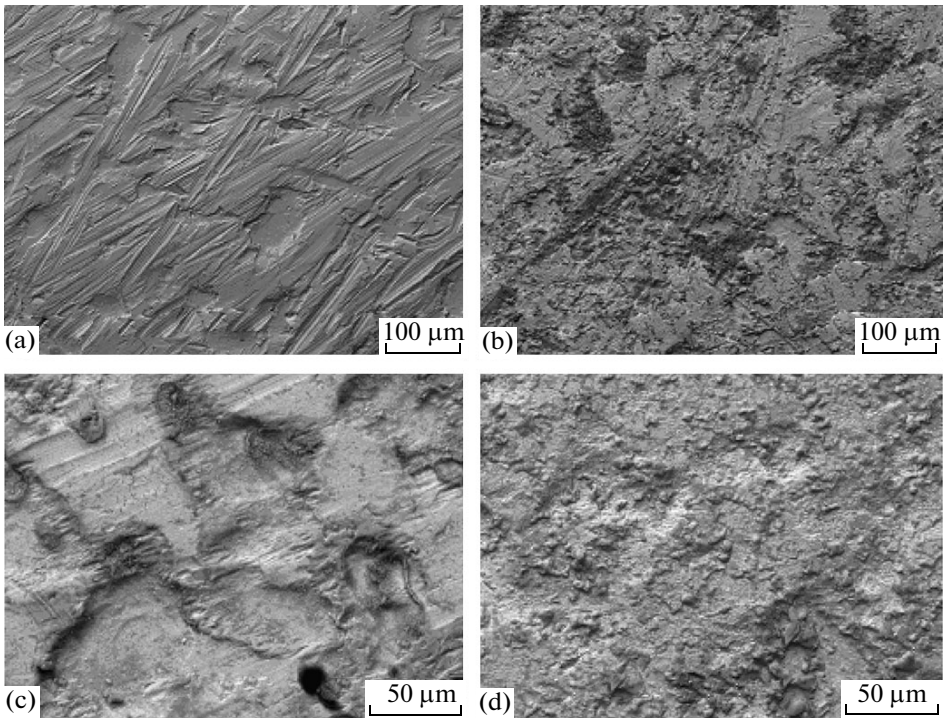

Fig. 1. SEM micrographs of: (a) Steel-Nickel made by sputtering process, (b) Steel-Nickel made by electrolytic process, (c) Steel-Nickel made by sputtering with a nickel oxide film, (d) Steel-Nickel made by electrolytic process with a nickel oxide film.

was galvanostatically carried out with a current density of 0.08 A/cm^2 and a pH = 4. The steel samples were immersed in the bath at 60°C for 90 s. The second technique carried out during the study was the magnetron sputtering technique using a 99.99% nickel circular target with a 500 mm diameter and a 6 mm thickness. 99.99% purity argon was used as the gas during the plasma process. The sputtering pressure, the potential and the time during the deposit were 34.6 Pa, 1000 V and 15 minutes, respectively. These values were kept constant during all the deposits.

Structural, morphological and topological studies of the samples surfaces were carried out using a scanning electron microscope Jeol 5600-LV. The SEM micrographs were obtained with backscattering electrons at 20 kV. Samples were observed without any special (metallic) recovering in order to study the surface characteristics of the as-deposited films, as well as the ones that were electrochemically attacked during the corrosion processes. Cross fractured sectional samples were also prepared to determine the films thickness from SEM observations.

For this study, the nickel oxide film NiO_2 [12–15] was electrochemically obtained. The synthesis of nickel oxide thin films procedure was controlled by an ACM Gill AC potentiostat version 4.2.9 used in the polarization mode. An over potential around 1500 mV and a 15 min exposure in a solution of 28 wt % NaOH at pH 12 (current density = 6.5 mV/min) was used. The Electrochemical Impedance Spectroscopy (EIS) technique was employed for the evaluation and characterization of the nickel thin films in order to identify imperfections in the films and to evaluate the protective properties when the metal is put in contact with the acid medium. The typical configuration of three electrodes was the following: platinum wires were used as reference together with auxiliary electrodes, while a coated sample was used as the working electrode. The electrochemical measurements were carried out in an aggressive acid media (saturated, pH = 3): $H_2O + H_2S$. The impedance conditions used during this test were the following: maximum and minimum frequencies 10.000 and 0.01 Hz, respectively; amplitude of 10 mV and the number of integration of 10 cycles.

3. RESULTS AND DISCUSSION

3.1. SEM Results

From SEM observations, it was found that film thickness was 1300 nm in average. The SEM micrographs show an irregular texture in the surface of the mild steel in all the samples. After applying the different nickel deposits and evaluating them by SEM, difference in texture and morphology has been detected. It was observed that samples made by the electrolytic deposition technique (Figs. 1b and d) show an increase in their surface roughness compared to those made by the sputtering technique (Figs. 1a and c). This behavior can be due to the way the samples were made. In the case of the sputtering deposition, the film

is deposited in a regular way forming a homogenous film, contrary to the way it is formed when the electrolytic technique is used. The heterogeneity of the sample's surface made by electrolytic deposit is shown as roughness, porosity, unfilled zones and fractures. This heterogeneity was observed on the samples even before their exposure to the corrosive environment, what make us think that the nickel deposit made by the Watt's bath technique is a deficient deposit technique. Actually, nickel deposit coming from the acid bath produces internal stresses in the coating as is explain in references [16–18]. Samples with the nickel oxide layer also show non regular deposits (see Fig. 1d) and imperfections in the surface that could result in localized corrosion.

On the other hand, the surface of Steel-Nickel coating made by sputtering is shown in Fig. 1a. A more regular texture in almost all specimens made by this technique was obtained. The morphology of the coating shows that nickel has grown in the same way as the steel substrate without any pores or pollution.

After oxidation of these non homogenous films a localized damage can be observed. This oxidation is promoted by the defects produced during the electrolytic deposit as can be seen if Fig. 1d, and not due to the NaOH electrolyte. This is a clear example that a poor application of a protective coating at a small depth in a material results in localized corrosion and damage, instead of getting a protective layer on the substrate.

Figure 1c does not show the presence of localized corrosion for the sputtering deposit of nickel followed by the film oxidation. We think that the sputtering process is able to cover the "valleys and peaks" present in the steel surface. Even if this surface seems to be more heterogeneous than the electrolytic nickel one, no defects were observed in the coating.

3.2. Electrochemical Impedance Spectroscopy (EIS)

Nyquist and Bode diagrams present the spectra of corrosion process evaluating the different coatings. A noisy signal as well as some disperse points complicated the explanation of the behavior of Nyquist diagrams. In the same way, Bode diagrams show different time mechanism for all the deposits and techniques, which didn't allow making any kind of analysis for the results, even using a Faraday's cell. We continue working on Bode diagram in order to get a better understanding of our results. To explain three different steps during the electrochemical process, Bode values that correspond to three zones with different frequencies (10^0, 10^1, 10^2 Hz) were chosen Fig. 2 shows the impedance spectroscopy results in presence of $H_2O + H_2S$ (sat) that correspond to the mild steel, the sputtering and the electrolytic techniques, as well as their respective oxides. The aim of this test was to compare both deposit techniques.

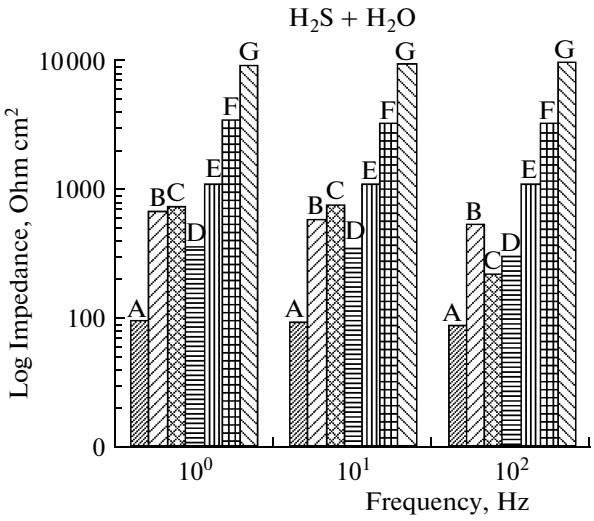

Fig. 2. Behavior of different materials exposed to $H_2O + H_2S$ electrolyte for frequencies of 10^0, 10^1 and 10^2 Hz with the Bode values, for the following coatings materials: (A) mild steel, (B) Ni bulk, (C) Ni bulk oxide, (D) steel Ni electrolytic, (E) steel Ni electrolytic oxide, (F) steel Ni sputtering, (G) steel Ni sputtering oxide.

As can be seen in Fig. 2 the impedance's value of mild steel exposed to this media is the lower value obtained for all the frequencies used in this work. It means that mild steel behaves as the most corrosive material even though it is compared with the films made by the electrolyte deposit. The corrosion rate can be measured by an indirect way using the impedance values and the Stern and Geary equation. The impedance values indicate an inverse relation with Rp.

The results show that nickel bulk and his oxide layer present a better behavior than mild steel for any frequency. This fact demonstrates that nickel is a good option to be used as an inhibitor barrier for this media. The nickel thin film coating in any configuration presents better impedance values than the one obtained by the naked steel. It was also seen that nickel and nickel oxide deposited by the electrolytic technique show better properties than the mild steel and even than the nickel bulk for all the frequencies studied in this work. The electrolytic depositions showed total protection for this medium.

Nickel and the nickel oxide deposited by sputtering show the higher impedance value compared with other deposits. From another point of view, the corrosion rate is lower in the presence of the steel nickel sputtering oxide when compared to mild steel. These values are those who have the higher anticorrosive properties for this media.

When performing the impedance characterization to the Nickel/Nickel oxide (NiO_2) it shows that its anticorrosive protection is much better than the protective coating formed on other samples. In the presence of saturated water with sulfhidric acid, the nickel

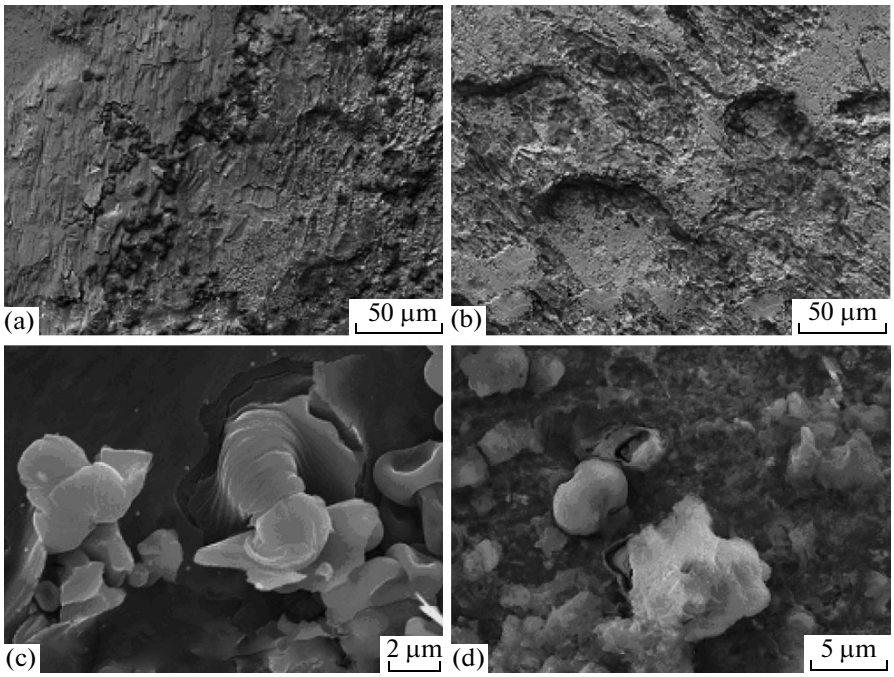

Fig. 3. SEM micrographs of nickel corrosion products in the thin film deposits after Impedance technique with $H_2O + H_2S$ (Sat) electrolyte. (a, c) Steel-Nickel Sputtering Oxide, (b, d) Steel-Nickel electrolytic Oxide.

oxide can act as a protective film that presents the properties of being highly adherent and stable.

Differences between the nickel film textures made by the sputtering process and the electrolytic deposit are shown in Figs. 3a and b, respectively. The coating which presents the worst deterioration in the surface is the electrolytic nickel oxide. However, this was observed before the pre-oxidation process and also after the coating was exposed to the sulphur media.

The coatings, after the electrochemical test, present surface corrosion attack. The coating in both cases has been deteriorated, but in the case of the electrochemical coating the destruction of the film was more aggressive than the one presented when it was done by the sputtering coating.

The behavior observed during the impedance test can be related with the SEM micrographs. The best impedance values got from the nickel coatings were obtained by the sputtering technique. In Fig. 3c, the film brake down in located corrosion type. This micrograph shows that the film is not destroyed completely, but the corrosion product grew from inside the metal to its surface. A devastation of the surface sample in the case of the electrolytic process in shown in Fig. 3d, where steel nude zones are exhibited and no presence of the nickel film is observed. The best anticorrosive properties are presented in the case of the steel-nickel sputtering oxide thin film. The presence of the oxide in the film created a dramatic modification of the surface film, which promoted a passive barrier. This effect inhibited the interaction of electrons between the metallic interphase and the electrolyte reducing the corrosion rate.

The corrosion behavior of the coated steel is strongly influenced by the deposit technique. It not only depends on the electrochemical properties of the coating, but also on the surface defects (such as roughness, deposited droplets, porosity, cracks and scratches) present in the coating. This result can be observed in the micrographs showed in this work.

4. CONCLUSIONS

The nickel coatings made by sputtering present homogeneity in the entire surface, contrary to the results obtained by the electrolytic deposit, which can be corroborated by the impedance results. Electrochemical characterization shows that work must be done in the electrolytic deposit process in order to form a thicker coating that can be able to protect the steel from the corrosive acid media. We obtained that nickel oxide sputtering thin film supports the corrosive media much better than the other coating techniques do. The EIS technique seems to be suitable to evaluate the optimal thickness in the metallic thin film.

ACKNOWLEDGMENTS

The authors wish to thanks to J. Genescá, C. Ojeda, G. Rayo, J. Morales, H. Manjarrez, J. Martínez, N. González, C. Ramirez, C. Rodriguez, M. Aguilar and I. Puente, as well as the Laboratorio

Central de Microscopía IFUNAM for the performance in this work.

REFERENCES

1. Albarran, J.L., Martinez, L., and Lopez, H.F., Effect of Heat Treatment on the Stress Corrosion Resistance of a Microalloyed Pipeline Steel, *Corros. Sci.*, 1999, vol. 41, pp. 1037–1049.
2. Tresseder, R.S., Staehhle, R.W., et al., *Stress Corrosion Cracking and Hydrogen Embrittlement of Iron Base Alloy*, NACE, Houston: TX, 1977.
3. Naki, Y., Kurahashi, H., Emi, T., and Haida, O., Macrosegregation in Steel Strands and Ingots: Characterisation, Formation and Consequences, *ISIJ Trans.*, 1979, vol. 19, pp. 401–410.
4. Vacandio, F., Massiani, Y., et al., Influence of Various Nickel Under-Layers on the Corrosion Behaviour of AIN Films Deposited by Reactive Sputtering, *Surf. Coat. Technol.*, 2001, vol. 137, pp. 284–292.
5. Franco, C.V., Fontana, L.C., et al., An Electrochemical Study of Magnetron-Sputtered Ti- and TiN-Coated Steel, *Corros. Sci.*, 1998, vol. 40, pp. 103–112.
6. Sanders, D.M. and Anders, A., Review of Cathodic Arc Deposition Technology at the Start of the New Millennium, *Surf. Coat. Technol.*, 2000, vols. 133, 134, pp. 78–90.
7. Ordine, A., Achete, C.A., Mattos, O.R., Margarit, I.C.P., Camargo, S.S., Jr., and Hirsch, T., Magnetron Sputtered SiC Coatings as Corrosion Protection Barriers for Steels, *Surf. Coat. Technol.*, 2000, vols. 133, 134, pp. 583–588.
8. Mankowski, J., The Pitting Corrosion of Plasma Nitrided Chromium Steels in Sulphate Solution, *J. Flis, Corros. Sci.*, 1993, vol. 35, pp. 111–116.
9. Morita, R., Azuma, K., Inoue, S., et al., Corrosion Resistance of TiN Coatings Produced by Various Dry Processes, *Surf. Coat. Technol.*, 2001, vol. 136, pp. 207–210.
10. Mehmood, M., Akiyama, E., Habazaki, H., et al., The Effect of Heat Treatment on the Corrosion Behavior of Sputter-Deposited Aluminum-Chromium Alloys, *Corros. Sci.*, 1998, vol. 41, pp. 477–499.
11. *A.S.M. Handbook Corrosion*, 9th, Ed. by American Society of Metals, USA: International Committee, 1992, vol. 13.
12. Abdusalam, M.I. and Pickering, H.W., Effect of the Applied Potential on the Potential and Current Distributions within Crevices in Pure Nickel, *Corros. Sci.,* 1999, vol. 41, pp. 351–352.
13. Cheng, X., Ma, H., et al., Corrosion of Nickel in Acid Solutions with Hydrogen Sulphide, *Corros. Sci.*, 2000, vol. 42, pp. 299–311.
14. Czerwinski, F. and Szpuunar, J.A., Controlling the Surface Texture of Nickel for Hightemperature Oxidation Inhibition, *Corros. Sci.*, 1999, vol. 41, pp. 729–740.
15. De Gromoboy, T.S. and Shreir, L.L., The Formation of Nickel Oxides during the Passivation of Nickel in Relation to the Potential/pH Diagram, *Electrochim. Acta*, 1996, vol. 11, pp. 895–904.
16. Perdomo, J.J. and Song, I., Chemical and Electrochemical Conditions on Steel under Disbonded Coatings: the Effect of Applied Potential, Solution Resistivity, Crevice Thickness and Holiday Size, *Corros. Sci.*, 2000, vol. 42, pp. 1389–1415.
17. Seah, K.H.W., Thampuran, R., and Teoh, S.H., The Influence of Pore Morphology on Corrosion, *Corros. Sci.*, 1998, vol. 40, pp. 547–556.
18. Park, H. and Szpuunar, J.A., The Role of Texture and Morphology in Optimizing the Corrosion Resistance of Zinc-Based Electrogalvanized Coatings, *Corros. Sci.*, 1998, vol. 40, pp. 525–545.

ISSN 1068-3755, Surface Engineering and Applied Electrochemistry, 2010, Vol. 46, No. 2, pp. 120–126. © Allerton Press, Inc., 2010.
Original Russian Text © A.I. Grigor'ev, V.A. Koromyslov, S.O. Shiryaeva, 2010, published in Elektronnaya Obrabotka Materialov, 2010, No. 2, pp. 41–48.

ELECTRICAL PROCESSES IN ENGINEERING AND CHEMISTRY

On Corona Discharge near the Surface of a Water Layer Nonlinear Oscillating in an External Electrostatic Field on the Surface of a Melting Hailstone

A. I. Grigor'ev, V. A. Koromyslov, and S. O. Shiryaeva

Demidov State University, Yaroslavl, ul Sovetskaya 14, Yaroslavl, 150000 Russia

e-mail: grig@uniyar.ac.ru

Received November 10, 2009

Abstract—The solution to the problem of nonlinear oscillations of a water layer on the surface of a melting hailstone in a uniform external field is found. The electric field intensity near a hailstone's surface is calculated. It is shown that the electric field intensity on the hailstone tops is sufficiently high for the ignition of a corona discharge.

DOI: 10.3103/S1068375510020067

INTRODUCTION

The study of the possibility of the ignition of a corona discharge near the surface of a melting hailstone in a cumulonimbus cloud is of considerable interest for the theory of thunderstorm electricity [1–3], because, according to the current conceptions, it is this discharge that initiates lightning strikes. Nevertheless, many problems related to the possibility of corona discharge ignition in the neighborhood of large droplets and melting hailstones have been scarcely studied up till now. This situation has initiated this work.

FORMULATION OF THE PROBLEM

We shall solve the problem of the determination of the electric field intensity near the surface of a nonlinear oscillating spherical layer of a perfectly conducting incompressible liquid with the radius R on the surface of a solid spherical nucleus R_0. We shall assume that the liquid has the density ρ and the surface tension coefficient σ and that the entire hailstone is situated in a uniform electrostatic field with the intensity E_0. The whole analysis will be exercised in dimensionless variables where $R = \sigma = \rho = 1$ in spherical coordinates with the origin in the center of mass of the system. Thereupon, the free liquid surface equation is written in the form

$$F(r, \vartheta, t) = r - 1 - \xi(\vartheta, t) = 0, \quad |\xi| \ll 1.$$

The liquid flow is set to be potential; that is, we shall assume that the field of the velocities $V(r, t)$ (the wave motion in the liquid layer) is completely determined by the velocity potential function $\psi(r, t)$ by the known correlation: $V(r, t) \equiv \nabla\psi(r, t)$.

The mathematical formulation of the problem of the calculation of the nonlinear oscillations of a liquid layer on the surface of a solid spherical nucleus consists of the Laplace equations for the velocity field potential $\psi(r, t)$ and the electrostatic potential $\Phi(r, t)$:

$$\Delta\psi(r, t) = 0; \quad \Delta\Phi(r, t) = 0,$$

and the boundary conditions to them:

$$r = 1 + \xi: \quad \Phi(r, t) = 0; \quad \frac{\partial\xi}{\partial t} = \frac{\partial\psi}{\partial r} - \frac{1}{r^2}\frac{\partial\psi}{\partial\vartheta}\frac{\partial\xi}{\partial\vartheta};$$

$$-\frac{\partial\psi}{\partial t} - \frac{1}{2}(\nabla\psi)^2 + \frac{(\nabla\Phi)^2}{8\pi} - div\, n = 0;$$

$$r \longrightarrow \infty: \quad -\nabla\Phi(r, t) \longrightarrow E_0; \quad r = R_0: \quad \partial\psi(r, t)/\partial r = 0.$$

In the written correlations, Δp is the constant pressure difference inside and outside the liquid in the equilibrium state, and $n \equiv \nabla F(r, \vartheta, t)/|\nabla F(r, \vartheta, t)|$ is the unit vector of the outer normal to the droplet surface.

The following conditions must also be taken into account: the absence of an intrinsic electric charge of the hailstone at the initial instant:

$$-\frac{1}{4\pi}\oint_S (n\nabla\Phi)dS = 0; \quad S = \begin{cases} r = 1 + \xi(\vartheta, t); \\ 0 \le \vartheta \le \pi; \\ 0 \le \varphi \le 2\pi; \end{cases}$$

the constancy of the liquid layer volume:

$$\int_{V_1} r^2 dr \sin\vartheta\, d\vartheta\, d\varphi = \frac{4}{3}\pi(1 - R_0^3);$$

$$V_1 = \begin{cases} R_0 \le r \le 1 + \xi(\vartheta, t); \\ 0 \le \vartheta \le \pi; \\ 0 \le \varphi \le 2\pi; \end{cases}$$

and the immobility of the hailstone's mass center:

$$\frac{\int\limits_{V_1} r dV_1 + \rho_* \int\limits_{V_2} r dV_2}{\int\limits_{V_1} dV_1 + \rho_* \int\limits_{V_2} dV_2} = 0; \quad V_2 = \begin{cases} 0 \le r \le R_0; \\ 0 \le \vartheta \le \pi; \\ 0 \le \varphi \le 2\pi; \end{cases}$$

ρ_* is the dimensionless density of the solid nucleus.

Let us formulate the initial conditions for the problem by way of setting the initial axisymmetric deformation of the equilibrium spherical form of the free surface of the liquid layer and by setting the initial velocity of the motion of the free surface to zero:

$$t = 0: \quad \xi(\vartheta, t) = \xi_0 P_0(\mu) + \xi_1 P_1(\mu) + \varepsilon P_k(\mu);$$

$$(k \ge 2); \quad \mu \equiv \cos\vartheta; \quad \frac{\partial \xi(\vartheta, t)}{\partial t} = 0.$$

Here, ε is the dimensionless amplitude of the initial deformation being a small parameter of the problem; $P_k(\mu)$ is the kth order Legendre polynomial; and ξ_0 and ξ_1 are the constants determined by the conditions of the droplet volume constancy and the system's mass center immobility in the form

$$\xi_0 = -\varepsilon^2 \frac{1}{(2k+1)} + O(\varepsilon^2); \quad \xi_1 = 0 + O(\varepsilon^3).$$

THE PROBLEM'S EXPANSION IN ORDERS OF INFINITESIMALS

We shall solve the problem formulated in the quadratic approximation in ε by the method of multiple time scales as in [4–6]. For this purpose, we shall represent the desired functions $\xi(\vartheta, t)$, $\psi(r, t)$, and $\Phi(r, t)$ in the form of asymptotic expansions in powers of the small parameter ε and consider them to depend not just on the time t but on its various scales T_m defined by the correlation $T_m \equiv \varepsilon^m t$:

$$\xi(\vartheta, t) = \sum_{m=1}^{\infty} \varepsilon^m \xi^{(m)}(\vartheta, T_0, T_1, \ldots);$$

$$\psi(r, t) = \sum_{m=1}^{\infty} \varepsilon^m \psi^{(m)}(r, \vartheta, T_0, T_1, \ldots); \qquad (1)$$

$$\Phi(r, t) = \sum_{m=0}^{\infty} \varepsilon^m \Phi^{(m)}(r, \vartheta, T_0, T_1, \ldots).$$

Substituting expansions (1) into the initial set of equations and the boundary conditions to it and equating the summands of the same order of infinitesimals in each correlation, we can easily obtain a set of boundary problems for the time-series identification of the unknown functions $\xi^{(m)}$, $\psi^{(m)}$, and $\Phi^{(m)}$, which will be found for $m \ge 1$ as series in Legendre polynomials:

$$\xi^{(m)}(\vartheta, T_0, T_1, \ldots) = \sum_{n=0}^{\infty} M_n^{(m)}(T_0, T_1, \ldots) P_n(\mu).$$

$$\psi^{(m)}(\vartheta, T_0, T_1, \ldots) = \sum_{n=0}^{\infty} (H_n^{(m)}(T_0, T_1, \ldots) r^n + G_n^{(m)}(T_0 T_1, \ldots) r^{-n-1}) P_n(\mu); \qquad (2)$$

$$\Phi^{(m)}(r, \vartheta, T_0, T_1, \ldots) = \sum_{n-0}^{\infty} F_n^{(m)}(T_0, T_1, \ldots) r^{-n-1} P_n(\mu).$$

FINDING OF THE SOLUTION

In the zero order of infinitesimals in terms of the wave amplitude, the perturbations of the free surface of the liquid layer are absent; hence, the solution to the problem has the simple form

$$\Phi^{(0)} \equiv -E_0 \mu (r - r^{-2}); \quad M_n^{(0)} = E_n^{(0)} = H_n^{(0)} \equiv 0. \quad (3)$$

In calculations of the first order of infinitesimals, we obtain the infinite set of connected differential equations for finding the coefficients $F_n^{(1)}(T_0, T_1, \ldots)$, $H_n^{(1)}(T_0, T_1, \ldots)$,

$$G_n^{(1)}(T_0, T_1, \ldots), M_n^{(1)}(T_0, T_1, \ldots):$$

$$M_0^{(1)}(T_0, T_1, \ldots) \equiv 0; \quad M_1^{(1)}(T_0, T_1, \ldots) \equiv 0;$$

$$A_n M_{n-2}^{(1)}(T_0, T_1, \ldots) + \frac{\partial^2 M_n^{(1)}(T_0, T_1, \ldots)}{\partial T_0^2} + \omega_n^2 M_n^{(1)} \times (T_0, T_1, \ldots) + D_n M_{n+2}^{(1)}(T_0, T_1, \ldots) = 0; \quad n \ge 2;$$

$$A_n = -w\chi_n \frac{n(n-1)(n-2)}{(2n-3)(2n-1)};$$

$$D_n = -w\chi_n \frac{n(n+1)(n+2)}{(2n+3)(2n+5)};$$

$$\omega_n^2 = \chi_n \Big((n-1)[(n+2)] - w \frac{n(4n^3 + 2n^2 - 6n - 1)}{(2n-1)(2n+1)(2n+3)} \Big);$$

$$\chi_n = \frac{n(n+1)(1-R_0^{2n+1})}{n+1+nR_0^{2n+1}};$$

$$H_n^{(1)}(T_0, T_1, \ldots) = \frac{1}{n(1-R_0^{2n+1})} \times \frac{\partial M_n^{(1)}(T_0, T_1, \ldots)}{\partial T_0}; \quad (n \geq 2); \tag{4}$$

$$G_n^{(1)}(T_0, T_1, \ldots) = \frac{R_0^{2n+1}}{(n+1)(1-R_0^{2n+1})} \times \frac{\partial M_n^{(1)}(T_0, T_1, \ldots)}{\partial T_0}; \quad (n \geq 2);$$

$$F_0^{(1)}(T_0, T_1, \ldots) \equiv 0; \quad F_1^{(1)}(T_0, T_1, \ldots) \equiv 0;$$

$$F_n^{(1)}(T_0, T_1, \ldots) = 3E_0\mu M_n^{(1)}(T_0, T_1, \ldots); \quad n \geq 2.$$

In the calculations of the second order of infinitesimals, we also obtain the set of inhomogeneous differential equations for finding the unknown coefficients $M_n^{(2)}(T_0, T_1, \ldots)$:

$$M_0^{(2)}(T_0) = \sum_{n=0}^{\infty} \frac{1}{2n+1}(M_n^{(1)}(T_0))^2;$$

$$A_n M_{n-2}^{(2)}(T_0, T_1, \ldots) + \frac{\partial^2 M_n^{(2)}(T_0, T_1, \ldots)}{\partial T_0^2} + \omega_n^2 M_n^{(2)}(T_0, T_1, \ldots) + D_n M_{n+2}^{(2)}(T_0, T_1, \ldots) = f_n(T_0); \quad n \geq 1;$$

$$f_n(T_0) = \chi_n \sum_{m=2}^{\infty}\sum_{l=2}^{\infty}\left\{\frac{\partial^2 M_m^{(1)}(T_0)}{\partial T_0^2} M_l^{(1)}(T_0) \times \left[K_{m,l,n}\left(\frac{\nu_m}{\chi_n} - 1\right) - \frac{\alpha_{m,l,n}}{\chi_n\chi_m}\right] + \frac{\partial M_m^{(1)}(T_0)}{\partial T_0}\frac{\partial M_l^{(1)}(T_0)}{\partial T_0} \times \left[K_{m,l,n}\left(\frac{\nu_m}{\chi_n} - \frac{1}{2}\right) - \frac{\alpha_{m,l,n}}{\chi_m}\left(\frac{1}{\chi_n} + \frac{1}{2\chi_l}\right)\right] + M_m^{(1)}(T_0)M_l^{(1)} \times (T_0)\left\{K_{m,l,n}\left(2[l(l+1)-1] + w\frac{(13m(m+1)-7)}{(2m-1)(2m+3)}\right) + \frac{11w}{2(2m+1)}\left[\frac{m(m-1)}{(2m-1)}K_{m-2,l,n} + \frac{(m+1)(m+2)}{(2m+3)}K_{m+2,l,n}\right] + \left(\frac{m}{(2m-1)}M_{m-1}^{(1)}(T_0) + \frac{(m+1)}{(2m+3)}M_{m+1}^{(1)}(T_0)\right)M_l^{(1)}(T_0) \times \left\{mw\left[\frac{n^2}{2n-1}K_{m,l,n-1} + \frac{(n+1)(n+2)}{2n+3}K_{m,l,n+1}\right] - w\frac{m+1}{2m+3}[(m+2)^2K_{m+1,l,n} + m(m+5)K_{m-1,l,n}]\right\} + \frac{1}{2}[(m+1)(l+1)K_{m,l,n} + \alpha_{m,l,n}] \times \left(\frac{lM_{l-1}^{(1)}(T_0)}{(2l-1)} + \frac{(l+1)M_{m+1}^{(1)}(T_0)}{(2l+3)}\right)\left\{w\left(\frac{mM_{m-1}^{(1)}(T_0)}{2m-1} + \frac{(m+1)M_{m+1}^{(1)}(T_0)}{2m+3}\right)\right\}\right\}; \tag{5}$$

$$\nu_m = \frac{m-1+(m+2)R_0^{2m+1}}{1-R_0^{2m+1}}; \quad K_{m,l,n} \equiv [C_{m0l0}^{n0}]^2;$$

$$\alpha_{m,l,n} \equiv -\sqrt{m(m+1)l(l+1)}C_{m0l0}^{n0}C_{m-1l0}^{n0};$$

where C_{m0l0}^{n0} and C_{m-1l0}^{n0} are the Clebsch–Gordan coefficients [7].

The problem's analysis in the quadratic approximation in ε allows determining the dependence of the coefficients $M_n^{(2)}(T_0, T_1)$ only on the time scale $T_0 \equiv t$. In addition, $M_n^{(2)}(T_0, T_1) \approx M_n^{(2)}(t) + O(T_1)$; for the surface perturbation, we obtain the following estimate:

$$\xi(\vartheta, t) = \varepsilon\xi^{(1)}(\vartheta, t) + \varepsilon^2\xi^{(2)}(\vartheta, t) + O(\varepsilon^3 t) = \varepsilon\sum_{n=0}^{\infty} M_n^{(1)}(t)P_n(\mu) + \varepsilon^2\sum_{n=0}^{\infty} M_n^{(2)}(t)P_n(\mu) + O(\varepsilon^3 t). \tag{6}$$

The unknown coefficients $M_n^{(1)}$ and $M_n^{(2)}$ are obtained as a result of the numerical calculation of sets (4) and (5) by the method of successive approximations. Thereupon, the coefficients $F_n^{(2)}(T_0, T_1, \ldots)$, $H_n^{(2)}(T_0, T_1, \ldots)$, and $G_n^{(2)}(T_0, T_1, \ldots)$ with regard for (6) can be defined as follows:

$$H_n^{(2)}(T_0, T_1, \ldots) \equiv H_n^{(2)}(t) = \frac{1}{n(1-R_0^{2n+1})}\left\{\frac{\partial M_n^{(2)}(t)}{\partial t} - \sum_{m=2}^{\infty}\sum_{l=2}^{\infty}\left[\nu_m K_{m,l,n} - \frac{\alpha_{m,l,n}}{\chi_m}\right]\frac{\partial M_m^{(1)}(t)}{\partial t}M_l^{(1)}(t)\right\};$$

$$G_n^{(2)}(T_0, T_1, \ldots) \equiv G_n^{(2)}(t) = \frac{R_0^{2n+1}}{(n+1)(1-R_0^{2n+1})}$$

$$\times \left\{ \frac{\partial M_n^{(2)}(t)}{\partial t} - \sum_{m=2}^{\infty}\sum_{l=2}^{\infty}\left[\nu_m K_{m,l,n} - \frac{\alpha_{m,l,n}}{\chi_m}\right]\frac{\partial M_n^{(1)}(t)}{\partial t} M_l^{(1)}(t)\right\}; \quad F_0^{(2)}(t) = 0;$$

$$F_0^{(2)}(t) \equiv 3E_0\left[M_n^{(2)}(t) + \sum_{m=1}^{\infty}\sum_{l=1}^{\infty} m M_m^{(2)}(t) M_l^{(2)}(t)\right]; \quad n \geq 1.$$

Thus, the expression for the electric field potential corrected for the constant depending only on the time has the form

$$\Phi = \Phi^{(0)} + \varepsilon\Phi^{(1)} + \varepsilon^2\Phi^{(2)} = -E_0\mu(r - r^{-2}) + \varepsilon\sum_{n=0}^{\infty}(F_n^{(1)}(t) + \varepsilon F_n^{(2)}(t))r^{-(n+1)}P_n(\mu).$$

DERIVATION OF THE ANALYTIC EXPRESSION FOR THE ELECTRIC FIELD INTENSITY NEAR THE SURFACE OF A CHARGED HAILSTONE

The expression for the electric field intensity $E(r, t) \equiv -\nabla\Phi(r, t)$ in the neighborhood of the free surface of a nonlinear oscillating liquid layer has the form

$$r \geq 1 + \xi(\vartheta, t): \quad E = E^{(0)} + \varepsilon E^{(1)} + \varepsilon^2 E^{(2)};$$

$$E^{(0)} = e_r\left(E_0\cos\vartheta\left(1 + \frac{2}{r^3}\right)\right) - e_\vartheta E_0\sin\vartheta\left(1 - \frac{1}{r^3}\right);$$

$$E^{(1)} = e_r 3E_0\mu\sum_{n=0}^{\infty}(n+1)M_n^{(1)}r^{-(n+2)}P_n(\mu) - e_\vartheta 3E_0\mu\sum_{n=0}^{\infty}M_n^{(1)}r^{-(n+2)}\frac{\partial P_n(\mu)}{\partial\vartheta}; \quad (7)$$

$$E^{(2)} = e_r\sum_{n=0}^{\infty}(n+1)F_n^{(2)}(t)r^{-(n+2)}P_n(\mu) - e_\vartheta\sum_{n=0}^{\infty}F_n^{(2)}(t)r^{-(n+2)}\frac{\partial P_n(\mu)}{\partial\vartheta},$$

where e_r and e_ε are the unitary vectors of the spherical coordinates. From expression (7), we shall find the electric field intensity on the unperturbed spherical surface of the free droplet surface. For this purpose, we expand (7) in the neighborhood of the equilibrium spherical form in terms of the deformation amplitude and multiply it by the expression for the normal vector near the free liquid surface:

$$n \equiv \nabla F(r, \vartheta, t)/|\nabla F(r, \vartheta, t)| = n_r e_r + n_\vartheta e_\vartheta.$$

$$r = 1: \quad n_r = 1 - \varepsilon^2\frac{1}{2}(\partial_\vartheta\xi^{(1)})^2 = 1 - \varepsilon^2\frac{1}{2}\sum_{m=0}^{\infty}\sum_{l=0}^{\infty}M_m^{(1)}M_l^{(1)}\frac{\partial P_m(\mu)}{\partial\vartheta}\frac{\partial P_l(\mu)}{\partial\vartheta};$$

$$n_\vartheta = -\varepsilon\partial_\vartheta\xi^{(1)} + \varepsilon^2(\xi^{(1)}\partial_\vartheta\xi^{(1)} + \partial_\vartheta\xi^{(2)}) = -\varepsilon\sum_{n=0}^{\infty}M_n^{(1)}\frac{\partial P_n(\mu)}{\partial\vartheta} + \varepsilon^2\left(\sum_{m=0}^{\infty}\sum_{l=0}^{\infty}M_m^{(1)}(t)M_l^{(1)}(t) \times P_m(\mu)\frac{\partial P_l(\mu)}{\partial\vartheta} + \sum_{n=0}^{\infty}M_n^{(2)}(t)\frac{\partial P_n(\mu)}{\partial\vartheta}\right).$$

As a result, we obtain the analytic expression for the normal component of the electric field intensity on the hailstone surface:

$$E_n = 3E_0\mu + \varepsilon\sum_{n=0}^{\infty}\{(1+n)F_n^{(1)} - 2(3E_0\mu)M_n^{(1)}\}P_n(\mu) + \varepsilon^2\sum_{n=0}^{\infty}\{(1+n)F_n^{(2)} - 6E_0\mu M_n^{(2)}\} + \sum_{m=0}^{\infty}\sum_{l=0}^{\infty}\left\{[3(4E_0\mu)M_m^{(1)}M_l^{(2)} - (m+1)(m+2) \times M_m^{(1)}F_l^{(1)}]K_{m,l,n} + \frac{3m(m+1)}{2m+1}E_0M_m^{(1)}M_l^{(1)}[K_{m+1,l,n} - K_{m-1,l,n}]\right\}P_n(\mu). \quad (8)$$

ANALYSIS OF THE RESULTS

Before we study the expression for the electric field intensity (8), we should obtain solutions to sets of equations (4) and (5) for finding the coefficients $M_m^{(1)}(t)$ and $M_m^{(2)}(t)$. The preliminary calculations showed that, upon the initial excitation of the kth mode, an appreciable contribution to the capillary mode spectrum comes only from the modes being close in number to the initial excited one. In addition, the amplitude of the nearest-neighbor modes with the numbers $n + 1$ and $n - 1$ is less than the kth mode amplitude by approximately an order; that of the modes with numbers $n + 2$ and $n - 2$ is less than the kth mode by approximately two orders, etc. Thus, in

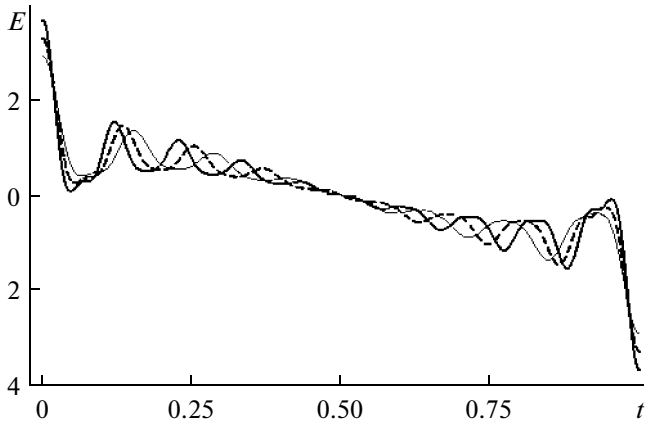

Fig. 1. The polar angle ϑ dependences of the dimensionless intensity of the electric field in the neighborhood of the free surface of the charged liquid layer on the surface of a wet hailstone when the initial deformation is determined by the mode with the number $k = 14$ (thin curve), $k = 16$ (dashed curve), and $k = 18$ (thick curve) at $t = 0$; $W = 0.1$, $w = 0.1$, $\varepsilon = 0.1$; $R_0 = 0.98$. Here and in the other figures, the straight line $E = 2.5$ parallel to the axis of the abscissas corresponds to the nondimensional intensity of the electrostatic field of 20 kV/cm, which is critical for the corona discharge ignition in a cloud at a height of 4–5 km.

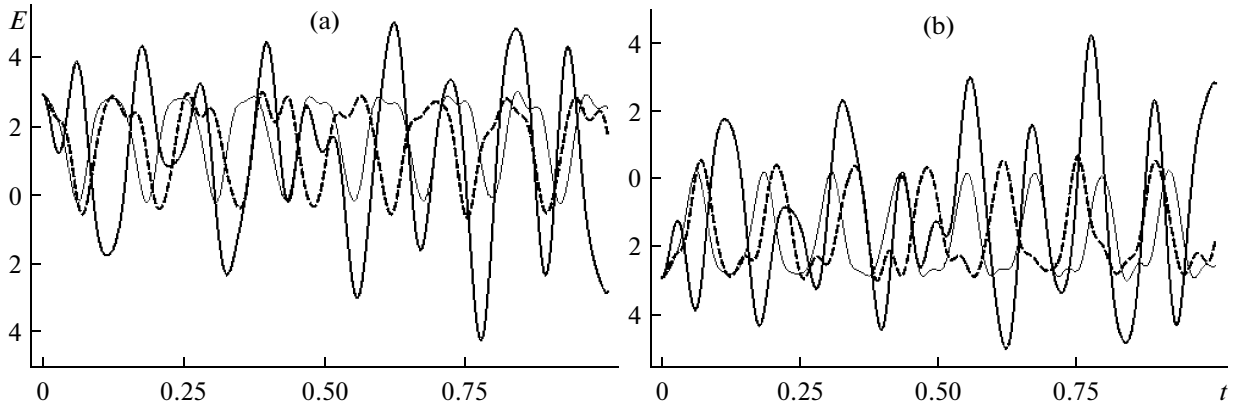

Fig. 2. Time dependence of the dimensionless intensity of the electric field on the surface of a watered hailstone on the axis of symmetry of the system $\vartheta = 0$ (a) and $\vartheta = \pi$ (b) for various values of the liquid layer thickness $R_0 = 0.9$ (thin curve), $R_0 = 0.94$ (dashed curve), and $R_0 = 0.98$ (thick curve) when the initial deformation is determined by the fourteenth mode ($n = 14$) at $W = 0$, $w = 0.1$, and $\varepsilon = 0.1$.

the following calculations, in the first order of infinitesimals, only five modes were taken into account: $(n, n \pm 1, n \pm 2)$. In the second-order calculations, the modes with numbers from 0 to $2n + 4$ were considered. Here, we take into account that, in the calculations of the second order of infinitesimals for single-mode initial deformation, all the even modes with numbers from 0 to $2n$ are excited due to nonlinear interaction [3–6].

Figures 1–4 depict the results of the calculations by (8) when the initial deformation of the equilibrium spherical form of the water layer on the hailstone surface is determined by one of the oscillation modes with the number $n \gg 2$. Figure 1 illustrates the polar angle ϑ dependences of the dimensionless intensity of the electric field in the neighborhood of the free surface of the charged liquid layer on the surface of a wet hailstone calculated for the initial instant. One can easily see that the field intensity distribution depending on the angle ϑ has a symmetrical form and that the field intensity achieves the value of corona discharge ignition only in the neighborhood of the tops $\vartheta \approx 0$ and $\vartheta \approx \pi$.

Figures 2–4 represent the nondimensional time dependences of the nondimensional electric field intensity on the wet hailstone's surface on the system's symmetry axis for various thicknesses of the liquid layer in the situations when the initial deformation is determined by various high modes. It is seen from the figures that the field intensity on the hailstone tops increases with the growing mode number and with the decreasing water layer thickness on the hailstone's surface.

Finally, we should note that the above illustrations of analytic expression (8) for the field intensity value on the hailstone tops are of qualitative nature; they

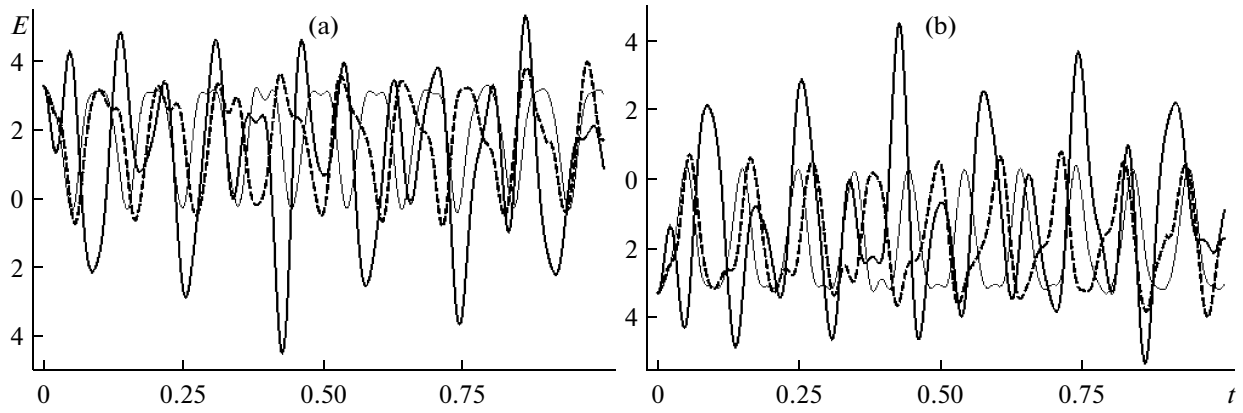

Fig. 3. The same as in Fig. 2 yet for the sixteenth mode ($n = 16$).

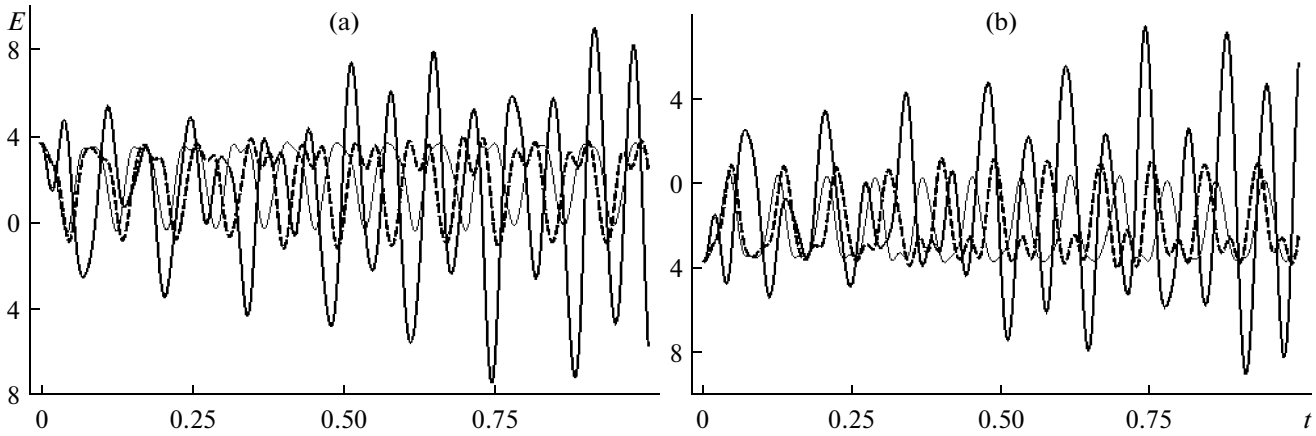

Fig. 4. The same as in Fig. 2 yet for the eighteenth mode ($n = 18$).

demonstrate only the tendencies of variation of the intensity upon the variation in the physical parameters, because they are calculated with violation of the asymptotic property.

CONCLUSIONS

In the quadratic approximation in terms of the amplitude of the oscillations of the water layer on the surface of a wet hailstone in a uniform external electrostatic field, the expression for the electric field intensity in its neighborhood has been obtained and analyzed. It has been found that, even at low values of the intensity of the external electric field, the intensity of the electrostatic field near the capillary wave crests in the water layer on the surface of a hailstone in the neighborhood of its tops is sufficiently high for the ignition of a corona discharge.

ACKNOWLEDGMENTS

This work was supported by the Federal Education Agency of Russia (project no. 2.1.1/3776) and the Russian Foundation for Basic Research (project no. 09-01-00084).

REFERENCES

1. D'yachuk, V.A. and Muchnik, V.A, Corona Discharge from a Watered Hailstone, the Basic Mechanism of Initiation of Lightning, *Dokl. Akad. Nauk SSSR*, 1979, vol. 248, no. 1, pp. 60–63.
2. Grigor'ev, A.I. and Shiryaeva, S.O., The Possible Physical Mechanism of Initiation and Growth of Lightning, *Phys. Scr.*, 1996, vol. 54, pp. 660–666.
3. Shiryaeva, S.O. and Grigor'ev, A.I., *Zaryazhennaya kaplya v grozovom oblake* (Charged Droplet in a Cumulonimbus Cloud), Yaroslavl: Demidov YarGU, 2008.

4. Grigor'ev, A.I., Koromyslov, V.A., Shiryaeva, S.O., and Volkova, M.V., On Nonlinear Oscillations of a Charged Droplet in an Aerodynamic Flow, *Elektron. Obrab. Mater.*, 2004, no. 6, pp. 25–31.

5. Koromyslov V.A. and Grigor'ev, A.I., Nonlinear Oscillations of a Charged Layer of Conducting Liquid on the Surface of a Solid Spherical Nucleus, *Zh. Tekh. Fiz.*, 2008, vol. 78, no. 2, pp. 42–50.

6. Grigor'ev, A.I., Koromyslov, V.A., and Shiryaeva, S.O., On the Possibility of Corona Discharge Ignition near the Surface of a Nonlinear-Oscillating Liquid Layer on the Surface of a Charged Hailstone, *Zh. Tekh. Fiz.*, 2009, vol. 79, no. 11, pp. 10–19.

7. Varshalovich, D.A., Moskalev, A.N., and Khersonskii, V.K, *Kvantovaya teoriya uglovogo momenta* (Quantum Theory of Angular Momentum), Leningrad: Nauka, 197s5.

ISSN 1068-3755, Surface Engineering and Applied Electrochemistry, 2010, Vol. 46, No. 2, pp. 127–130. © Allerton Press, Inc., 2010.
Original Russian Text © Yu.V. Titova, V.G. Stokozenko, A.I. Maksimov, 2010, published in Elektronnaya Obrabotka Materialov, 2010, No. 2, pp. 49–52.

ELECTRICAL PROCESSES IN ENGINEERING AND CHEMISTRY

The Influence of Plasma-Solution Treatment on the Properties of Hemp Fiber Lignin

Yu. V. Titova, V. G. Stokozenko, and A. I. Maksimov

Institute of the Chemistry of Nonaqueous Solutions, Russian Academy of Sciences, ul. Akademicheskaya 1, Ivanovo, 153045 Russia

e-mail: jvt@isc-ras.ru; vgs@isc-ras.ru

Received November 10, 2009

Abstract—The effect of an atmospheric pressure gas discharge generated inside an electrolyte solution on hemp lignin has been investigated by the methods of IR spectroscopy. It is shown that the gas-discharge activation causes a threefold increase of the lignin solubility with the further chemical treatment. The feasible processes of the interaction of the active particles generated in the electrolyte solution under the discharge action with the lignin macromolecules are considered.

DOI: 10.3103/S1068375510020079

INTRODUCTION

It has been shown in works [1, 2] that plasma-solution activation starts the processes of delignification of stem fibers, thus greatly increasing the degree of lignin dissolution at the stage of the following alkaline treatment in comparison with the known methods based on the usage of special chemical reagents. It is established that, for the hemp stem fiber produced from the noncannabinoid hemp varieties, when treated by a gas discharge in an electrolyte, there are some "latent" destructive processes effecting the lignin carbohydrate complex. This leads to the weakening of the chemical bonds in the lignin macromolecules causing its destruction and quick dissolution with the further action of alkaline solutions. The degree of lignin removal from the hemp fiber is up to 64%, whereas, under the conditions of the chemical treatments, only a value of 38% has been attained [3, 4].

The high wearing quality, shrinkage capacity, durability, good hygienic properties, and capacity to absorb up to 95% of the ultraviolet rays are the main and evidently attractive features of textile products produced from hemp fibers. However, their coarseness and rigidity are their fundamental defects. Two countries (France and Australia) know the secret of manufacturing soft cloth. A long and complicated process of making the fibers and textile materials agreeable to the touch is responsible for the high price of the final hemp products, thus they have become elite and exclusive.

We think that the production of chemically modified hemp fibers having a complex of both technological and service properties is rather promising and economically sound.

The development of the optimum conditions of the process of the chemical fiber modification and the obtaining of raw materials with the physical and mechanical properties necessary for the further processing into textile products should be based on clear ideas on the properties of these fibers, on the composition of the main impurities, and the behavior characteristics at different kinds of chemical treatments.

The aim of this work is to investigate the influence of the treatment by an atmospheric pressure gas discharge originating inside an electrolyte on the hemp fiber's lignin properties.

EXPERIMENTAL TECHNIQUE

A lignin specimen produced from hemp fiber using the sulfuric acid method [5] was the subject of the study in this work. The yield was 5.4% by mass.

The lignin specimens were subjected to alkaline boiling under conditions similar to those used for the chemical modification of the fiber: the sodium hydroxide concentration was in the range from 5 to 20 g/l, the temperature was 100°C, and the duration was up to 120 min [1–4]. The treatment in the plasma-solution system was carried out in sodium hydroxide with a concentration of 0.4 g/l at a discharge current of ~1 A. The system's volume was 0.8 l, the lignin's weight was 2 g, and the treatment duration was 20 min. The reactor's schematic sketch, the electric circuit, and the discharge description are given in [2, 6, 7]. The lignin's dissolution degree was determined using the gravimetrical method according to the difference in the specimen's weight before and after the treatment. The infrared spectroscopy procedure was utilized to investigate the chemical structure of the lignin. The

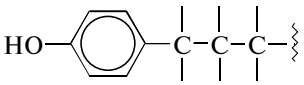

Fig. 1. The lignin *n*-hydroxyphenylpropanoic structure.

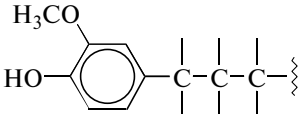

Fig. 2. The lignin guaiacyl structure.

infrared spectra were obtained with the help of a VERTEX 80v spectrophotometer in the range from 4000 to 600 cm^{-1} in tablets with KBr.

RESULTS AND DISCUSSION

Lignin is a natural polymer with an extremely complex composition with phenylpropane structures being the basis of it connected between each other by simple ester and carbon–carbon bonds. There are *p*-hydroxyphenylpropanoic (Fig. 1) and guaiacyl (Fig. 2) structures in hemp fiber lignin. Forming rigid links with the cellulose constituent, the lignin "armours" the elementary fibers fastening them into long and hard complex bunches.

The data obtained at the treatment of the lignin extracted from the hemp fiber using the conventional technology are presented in Table 1.

It can be seen that, even at the high alkali concentration (20 g/l), the lignin dissolution degree does not exceed 25%, though the fiber delignification degree should be not less then 50% to produce a fiber with the properties necessary for the further processing [3, 4].

Here are also presented (the bottom line) the data on the lignin solubility as a result of the two-stage treatment: stage 1—the treatment in the plasma-solution system when the atmospheric pressure gas discharge is originated inside the electrolyte (NaOH, 0.4 g/l) for 20 min; stage 2—the boiling in an alkaline medium for 60 min at a different concentration of the alkali.

With such a treatment procedure, the lignin's solubility is three times as much even at the smallest alkali concentration. The influence of the plasma-solution treatment on the lignin was investigated using the IR spectroscopy method. In Fig. 3, there are presented the IR spectra of the lignin specimen produced from the hemp fiber, and, in Fig. 4, there is depicted its spectrum after the plasma-solution treatment. The characteristic absorption bands of the lignin specimens are presented in Table 2.

When analyzing the changes in the IR spectra of the hemp fiber lignin specimens (*1*, *2*) occurring under the action of the plasma-solution treatment, it should be noted that, in spectra *2*, there disappear weak bands at 955–967 and 1650 cm^{-1} corresponding to the different kinds of vibrations of the ethylenic bonds. Thus, the interaction of the original ($OH^{\bullet}$, H, e_{solv}) and the secondary active particles generated in the plasma-solution system in the alkaline medium (O^{-}, HO_2,

Table 1. Solubility of the stem fiber lignin during the alkaline and plasma-solution treatments

Time of the treatment by the alkali, min	Lignin dissolution degree (weight % of the initial one) at different NaOH concentrations (g/l)		
	5	10	20
30	10.1	13.0	17.0
60	14.0	17.0	21.0
120	16.9	21.0	24.4
Plasma-solution treatment (20 min) + chemical treatment (60 min)	44.0	57.0	56.4

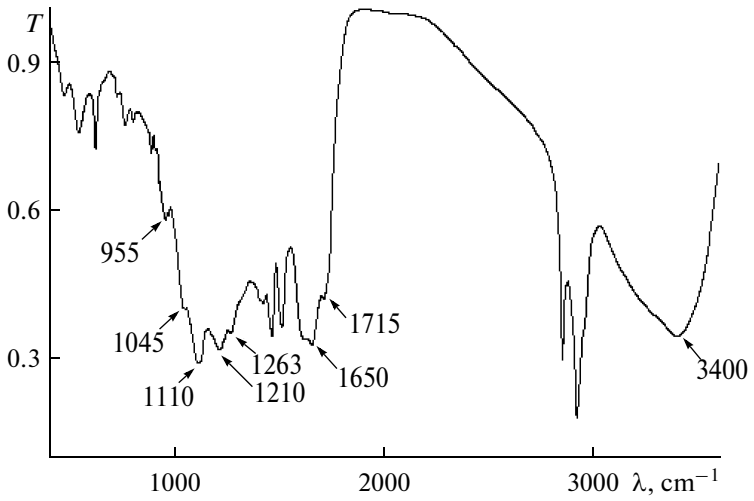

Fig. 3. IR spectrum of the hemp fiber lignin.

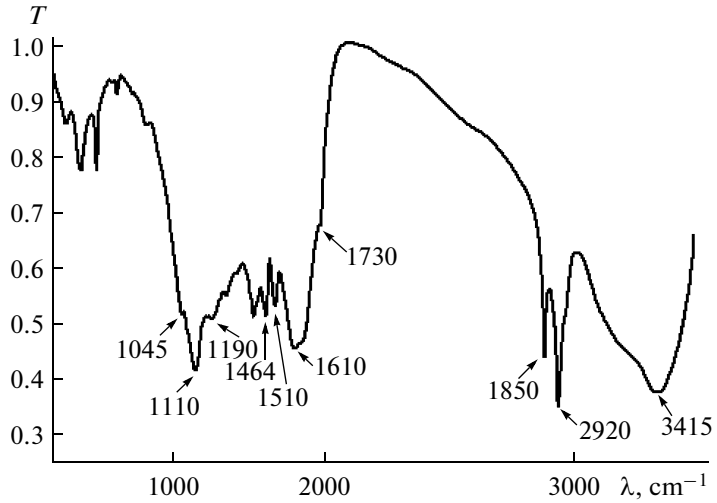

Fig. 4. IR spectrum of the hemp fiber lignin after the plasma-solution treatment.

O_2^-, H_2O_2, etc.) [9, 10] with the lignin proceeds, in particular, over double bonds, some number of which exist in its composition. The band at 1210 cm^{-1} in *1* shifts in *2* toward the smaller wave numbers, and the absorption intensity grows, most likely indicating the appearance of new C–O bonds and new OH-groups forming in the lignin macromolecule. Probably, this band shift is caused by the change of the substituent's morphology in the phenylpropane and guaiacyl structures of the lignin. The position and the form of the aromatic rings in *1* and *2* do not change, and the absorption intensity in *2* is somewhat higher than in *1*, being most likely connected with the elimination of the relatively low molecular fragments from the propane chains at their interaction with the active particles generated in the plasma-solution system and the transition of them into the solution.

The increase of the solubity of the lignin specimen after plasma-solution interaction at the subsequent alkaline chemical treatment cfn be explained by the introduction of the additional hydroxyl groups in aliphatic part of macromolecules, as well as those, that change the structure of propane components of the macromolecule of the lignin inhibits the flow of the condensation reaction and thus impedes the transition of lignin into water-soluble form in alkaline medium [11].

Moreover, the phenol rings of the lignin macromolecule also begin to interact with the active particles in

Table 2. Absorption bands in the infrared spectra of the lignin specimens [8]

Absorption band maximum, cm^{-1}		Absorption band assignment
The initial hemp lignin specimen (*1*)	The hemp lignin specimen after the plasma-solution treatment (*2*)	
3400	3415	O–H Valence vibrations
2920	2920	C–H Valence vibrations in $-CH_3$ and $-CH_2^-$
1850	1850	
1715	1730	C=O Valence vibrations
1650	–	Ethylenic double bonds a, b
1610	1610	Skeletal vibrations of the aromatic ring
1510	1510	
1464	1464	Deformation vibrations of the C–H bond in groups $-CH_3$ and $-CH_2$
1400–1415	1400	Deformation vibrations of the OH groups in phenols
1263	1263	Skeletal vibrations of the guaiacyl structures
1210	1190	Deformation vibrations of the OH groups in phenols and the valence vibrations of the $C-O^-$ bonds
1110	1110	Symmetric and asymmetric C–O–C simple ester bonds in aliphatic esters
1045	1045	
970	–	Deformation vibrations of $C-H^-$ bonds with the ethylenic double bond
955	–	

the solution with the formation of various products. These groups oxidizing there generate aromatic aldehydes and ketones with different compositions, in particular, vanillin, *n*-hydroxybenzaldehyde, and so on [12], which is indicated by the change of the intensity and shape of the band corresponding to the deformation vibrations of the OH groups in the phenols. More complicated processes causing the opening of the aromatic rings and the generation of relatively low molecular carboxylic acids must not be ruled out.

REFERENCES

1. Titova, Yu.V., Voronova, M.I., Stokozenko, V.G., Konycheva, M.V., Ermolaeva, N.A., and Maksimov, A.I., The Influence of Gas Discharge Plasma Treatment in the Electrolyte on the Cellulose Material Properties, *Trudy 5 Mezhdunarodnogo simpoziuma po teoreticheskoi i prikladnoi plazmokhimii* (Proc. 5th Int. Simp. on Theoretical and Applied Plasma Chemistry), Ivanovo, 2008, vol. 2, pp. 470–473.
2. Titova, Yu.V., Stokozenko, V.G., and Maksimov, A.I., The Usage of Plasma–Soluble Treatment to Modify the Stem Fiber, *Elektr. Obrab. Mater.*, 2009, no. 1, pp. 20–24.
3. Gubina, S.M. and Stolozenko, V.G., Analytical and Technological Aspects of Chemical Cottonizing, *Tekst. Prom.*, 2006, no. 1, pp. 18–20.
4. Nemanova, Yu.V., Stokozenko, V.G., Gubina, S.M., and Ermolaeva, N.A., Influence of Alkali–Reducing and Alkali–Oxidizing Treatments on the Hemp Lignin Solubility, *Izv. VUZov. Tekh. Tekst. Prom.*, 2007, no. 5, pp. 35–38.
5. Khabarov, Yu.G. and Pes'yakova, L.A. *Analiticheskaya khimiya ligninov* (Analytical Chemistry of Lignins), Arkhangelsk, 2008.
6. Maksimov, A.I., Physics, Chemistry and Applications of the AC Diaphragm Discharge and Related Discharges in Electrolyte Solutions, *Contr. Plasma Phys.*, 2007, vol. 46, nos. 1–2, pp. 1–8.
7. Titova, Yu.V., Voronova, M.I., and Maksimov, A.I., Influence of Gas Discharge Plasma inside Electrolyte on Cellulose Properties, *Zh. Prikl. Khim.*, 2008, vol. 81, no. 5, pp. 817–820.
8. Bazarnova, N.G. et al., *Metody isledovaniya drevesiny* (Timber Investigation Methods), Barnaul: Izd-vo Alt. gos. un-ta, 2002.
9. Maksimov, A.I and Nikiforov, A.Yu. *Khim. Vys. Energ.*, 2007, v. 41, no. 6, pp. 513–519.
10. Kutepov, A.M., Zakharov, A.G., and Maksimov, A.I., *Vakuumno-plazmennoe i plazmenno-rastvornoe modifitsirovanie polimernykh materialov* (Vacuu–Plasma and Plasm–Solution Modification of Polymer Materials), Moscow: Nauka, 2004, p. 496.
11. Obolenskaya, A.V. *Khimiya ligninov* (Chemistry of Lignins), St. Petersburg: LTA, 1993, p. 78.
12. Taraban'ko, V.E. and Koropachinskaya, N.V. Catalytic Methods of Production of Aromatic Aldehydes from Lignin Containing Raw Materials, *Khim. Rast. Syr'ya*, 2003, no. 1, pp. 5–25.

ISSN 1068-3755, Surface Engineering and Applied Electrochemistry, 2010, Vol. 46, No. 2, pp. 131–137. © Allerton Press, Inc., 2010.
Original Russian Text © L.Z. Boguslavskii, 2010, published in Elektronnaya Obrabotka Materialov, 2010, No. 2, pp. 53–60.

ELECTRICAL PROCESSES IN ENGINEERING AND CHEMISTRY

Engineering Methods for the Calculation of the Technological Parameters of a Pulsed Corona Discharge in Strong Electrolytes and for the Extensive Plasma Piston

L. Z. Boguslavskii

Institute of Pulse Processes and Technologies, National Academy of Sciences of Ukraine, pr. Oktyabrskii 43A, Nikolaev, 54018 Ukraine

e-mail: iipt@iipt.com.ua

Received December 7, 2009

Abstract—An engineering technique for the calculation of the technological parameters of a pulse corona discharge with extensive plasma pistons formed on linear and disk electrodes is offered. Calculations are performed for the maximal pressure on the wall of the continuous extensive plasma piston, the radial distribution of the maximal pressure on the compression wave front, the electroacoustic discharge coefficient of the efficiency at the selectable external adjustable parameters of the built-in pulse generator of the technological electrodischarge facility, and the parameters of the operating environment and working electrode. The calculation of the parameters for extensive plasma pistons in symmetry about a cylinder and torus is presented in the third part of work.

DOI: 10.3103/S1068375510020080

INTRODUCTION

The engineering techniques of the calculation of the pulsed corona discharge (PCD) characteristics in strongly conducting liquids when a fork corona turns into a continuous plasma formation (CPF) offered in the first and second parts of the present paper [1, 2] were tested for single- and multipoint electrode systems. The adjustable parameters of the pulse generator and the geometrical dimensions of the electrodes selected in accordance with the given methods and with respect to the parameters of the medium, along with the requirements of the technological parameters of the process, showed reliable compliance with the known experimental results.

The PCD technological applications make it possible to form fields of pressures of a specified configuration in liquids using a great number of semispherical points with the CPF distributed in space [3, 4]. On the other hand, the PCD with the CPF can cover the extended points of a random shape [5–7]. This PCD property allows one to create plasma areas actually of any preset configuration and fields of pressures relevant to them. Figure 1 presents images of the PCD ignition with plasma areas of various configurations: a linear semicylinder limited by the dielectric, which covers the metal edge, and a semitorus with an external broadening on a disk electrode. In addition to the creation of complex profiles of pulsed pressures in the conventional technological applications of such pulsed discharges, extended plasma pistons make it possible to process the liquid media in plasmachemical reactors, thus embracing far greater volumes of the liquids subjected to the processing in comparison with common spark discharge.

The third part of the paper deals with the elaboration of the engineering methods of the calculation for the PCD technological parameters at the selectable parameters of the pulse power center for extensive plasma pistons using the example of a linear semicylinder and an exterior semitorus, formed by the relevant electrode systems. One of the peculiarities of such extensive PCD with CPF, unlike the preceding ones, is that, upon the initial electroconductivity of the electrolyte above 2.2 Sm/m (the Black Sea water conductivity), a discharge may pass from the critical into the oscillatory mode provided the linear size value of the extended piston is adequate.

THE IGNITION OF THE PCD THAT FORMS THE EXTENSIVE PLASMA PISTON

At elaborating the engineering methods for the PCD calculation in this case, a condition correlated with the simultaneous ignition of a discharge along the entire length of the point arises. Similarly to the simultaneous ignition on a multipoint electrode system [2], the time of the plasma layer formation for an extended point is characterized by the development of the overheating instability along the entire point t_n and its comparison with the discharge time of the capacitive storage C [8]:

$$t_n \ll R_{\text{in}}C. \quad (1)$$

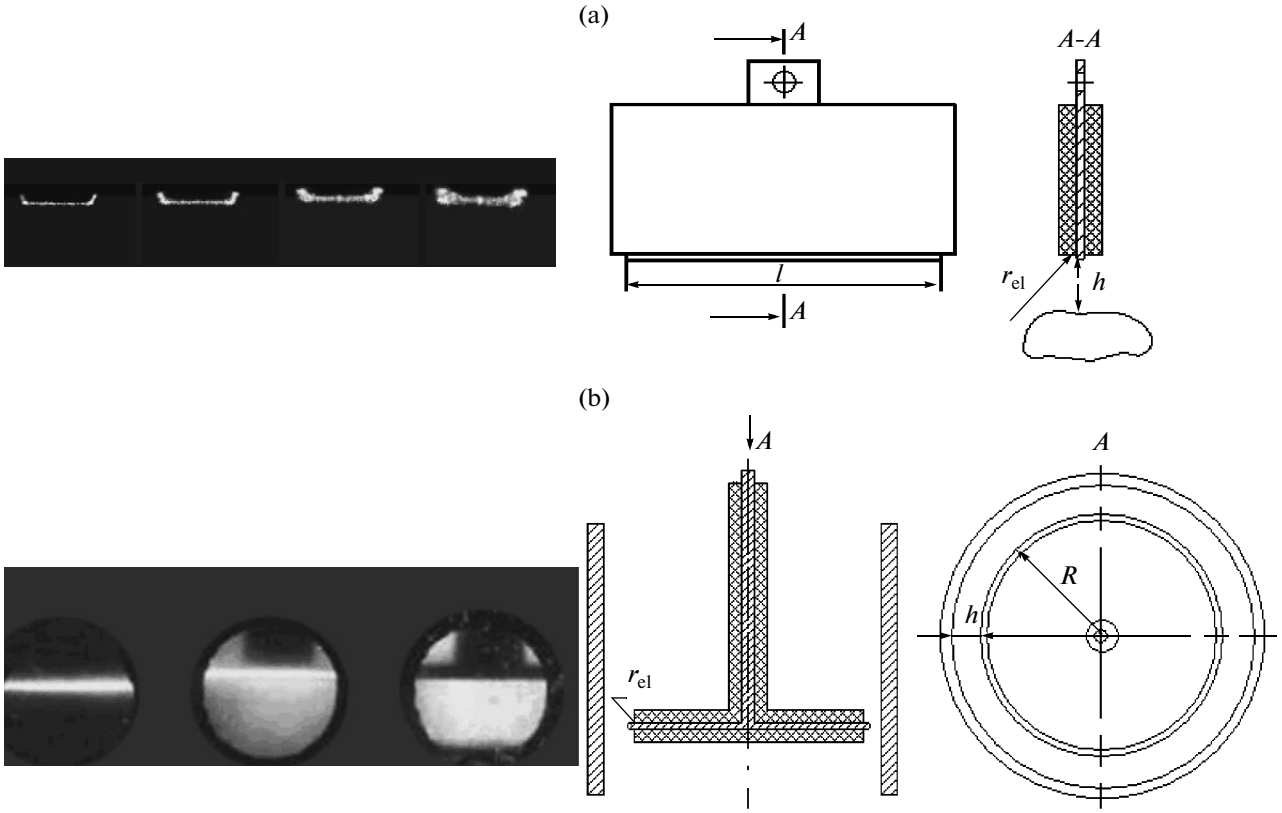

Fig. 1. Photodiagram of the process dynamics of an extensive plasma piston on linear (a) and disk (b) electrodes. The time interval between the images is 8 μs (a) and 25 μs (b).

The initial resistance of the gap in the case of a model with semicylindrical layers will be determined as follows:

$$R_{in} = \frac{1}{\pi l \sigma_0}\int_{r_{el}}^{h}\frac{dr}{r} = \frac{1}{\pi l \sigma_0}\ln\frac{h}{r_{el}}, \quad (2)$$

where l and r_{el} are the linear size and the point rounding radius, h denotes the distance to the cathode (i.e., the processed item or the discharge chamber wall), and σ_0 designates the initial electroconductivity of the electrolyte.

The time of the heating instability development in [8] and the geometry under study are determined as

$$t_n = \frac{\rho_0 c_p}{a}\frac{1}{\sigma_0 E_0^2} = \frac{\rho_0 c_p}{a}\frac{r_{el}^2\left(\ln\frac{h}{r_{el}}\right)^2}{\sigma_0 U_0^2}, \quad (3)$$

where ρ_0 is the density of the liquid, c_p symbolizes the heat capacity, α stands for the temperature coefficient of the electroconductivity of the liquid, E_0 denotes the intensity of the electric field of the point, and U_0 designates the initial voltage at the capacitive storage.

Thus, by way of comparison of these values under the terms of (1), we shall have the maximal linear size of the l_m point on which the PCD will ignite along its entire length without fail:

$$l_m = \frac{0.1a}{\rho_0 c_p}\frac{U_0^2 C}{\pi r_{el}^2 \ln\frac{h}{r_{el}}}. \quad (4)$$

The l_m naximum value estimations for the parameters of the pulsed power sources most frequently used in practice ($U_0 = 5$–50 kV, $C = 1$–100 μF, $r_{el} = 0.5$–2 mm) lie in the range of 0.01–0.6 m, which agrees with the experimental data [5, 7].

Similarly, for the ignition of a plasma piston on a disk electrode with the R radius, the value of the disk's maximal radius can be obtained as follows:

$$R_m = \frac{0.1a}{\rho_0 c_p}\frac{U_0^2 C}{2\pi^2 r_{el}^2 \ln\frac{h}{r_{el}}}. \quad (5)$$

The transition threshold of the forked pulse corona with the CPF, as before [1, 2], is controlled by the

dimensionless criterion [9]:

$$\beta = \frac{\sigma_0 U_0^2 (LC)^{\frac{2}{3}}}{\rho_0 r_{el}^4}, \quad (6)$$

where L is the inductance of the discharge framing. The criterion of β is a measure of the ratio of the current densities of the electric field energy and the energy of the dynamic pressure of the liquid medium per unit of length for both the point's linear dimension and the circle perimeter length of the disk electrode. Just as in the preceding events, one may discuss the PCD with the CPF at $\beta > 0.2$.

THE CALCULATION OF THE HYDRODYNAMIC PARAMETERS OF THE PCD WITH EXTENSIVE PLASMA PISTONS

After the ignition of the PCD with the CPF, the pressure inside of it abruptly increases and, due to the plasma area's expansion, the surrounding liquid is forced out. The equation of the energy balance with account for the CPF model in the shape of an expanding semicylinder with the radius $a(t)$, the volume $V(t) = \frac{\pi l}{2}(a(t)^2 - r_{el}^2)$, and the accepted in [1] allowances is reduced to the form

$$\frac{\pi l a(t)}{2(\gamma - 1)}\left[\gamma P_a(t)\frac{da(t)}{dt} + \frac{a(t)}{2}\frac{dP_a(t)}{dt}\right] = N_a(t), \quad (7)$$

where γ is the efficient index of the discharge plasma adiabat, $P_a(t)$ denotes the pressure on the piston wall, and the power $N_a(t) = I^2 R_a$, being released in the CPF, is expressed through the current I in the discharge circuit and the plasma resistance R_a.

The discharge current is obtained using the circuit equation:

$$L\frac{dI}{dt} = \frac{1}{C}\int_0^t I dt + I(R_a + R_l) = U_0, \quad (8)$$

where R_l is the resistance of the electrolyte layer, and the R_a resistance at the approximation of the plasma uniformity properties with account for the radius and length of the CPF linear piston is expressed as

$$R_a = \frac{1}{\pi l \sigma_a}\ln\left(\frac{a(t)}{r_{el}}\right). \quad (9)$$

Whereby, for the plasma formation, the spark approximation is valid, which unites the P_a pressure and the a conductivity through the A_s spark constant, which corresponds to the undersurface spark discharge [10]:

$$P_a = A_s(\gamma - 1)\sigma_a. \quad (10)$$

Upon reaching the power maximum, which for the PCD is relevant to the maximal pressure [5], by the moment t, the parameters will take on the following values: $a(t) = a_m$; $P_a(t) = P_{am}$; $N_a(t) = N_{am}$; $d_{am}/d_{tm} = v_{am}$. From (7) we obtain

$$P_{am} = \frac{2(\gamma - 1)}{\gamma}\frac{N_{am}}{\pi l a_m v_{am}}. \quad (11)$$

To calculate the maximum power at a nonlinear character of the load, let us accept, as in [1], that the maximum current corresponds to the power maximum and is determined according to the character of the electric discharge of the capacitive storage on the load. The decrement of the attenuation of the discharge oscillations for the symmetry of the semicylinder is as follows:

$$\delta = \frac{\ln\left(\frac{h}{r_{el}}\right)}{2\pi\sigma_0 l}\sqrt{\frac{C}{L}}. \quad (12)$$

In this case, the maximal power with account for (9) and (10) will be

$$N_{am} = \frac{A_s(\gamma - 1)U_0^2 C k}{\pi l L P_{am}}\ln\left(\frac{a_m}{r_{el}}\right), \quad (13)$$

where $k = e^{-2}$ for the critical discharge ($\delta \approx 1$), $k = B^{\frac{-2\delta}{\sqrt{\delta^2 - 1}}}$ at $B = \delta + \sqrt{\delta^2 - 1}$ for the aperiodic discharge ($\delta > 1$), or $k = \exp\left(-\frac{\delta}{\sqrt{1 - \delta^2}}\arcsin\sqrt{1 - \delta^2}\right)$ for the oscillation discharge ($\delta < 1$) [11].

With account for (13), expression (11) takes the following form:

$$P_{am} = \frac{(\gamma - 1)}{\pi l}\left[\frac{A_s U_0^2 C k k^* \sigma_0 \ln\left(\frac{a_m}{r_{el}}\right)}{\gamma L a_m v_{am}}\right]^{1/2}. \quad (14)$$

The k^* coupling coefficient of the pressure maximum with the electroconductivity is calculated in [1] using the data of [12] and is estimated to equal 0.126 m/Sm.

Having performed similar calculations for the geometry of the plasma piston in the shape of a semitorus with account for the attenuation decrement

$$\delta = \frac{\ln\left(\frac{h}{r_{el}}\right)}{4\pi^2\sigma_0 R}\sqrt{\frac{C}{L}}, \quad (15)$$

we shall have

$$P_{am} = \frac{(\gamma-1)}{\pi^2 R}\left(\frac{(\gamma-1)^2 A_s U_0^2 C k k^* \sigma_0 \ln\left(\frac{a_m}{r_{el}}\right)}{\pi^4 \gamma R^2 L a_m v_{am}}\right)^{1/2}. \quad (16)$$

The parameters of the compression wave calculated using those of the plasma piston in the acoustic approximation [13] at the distance r from the cylindrical symmetry axis have the following form of their distribution:

$$P_m = \frac{P_{am}}{\sqrt{\bar{r}}}, \quad (17)$$

where $\bar{r} = \frac{r}{a_m}$, and r is the current radius of the cylinder, which varies from a_m to h.

Then, with account for the accumulated energy in the capacitive storage $W_0 = \frac{CU_0^2}{2}$ and in the approximation of the linear law of the plasma piston's expansion till the moment the power reaches its maximum, we shall obtain the following expression of the pressure distribution at the moment of the power attaining its maximum for the cylindrical symmetry:

$$P_m = \frac{(\gamma-1)}{\pi l\sqrt{r}}\left(\frac{2A_s W_0 k k^* \sigma_0 \ln(b)}{\gamma v_{am} L}\right)^{1/2}, \quad (18)$$

and for the torus

$$P_m = \frac{(\gamma-1)}{\pi^2 R\sqrt{r}}\left(\frac{2A_s W_0 k k^* \sigma_0 \ln(b)}{\gamma v_{am} L}\right)^{1/2}, \quad (19)$$

where $b = 1 + \frac{v_{am} k_1 \sqrt{LC}}{r_{el}}$, $k_1 = 1$ at $\delta \approx 1$, and $k_1 = \frac{\ln B}{\sqrt{1-\delta^2}}$ at $\delta > 1$ or $k_1 = \frac{1}{\sqrt{1-\delta^2}}\arcsin\sqrt{1-\delta^2}$ at $\delta < 1$.

The parameter δ was calculated with account for the plasma piston's symmetry (12) or (15). The indefinite parameter v_{am} in the extended pistons, according to the experimental data of [7], accepts a value in the range of 100–180 m/s, which is less by an order than for the semispherical symmetry of the plasma piston's development [12].

The acoustic coefficient of the efficiency of the PCD indicating the share of the energy transferred into the acoustic W_{ac} (the compression wave) is determined as in [14]:

$$\eta = \frac{W_{ac}}{W_0}. \quad (20)$$

The dependency for the acoustic energy on P_m for the time when the pressure becomes 10 times less in the cylindrical symmetry looks as follows [13]:

$$W_{ac} = \frac{2\pi l r}{\rho_0 c_0}\frac{P_m^2 0.74\sqrt{LC}^4\sqrt{\bar{r}}}{2\ln(10)}, \quad (21)$$

where τ is the time of the energy release, and c_0 denotes the sound velocity in the liquid. Then, for the electroacoustic coefficient of the efficiency for the PCD with a linear plasma piston, one has

$$\eta = \frac{1.64(\gamma-1)^2 A_s k k^* \sigma_0 (r_{el}/b)^{1/4}\ln b}{\gamma\rho_0 c_0 l v_{am} r^{3/4}\sqrt{\frac{L}{C}}}, \quad (22)$$

and, respectively, for the torus, one gets

$$\eta = \frac{0.26(\gamma-1)^2 A_s k k^* \sigma_0 (r_{el}/b)^{1/4}\ln b}{\gamma\rho_0 c_0 R v_{am} r^{3/4}\sqrt{\frac{L}{C}}}. \quad (23)$$

ENGINEERING METHODS OF THE CALCULATION

The initial parameters that determine the PCD mode appear to be the following: U_0 is the voltage of the capacitive storage, C denotes the storage capacity, W_0 designates the potential energy of the accumulator, L stands for the discharge circuit's inductance, σ_0 is relevant to the electrolyte's electroconductivity, r_{el} implies the round-up radius of the electrode point, h symbolizes the distance from the point to the area being processed, and ρ_0 corresponds to the density of the electrolyte (the type of the electrode point is a linear or a disk one).

The constants and physical parameters used for the calculations are as follows: $A_s = 105$ B^2 s/m^2 is the spark constant, $c_0 = 1400$ m/s is the sound velocity in water, $\gamma = 1.26$ is the index of the impact adiabat, $k^* = 0.126$ m/Sm is a coefficient that considers the electrolyte's conductivity effect, and $v_{am} = 102$ m/s is the expansion rate of the CPF by the peak current moment.

Calculation of the PCD Characteristics

Step I. Calculation of the condition of the PCD with the CPF obtaining per unit of the electrode length (5):

$$\beta = \frac{\sigma_0 U_0^2 (LC)^{\frac{2}{3}}}{\rho_0 r_{el}^4}.$$

If $\beta > 0.2$, the PCD with CPF will occur; if $\beta < 0.2$, then one has to change the external adjustable parameters of U_0, C, and r_{el} to obtain the PCD with CPF.

Step II. Calculation of the maximum linear size of the point (4),

$$l_m = \frac{0.1a}{\rho_0 c_p} \frac{U_0^2 C}{\pi r_{el}^2 \ln \frac{h}{r_{el}}},$$

or the maximum radius of the disk electrode (5),

$$R_m = \frac{0.1a}{\rho_0 c_p} \frac{U_0^2 C}{2\pi^2 r_{el}^2 \ln \frac{h}{r_{el}}}.$$

The electrode size has to be selected with a value of either less than l_m or R_m. If it is selected in advance and exceeds the maximal value, then either the parameters of U_0 and C should be increased or r_{el} should be decreased. After that, one has to return to Step I to verify the value of the β criterion.

Step III. Calculation of the electric discharge mode for the linear point (12),

$$\delta = \frac{\ln\left(\frac{h}{r_{el}}\right)}{2\pi\sigma_0 l}\sqrt{\frac{C}{L}},$$

or for the disk (15),

$$\delta = \frac{\ln\left(\frac{h}{r_{el}}\right)}{4\pi^2\sigma_0 R}\sqrt{\frac{C}{L}}.$$

If $\delta \approx 1$, the coefficient $k = e^{-2}$, $k_1 = 1$ should be selected.

If $\delta > 1$, the coefficient $k = B^{\frac{-\delta}{\sqrt{\delta^2-1}}}$, $k_1 = \frac{\ln B}{\sqrt{\delta^2-1}}$ should be selected, where $B = \delta + \sqrt{\delta^2 - 1}$. If $\delta < 1$, the coefficient $k = \exp\left(-\frac{\delta}{\sqrt{1-\delta^2}}\arcsin\sqrt{1-\delta^2}\right)$, $k_1 = \frac{1}{\sqrt{1-\delta^2}}\arcsin\sqrt{1-\delta^2}$ should be selected.

Step IV. Calculation of the maximal pressure on the compression wave front for the cylindrical symmetry of the piston (18),

$$P_m = \frac{(\gamma-1)}{\pi l\sqrt{h}}\left(\frac{2A_s W_0 kk^* \sigma_0 \ln(b)}{\gamma v_{am} L}\right)^{1/2},$$

or, for the torus (19),

$$P_m = \frac{(\gamma-1)}{\pi^2 R\sqrt{h}}\left(\frac{2A_s W_0 kk^* \sigma_0 \ln(b)}{\gamma v_{am} L}\right)^{1/2},$$

where $b = 1 + \frac{v_{am} k_1 \sqrt{LC}}{r_{el}}$.

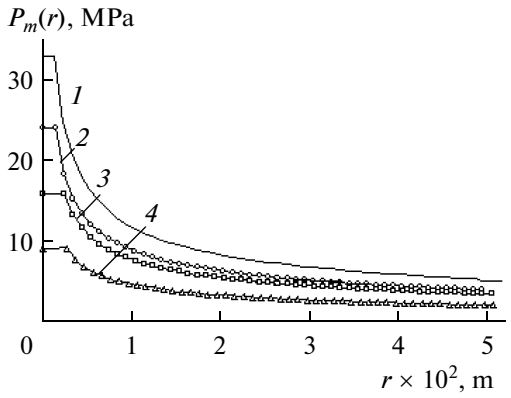

Fig. 2. Calculation of the maximum pressures on the wall of the cylindrical plasma piston and on the compression wave front considering the distance to the CPF for C = 3 μF, U_0 = 50 kV, L = 6 μG, σ_0 = 10 Sm/m, h = 0.1 m, and r_{el} = 0.001 m at various l(m) lengths of the linear electrode (l_m = 0.247 m): *1*—0.02, *2*—0.04, *3*—0.1, *4*—0.2.

Step V. Calculation of the electroacoustic coefficient of the efficiency of the PCD with a linear plasma piston (22),

$$\eta = \frac{1.64(\gamma-1)^2 A_s kk^* \sigma_0 (r_{el}/b)^{1/4} \ln b}{\gamma\rho_0 c_0 l v_{am} r^{3/4}\sqrt{\frac{L}{C}}},$$

or, for the torus (23),

$$\eta = \frac{0.26(\gamma-1)^2 A_s kk^* \sigma_0 (r_{el}/b)^{1/4} \ln b}{\gamma\rho_0 c_0 R v_{am} r^{3/4}\sqrt{\frac{L}{C}}}.$$

The calculation results based on the proposed methods of the maximum of the pressures on the wall of the extensive plasma pistons and the pressures on the compression wave front are presented in Figs. 2–4 for the pistons with the cylindrical and toroid symmetries at various lengths of the linear electrode and radii of the disk electrode along with the point rounding radius (r_{el}). The small plateaus on the graphs show the pressures in the plasma piston. Parenthesized in the figure captions are the maximal values of l_m and R_m for the relevant parameters of the pulse generator, the operation medium, and the geometrical parameters of the electrode system. The analysis of the results shows that the maximum of the pressure on the wall of the extended piston is found to be around 3 times less than of the semispherical symmetry PCD [1]. However, the pressure of the compression wave-front becomes almost equal for various symmetries at a distance of approximately 4–5 cm from the piston boundary. The latter is indicative of the high potential of the technological applicabilities of the PCD with extensive plasma pistons. However, the electroacoustic coeffi-

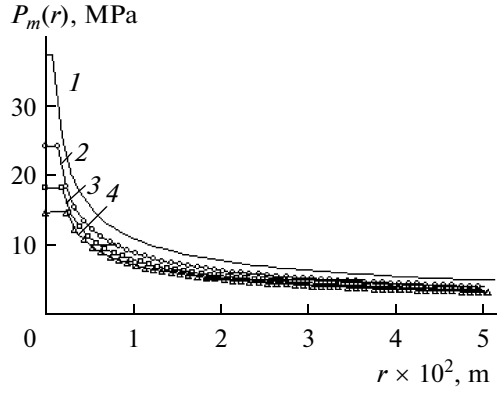

Fig. 3. The electrode radius r_{el} (m) effect on the maximum pressures considering the distance to the CPF for $C = 3$ μF, $U_0 = 50$ kV, $L = 6$ μG, $\sigma_0 = 10$ Sm/m, $h = 0.1$ m, and $l = 0.04$ m: *1*—0.0005 ($l_m = 0.85$ m), *2*—0.001 ($l_m = 0.247$ m), *3*—0.0015 ($l_m = 0.12$ m), and *4*—0.002 ($l_m = 0.073$ m). Parenthesized is the relevant maximal length of the linear electrode.

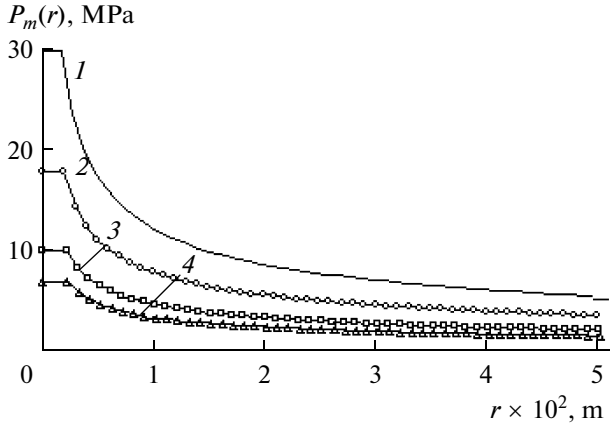

Fig. 4. Calculation of the maximum pressures on the wall of a toroidal plasma piston and on the compression wave front considering the distance to the CPF for $C = 3$ μF, $U_0 = 50$ kV, $L = 6$ μG, $\sigma_0 = 10$ Sm/m, $h = 0.1$ m, and $r_{el} = 0.0005$ m at various R (m) radii of the disk electrode ($R_m = 0.137$ m): *1*—0.01, *2*—0.02, *3*—0.04, *4*—0.6.

cient of the efficiency of such discharges calculated using expressions (22) and (23) makes up less than 1%, unlike the semispherical discharges, whose coefficient of efficiency may attain 8% at certain parameters [1]. On the whole, the character of the modifications of the obtained calculation parameters agrees well with the known experimental data of [5, 7].

CONCLUSIONS

The proposed engineering technique for the calculation of the PCD characteristics with extensive plasma pistons makes it possible to carry out the predictive evaluation of the pressures on the compression wave front in the proximity of the item being processed based on the external adjustable parameters of the pulse generator as a component part of the technological electrodischarge device with account of the operating medium's parameters and the electrode system's geometry. Similarly to the offered methods for the cylindrical and toroid geometry of the extensive plasma pistons discussed in the paper, there may be performed calculations for random geometry of extended pistons.

REFERENCES

1. Boguslavskii, L.Z., Engineering Methods for the Calculation of the Technological Parameters of a Pulsed Corona Discharge in Strong Electrolytes. Part I. A Single Point Electrode System, *Elektron. Obrab. Mater.*, 2009, no. 5. pp. 48–56.
2. Boguslavskii, L.Z., Engineering Methods for the Calculation of the Technological Parameters of a Pulsed Corona Discharge in Strong Electrolytes. Part II. A Multipoint Electrode System, *Elektron. Obrab. Mater.*, 2009, no. 6. pp. 68–70.
3. Boguslavskii, L.Z., Bristetskii, E.V., Krivitskii, E.V., and Petrichenko, V.N., Investigation of the Ignition of a Multiple Corona Discharge in Weakly Conducting Electrolytes, *Teoriya, Eksperiment, Praktika Elektrotazryadnykh Tekhnologii*, 2002, no. 4, pp.7–15.
4. Rizun, A.P., Boguslavskii, L.Z., Golen', Yu.V., and Denisyuk, T.D., Elaboration and Practical Application of the Technological Process of the Electrodischarge Treatment of the Offshore Platforms off the Biological Fouling, *Nauka ta Innovatsii*, 2008, vol. 4, no. 6, pp. 66–70.
5. Boguslavskii, L.Z., Kucherenko, V.V., and Krivitskii, E.V., Dynamics of the Pulsed Corona Discharge in the Aqueous Electrolytes, *Preprint of Ukraine National Acad. Sci., Inst. Pulse Processes and Technologies*, Nikolaev, 1993, no. 22.
6. Petrichenko, S.V., Boguslavskii, L.Z., Kuprin, D.E., and Petrichenko, V.M., Ukraine Deklaratsiinyi patent na vynakhid no. 50528A, Byull., 2002, no. 10.
7. Petrichenko, S.V., The Extensive Corona Discharge in Strong Aqueous Electrolytes, *Elektron. Obrab. Mater.*, 2005, no. 2, pp. 58–63.
8. Zhekul, V.G. and Rakovskii, G.B., On a Theory of the Electric Discharge Formation in a Conducting Liquid, *Zh.Tekh. Fiz.,* 1983, vol. 53, no. 1, pp. 8–14.
9. Shamko, V.V., Krivitskii, E.V., and Kucherenko, V.V., Approximated Similarity of Electrophysical and Kinematic Processes at the Pulsed Corona Discharge in the Strong Aqueous Electrolytes, *Zh. Tekh. Fiz.*, 1999, vol. 69, no. 5, pp. 30–34.
10. Krivitskii, E.V., Dinamika elektrovzryva v zhidkosti (Dynamics of Electroblast in Liquids), Kiev: Naukova Dumka, 1986.

11. Tekhnika ta elektrofizika vysokikh naprug, Brzhezitskii, V.O., Mikhailova, V.M. (Eds.), Kharkiv: NTU KhPI Tornado, 2005.
12. Khainatskii, S.A., Shamko, V.V., and Boguslavskii, L.Z., Determination of the Rate of the Pulsed Corona Discharge Arising in the Strong Electrolytes, *Elektron. Obrab. Mater.*, 2005, no. 5, pp. 42–47.
13. Shamko, V.V. and Kucherenko, V.V., Theoretical Backgrounds for the Engineering Calculations of the Energy and Hydrodynamic Parameters of the Undersurface Spark Discharge, *Preprint of Ukraine National Acad. Sci., Inst. Pulse Processes and Technologies*, Nikolaev, 1991, no. 18.
14. Kalinin, A.V., Kalinin, V.V., and Pivovarov, B.L., *Seismoakusticheskie issledovaniya na akvatoriyakh* (Siesmic-Acoustic Investigations in the Aquatic Areas), Moscow: Nedra, 1983.

ISSN 1068-3755, Surface Engineering and Applied Electrochemistry, 2010, Vol. 46, No. 2, pp. 138–143. © Allerton Press, Inc., 2010.
Original Russian Text © E.V. Kuvaldina, 2010, published in Elektronnaya Obrabotka Materialov, 2010, No. 2, pp. 61–66.

ELECTRICAL PROCESSES IN ENGINEERING AND CHEMISTRY

Loading Effect at Etching of Polypropylene Films in Oxygen–Nitrogen Plasma

E. V. Kuvaldina

Ivanovo State Chemicotechnological University, pr. F. Engel'sa 7, Ivanovo, Russia

e-mail: evk@isuct.ru

Received December 10, 2009

Abstract—The results of the studies of the loading effect under the action of a low temperature plasma of an oxygen–nitrogen mixture on the surface of a polypropylene (PP) film are presented. A gravimetric method was used to study the kinetics of the material's etching. The composition of the functional groups on the PP surface was characterized by the method of Fourier Transform Infrared by Attenuated Total Reflectance (FT-IR ATR). The loading effect was observed in the entire range of the gas compositions. It is accompanied by the increasing of the content of the functional groups in the modified layer; namely, of the double bonds for any gas composition and oxygen- or nitrogen-containing species dependent on the mixture composition. In the general case, the loading effect is more pronounced when the initial gas contains less oxygen. The degree of this dependence differs strongly for various $O_2 : N_2$ ratios. This is probably associated with the extreme character of the changes in the fluxes of the active particles from the plasma to the sample. The influence of the gas composition on the loading effect is relatively small when the O_2 fraction in the mixture constitutes 100–10%. The increasing of the load degree results in the increasing of the concentration of the oxygen-containing groups on the surface; the nitrogen-containing groups were not registered. When the O_2 fraction in the mixture is lower than 10%, the reciprocal influence of the volumetric and heterogeneous processes is enhanced considerably. The water vapors enter into the reactions of etching owing to the oxygen deficit. The nitriding of the surface occurs simultaneously with its oxidation. The competition of these processes is more pronounced for larger loads of the reactor.

DOI: 10.3103/S1068375510020092

INTRODUCTION

During the plasmochemical etching of polymer materials (fabrics and films), an effect of loading is observed; i.e., the specific rate of etching of the material diminishes with the increase of its amount. The effect of loading is associated with the formation of gaseous products of heterogeneous reactions and the variation of the boundary conditions for the active particles [1, 2]. As a result, the physical parameters of the plasma; the rates of the generation of the active particles; and, consequently, the rate of the end process change. The features of manifestation of this effect are determined by numerous factors involving the composition of the plasma-forming gas and the chemical composition and geometrical structure of the polymer. The studies of the plasmolysis of fabrics of polyethylenetherephthalate (PETP) fibers in air [3] and oxygen [4] have shown the following. For all the other conditions being equal, the oxygen plasma is more stable to the loading effect than the air plasma. In oxygen, the rates of the mass loss and formation of gaseous products of etching occur relatively slowly when the area of the fabric increases. In both the cases, the rates of generation of active particles in the discharge diminish. Moreover, in the air plasma, the ratio of the fluxes of the active particles on the sample changes; in particular, the relative fraction of $O(^3P)$ atoms decreases and the ratio of the channels of heterogeneous reactions, respectively, changes.

The obtained data allowed one to suggest that the loading effect in any case should be accompanied by changes of the content of various functional groups on the polymer surface disproportional to the surface area. Actually, it was stated that, under the action of oxygen plasma on the surface of a polypropylene (PP) film, the concentrations of all the analyzed groups increase in the case when the load is large [5].

The aim of the present study was to investigate the effect of loading on the kinetics of etching and the content of various functional groups under the action of an oxygen–nitrogen plasma on the surface of PP films.

EXPERIMENTAL METHOD

Experiments were performed by virtue of the installation whose scheme is presented in [5]. The same experimental method and parameters were used. The plasma-forming gas was prepared in a vessel by mixing nitrogen and oxygen; their proportion was controlled by measuring their pressure. More accurately, the composition was determined directly in the

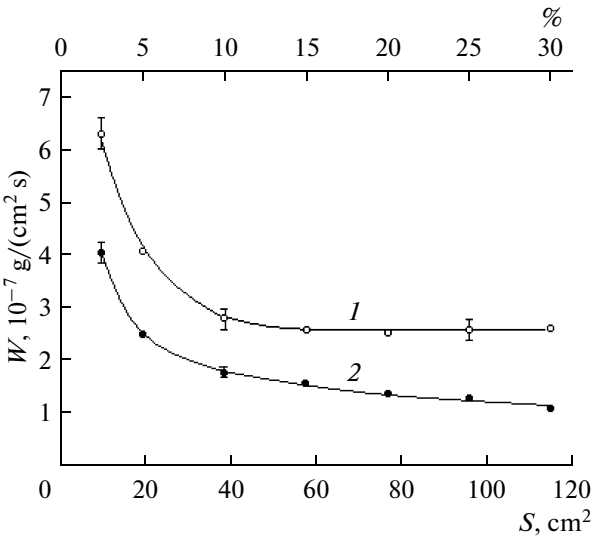

Fig. 1. The rate of the mass loss of PP in the oxygen (*1*) and air plasma (*2*) versus the reactor loading ratio.

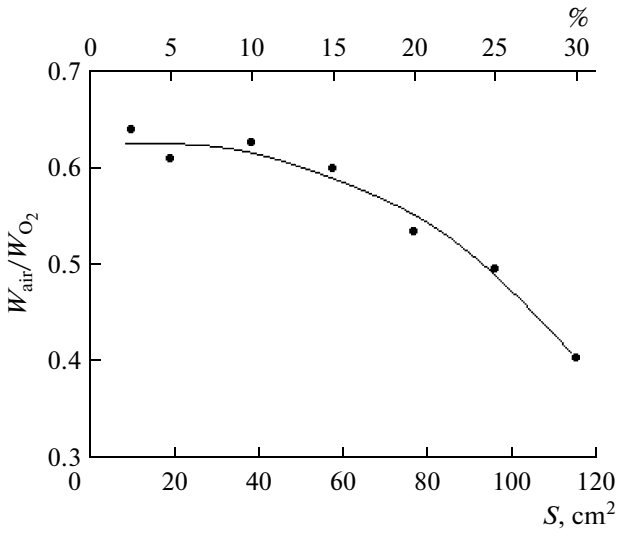

Fig. 2. Ratio of the mass loss of PP in the air and oxygen plasma versus the reactor loading ratio.

reactor according to the mass-spectral measurements without discharge. The gas pressure in the reactor was 100 Pa, the discharge current was 80 mA, the linear flow rate recalculated for the normal conditions was 30 cm/s, and the process time was 10 min. During this time, the optical densities of the oxygen-containing functional groups reached their stationary values. Samples of commercial films of isotactic PP (GOST 26996-86) with a thickness of 70 μm were placed as a cylinder on the thermostated wall of the reactor (T = 333 K) in the zone of the positive column. The generatrix of the polymer cylinder was varied in the limits of 1–12 cm. The position of the left edge of the sample remained unchanged, and the fraction of the reactor surface covered by the polymer increased from 2.5 to 30%.

The mass loss of the samples was determined by weighing on an analytical balance (WA-34). The weighing accuracy was 1×10^{-4} g.

The composition of the PP surface layer was studied by the method of Fourier Transform Infrared by Attenuated Total Reflection (FT-IR ATR). An Avatar-360 spectrometer (Nicolet, USA) was used. A zink selenide crystal with twelve-fold reflection was used as the ATR crystal. The regime of signal accumulation over the results of 32 scans was used; the resolution was 2 cm^{-1}. The band of the symmetrical stretching oscillations of C–H in the $-CH_2$ group of the main polymer chain with the maximum corresponding to the wave number 2915 cm^{-1} was used as the reference band. The results of the measurements of the optical densities of the bands were averaged over the data obtained for more than five samples processed in plasma in identical conditions. The time interval between the sample removal from the reactor and the measurement did not exceed 10 min.

RESULTS AND DISCUSSION

Fig. 1 shows the average specific rates (W) of the mass loss for the film treated in the air and oxygen discharge dependent on the reactor loading degree; in Fig. 2, their ratio is presented. As in oxygen, in the air, the load evidently influenced the kinetics of the destruction process for small quantities of the treated material when the fraction of the reactor surface covered by the sample was less than 10%. Further, the rate changes become less significant. The data presented in Fig. 2 show that the effect of loading of the reactor by the material is greater for the air plasma than for the oxygen plasma. This is qualitatively similar to the result obtained earlier for fabrics of PETP fibers.

The further research was carried out in a wide range of the $O_2 : N_2$ ratios in the plasma-forming gas. Using the results obtained above, we studied in detail the samples with the generatrix of the polymer cylinder of 2 cm (the fraction of the reactor surface covered with the sample was 5%) and 12 cm (the fraction of the reactor surface covered with the sample was 30%). Denote them as the low load ratio (LLR) and the high load ratio (HLR).

The data for the etching rates of the small and large samples for the transition from O_2 to N_2 are shown in Fig. 3 (W_{LLR} and W_{HLR} are the specific rates of the mass loss for the respective sample); the ratio of the W_{LLR}/W_{HLR} rates is shown in Fig. 4. It can be seen that the loading effect occurs in the entire range of the compositions of the plasma-forming gas and it is more pronounced for the lower oxygen content in the mixture. From the point of view of the intensity of the influence of the composition of the plasma-forming gas on the loading effect, two intervals can be noted in the range of compositions of the $O_2 : N_2$.

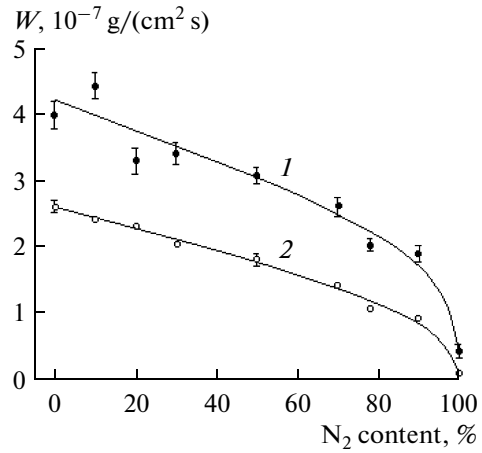

Fig. 3. Rate of the mass loss of the PP samples versus the composition of the initial gas. (*1*) LLR, (*2*) HLR.

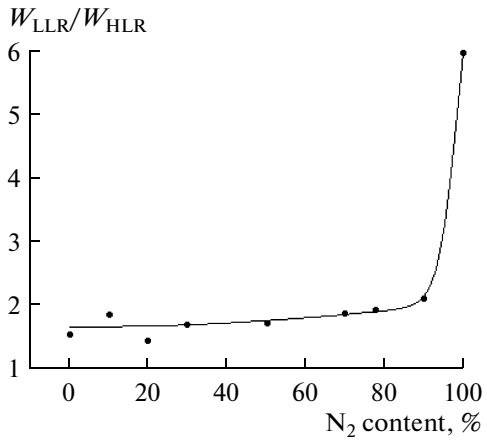

Fig. 4. Ratio of the rates of the mass loss of the PP samples corresponding to the LLR and HLR versus the composition of the initial gas.

In the first interval, when the O_2 content in the plasma-forming gas changes from 100 to 10%, the rates of the mass loss diminish approximately linearly and relatively slowly both for the LLR and HLR; the rate of etching diminishes by a factor of 2.5 on average when the fraction of O_2 molecules diminishes by a factor of 10. As was shown earlier [6], the oxidation of the PP surface in oxygen plasma was reached at the combined action of $O_2(a^1\Delta_g)$ molecules and oxygen molecules in the ground state, while the $O(^3P)$ atoms are involved both in the processes of oxidation and destruction of the oxygen-containing groups that lead to the formation of gaseous products. Evidently, the kinetics of the destruction of the polymer in the first interval to a large degree are defined by the competition of the processes involving the molecular and atomic oxygen. Actually, according to the data in [7] obtained for air plasma, in the $O_2 : N_2$, simultaneously with the channel of dissociation of the O_2 by a direct electron impact, new channels of dissociation of oxygen appear owing to the reactions involving the excited states $N_2(A^3\Sigma_u^+)$ and $N_2(B^3\Pi_g)$. As a result, the flux of $O(^3P)$ atoms on the reactor wall diminishes significantly less than one might expect based on the decrease of the concentration of O_2 molecules in the initial plasma-forming gas. The metastable state $O_2(a^1\Delta_g)$ is deactivated in the bulk of the plasma at collisions with NO molecules. A large quantity of novel particles appear possessing accumulated energy, which can dissipate this energy; in the first place, those are the oscillatory-excited nitrogen molecules. Consequently, the quantity of the surface-active centers on the surface of the treated material and, hence, the possibility of interaction of the oxygen with the polymer should increase. As a result, when the oxygen content in the initial gas decreases, the fraction of the gaseous products of the polymer etching with respect to the reagent (oxygen) increases; i.e., the loading effect becomes more significant. The difference between the W_{LLR} and W_{HLR} rates in this interval slowly increases approximately from 1.5 to 2 (Fig. 4); i.e., the influence of the composition of the initial gas on the loading effect of the PP is not large. For a woven fabric, for all the other conditions being equal, the reciprocal influence of the gas composition and the surface area of the polymer is more pronounced, since the effective (real) surface of the fabric subjected to the action of the active particles is larger than the geometrical surface area [4].

In the second interval, when the N_2 content in the mixture amounts to 90–100%, the rate of etching sharply falls and the W_{LLR}/W_{HLR} ratio increases from 2 to 6; i.e., the influence of the loading degree significantly increases. The rates of the channels of the oxygen dissociation should extremely depend on the composition of the gas mixture owing both to the changes of the ratio of the concentrations of N_2 and O_2 and the electrophysical parameters of the plasma. Evidently, all the channels of formation of atomic oxygen begin to close when the O_2 content in the mixture is lower than 10%. According to [8], in these conditions, in the gas phase, the fraction of the products increases whose formation needs less oxygen (CO and H_2). Their yield increases nonlinearly; the water from the products of the reaction becomes a reagent. When the N_2 content exceeds 0.95, NH_3 molecules appear among the products of the destruction of the PP; the oxygen expenditure in the reactions of etching becomes much more intensive. The increasing reciprocal influence of the heterogeneous and volumetric processes facilitates the fast increasing of the influence of the loading effect.

For the identification of the IR spectra of the samples of the treated and untreated PP samples, the data of works [9–12] were used. It was stated that the plasma action on the surface of the PP leads to the for-

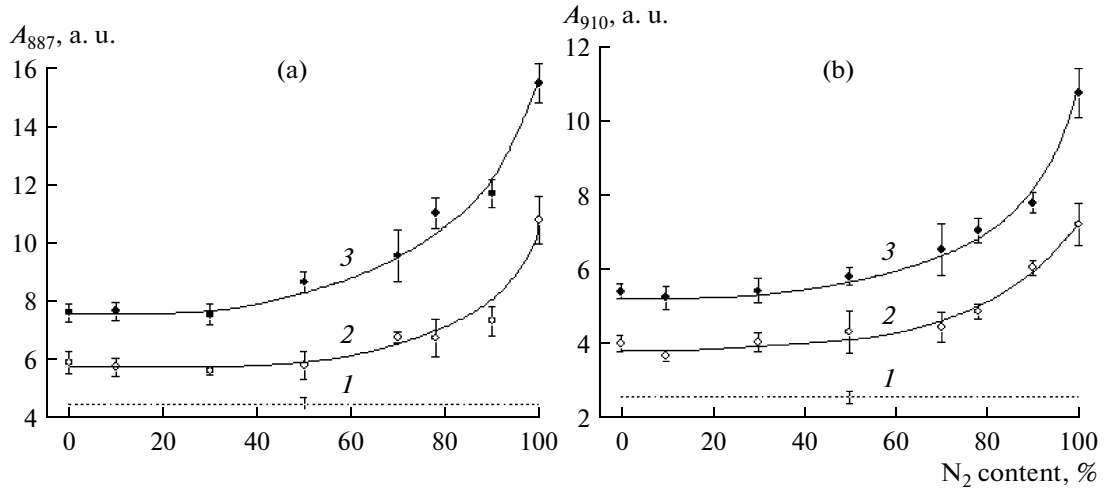

Fig. 5. Optical density of the absorption bands of the deformation oscillations of the double bonds of the VD type A_{887} (a) and the V type A_{910} (b) on the PP surface. (*1*) Untreated polymer, (*2*) LLR, (*3*) HLR.

mation of end double bonds of the vinyl (V) and vinylidene (VD) type independent of the composition of the mixture and the dimensions of the sample of the film. The appearance of the bands of deformation oscillations of C–H groups (910 and 889 cm^{-1}, respectively) confirms this fact.

The double bonds are formed under the action of the main physical factors of the plasma (UV radiation quanta and ionic bombardment); the $O_2(a^1\Delta_g)$ molecules mainly contribute the processes of their destruction, and $O(^3P)$ atoms are also involved to a certain degree [6]. In the plasma of the O_2 and N_2 mixture, the flux of quanta of UV radiation associated with the excited states of the atomic oxygen diminishes in comparison with the oxygen plasma. However, the UV radiation with a longer wavelength ($\lambda = 215–350$ nm) arises owing primarily to the luminescence of the excited states of the $NO(A^2\Sigma)$ molecule [7]. The consequence of the loading effect is the decreasing of the flux of $O(^3P)$ atoms on the sample. Since the ratio of the rates of the processes of formation and destruction of the double bonds changes, their concentrations on the PP surface increase both with the increasing of the N_2 fraction in the mixture and the loading degree (Fig. 5). The ratio of the concentrations of the double bonds for LLR and HLR virtually does not depend on the gas composition.

For all the compositions of the plasma-forming gas, including nitrogen, the oxygen-containing groups form at the PP surface. The increase of the absorption intensity was registered in the IR spectra of the treated samples in the following ranges: in the range of 1600–1800 cm^{-1} related to the stretching oscillations of the carbonyl group in various neighborhoods; in the range of 1000–1350 cm^{-1}, where the bands of the stretching oscillations of the C–O bond and the deformation oscillations of the O–H bond of acids, alcohols, and ethers are located; and in the range of 3100–3400 cm^{-1} corresponding to the stretching oscillations of the O–H bonds in alcohols. The presence of oxygen-containing groups on the surface modified in nitrogen can be explained in the following way. The concept of pure nitrogen is conventional, since, according to the data of the mass-spectral analysis, it contains not less than 0.2% oxygen and approximately the same amount of water vapor. Moreover, at the initiation of the discharge, some quantity of impurities (mainly water vapors) is eliminated from the reactor walls; a small addition of oxygen can appear owing to the cleanup of the electrodes in the gas.

The formation of ammonia in the reactions of destruction of the PP in mixtures rich in nitrogen gives evidence that nitrogen-containing groups are present at the surface treated in these conditions. Imines were reliably identified ($\nu = 1550$ cm^{-1} and 3300–3400 cm^{-1} correspond to the deformation and stretching oscillations of the N–H group, respectively; $\nu = 1660$ cm^{-1} corresponds to the stretching oscillations of the C=N group). The presence of primary amines is also possible ($\nu = 1620$ cm^{-1} and 3100–3400 cm^{-1} correspond to the deformation and stretching oscillations of the N–H group, respectively). As can be seen, the bands of the absorption of oxygen- and nitrogen-containing groups can overlap each other; therefore, it is difficult to interpret the results.

The data related to the character of the variation of the optical densities of several bands are presented in Figs. 6–8. From the set of the carbonyl bands, we considered those that do not fall in the range of absorption of double bonds ($\nu = 1640–1670$ cm^{-1} corresponds to the stretching oscillations of C=C bonds) and nitrogen-containing groups. This is the band of stretching

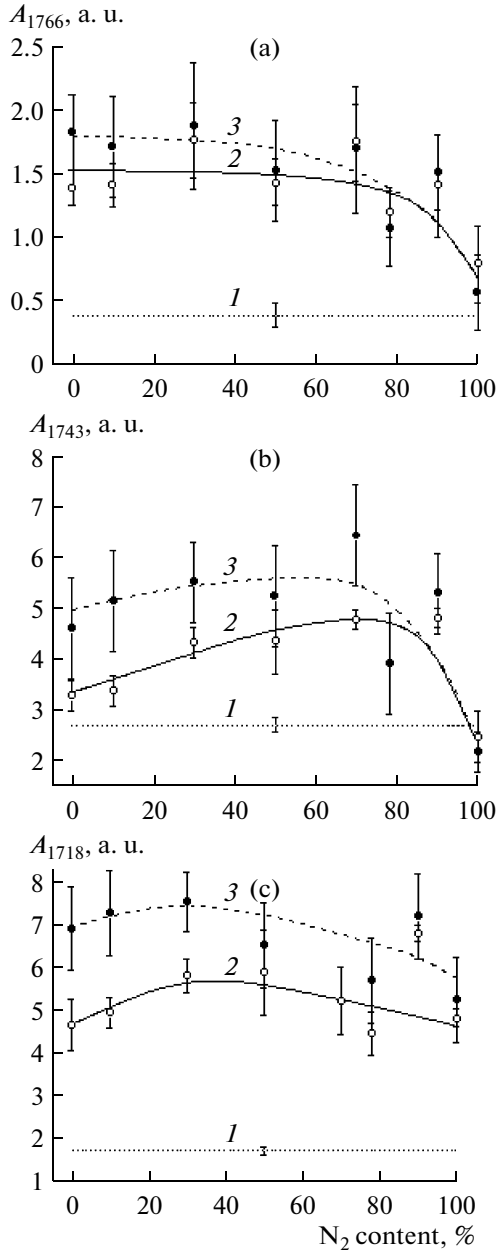

Fig. 6. Optical density of the absorption bands of the stretching oscillations of the carbonyl groups A_{1766} (a), A_{1743} (b), and A_{1718} (c) on the PP surface. (*1*) Untreated polymer, (*2*) LLR, (3) HLR.

vibrations of the carbonyl group in γ-lactones (ν ~ 1766 cm^{-1}), esters (ν ~ 1743 cm^{-1}), and ketones (ν ~ 1718 cm^{-1}). The wide bands of the stretching oscillations of the OH and NH groups are located in the same spectral range. The absorption corresponding to ν = 3340 cm^{-1} qualitatively reflects the changes in the integral band. The value of the optical density of the band ν = 1550 cm^{-1} allows one to estimate the relative content of imine groups on the surface.

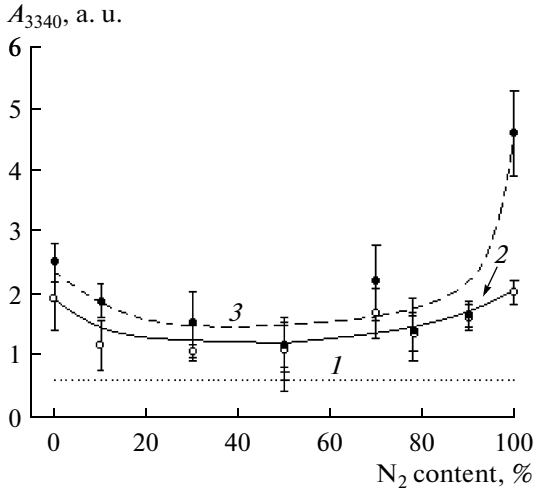

Fig. 7. Optical density of the band of integral absorption of stretching oscillations of O–H and N–H groups A_{3340} on the PP surface. (*1*) Untreated polymer, (*2*) LLR, (*3*) HLR.

The analysis of the obtained data showed the following.

In the range of compositions of O_2 : N_2, the same two intervals can be noted as those observed when we studied the kinetics of the etching. This agrees with the fact that the balance of the processes of formation and degradation of oxygen-containing groups, on the one hand, to a large degree defines the rate of etching of the polymer and, on the other hand, the content of these groups on the surface. In the first interval, where the O_2 content in the mixture amounts to 100–10%, the concentrations of compounds that contain oxygen groups on the whole weakly depend on the composition of the mixture. Increasing of the load leads to the shift of the balance to the direction of formation of these groups and, hence, to the increasing of their content in the modified layer (Figs. 6 and 7). The nitrogen-containing groups are absent on the surface, or their concentration is relatively small.

In the second interval, when the O_2 content in the mixture is less than 10%, the concentrations of oxygen-containing groups to a certain degree diminish and sometimes reach their initial values (Fig. 6). A redistribution of these groups occurs; the effect of loading on their content partly or completely disappears. Simultaneously with the oxidation, the nitriding of the surface was registered. According to the data shown in Fig. 8, the concentration of imines increases faster than linearly when both the N_2 content in the mixture and the load increase. In connection with this, one can suggest that the absorption owing to the oscillations of the N–H bond becomes prevailing (Fig. 7) in the integral band corresponding to ν = 3340 cm^{-1}. If we assume that the interaction of the chemically active particles of oxygen, water vapor, and nitrogen with the polymer involves the same surface active centers, the processes of

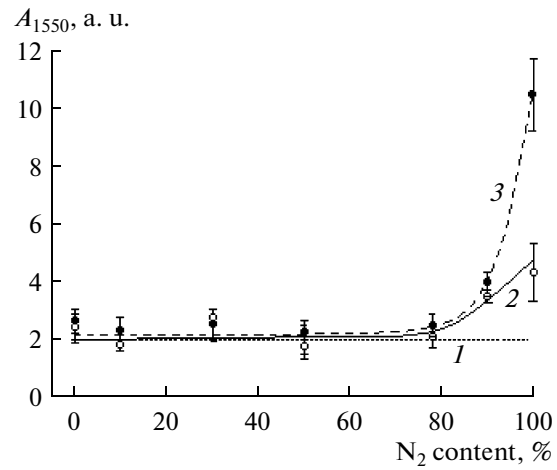

Fig. 8. Optical density of the absorption band of deformation oscillations of the N–H group in imines A_{1550} on the PP surface. (*1*) Untreated polymer, (*2*) LLR, (*3*) HLR.

the oxidation and nitriding of the polymer surface compete. This competition becomes more distinct when the loading degree of the reactor increases.

CONCLUSIONS

During the plasma-chemical etching of the PP film in the oxygen and nitrogen mixture, the effect of loading is observed in the entire range of the compositions of the initial gas. The effect of loading means that, when the quantity of the treated material increases, the specific rates of the etching decrease; at the same time, the concentrations of the functional groups (the double bonds in any case, oxygen- or nitrogen-containing groups dependent on the composition) on the polymer surface increase. The loading effect is generally more pronounced in the case when the initial gas contains less oxygen. The entire range of $O_2 : N_2$ ratios can be divided into two parts according to the degree of the influence of the mixture's composition on the loading effect. When the fraction of O_2 in the mixture amounts to 100–10%, the influence of the gas's composition on the loading effect is relatively small; the kinetics of the polymer destruction process are primarily determined by the competition of the processes involving the molecular and atomic oxygen. The increasing of the load leads to the increasing of the concentration of the oxygen-containing groups on the PP surface; the nitrogen-containing groups were not registered. When the fraction of O_2 in the mixture is lower than 10%, the reciprocal influence of the volumetric and heterogeneous processes significantly increases. Owing to the oxygen deficiency, water vapors enter the reactions of etching and, at the same time as oxidation, the nitriding of the polymer surface takes place. The competition of the processes of the oxidation and nitriding occurs, which is more pronounced when the degree of the reactor loading is larger.

REFERENCES

1. Maksimov, A.I., Gorberg, B.L., and Titov V.A., Facilities and Problems of Plasma Treatment of Fabrics and Polymer Materials, *Tekst. Khim.*, 1992, no. 1, pp. 101–117.
2. Maximov A.I., Rybkin V.V., Kuvaldina E.V., and Titov V.A., Loading Effect as a Result of Feedback in Chemically Reacting Plasma, *Proc. 14th Int. Symp. on Plasma Chem.*, Prague, 1999, vol. II, pp. 753–757.
3. Kuvaldina, E.V., Loading Effect at Air Plasma Etching of Fabric of Polyethylene Terephthalate Fibers, *Surf. Eng. Appl. Electrochem.*, 2008, no. 2, pp. 127–132.
4. Kuvaldina, E.V., Loading Effect at Oxygen Plasma Etching of Fabric of Polyethylene Terephthalate Monofilament Fibers, *Surf. Eng. Appl. Electrochem.*, 2009, no. 1, pp. 42–46.
5. Kuvaldina, E.V., and Rybkin, V.V., Manifestation of the Loading Effect in Polypropylene Oxidative Plasma Degradation Processes, *High Energ. Chem.*, 2007, vol. 41, no. 2, pp. 122–125.
6. Kuvaldina, E.V., and Rybkin, V.V., Interaction of Active Particles of Oxygen Plasma with Polypropylene, *High Energ. Chem.*, 2008, vol. 42, no. 1, pp. 59–63.
7. Rybkin, V.V., and Titov, V.A., Kinetics and Interaction Mechanisms of Oxydation Plasma with Polymers, *Entsiklopedia nizkotemperaturnoi plazmy. Ser. B. T. YIII-1. Khimiya nizkotemperaturnoi plazmy* (Encyclopedia of Low-temperature Plasma. Ser. B. Vol. YIII-1. Chemistry of Low-temperature Plasma, Moscow, 2005, pp. 130–170.
8. Kuvaldina, E.V., Shutov, D.A., Rybkin, V.V., and Smirnov, S.A., Kinetics of Gaseous Product Formation in the Surface Treatment of Polypropylene with Nitrogen–Oxygen Plasma, *High Energ. Chem.*, 2004, vol. 38, no. 3, pp. 200–202.
9. Zbinden, R., *Infrared Spectroscopy of High Polymers,* New York: Academic Press, 1964.
10. Dechant, J., Danz, R., Kimmer, W., and Schmolke R., *Ultrarot-spektroskopische Untersuchungen an Polymeren*, Berlin: Akademie-Verlag, 1972.
11. Cross, A. D., *An Introduction to Practical Infra-Red Spectroscopy*, London: Butterworths Sci. Publ., 1960.
12. Bellami, L.J., *The Infrared Spectra of Complex Molecules*, New York: Wiley, 1957.

ISSN 1068-3755, Surface Engineering and Applied Electrochemistry, 2010, Vol. 46, No. 2, pp. 144–148. © Allerton Press, Inc., 2010.
Original Russian Text © V.A. Khokhlov, 2010, published in Elektronnaya Obrabotka Materialov, 2010, No. 2, pp. 67–71.

ELECTRICAL PROCESSES IN ENGINEERING AND CHEMISTRY

Experimental Studies of Cation-Anion-Deficient $Nd_{1-x}Sr_xMnO_{3-y}$ ($x = 0.45$) Films with Various Thicknesses

V. A. Khokhlov

Galkin Institute for Physics and Engineering, Donetsk, National Academy of Sciences of Ukraine, ul. Rozy Lyurksemburg 72, Donetsk, 83114 Ukraine

e-mail: ayup@levch.fti.ac.donetsk.ua

Received November 3, 2009

Abstract—The magnetic and electroconducting properties of $Nd_{1-x}Sr_xMnO_{3-y}$ films with various thicknesses are studied. It is shown that all the films exhibit considerably high conductivity at a temperature of 300 K and that they are not a paramagnetic insulator as should be the case according to the phase diagram of this compound. The temperature dependence of the resistance exhibits a semiconductor behavior with decreasing temperature and has a maximum R_{max} at the temperature T_{max} being significantly different from the Curie point. A negative magnetic moment is observed in all the studied films at high temperatures. The possible causes of this phenomenon are discussed.

DOI: 10.3103/S1068375510020109

Despite the fact that many works are concerned with $NdSrMnO_3$ compounds [1–5] and that their state diagram has been composed [3], interest in them is still significant. It is well known that the magnetic and electric properties of these compounds strongly depend not only on the composition but also on the degree of crystallinity; the type of substrate; and, as a consequence, on the stresses that appear at the interface [6], on the availability of vacancies in the sample under study, and on the film thickness [7]. The aim of this work is to study the effect of the thickness and of the method of deposition (RF magnetron sputtering [5] and DC magnetron sputtering) on the magnetic and conducting properties of semidoped NdSrMnO films with various thicknesses with a deficiency of manganese and oxygen ions.

The films were obtained by DC magnetron sputtering from a ceramic substrate. The target was prepared using a traditional ceramic processing technology with a small deficiency of manganese. The assumed chemical formula of the target (by loading of oxides) is $Nd_{0.5}Sr_{0.5}Mn_{1-x}O_{3-y}$. According to the X-ray investigation of the target, it has an orthorhombic symmetry with the lattice parameters $a = 5.4302$, $b = 7.6177$, and $c = 5.4860$ Å. Additional studies of the target by the method of scanning electron microscopy using an X-ray microanalyzer on a JSM-6490LV scanning electron microscope (JEOL, Japan) showed that the chemical composition of the target is closer to the formula $Nd_{0.55}Sr_{0.45}Mn_{1-x}O_{1-y}$ (with $x < 0.1$). The films were sputtered on a substrate of $SrTiO_3$ (100). The substrate temperature was 650°C. According to the data of the X-ray diffraction, the films appeared to be single-phase with "cube-on-cube" epitaxial growth and with the parameter $a = 3.774$ Å. The parameter of the substrate is $a = 3.896$ Å; that is, it "compresses" the film (the $2a$ parameter of the film is less than the b parameter of the target by 0.9%). The annealing of the films was carried out at 900°C during 2 h in the air with subsequent slow cooling. Three films were grown: HC-1 (60 nm thick), HC-2 (120 nm), and HC-3 (240 nm). The film thickness was determined by the time of the sputtering. The HC-2 film thickness was measured using an MII-4 interference microscope to be 120 ± 20 nm.

The magnetic moment was studied using a SQUID magnetometer; the resistance was measured by the traditional four-point probe technique. The x-ray patterns were measured by a DRON installation.

Figure 1 depicts the field dependences of the magnetic moment of the three films measured at various temperatures; Fig. 2 shows the temperature dependences of the resistance of the same films. It is seen from Fig. 1 that, at low temperatures, the $m(H)$ curves are a sum of certain spontaneous values of the magnetic moment and the $m(H)$ dependence, being almost linear with the field characteristics of an antiferromagnetic or a paramagnetic. Using the extrapolation of this part of the magnetic moment to the zero field at the temperature $T = 10$ K, the values of the spontaneous moment m_0 were obtained and then calculated in μ_B units per formula unit (f.unit). These values are as follows: 0.96 for HC-1; 1.83 for HC-2; and 2.31 for HC-3, which is less than the value of 3.6 that corresponds to the complete ferromagnetic (FM) ordering of the spins of the Mn^{4+} and Mn^{3+} ions. These data allow reaching the conclusion that, at low temperatures, the film state is magnetic two-phase (MTP). An antiferromagnetic (or paramagnetic)

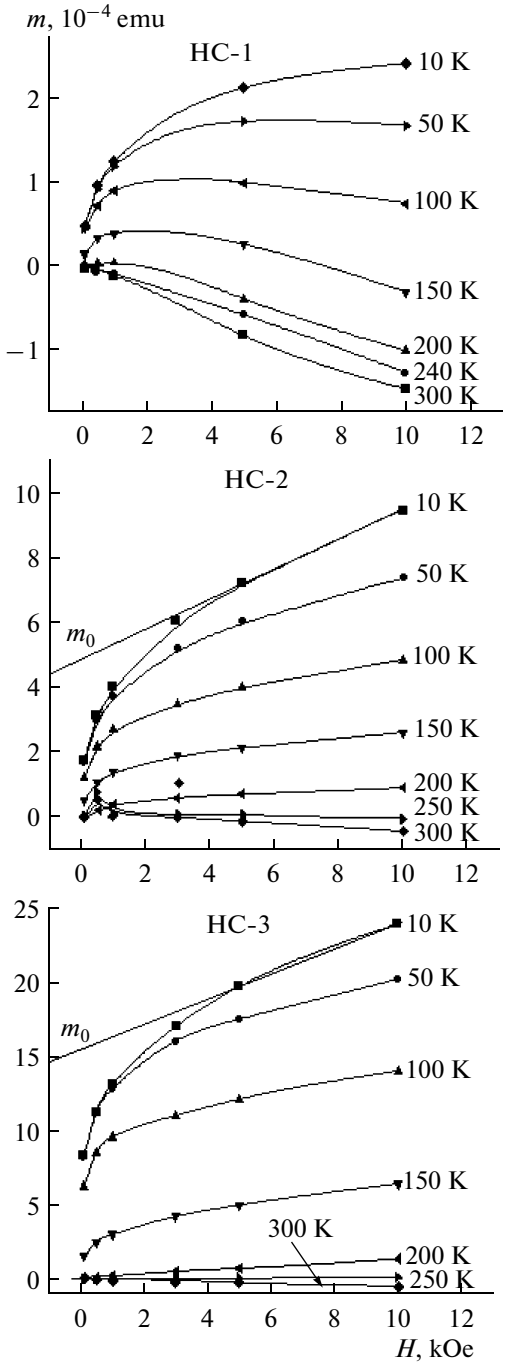

Fig. 1. Field dependences of the magnetic moment of the CH-1, CH-2, and CH-3 films measured at various temperatures.

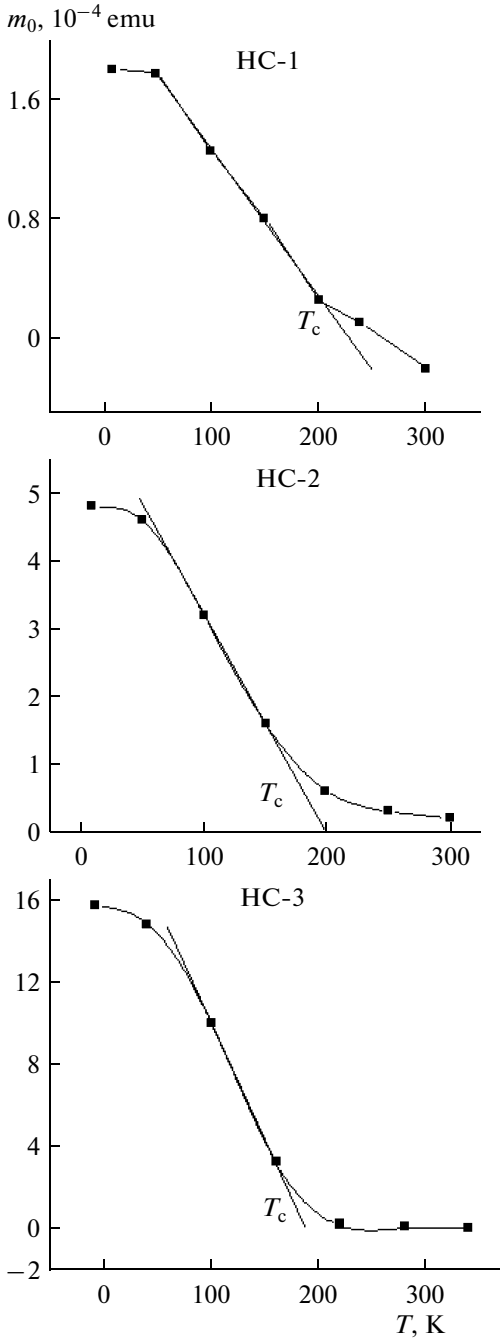

Fig. 2. Temperature dependences of the resistance of the CH-1, CH-2, and CH-3 films.

matrix comprises FM clusters; in addition, the size of the latter increases as the film thickness grows. Figure 3 shows the temperature dependence m_0 for all three films. The Curie point T_C was determined by extrapolating the steepest part of the $m_0(T)$ dependence to the zero value of the magnetic moment. The Curie point T_C is 230 K for the HC-1 film; 200 K for the HC-2, and 175 K for the HC-3. Thus, we can see that, as the thickness of the films increases, their T_C decreases.

As is seen from Fig. 2, all the films at room temperature exhibit a low resistance, which increases with lowering temperature. Except for the HC-1 film, in which the $R(T)$ maximum is not observed even at 77 K, the thicker films have the maximum tempera-

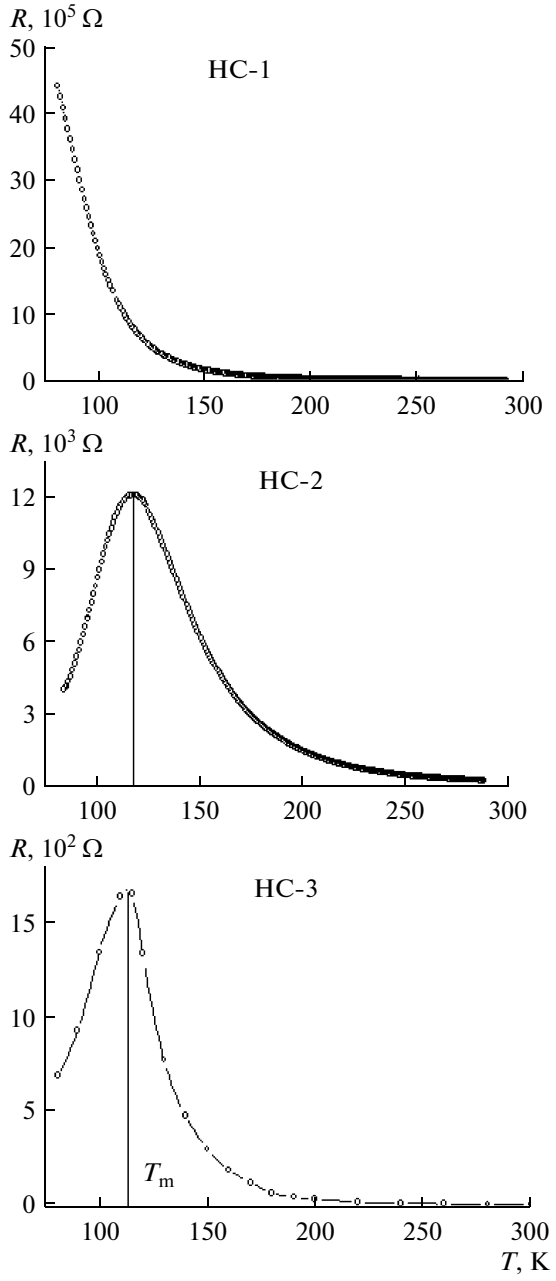

Fig. 3. Temperature dependences of the spontaneous magnetic moment of the CH-1, CH-2, and CH-3 films.

ture T_{max} of the film resistance (on the order of 118 K), below which the resistance decreases again. As the temperature falls from 300 K down to T_{max}, $R(T)$ exhibits a semiconductor behavior; below, a metallic one. The $R_{max}/R(300\ K)$ ratio for the HC-1 film is more than 2000; HC-2 = 68, and HC-3 = 48; that is, as the film thickness increases, this ratio appreciably decreases, particularly in the thickness range from 60 to 120 nm. Usually, the values of T_C and T_{max} are close to each other. In our case, they are significantly different. The great value of $R_{max}/R(300\ K)$ for the 60-nm-thick film cannot be explained by the possible "insular" pattern of the sputtering, because, at 300 K, their resistances differ insignificantly. The source of which such strong scattering of the charge carriers occurs in a thin film remains not to be seen.

Thus, the magnetic and electric properties of the films under study show that the chemical composition of the films is really such that, at low temperatures, it must be described by the left-hand side of phase diagram (3), i.e., by the region of an FM metal. At high temperatures, all the samples had a low resistance; that is, they did not transit into the paramagnetic insulating phase as shown in phase diagram (3), and the magnetic moment exhibited a diamagnetic behavior.

The most interesting result of the magnetic measurements of the films is the revealing of the diamagnetic properties in them at high temperatures. The temperature dependences of the susceptibility χ defined as the $\Delta m/\Delta H$ ratio are represented in Fig. 4. At 300 K, the highest value of χ in units of 10^{-8} emu/Oe is 1.48 for the HC-1 film, 0.629 for the HC-2, and 0.45 for the HC-3. It is seen that, as the film thickness increases by fourfold, the diamagnetic susceptibility decreases by more than 3 times.

An increase in temperature in HC-1 leads to a jump of the magnetic moment from a positive value to a negative one in the region of 140 K in the field $H =$ 10 kOe and in the region of 170 K in a field of 5 kOe. In fields of 1 kOe and below, no jumps of the magnetic moment are observed. The temperature of the "nulling" of the susceptibility increases from 196 K in the HC-1 film to 253 K in the HC-3.

The cause of the appearance of diamagnetism at high temperatures in our films can be explained if we take into account the following:

(i) The observed diamagnetism is not caused by the substrate, because, even if it appeared to be diamagnetic by chance, then its contribution would be almost equal for all the three films, since its thickness is four orders higher than that of the films.

(ii) The strong decrease in the negative magnetic moment with the increasing film thickness can be explained by the possible occurrence of a layer with diamagnetic properties near the interface. Such a layer was observed in [5], though it was FM.

(iii) Diamagnetism at high temperatures was observed in metal glass in [8], where it was shown that the particular connection between the FM particles and an amorphous matrix can lead to a giant diamagnetic response. Diamagnetism above the Curie point was also observed in a nanocrystalline sample of manganite [9]. The authors assumed that it can be caused by a metastable nanocrystalline configuration resulting in the localization of wave functions of electrons with a large orbital radius and that it appears in a strongly inhomogeneous stressed sample. Thereupon, there is a good probability of the appearance of localized electron orbits with a radius of tens of nanometers limited by the dislocation network. T.A. Onishchenko

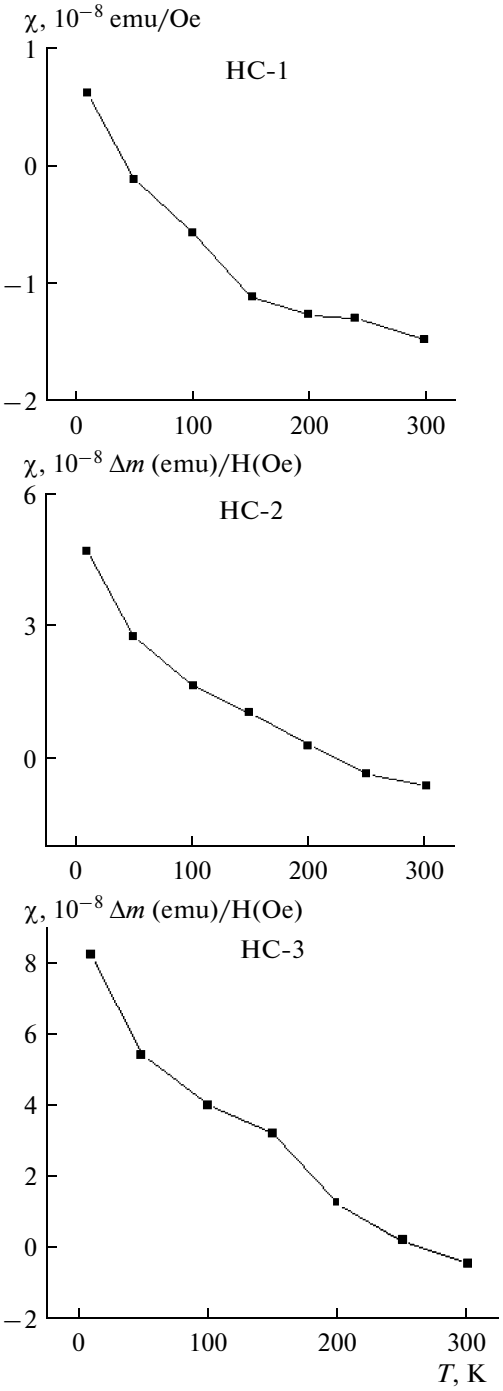

Fig. 4. Temperature dependences of the susceptibility of the CH-1, CH-2, and CH-3 films.

[10] showed that the macroscopic inhomogeneity of crystals, which is attributed, e.g., to deformations, leads to the electron spectrum dependence on the space coordinates. If the depth of the space modulation of the energy is much higher than the band width E_0 and if the band gaps e_g are considerably wide (which is not improbable in our narrow-band material), then the electron wave functions must be localized, and they can generate diamagnetism being a few orders higher than the Landau diamagnetism.

It follows from the above that the necessary condition of the occurrence of diamagnetism is the localization of electron wave functions at least in separate small-volume regions of the sample under study. This requires the macroscopic inhomogeneity of the sample (or layer) induced by stresses with the formation of a dislocation network or other causes. At the interface of our samples, due to the disagreement of the sizes of the unit cells of the film and the substrate, stresses appear in the film and form a dislocation network. As the film thickness grows, the stress relaxation takes place and the dislocation network broadens considerably. It is known that the current carrier motion in manganites occurs along the intraplanar chains Mn–O–Mn. Due to the deficiency of manganese and oxygen ions, these chains will be broken much more frequently than in nondeficient samples and form separate properly conducting regions. The totality of the regions limited by the dislocation network and the regions with proper conductivity can induce the desired space modulation of the energy in separate regions for the localization of electrons. The orbital moment of such localized electrons is the probable origin of the diamagnetism in a thin layer of the samples near the interface.

ACKNOWLEGMENTS

The author thanks V.P. Pashchenko for providing the target and Yu.M. Nikolaenko for the film sputtering using this target.

REFERENCES

1. Kawano, H., Kajimoto, R., Yashizawa, H., Tomioka, Y., Kuwahara, H., and Tokura, Y., Magnetic Ordering and Relation to the Metal–Insulator Transition in $Pr_{1-x}Sr_xMnO_3$ and $Nd_{1-x}Sr_xMnO_3$ with $x \sim 1/2$, *Phys. Rev. Lett.*, 1997, vol. 78, pp. 4253–4256.
2. Tokura, Y. and Tomioka, Y., Colossal Magnetoresistive Manganites, *J. Magn. Magn. Mater.*, 1999, vol. 200, pp. 1–23.
3. Kajimoto, R., Yoshizawa, H., Kuwahara, H., Tokura, Y., Ohoyama, K., and Ohashi, M., Hole-Concentration-Induced Transformation of the Magnetic and Orbital Structures in $Nd_{1-x}Sr_xMnO_3$, *Phys. Rev. B*, 1999, vol. 60, pp. 9506–9517.
4. Cui, C., Tyson, T.A., Chen, Zh., and Zhong, Zh., Transport and Structural Study of Pressure-Induced Magnetic States in $Nd_{0.55}Sr_{0.45}MnO_3$ and $Nd_{0.5}Sr_{0.5}MnO_3$, *Phys. Rev. B*, 2003, vol. 68, p. 214417.
5. Prokhorov, V.G., Kaminsky, G.G., Komashko, V.A., Lee, Y.P., Park, S.Y., Hyin, Y.H., Kim, J.B., Park, J.S., Svechnikov, V.L., Pashchenko, V.P., and Khokhlov, V.A., Nonclassical Magnetic Dynamics and Negative Exchange Bias in $Nd_{0.5}Sr_{0.5}MnO_3$ Films, *Fiz. Nizk. Temp.*,., 2007, vol. 33, no. 8, pp. 889–896.

6. Ogimoto, Y., Nakamura, M., Takubo, N., Tamaru, H., Izumi, M., and Miyano, K., Strain-Induced Crossover of the Metal–Isolator Transition in Perovskite Manganites, *Phys. Rev. B*, 2005, vol. 71, p. 060403(R).

7. Prellier, W., Biswas, A., Raeswari, M., Venkatesan, T., and Greene, R.G., Effect of Substrate-Induced Strain of the Charge–Ordering Transition in $Nd_{0.5}Sr_{0.5}MnO_3$ Thin Films, *Appl. Phys. Lett.*, 1999, vol. 75, no. 3, pp. 397–399.

8. Wang, Y.T., Pan, M.X., Zhao, D.Q., Wang, W.H., and Wang W.L., Unusual Diamagnetic Response in PrAlNiCuFe Metallic Glass, *Appl. Phys. Lett.*, 2004, vol. 85, no. 14, pp. 2881–2883.

9. Marcovich, V., Fita, I., Ruznak, R., Martin, C., Kikoin, K., Wisniewski, A., Hebert, S., Maignan, A., and Gorodetsky, G., Metastable Diamagnetism in the Manganite $Sm_{0.1}Ca_{0.84}Sr_{0.06}MnO_3$, *Phys. Rev. B*, 2006, vol. 74, p. 174 408.

10. Onishchenko, T.A., Diamagnetism of Band Electrons in Macroscopically Inhomogeneous Crystals, *Pis'ma Zh. Eksp. Teor. Fiz.*, 1981, vol. 33, no. 2, pp. 93–97.

ISSN 1068-3755, Surface Engineering and Applied Electrochemistry, 2010, Vol. 46, No. 2, pp. 149–153. © Allerton Press, Inc., 2010.
Original Russian Text © N.I. Kuskova, A.N. Yushchishina, A.P. Malyushevskaya, P.L. Tsolin, L.A. Petrichenko, A.A. Smal'ko, 2010, published in Elektronnaya Obrabotka Materialov, 2010, No. 2, pp. 72–76.

ELECTRICAL PROCESSES IN ENGINEERING AND CHEMISTRY

Production of Carbonic Nanomaterials in the Course of Electrodischarge Treatment of Organic Liquids

N. I. Kuskova, A. N. Yushchishina, A. P. Malyushevskaya, P. L. Tsolin, L. A. Petrichenko, and A. A. Smal'ko

Institute of Pulse Processes and Technologies, National Academy of Sciences of Ukraine, pr. Oktyabrskii 43a, Nikolaev, 54018 Ukraine

e-mail: iipt@iipt.com.ua

Received December 8, 2009

Abstract—The processes of electrodischarge destruction of liquid hydrocarbons to produce carbon nanomaterials have been studied. It has been shown that the product yield increases with the growth of the carbon chain length of the initial hydrocarbon. It has been established that, in the course of the treatment, both solid carbon nanomaterials and gas products are formed. The gas products consist of hydrogen and low molecular weight alkanes. It is shown that the hydrocarbon destruction process is accompanied by the change of the carbon atom hybridization, thus influencing the qualitative composition of the carbon nanomaterials.

DOI: 10.3103/S1068375510020110

The usage of an electric discharge to produce carbonic nanomaterials (CNM) holds a firm place among similar methods [1–3].

The chief advantage of this approach lies in the fact that liquid hydrocarbons are used as the initial raw material without any special ways of supply into the reaction zone; the process is conducted at normal pressure and room temperature. Furthermore, discharge-pulse methods, including the electric discharge in a liquid, are based on thoroughly elaborated analytical [4] and electrotechnical [5] principles.

The obtained carbonic materials are mainly in the solid phase, so they are easily liberated from the initial raw materials through such conventional methods as centrifugation and filtration.

The study of the quantitative regularities of the process of the electrodischarge destruction of liquid hydrocarbons with different contents of carbon atoms, as well as with different degrees of the carbon atom hybridization, is the purpose of this work.

EXPERIMENT

Such substances as hexane (AR grade), cyclohexane (AR grade), cyclohexanone (undiluted), benzol (AR grade), kerosene TC-1 (GOST 10227-86), white spirit (GOST 3134-78), and solar oil (GOST 305-82) were selected as the subject of the investigation.

The discharge installation diagram is presented in Fig. 1. The experiments were carried out under the following electric parameters: the working voltage was varied from 3 to 35 kV; pulse energy was from 100 J to 10 kJ.

The refraction factors (nD) were measured with the help of a universal laboratory refractometer (URL TU 25-05-1540-74) in order to ascertain the changes in the composition of the organic liquids in the course of the electrodischarge treatment.

The mass spectra of the gases adsorbed by the produced powders were registered with the aid of a mass spectrometer (МИ 1201В). The powered samples were heated in vacuum to perform the desorption of these gases. The gas ionization in the ionic source of

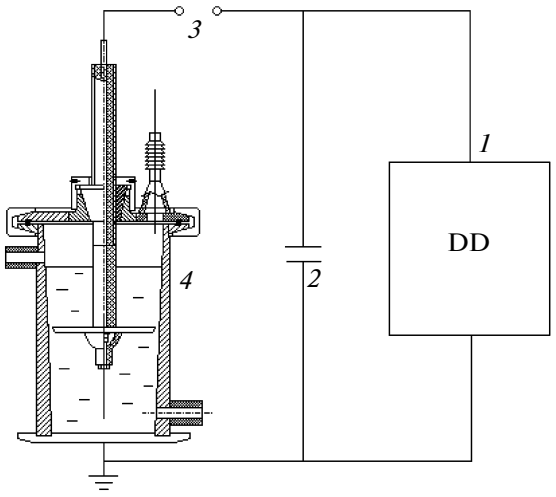

Fig. 1. The discharge installation diagram. *1*—discharge device, *2*—capacitive storage, *3*—multiplexer switch, *4*—discharge reactor.

Table 1. Dependence of the CNM yield on the carbon source at the electrodischarge treatment of the organic liquid

Carbon source	Number of atoms in the molecule	Raw material weight, kg	CNM weight after the ultra-centrifuge process, kg	Dried CNM weight, kg	CNM yield, %
Hexane	6	0.660	0.150	0.015	2.27
White spirit	10	0.600	0.200	0.023	3.83
Kerosene	from 10 to 14	0.660	0.330	0.040	6.06
Solar oil	frpm 11 to 20	0.720	0.380	0.067	9.30

the spectrometer was carried out by an electron bunch with energy of 70 eV. The measurements were conducted in the range of $1 \le m/z \le 250$, where m/z is the ion mass–charge ratio, a.u.m. (atomic unit of mass).

The yield of the carbonic nanomaterials was determined gravimetrically after the previous centrifuge processing of the produced suspension (3000 r/min) and the removal of the initial remaining liquid residue by drying the powder to a constant weight at a temperature from 80 to 100°C.

RESULTS AND DISCUSSION

With high-power electrodischarge pulses influencing the liquid hydrocarbons, there appears a region of high pressure and temperatures where the destruction and the decompounding of the hydrocarbon molecules take place with carbon in the solid form and hydrogen in the gas form being the final products. The carbon can evolve in different allotropic modifications, the type of which should depend, in our opinion, on the initial raw materials. It is supposed that the synthesis of fullerenes, carbonic nanotubes, and diamond or carbine from organic compounds having their hybridization degree equal or close to the hybridization degree of the produced material will proceed with a minimum energy input.

The investigation results on the influence of the liquid hydrocarbon carbon skeleton length on the yield of the solid carbonic materials are presented in Table 1.

It is easily seen that, with the carbon chain length growing, the ultimate product yield increases almost in direct proportion at the same energy input. Thus, if a mixture of carbon nanomaterials is the desired ultimate product, the solar oil can be suggested as an initial raw material. However, to produce certain allotropic modifications of the carbon (fullerenes, nanodiamonds, carbine), it is necessary to use a raw material with the carbon atom hybridization degree similar to that in the ultimate product [6].

In order to elucidate the mechanism of the hydrocarbon destruction process under the action of the electric discharge, we measured the refractive index of the liquids under treatment before and after such an impact. The data of these measurements are presented in Table 2.

The minor changes of the refractive index of the hydrocarbons indicate that no other liquid hydrocarbons with a smaller number of C atoms are generated during the process of the electrodischarge treatment. That is, the formation of the carbonic materials occurs through the complete dehydrogenation of the molecules of alkanes and can be described by such an overall equation as $C_nH_{2n} + 2 \longrightarrow nC + (n + 1)H_2$.

In order to elucidate the gaseous product composition, we carried out the investigation of the mass spectra of the gases adsorbed by the carbonic powder.

The mass spectra of the gases of the powder produced at the electrodischarge treatment of kerosene are presented in Fig. 2. The mass spectroscopy data allow reaching a conclusion on the presence of the following gaseous substances adsorbed on the solid phase material: H_2 ($m/z = 2$), H_2O ($m/z = 18$), C_2H_4 ($m/z = 28$), C_3H_6 ($m/z = 42$), and C3H8 ($m/z = 44$).

The presence of hydrogen confirms the proceeding of the alkane dehydration process, yet the presence of the gaseous hydrocarbons C_2H_4, C_3H_6, and C_3H_8 points to the more complicated mechanism of this process. Based on these data and taking into consideration that the reactions with the participation of alkanes mainly proceed according to the free-radical mechanism, the pattern of the electrodischarge destruction process can be presented by the example of *n*-hexane in the following form:

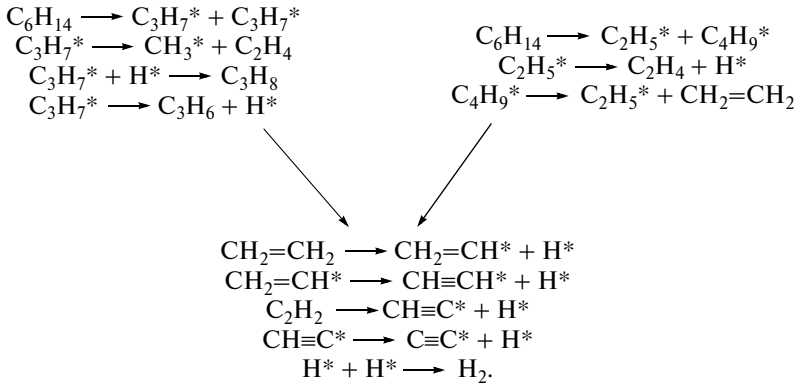

(H*, CH_3*, C_2H_5*, C_3H_7*, C_4H_9* are the radical particles).

This pattern explains both the formation of the solid phase of the C and CNM and the gaseous phase composition. It is peculiar that the realization of this pattern results in the change of the hybridization degree of the carbon atoms from *sp*3 (C–C) to *sp*2 (C=C) and sp (C≡C) during the treatment process. This should influence the phase composition of the produced carbon nanomaterials.

It is clearly seen from the microphotos typical for the CNM produced using the electrodischarge method presented in Fig 3 that the CNM have a developed surface (with the specific area of the surface being ~150 m^2/g) and a complex hierarchy structure with the size of the single constituent particles being ~100–200 nm.

In Fig. 4, there are shown the common diffraction patterns of the CNM produced in kerosene (the upper curve), hexane (the middle curve), and cyclohexane (the lower curve), which are characterized by a wide halo of about $2\theta \approx 30°$ in Co K_α radiation being typical for the amorphous structures.

Thus, the process of the electrodischarge destruction of the liquid hydrocarbons is governed by the following regularities. The overall product yield increases with the growth of the carbon chain of the initial hydrocarbon raw materials: the destruction of the hydrocarbons is accompanied by the formation of the solid phase carbon materials with amorphous structures and of the gaseous products containing, along with hydrogen, lower hydrocarbons with different degrees of the saturation of the carbonic bonds; the liquid phase product after the treatment does not contain other liquid hydrocarbons besides the initial one.

Table 2. Refractive indices *nD* of the carbonic liquids before and after the electrodischarge treatment measured at 20°C

Carbon source	Number of pulses	*nD*, before treatment	*nD*, after treatment
Hexane	1100	1.3832	1.3841
Cyclohexane	7200	1.4261	1.4296
Cyclohexanon	7200	1.4502	1.4502
Benzol	7200	1.5008	1.5037
Kerosene	300	1.4406	1.4425
Kerosene	1000	1.4406	1.4444
White spirit	1000	1.4441	1.4439
Solar oil + kerosene (1 : 1)	300	1.4529	1.4541
Solar oil + kerosene (3 : 1)	100	1.4589	1.4595
Solar oil + kerosene (3 : 1)	300	1.4589	1.4590
Solar oil + kerosene (3 : 1)	500	1.4589	1.4599

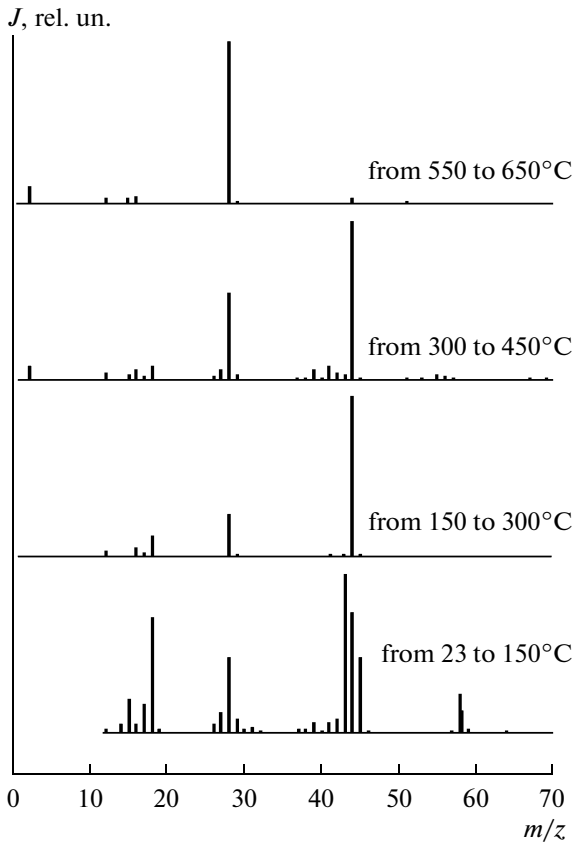

Fig. 2. Mass spectra of the gases liberated by the specimens under study. (All the spectra are normalized to the peak with the highest intensity).

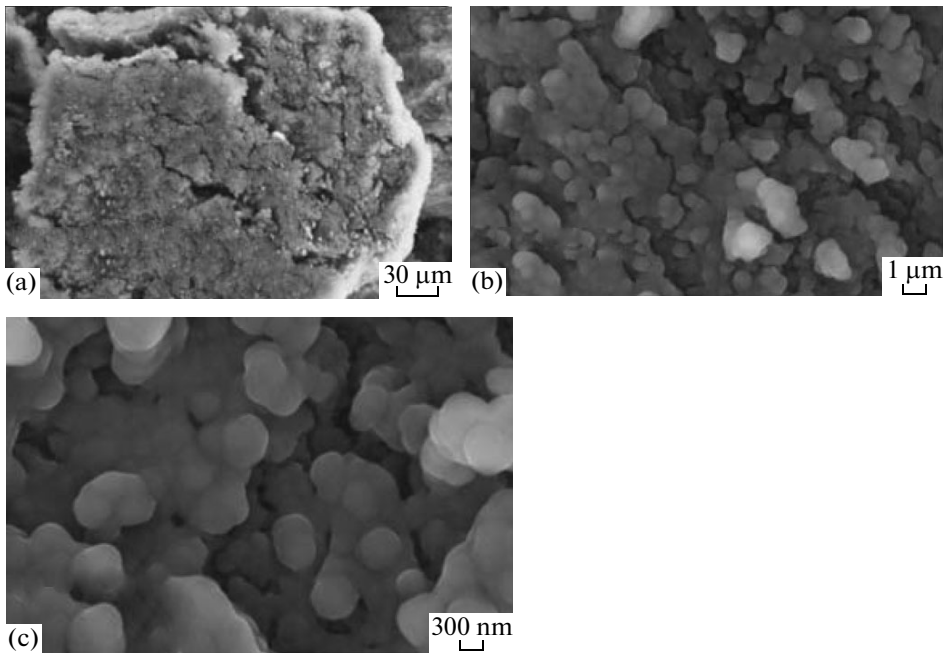

Fig. 3. Electron microphotos of the products of the electrodischarge treatment of kerosene: (a) a separate particle–agglomerate, 30 μm; (b) a particle, 1 μm; (c) a particle, 300 nm.

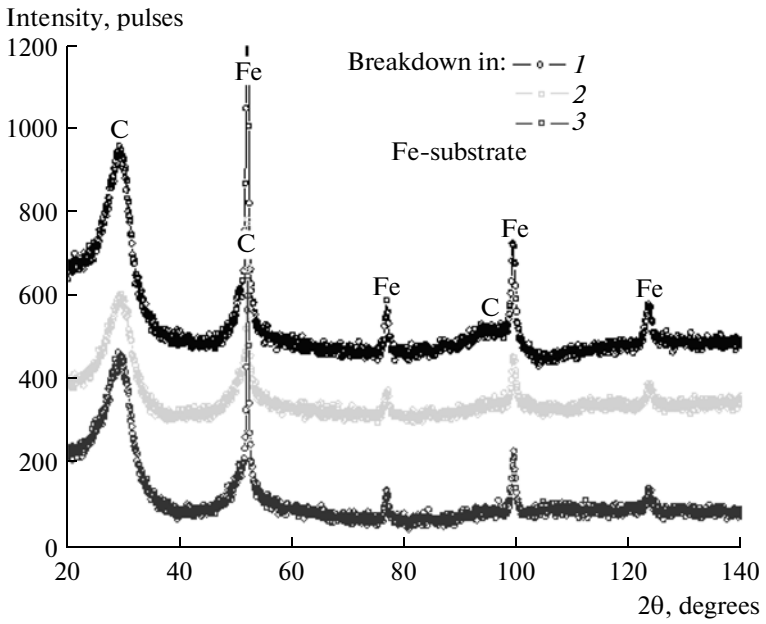

Fig. 4. A fragment of the diffraction pattern of the products of destruction of kerosene (1), hexane (2) and cyclohexane (3) as a result of the passage of the electrodischarge current pulses, Co K_α, Fe substrate.

The obtained data should be taken into consideration at the development of the discharge-pulse methods of production of carbon nanomaterials.

REFERENCES

1. Boguslavskaya, L.Z., Kuskova, N.I., Dyupin, V.A., et al, Ukraine Patent 45181, *Byull. Izobret.*, 2004, no. 7, p. 3.
2. Vovchenko, O.I., Kuskova, N.I., Shvets, I.S., Ishchenko, Zh.M., Petrichenko, S.V., and Yakimenko, O.A., Ukraine Patent 77347, *Byull. Izobret.*, 2006, no. 11, p. 3.
3. Vovchenko, O.I., Gorodyan, V.I., Kuskova, N.I., Razmenov, E.P., and Shvets, I.S., Ukraine Patent 77370, *Byull. Izobret.*, 2006, no. 11, p. 3.
4. Krivitskii. E.V., *Dinamika elektrovzryva v zhidkosti* (Dynamics of Electroexplosion in Liquid), Kiev: Naukova dumka, 1986, p. 272.
5. Malyushevskii, P.P., *Osnovy razryadno-impul'snoi tekhnologii* (Foundations of the Discharge–Pulse Technology), Kiec: Naukova dumka, 1983, p. 272.
6. Rud', A.D., Structure State of Amorphous Carbon Produced by the Method of Electric Breakdown of Hydrocarbon Liquids, *Tezisy dokladov 11-oi mezhdunarodnoi konferentsii Vodorodnoe materialovedenie i khimiya uglerodnykh nanomaterialov* (Abstr. 11 th Int. Conf. on Hydrogen Material Science and Chemistry of Carbon Nanomaterials), Kiev, 2009, pp. 542–543.

ISSN 1068-3755, Surface Engineering and Applied Electrochemistry, 2010, Vol. 46, No. 2, pp. 154–156. © Allerton Press, Inc., 2010.
Original Russian Text © R.S. Madatov, A.I. Nadzhafov, V.S. Mamedov, M.A. Mamedov, 2010, published in Elektronnaya Obrabotka Materialov, 2010, No. 2, pp. 77–79.

ELECTRICAL PROCESSES IN ENGINEERING AND CHEMISTRY

Anisotropy of Electric Conductivity in Irradiated $TlInS_2$ Crystals

R. S. Madatov, A. I. Nadzhafov, V. S. Mamedov, and M. A. Mamedov

Institute of Radiation Problems, National Academy of Sciences of Azerbaijan, ul. Agaeva 9, Baku, AZ-1143 Republic of Azerbaijan

e-mail: msrahim@rambler.ru

Received October 7, 2009

Abstract—The anisotropy of electric conductivity in hexagonal $TlInS_2$ crystals irradiated with γ-quanta are studied. It is found that, upon light exposure (~50 krad), radiation defects accumulate in the interlayer space and in the layer plane. As a result, the electric conductivity $\sigma_\perp$ and $\sigma_{||}$ decreases. As the exposure dose increases (above 200 krad), due to the interaction between the radiation defects and the initial inhomogeneities, complex defects appear with the result that the electric conductivity in either direction increases exponentially.

DOI: 10.3103/S1068375510020122

INTRODUCTION

The data on a significant concentration of defects in the anion sublattice of binary and ternary chalcogenides of the A^3B^6 and $A^3B^3C_2^6$ type are available in the literature [1–3]. This fact is particularly pronounced in sulfides of the above compounds. $TlInS_2$ is one of a few semiconductor compounds whose crystals of monoclinic modification exhibit a sequence of incommensurate and ferroelectric phase transitions. It is obvious that the vacancies available in the anion sublattice of these compounds must affect the features of the electric conductivity in the temperature range of 170–220 K and the photoelectric properties.

A characteristic feature of $TlInS_2$ crystals is their capability of forming stacking faults that have a strong effect on the electric conductivity of these crystals [4, 5]. To all appearances, this high concentration of intrinsic defects is attributed to the strong anisotropy of the bonding forces in such structures, which contributes to the appearance of many defects of layer interfacing, vacancies, and dislocations. This leads to a violation of the translation invariance of the crystalline structure and to the appearance of localized states in the band gap of the crystal. The effect of stacking faults on the electric properties of imperfect crystals and the interaction between these faults and the radiation defects have not been studied until now.

In this work, we discuss the results of the study of the anisotropy of the electric conductivity of $TlInS_2$ crystals of the hexagonal modification (HM) irradiated with γ-quanta at room temperature.

MEASUREMENT TECHNIQUE

For the study, we grew $TlInS_2$ single crystals by annealing single crystals of the monoclinic modification at 650 K for 30 days. The crystals exhibited the *n*-type conduction and a resistivity of $(1–6) \times 10^6$ Ω cm. The unit cell parameters of these crystals had the following values: $a = 3.82$ Å and $c = 14.85$ Å. Indium was used as ohmic contacts. The measurements were carried out in the direction parallel and perpendicular to the *c* axis of the crystals [6]. The samples were irradiated with γ-quanta by means of a Co^{60} installation at room temperature. In the process, in order to avoid heating of the crystals, they were cooled by liquid nitrogen vapors, and their temperature did not rise above 290 K.

RESULTS AND DISCUSSION

Figures 1 and 2 depict the temperature dependences of the electric conductivity of $TlInS_2$ crystals of the HM in the direction perpendicular ($\sigma_\perp$) and parallel ($\sigma_{||}$) to the *c* axis irradiated with γ-quanta at 300 K. As is seen from Fig. 1, the electric conductivity of the unexposed crystals in the direction $\sigma_\perp$ in the temperature range of 210–220 K exhibits a deep minimum with the activation energy $E + 0.49$ eV and undergoes exponential growth at a further decrease in the temperature (curve *1*). Upon the exposure of the samples to doses of 50 and 100 krad, the electric conductivity of the crystal increases and the dependence behavior remains unchanged; however, the shift of the minimum towards high temperatures (250 K) is observed. As a result, its depth and width decrease (curves *2* and *3*). Figure 2 also shows a minimum in the curve of the dependence $\sigma(T)$ in the temperature range of 180–190 K; it also shifts towards high temperatures, and its depth and width decrease as the exposure dose increases. The analysis of the temperature dependence of the electric conductivity showed that, according to the data of [7, 8], in the $TlInS_2$ crystals of the HM, the

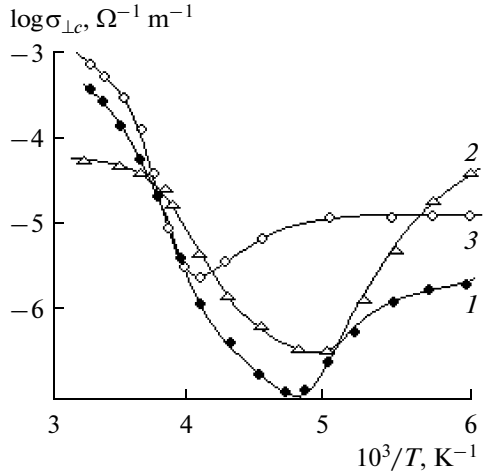

Fig. 1. Temperature dependences of the electric conductivity of the *n*-$TlInS_2$ of the HM in the $\sigma_{\perp c}$ direction before (*1*) and after irradiation with γ-quanta with a dose of 50 (*2*) and 100 krad (*3*).

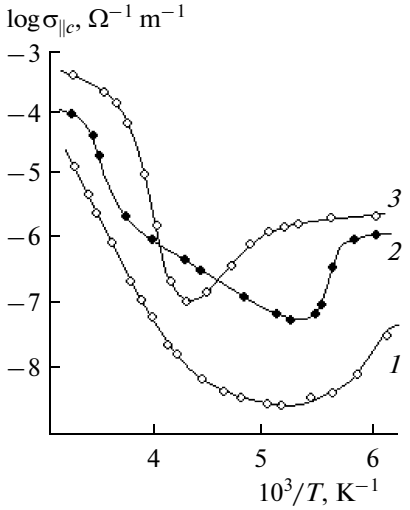

Fig. 2. Temperature dependences of the electric conductivity of the *n*-$TlInS_2$ of the HM in the $\sigma_{\parallel c}$ direction before (*1*) and after irradiation with γ-quanta with a dose of 50 (*2*) and 100 krad (*3*).

difference in the conductivity mechanisms in the different crystal directions results from the influence of uncontrolled impurities precipitating on stacking faults. In all probability, this is the cause of the decrease in the anisotropy of the electric conductivity in the entire temperature range with the increasing exposure dose.

Figure 3 represents the dependences $\sigma_{\perp c}$ and $\sigma_{\parallel c}$ on the exposure dose at room temperature. As we can see from the figure, at doses up to 30 krad, the electric conductivity of the crystals varies insignificantly in either direction. For exposure doses in the range of 30–120 krad (curve *1*), the $\sigma_{\perp c} \sim f(D)$ dependence, passing through the minimum, increases sharply; an insignificant rise in the electric conductivity is observed at a further increase in the irradiation dose. It is pertinent to note that, in the range of 30–120 krad, the electric conductivity increases exponentially in the direction parallel to the *c* axis ($\sigma_{\parallel c}$); subsequently, the behavior of the $\sigma_{\parallel c} \sim f(D)$ dependence is repeated as in the case of $\sigma_{\perp c} \sim f(D)$. The comparison of curves *1* and *2* (Fig. 3) shows that, under light exposure of nondoped *n*-$TlInS_2$ of the HM, radiation defects of the intrinsic acceptor type are introduced into the bulk and the interlayer space of the crystal.

In point of fact, the results show that the difference in the conductivity mechanisms in the different crystal directions is due to the influence of uncontrolled impurities precipitating on stacking faults of $TlInS_2$ crystals. The specified behavior of the electric conductivity of the *n*-$TlInS_2$ crystals of the HM shows that a continuous series of deep acceptor levels taking over a part of the electrons are formed in the band gap of the $TlInS_2$ upon the exposure [9]. Further irradiation leads to a change in the behavior of the dependence $\sigma_{\parallel}$ and $\sigma_{\perp c} \sim f(T)$ (Figs. 1, 2). This is attributed to the fact that long-term irradiation shifts the Fermi level closer to the middle of the band gap and that the radiation levels induced by the exposure appear to be of this level. Hence, as the temperature rises, the electric conductivity increases due to the increasing concentration of electrons in the conduction band. It is this which is the cause of the decreasing anisotropy of the electric conductivity in the entire temperature range with the increasing exposure dose. The decrease in $\sigma_{\perp c}$ in the dose interval up to 60 krad in comparison with $\sigma_{\parallel c}$ occurs due to the accumulation of radiation defects in the interlayer space of the crystal. This means that the accumulations of radiation defects in the interlayer spaces lead to a distortion of the conduc-

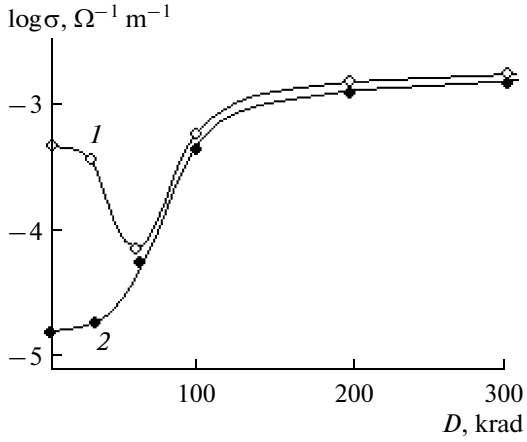

Fig. 3. Dependence of the specific conductivity (at 293 K) of *n*-$TlInS_2$ on the irradiation dose in the direction (*1*) perpendicular to the *c* axis and (*2*) parallel to the *c* axis.

tion band bottom and to the formation of potential wells for charge carriers. An increase in the amount of defects causes a disorder in the arrangement of the layers and so contributes to the growth of an interlayer barrier. The wide range of values of the anisotropy of the electric conductivity results from the presence of the above mentioned uncontrolled impurities, which, precipitating on stacking faults, introduce a disorder along the *c* axis. The dislocation of these impurity inclusions under heat treatment favors the manifestation of the three-dimensional pattern of the "c" band of the $TlInS_2$ crystals of the HM.

The results, in particular, the decrease in σ upon light exposure, show that, starting with a dose (depending on the initial impurity concentration), the accumulation of radiation defects is observed in the interlayer space along the plane and in layers. As a result, the mobility of the majority the carriers and thus the electric conductivity in either direction decrease. As the irradiation dose increases, due to the interaction between the radiation defects and the initial inhomogeneities, complex defects are formed; as a result, the electric conductivity in either direction increases exponentially. We assume that the decrease in the electric conductivity upon light exposure in the case of $\sigma_{\perp c}$ is due to the partial compensation of the initial donor level. The high-dose irradiation (above 200 krad) of *n*-$TlInS_2$ of the HM leads to the accumulation of radiation defects in the interlayer space and to strong compensation of the material.

The analysis of the experimental results showed that the nonequilibrium point radiation defects formed in layers, migrating, accumulate in the interlayer space and so decrease the crystal anisotropy upon high-dose irradiation.

REFERENCES

1. Sheleg, A.U., Plyushch, O.B., and Aliev, V.A., X-ray Investigations of the Incommensurate Phase in β-$TlInS_2$ Crystals, *Fiz. Tverd. Tela*, 1994, vol. 36, no. 1, pp. 226–230.
2. Kerimova, E.M., Mustafaeva, S.N., and Magerramov, A.B., Effect of Doping with Ag, Cu, and Sn on the Electric and Photoelectric Properties of $TlInSe_2$ Single Crystals, *Neorg. Mater.*, 1997, vol. 33, no. 11, pp. 1325–1326 [*Inorg. Mater.* (Engl. Transl.), vol. 33, no. 11, p. 1121].
3. Mamedov, K.K., Abdullaev, A.M., and Kerimova, E.M., Heat Capacities of $TlInS_2$ Crystals at Low Temperatures, *Phys. Status Solidi A*, 1986, vol. 94, no. 1, pp. 115–119.
4. Aliev, S.N., Nadzhafov, A.I., and Alekperov, O.A., Obtaining and Studying of the Properties of Hexagonal $TlInS_2$, *Izv. Akad. Nauk SSSR, Ser. Neorg. Mater.*, 1991, vol. 27, no. 3, pp. 621–622.
5. Alekperov, O.A. and Nadzhafov, A.I., Dielectric Anomalies in Monoclinic TlInS2 Polytypes, *Neorg. Mater.*, 2004, vol. 40, no. 12, pp. 1423–1426 [*Inorg. Mater.* (Engl. Transl.), vol. 40, no. 12, p. 1248].
6. Lysov, V.F., *Praktikum po fizike poluprovodnikov* (Laboratory Course of Semiconductor Physics), Moscow: Prosveshchenie, 1976.
7. Sheleg, A.U., Iodkovskaya, K.V, Rodin, S.V., and Aliev, V.A., Effects of γ-Irradiation on the Dielectric Properties of β-$TlInS_2$ Crystals in the Region of Existence of an Incommensurate Phase, *Fiz. Tverd. Tela,* 1997, vol. 39, no. 6, pp. 1088–1090.
8. Mustafaeva, S.N., Aliev, V.A., and Asadov, M.M., Direct Current Hopping Conductivity in Single Crystals of $TlGaS_2$ and $TlInS_2$, *Fiz. Tverd. Tela*, 1996, vol. 40, no. 4, pp. 612–615.
9. Madatov, R.S., Nadzhafov, A.N., Mamedov, V.S., and Mamedov, M.A., Switching Effect in the $TlInS_2$ Single Crystals Exposed to γ-Quanta, *Izv. Akad. Nauk Azerb.*, 2008, vol. 27, no. s2, pp. 64–67.

ISSN 1068-3755, Surface Engineering and Applied Electrochemistry, 2010, Vol. 46, No. 2, pp. 157–159. © Allerton Press, Inc., 2010.
Original Russian Text © A.Ya. Papchenko, N.A. Popova, V.G. Chobanu, M.K. Bologa, 2010, published in Elektronnaya Obrabotka Materialov, 2010, No. 2, pp. 80–82.

ELECTRICAL TREATMENT OF BIOLOGICAL OBJECTS AND FOOD PRODUCTS

Electroplasmolysis in Processing of Red Grape Varieties

A. Ya. Papchenko, N. A. Popova, V. G. Chobanu, and M. K. Bologa

Institute of Applied Physics, Academy of Sciences of Moldova, ul. Akademiei 5, Chisinau, MD 2028 Republic of Moldova
e-mail: ipepv@phys.asm.md

Received August 25, 2009

Abstract—The results of the experimental investigation of the influence of electroplasmolysis on the juice yield for red grape varieties are presented.

DOI: 10.3103/S1068375510020134

The breakage of the tissue membranes is an important process in the food production engineering connected with the extraction of juice from vegetable resources. The juice yield and the expenditures for its extraction depend on the degree of the breakage of the cell membranes. It is also important that, after the treatment, the cellulose cell envelopes do not pass into the juice hindering its extraction and clarification. This can be attained by the previous processing of the vegetal resources by various physical methods before the juice extraction.

There are known different ways of increasing the permeability of the cell membranes of vegetal resources: mechanical, thermal, biological, and chemical treatments and electric, magnetic, acoustic, radioactive, and ray methods. The mechanical and thermal ways of vegetal resource treatment are the most extensively employed ones. The fermentation (biological) method is seldom used because of its long duration. The electrophysical methods are at the stage of optimization and production testing [1–5].

The use of short electric pulses, the action of which has some advantages over the other electric techniques, is promising for the electric processing of food products. The electric energy concentration and the following acute impulse action on the processed material lead to qualitatively new effects, which can be taken as the basis for the elaboration of highly efficient technological approaches [6–8].

Combined methods of influence on plant tissues are promising as well; mechanical crushing (grinding, cutting into chips, etc) is usually used at the first stage. The smashing of berries to ensure the fermentation process is employed in the case of grapes before the extraction of the juice to produce wine.

The results of the investigation of the electric impulse influence on the crushed grape permeability are presented in this work.

The dependence of the resistivity of the crushed mass of the grapes on the specific energy introduced into the electroplasmolysis zone (Fig. 1, curve *1*) is obtained, and it is seen that the increase of the introduced energy within the range from 0.5 to 30 W hr/kg causes the reduction of the resistivity of the crushed mass. This, in turn, points to the plasmolysis of the grape berries' tissue cell protoplasm. However, the specific energy consumption at the level of 30 W hr/kg is substantial. Thus, the research work was carried out with the aim to reduce the electric energy consumption and to provide the highest efficiency of the electroplasmolysis.

There was studied the possibility of the crushed grapes' mass plasmolysis with the previous heating up to the regime corresponding to the conventional manufacturing process. The infusing of the marc with heating is used at the processing of red grape varieties to intensify the diffusion of the coloring agents from the skin into the juice. The plasmolysis with the temperature rise leads to the reduction of the specific energy consumption (Fig. 1, curves *2–4*); it is about 30 W hr/kg at the temperature of 20°C and only 3 W hr/kg at 60°C.

It has been established experimentally that this manufacturing process ensures the growth of the free-flowing juice yield by 6% in comparison with the standard one. The juice yield at the crushed mass pressing after the removal of the free-flowing juice increases up to 2% (Fig/ 2). The content of coloring agents in the juice produced with the use of the electric treatment rises from 1.3 up to 1.95 g/l (Fig. 3).

A planned experiment on the study of the influence of the specific plasmolysis energy and the temperature on the resistivity of the grapes' tissue was carried out. A two-factor plan was used (see the table).

The processing of the results permitted us to obtain the following mathematical model to describe the crushed grapes' plasmolysis process:

$$R(\Delta W, \text{W hr/kg}; ^\circ\text{C}) = 62.978/X_1 + 170.257482/X_2 + 22.480538/X_1^3 - 11461/X_2^2 + 0.007454/X_1X_2 - 92.483914/X_1^2 + 0.013518X_1^2,$$

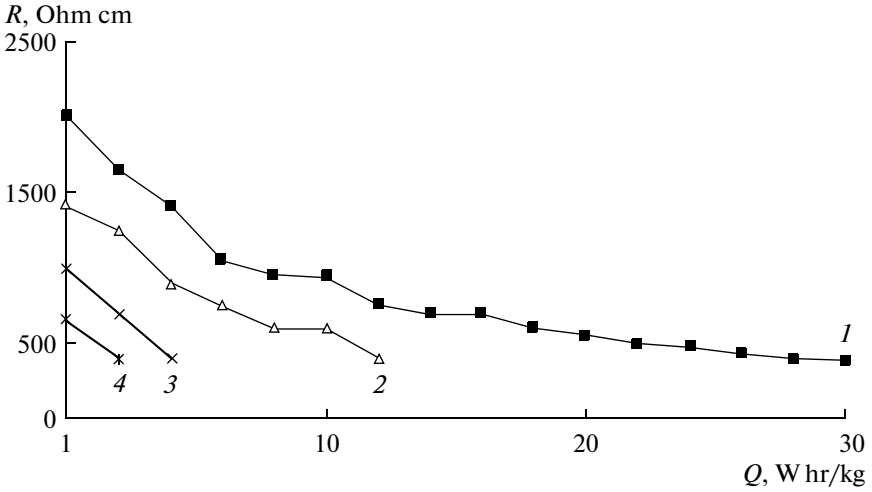

Fig. 1. The grapes' crushed mass resistivity versus the specific plasmolysis energy characteristic at the following temperatures, °C: *1*—20; *2*—40; *3*—50; *4*—60.

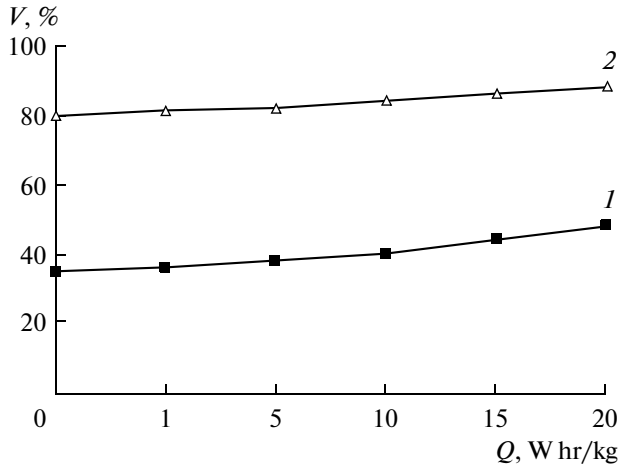

Fig. 2. The dependence of the free-flowing juice yield (curve *1*) and the total juice yield (curve *2*) on the specific energy consumption in the course of the electric treatment.

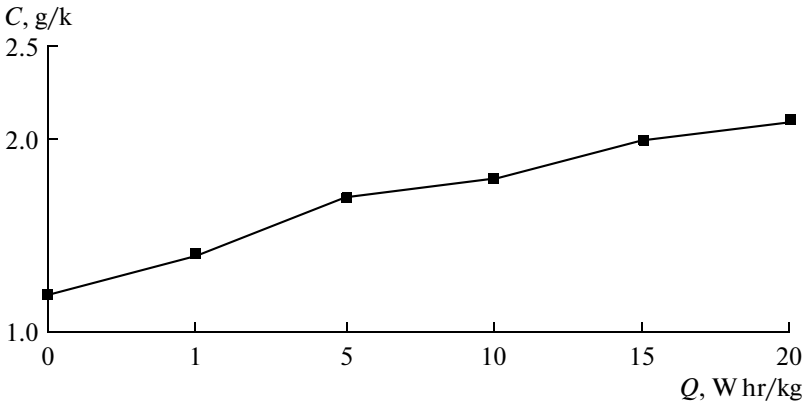

Fig. 3. The dependence of the coloring agents in the juice on the specific energy consumption in the course of the electric treatment.

Table

Factors	Specific electroplasmolysis energy ΔW, W hr/kg	Temperature, °C
The main level (X_{oi})	6	40
Variation ranges (ΔX_i)	4	20
Upper level ($x_i = X_{oi} + \Delta X_i$)	10	60
Lower level ($x_i = X_{oi} - \Delta X_i$)	2	20
Star point ($x_i = X_{oi} + 1.414\Delta X_i$)	11.6	68.3
Star point ($x_i = X_{oi} - 1.414\Delta X_i$)	0.35	12

where R is the grapes' tissue resistivity, kOhm cm; X_1 is the specific plasmolysis energy, W hr/kg; and X_2 is the grapes' tissue temperature, °C.

Thus, the electroplasmolysis of the previously heated to 60°C crushed grapes' mass allows one to increase the free-flowing juice yield and the coloring agent content and to reduce by 6–10 times the energy consumption for the plasmolysis process compared with the customary treatment of vegetal resources at a temperature in the range from 15 to 20°C.

REFERENCES

1. Bologa, M.K., Electrophysical and Chemical Investigations and Technology in the Institute of Applied Physics of the Academy of Sciences of Moldova, *Electr.Obrab.Mater.*, 2004, no. 2, pp. 4–11.
2. Papchenko, A.Ya., Popova, N.A., Chobanu, V.G., Berzoi, S.E., and Greku, G.D., Influence of the Electric Processing of Grapes "Izabela" on Juice Extraction and Quality, *Lukrerile Konferintsei Natsionale de Termotekhnika* (Proc. Nat.Conf. on Thermal Engineering), Ploesti, 2007.
3. Papchenko, A.Ya., Popova, N.A., Chobanu, V.G., Electroplasmolysis in Technology of Extraction of Juice from Grapes, *Conferentsa fizichienilor din Moldova* (Abstr. Conf. of Physical Scientists of Moldova), Kishinev, 2007.
4. Popova, N.A., The Analysis of Possibilities to Reduce the Specific Energy Consumption at the Production of Canned Vegetables, *Conferentsa fizichienilor din Moldova* (Abstr. Conf. of Physical Scientists of Moldova), Kishinev, 2007.
5. Chobanu, V.G., Bordeyanu, V., Papchenko, A.Ya., Bologa, M.K., and Berzoi, S.E., Installation for Electroplasmolysis of Vegetal Resources by Rotational Electric Field, *Conferentsa fizichienilor din Moldova* (Abstr. Conf. of Physical Scientists of Moldova), Kishinev, 2007.
6. Cobanu, V.G. and Papchenko, A.Ya., Peculiarities of the Previous Processing of Crushed Grapes, *Conferentsa fizichienilor din Moldova* (Abstr. Conf. of Physical Scientists of Moldova), Kishinev, 2007.
7. Papchenko, A.Ya., Popova, N.A., Chobanu, V.G., and Greku, G.D., Electrical Extractor for Processing of Vegetal Resources, *Konferntsa internatsionala "Konfort, eficientsa, konservarea energiei shi protektsia mediului"* (Abstr. Int.Conf. on Comfort, Efficiency, Energy Conservation and Environment Protection), Bucharest, 2006.
8. Chobanu, V.G., Papchenko, A.Ya., Berzoi, S.E., and Popov, N.A., Installation for Electroplasmolysis of Vegetal Resources, *Konferntsa internatsionala "Konfort, eficientsa, konservarea energiei shi protektsia mediului"* (Abstr. Int.Conf. on Comfort, Efficiency, Energy Conservation and Environment Protection), Bucharest, 2006.

ISSN 1068-3755, Surface Engineering and Applied Electrochemistry, 2010, Vol. 46, No. 2, pp. 160–164. © Allerton Press, Inc., 2010.
Original Russian Text © F.F. Yakhyayev, M.A. Kurbanov, I.S. Sultanakhmedova, F.N. Tatardar, G.Kh. Kulieva, 2010, published in Elektronnaya Obrabotka Materialov, 2010, No. 2, pp. 83–87.

EQUIPMENT AND INSTALLATIONS

A Device for the Complex Study of the Modes of Crystallization and Processing of Polymeric Composites under Electric Discharge Plasma and Temperature Effects

F. F. Yakhyayev, M. A. Kurbanov, I. S. Sultanakhmedova, F. N. Tatardar, and G. Kh. Kulieva

The Institute of Physics, National Academy of Sciences of Azerbaijan, pr. Dzhavida 33, Baku, Az-1143 Azerbaijan

e-mail: yafuad@rambler.ru

Received October 20, 2009

Abstract—A complex device for optimizing the modes of crystallization of polymer–piezoelectric ceramics composites under conditions of the simultaneous effect of the temperature and the electric discharge plasma arising in the air between the dielectrics (plasma crystallization) is created. A distinguishing feature of the present device is its applicability for the investigation of the charge state and the physicomechanical, electro-, and thermophysical properties of the composite materials.

DOI: 10.3103/S1068375510020146

INTRODUCTION

Highly informational and technological methods of modifying polymeric materials and multifunctional composites on their basis under the effect of various electrophysical, mechanical, electrochemical, and thermal factors have been elaborated [1–5]. Forecasting and optimizing of the modifying modes are considered to be urgent problems that require unifying a number of measuring systems for the determination of various physicochemical effects (the oxidation, the free radical state, the charge formation at an interphase boundary, the crystallization, the erosion, the interphase interactions, the synthesis of active gaseous low-molecular compounds [6–10], and the parameters of the modifying factors (the accelerated electrons, the ionizing irradiation, the mechanical and electric fields, and the electric discharge plasma of various natures) [11–13]). It is only the complex study and prediction of the parameters of the above modifying factors that will make it possible to optimize the modifying regimes and, namely, the crystallization of polymeric materials for the purposeful variation of their physicomechanical, electrophysical, photoelectrical, piezo- and piroelectrical, and electret properties.

EXPERIMENTAL

The creation of a complex device for the optimization of the modes of crystallization of polymer–segnetopiezoelectric ceramic composites based on the simultaneous effects of the temperature and the electric discharge plasma in the air medium between the dielectrics (electroplasmic crystallization) is described.

Figure 1 shows the principal scheme of the created complex device for the optimization of the plasma crystallization modes and the study of the properties of the polymer composites.

The development of the complex device for the composite's modification is aimed at the determination of the optimal modes of the composite's crystallization (under the simultaneous action of the electric discharge plasma and temperature) while revealing the correlation between the electric discharge parameters and the process of the modification of the physicochemical structure of the polymer matrix and the formation of a high–charged, thermo-, electroluminescent, and piezoelectric state in the polymer–piezoceramics composite. Heated to the melting temperature, the composite is exposed to the action of the electric discharge plasma in an electronegative gas. In addition, the processes that may eventually activate the formation of a high piezoelectric state may occur in the gaseous media and the composite:

- the introduction of nonequilibrium carriers of the electric charges from the zone of the charge's development into the composite;
- the oxidation of the composite's polymer phase and the origination of the localization centers for the introduced nonequilibrium charges from the plasma channels into the composite;
- the synthesis of the chemically active gaseous products in the plasma channels;
- the ionizing irradiation arising due to the recombination of the electric charge carriers;
- the free-radical state's origination and the development of the oxidative–destructive phenomena in the composite polymer phase.

The intensity of the above processes definitely depends on the energy parameters (the energy and the

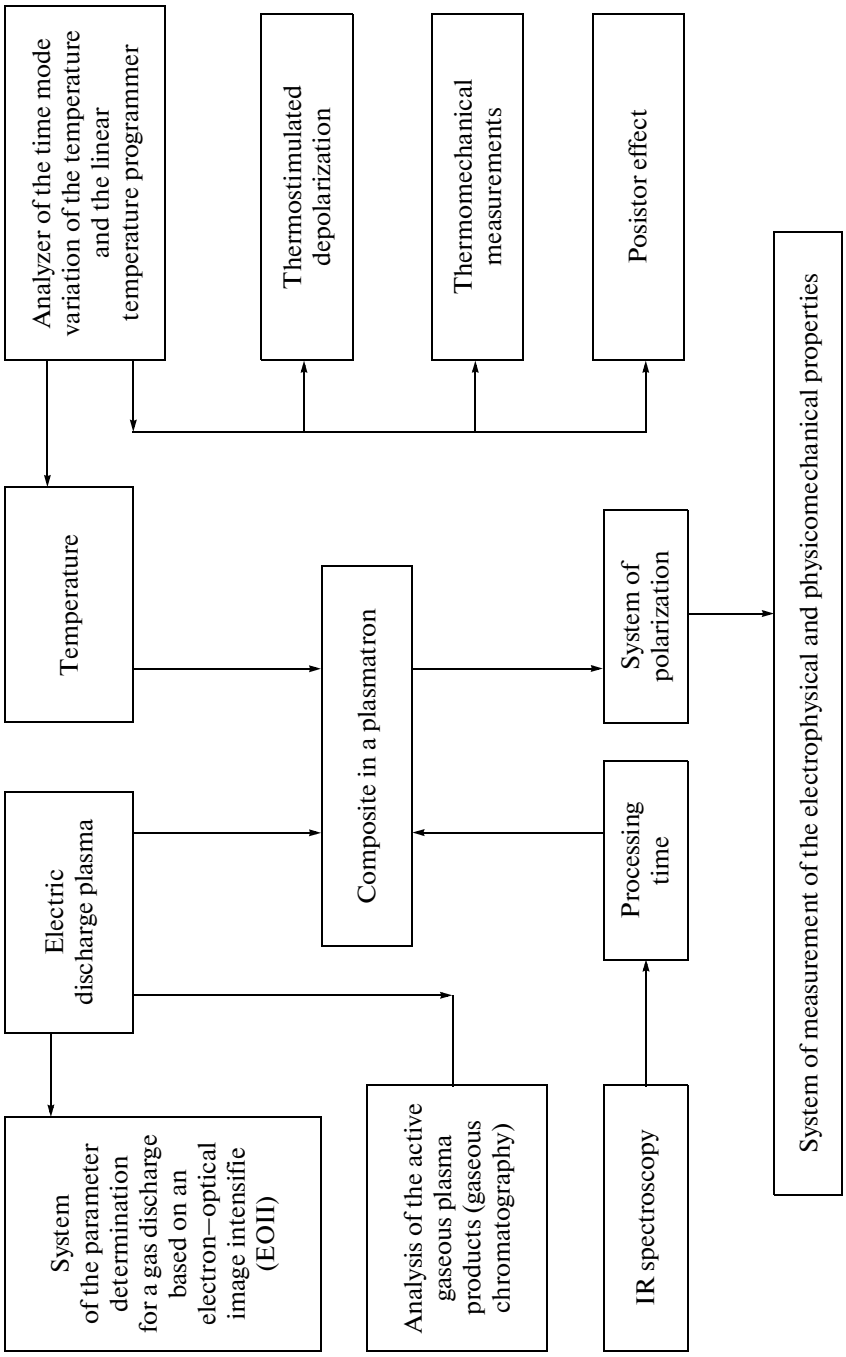

Fig. 1. The technology of modification of the composites under the condition of the simultaneous effect of the electric discharge plasma and the temperature (electroplasmic crystallization).

transferred charge) of certain plasma channels. Such factors as the temperature and the time of the composite's modification under the plasma action of the electric charge are important, whose incorrect selection involves the marked erosion of the composite's polymer phase and the consequent deterioration of the physicochemical, thermoxidative, mechanical, and piezoelectric properties. Therefore, the complex system of crystallization of the composites must comprise the functional units for the optimal task and purposeful variation of the following electrophysical factors:

• the parameters of the electric discharge plasma (the energy and transferred charge);

• the high and low temperature limits and the temperature rate variations under the conditions of the electric discharge plasma effect;

• the time of the plasma modification or the composite's crystallization;

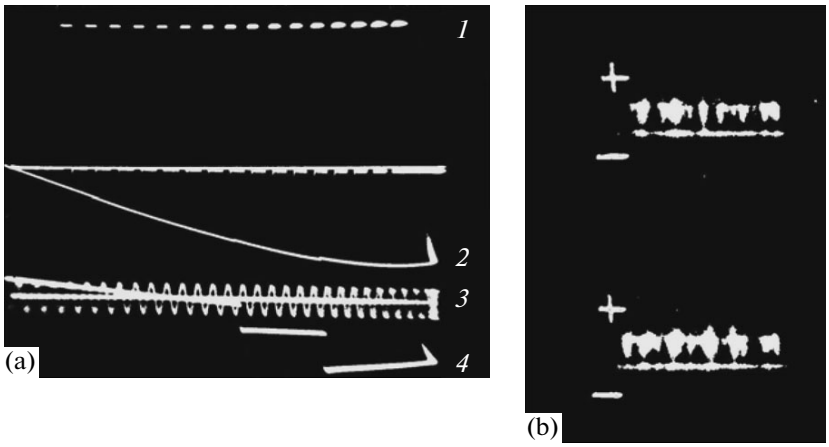

Fig. 2. Synchronously taken electric (a) and optical (b) images of the discharges in the gas medium. *1*—the closing pulse of the EOP; *2*—the cell voltage variation; *3*—the calibrating voltage; *4*—the voltage pulses at the moment of arising of separate series of microdischarges.

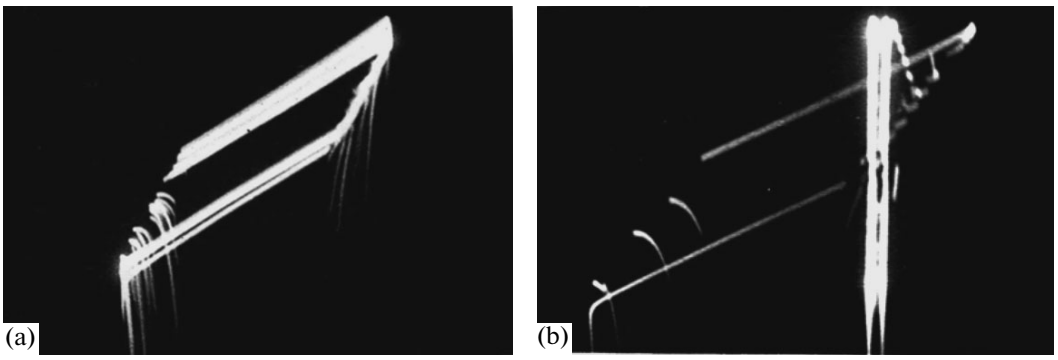

Fig. 3. Volt–coulomb characteristics of the discharge at continuous (a) and single (b) modes.

• the concentration of the active gaseous products (O, O_3, NO, OH, and CO) synthesized in the channels.

The Unit for Adjusting and Measuring the Parameters of the Electric Discharge (UAMED) in the Electronegative Gas Medium between the Dielectrics (the Barrier Discharge—BD)

Such a dielectric structure is created by limiting the air gap between the studied composites: the metal–composite–air layer–composite–metal. The discharge in such a dielectric medium makes it possible to uniformly process and oxidize the polymer phases of the composite. The electric discharge is initiated by the action in a high sinusoidal direction with an amplitude from 12×10^3 to 26×10^3 V and a frequency of $f =$ 50 Hz. The discharge parameters varied upon changing the dielectric characteristics (ε, $\mathrm{tg}\,\delta$, and ρ_v) of the composites, the gas medium (d), the composite thicknesses (h), and the amplitude of the voltage (U) applied to the dielectric structure. For the BD measuring, we used the method of synchronous registration of the spacial (an electron optical image of the microdischarge channel's development (EOP) (Fig. 2b)) and time (a pulse oscillogram of the voltage or current) image of the discharge (Fig. 2a). It is seen that each discharge is accompanied by the discrete arising of microplasma channels in space and time. The integral characteristics of the discharge (the energy and the charge for the period of the sinusoidal voltage) were determined by the method of the volt–coulomb characteristics. For this purpose, a special system (synchronizer) was developed that allows one to start the oscillograph at the moment of the zero value of the amplitude of the sinusoidal voltage applied to the testing cell. The dependency of the Q charge at the cell electrodes on the instantaneous value of the voltage U on it is observed at the oscilloscope display. The dependency we obtained, $Q = f(U)$, has the shape of a parallelogram (cyclogram) with a distinct transition from one area of this dependency to the other one (Fig. 3). However, in the investigation process, it was determined that the cyclograms appeared to be unstable. Therefore, the obtained images (due to the overlapping of a few dependencies $Q = f(U)$ at the oscilloscope display (Fig. 3a)) hardly make it possible to cal-

culate the U_z ignition voltage, the energy, and the charge of the discharge. To remove the above disadvantages, the oscillograph remained in the triggering mode only for 0.02 s, i.e., during a single period of the sinusoidal voltage. Thus, only one oscillogram of the dependency $Q = f(U)$ is formed at the oscilloscope screen (Fig. 3b).

The Unit for the Selection of the Temperature–Time Modes of the Composite's Crystallization

The selection of the temperature modes of the composite's crystallization is of great significance. It is important to determine the temperature of the melting for the composites and their temperature–time mode of crystallization (the heating and cooling rates) under the conditions of the plasma and mechanical tension effects. We developed devices for heating the investigated composite according to the linear law at various rates with stabilizing at any temperature selected from the operation range. The upper and lower limits of the operation interval were determined by the methods of thermomechanical (TM) measurements and obtaining the current spectra of the thermostimulated depolarization (TSD). A construction unit was provided for the synchronous registration of the thermodepolarized current at a mechanical impact on the composite specimen. The program positioner is constructed using the pattern of a digital–analog converter. The rate of the specimen's heating is set due to the frequency change of the clock pulse passing. In the mode of stabilization, the generator of the clock pulses disconnects the temperature selector. The main technical characteristics of the program's temperature selector are presented in [14]. The lower (393 K) and upper (433 K) temperature limits of the composites of the piezoceramics polyolefin and piezoceramics halogenous polymer were determined using the TSD and TM methods and the registration of the temperature dependence of the composite's specific resistance (the posistor effect) (Fig. 4). The lower limit of the crystallization temperature corresponds to the temperature of the TSD's first spectrum maximum (Fig. 4, curve *1*). The upper temperature limit for the plasmothermocrystallization is determined by averaging the temperatures corresponding to the TSD's second spectrum maximum (Fig. 4, curve *1*), the marked deformation growth (ε_d) of the thermomechanical dependency $\varepsilon_d = f(T)$ (Fig. 4, curve *2*), the maximum of the resistivity (ρ_v) of the dependency $\rho_v = f(T)$ (posistor peak, Fig. 4, curve *3*), and the marked decrease of the composite's density (Fig. 4, curve *4*).

The System of Determination of the Optimal Time for the Composite's Processing

The system of determination of the optimal time for the composite's processing under the electric discharge plasma effect is based on the infra-red spectra

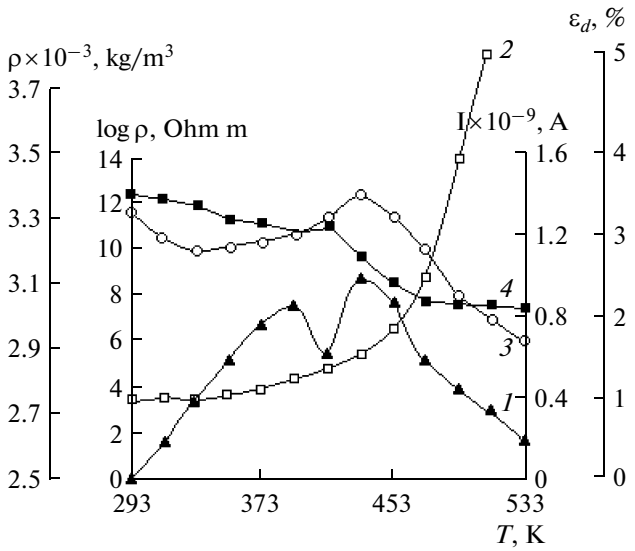

Fig. 4. The spectrum of the thermostimulated depolarized current (*1*) and the thermomechanical curve (*2*) of the PEHP–BT composite, and the temperature dependencies of the resistivity (*3*) and the specific density (*4*) of the PEHP–BT composite.

obtained using the spectrometer. The variations of the optical band of the absorption of the oxygeneous groups (C=O, OH, C–O–C) that appeared in the IR spectrum are studied. Upon the time increase of the composite's plasma crystallization, the optical density of the absorption of the above groups first increases and then tends to saturation. The time required for achieving the saturation by the band of the absorption of the oxygeneuos groups is regarded as the optimal time of the composite's modification.

The Systems of Polarization and Measurement of the Electrophysical and Physicomechanical Properties of the Plasmacrystallized Composites

The systems of polarization and measurement of the electrophysical and physicomechanical properties of the plasmacrystallized composites are the final functional units of the complex device for optimizing the crystallization process modes under the conditions of the electrodischarge plasma effect. The optimal modes of polarization (the electric field intensity E_n, the temperature T_n, and the time of the polarization t_n) of the piezoelectric composites are determined by the units of the TSD spectrum registration and the posistor peak (PP). The units of the TSD and the PP registration make it possible to determine the energy E_a of the activation and concentration of the charges stabilized during the electrothermopolarization at the local levels of the quasi-forbidden zone of the composite polymeric matrix. They also allow one to define the value of the potential barrier at the phase boundary (polymer–ferroelectric) of the composite.

The Unit of Registration of the Active Gaseous Products of the Discharge is based on a Gas Chromatograph of the Kristal–2000M Type

The concentration of the active gas products synthesized in the plasma channels of the discharge with respect to the energy parameters of the microdischarges may be determined.

CONCLUSION

The created device makes it possible to determine the optimal modes of the plasmacrystallization and the electrothermopolarization of the composites, along with the discharge parameters, in the dielectric–gas–dielectric system under whose effect the crystallization of the polymer composites is accomplished.

REFERENCES

1. Kalinin, Yu.E., Ponomarenko, A.T., Sitnikov. A.V., and Stognei, O.V., Nanocomposite Structures on their Way to Nanoelectronics, *Fizika i Khimiya Obrab. Metallov*, 2001, no. 5, pp. 14–20.
2. Yafarov, R.K., Manufacturing Nanodiamond Composite Materials in the Plasma of a Microwave Gas Discharge of Low Pressure, *Zh. Tekh. Fiz.*, 2006, vol. 76, no. 1, pp. 42–48.
3. Nil'son, L.E., *Mekhanicheskie svoistva polimerov i polimernykh kompozitov* (Mechanical Properties of Polymers and Polymeric Composites), Moscow: Khimiya, 1978.
4. Berlin, Al.Al., Topolkaraev, V.A., and Bazhenov, S.L., *Fizicheskie aspekty prognozirovaniya razrusheniya i deformirovaniya* (Physical Aspects of Destruction and Deformation), Leningrad: FTI, 1987.
5. Kerimov, M.K., Kurbanov, M.A., Agaev, F.T., Musaev, S.N., and Kerimov, E.A., Pyroelectric Effect in the Composites Crystallized under the Electric Discharge Plasma Effect, *Fiz. Tv. Tela*, 2005, vol. 47, no. 4, p. 686.
6. Abramov, R.Kh., Bagirov, M.A., Malin, V.P., and Oskolonov, V.A., On the Ozone Role in the Structure Modification of the Polymer Materials, *Vysokomol. Soedin., Ser. B*, 1974, vol. 16, no. 18, p. 604.
7. *Poverkhnosti razdela v polimernykh kompozitakh*, Plyudeman, E., Ed., Moscow: Mir, 1976.
8. Kerimov, M.K., Kerimov, E.A., Musaeva, S.N., Panich, A.V., and Kurbanov, M.A., Influence of the Structural and Electrophysical Parameters of a Pyrophase on the Pyroelectric Properties of a Polymer–Pyroelectric Ceramics Composite, *Fiz. Tv. Tela*, 2007, vol. 49, no. 5, p. 877.
9. Kurbanov, M.A., Kerimov, M.K., Musaeva, S.N., and Kerimov, E.A., Influence of the Crystallochemical Parameters of a Piezophase on the Piezo- and Pyroelectric Properties of a Polymer–Piezoceramics Composite, *Vysokomol. Soedin., Ser. B*, 2006, vol. 48, no. 10, p. 1892.
10. Kurbanov, M.A., Musaeva, S.N., and Kerimov, E.A., The Role of a Disordered Polymer Phase in the Formation of a Strong Local Field and a Piezoelectric Effect in a Polymer–Piezoceramics Composite, *Vysokomol. Soedin., Ser. B*, 2004, vol. 46, no. 12, p. 2100.
11. Bagirov, M.A., Kurbanov, M.A., and Shkilev, A.V., Investigation of the Electric Discharge in the Air between the Dielectric Coated Electrodes, *Zh. Tekh. Fiz.*, 1971, vol. 16, no. 6, pp. 1287–1292.
12. Bagirov, M.A., Burziev, K.S., and Kurbanov, M.A., Investigation of the Energy Characteristics of a Discharge Arising in the Air between the Dielectrics at Low Pressures, *Zh. Tekh. Fiz.*, 1979, vol. 49, no. 2, pp. 339–344.
13. Bagirov, M.A., Malin, V.P., and Abasov, S.A., *Elektricheskoe starenie polimernykh dielektrikov* (Electric Ageing of Poymeric Dielectrics), Baku: Azerb. Gos. Izd., 1987.
14. Aleskerov, F.K., Aliev, F.A., Kuliev, M.M., Kurbanov, M.A., Murshudli, M.M., and Murshudov, V.A., Cryostat with a Temperature Program Controller, *Pribory, tekhnika, eksperimenty*, 1986, no. 2, p. 230.

ISSN 1068-3755, Surface Engineering and Applied Electrochemistry, 2010, Vol. 46, No. 2, pp. 165–168. © Allerton Press, Inc., 2010.
Original Russian Text © Sh.M. Gasanly, A.Ya. Imanova, U.F. Samedova, 2010, published in Elektronnaya Obrabotka Materialov, 2010, No. 2, pp. 88–91.

EQUIPMENT AND INSTALLATIONS

Polypropilene and Silicon Thin-Film Composite Resistors

Sh. M. Gasanly, A. Ya. Imanova, and U. F. Samedova

Institute of Physics, National Academy of Sciences of Azerbaijan, pr. Dzhavida 33, Baku, AZ-1143 Republic of Azerbaijan
e-mail: hasanli_sh@rambler.ru

Received October 20, 2009

Abstract—It is stated from the analysis of the received results that, in the studied composites, the value of the resistivity significantly decreases and the dielectric permittivity increases with the increasing of the time of action of the electric discharge.

DOI: 10.3103/S1068375510020158

INTRODUCTION

The fabrication of polymer compositions with specific electrophysical, electrete, sensor, and tensosensitive properties, to a large degree, depends on the filler's nature; on the form, dimensions, and distribution of the particles; and on the interaction level between the components. Depending on the nature of the polymer matrix and the filler type, various methods are used to obtain an electroactive state. Various dielectric and electrophysical methods are used to study the peculiarities of the charge stabilization.

Numerous experimental data [1–5] give strong evidence that the electroactive properties of a heterogeneous polymer–filler system are primarily defined by the charge state of the phases, the specific features of the structure, the interphase interation, and the distribution of the polarization in the composite. The control over the charge accumulation and relaxation processes in polymer composites under the action of an electric discharge in air is of great scientific and practical interest since this allows us to clarify the interrelations between the polarization parameters and the peculiar features of the structure and interphase interaction.

The present work is devoted to the investigations of the influence of the electric discharge on the current–voltage characteristics (CVC), the resistivity value (at a constant voltage), and the dielectric permittivity of composites on the basis of the nonpolar polymer polypropylene (PP) and single-crystalline silicon.

1. EXPERIMENTAL METHOD

Monocrystalline semiconductor silicon (p-Si) and nonpolar polypropylene (PP) powder were used as the composite components. The composites were prepared from a homogeneous mixture of powders by hot pressing. The content of the composite components was varied in a wide range (1–60% for silicon and 99.99–40% for polypropylene, respectively). The following method was used to prepare the material of the specified composition for thin-film composite varistors. A necessary quantity of a mixture that consists of Si(C) and polypropylene (PP) is weighed and ground with the dimensions of the particles being less than 60 μm in a porcelain ball mill. Then, the mixture is placed in a mold and subjected to hot pressing according to the following procedure. First, the mixture is heated at a pressure of $P = 1$ MPa to the melting temperature ($T = 200$°C) during 20 minutes; then, the press pressure is increased to $P = 15$ MPa, and the melted mixture is held for five minutes at this pressure. The obtained thin-film composite varistor is cooled by quenching in water. This cooling method allows one to prepare more elastic films.

The thickness of the samples amounted to 150 μm. The electrodes for the measurements with their diameter of 6 mm were prepared by applying a silver paste on the samples.

The studied samples were subjected to a barrier electric discharge for 3–15 min. The installation shown in Fig. 1 was used to apply the electric discharge at room temperature.

The dependences of the current–voltage characteristics, resistivity, and dielectric permittivity versus the duration of the electric discharge were studied for all the samples. These parameters were registered at $T = 293$ K.

2. DISCUSSION OF THE EXPERIMENTAL RESULTS

The experimental results are shown in Figs. 2–5, which exhibit the influence of the duration of the electric discharge on the current–voltage characteristics and the dependences of the resistivity and dielectric permittivity of the composites.

Note that, for all the studied composites, a noticeable variation of the electric current was observed. As an example, in Fig. 2, the current–voltage character-

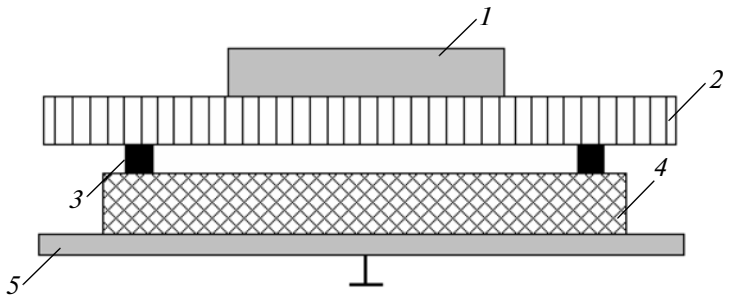

Fig. 1. Experimantal cell. (*1*) Upper electrode, (*2*) vitroceramic plate, (*3*) isolating supports, (*4*) sample, (*5*) lower electrode.

istic is shown of a composite of 30%(Si) + 70%(PP). The figure shows that the value of the electric current through the sample strongly increases after the barrier discharge and does not depend on the discharge duration. Particularly, after the discharge time $t_{discharge} = 15$ min, the current value through the composite changes by 2–3 orders (Fig. 2).

The dependence of the resistivity on the discharge duration is shown in Fig. 3. It is evident that the resistivity diminishes slowly until $t_{discharge} = 8$ min and then it sharply falls at $t_{discharge} = 15$ min.

According to published data [6–8], after the discharge, both the surface and bulk conduction of the composites increase. The increasing of the surface conduction is associated with the appearance of a semiconducting layer of moist and low-molecular products of the composite destruction or with the absorption of charged particles from the zone of the discharge action. The bulk conduction of the composite after the discharge can increase owing to the following reasons:

(1) the formation of a space charge (SC) inside the studied sample involving the injection of charged particles from the discharge zone;

(2) the diffusion inside the sample of low-molecular compounds formed as a result of the oxidative destruction of macromolecules of the surface layer; and

(3) the changes of the polarization processes in the sample, since its structure changes under the action of the discharges.

Note that the SC arises in the polymer since the charge carriers drift from the zone of action of the discharge or from the electrode surface into the sample. These charges lose their energy owing to collisions and spread between the polymer molecules in so-called traps, which appear owing to the irregular structure of the macromolecules. First these carriers are located in a zone near the sample surface, but, when all the traps in this zone become filled, they drift in the bulk of the sample owing to the diffusion in the field of the space charge till all the traps in the sample are filled.

Taking into account these facts, the observed decreasing of the resistivity (and increasing of the conduction) is obviously associated, on the one hand,

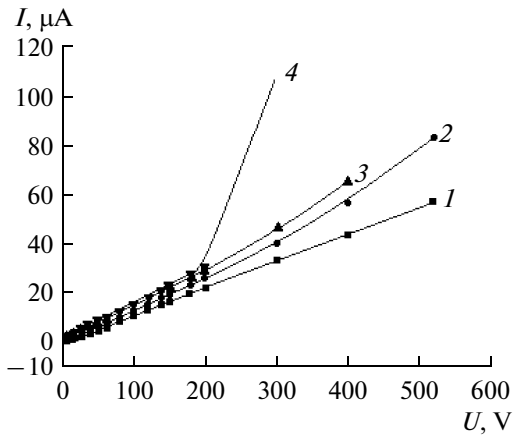

Fig. 2. Current–voltage characteristics of the 30%(Si) + 70%(PP) composite before and after the barrier discharge. The discharge duration, min: (*1*) 0, (*2*) 3, (*3*) 8, (*4*) 15.

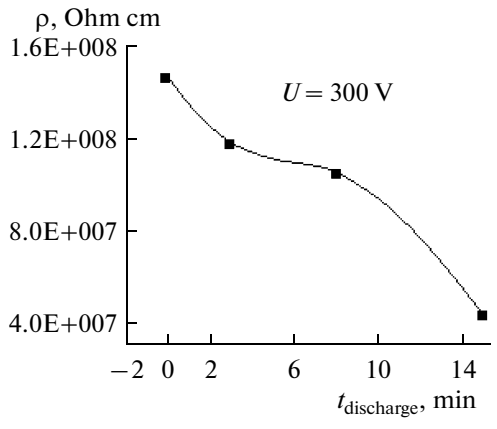

Fig. 3. Dependence of the resistivity on the discharge duration.

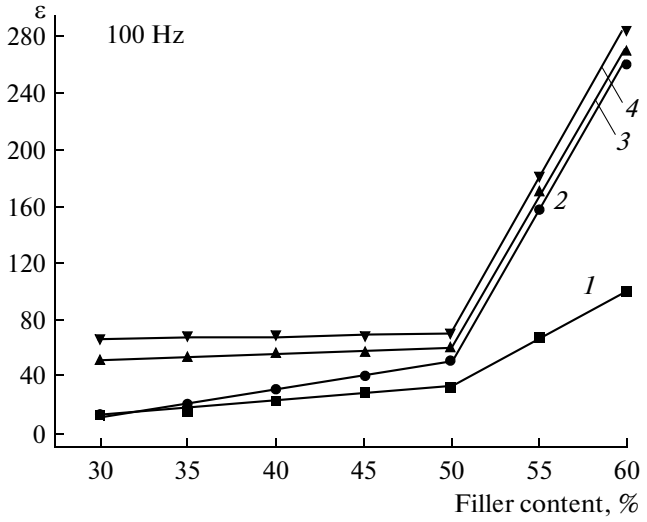

Fig. 4. Dependence of the dielectric permittivity on the filler percentage after the electric discharge at the frequency $F = 100$ Hz. The discharge duration, min: (*1*) 0, (*2*) 3, (*3*) 8, (*4*) 15.

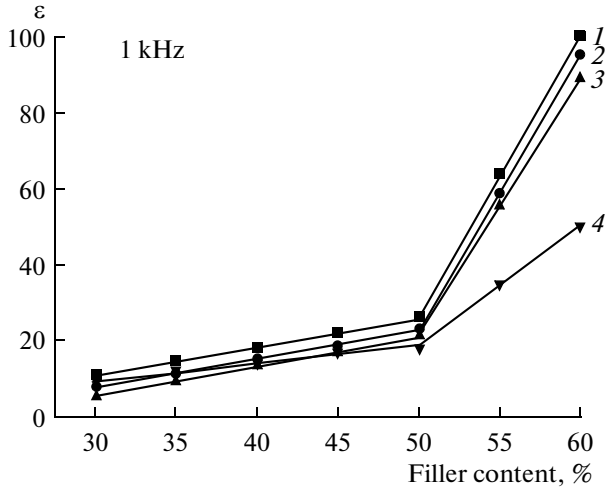

Fig. 5. Dependence of the dielectric permittivity on the filler percentage after the electric discharge at a frequency of $F = 1$ Hz. The discharge duration, min: (*1*) 0, (*2*) 3, (3) 8, (*4*) 15.

with the injection of the charged particles in the bulk of the composite and, on the other hand, with the increasing of the space charge in the composite. The sharp decreasing of the resistivity after $t_{discharge} = 8$ min gives evidence for this.

The observed dependence of the dielectric permittivity on the filler percentage (Fig. 4) also confirms the increasing of the space charge in the composite. Note that the role of destruction of the surface layer after the discharge also cannot be excluded.

The dependences of the dielectric permittivity on the filler percentage before and after the barrier discharge are shown in Figs. 4 and 5. The following features of the dependence $\varepsilon = f(t_{discharge})$ can be seen in the figures. First, independent of the frequency of the measurements ($f = 100$ Hz or $f = 1$ kHz), the value of the dielectric permittivity ε before and after the discharge sharply increases when the filler percentage increases. Second, the comparison of curves *1* and *4* in Fig. 4 shows that, after the electric discharge with the duration of $t_{discharge} = 15$ min, the ε value at the frequency $f = 100$ Hz is an order of magnitude larger than for $t_{discharge} = 0$ min.

The increasing of the dielectric permittivity with the increasing of the discharge duration can be explained as follows. When the discharge duration increases, the degree of polarization of the composite, in general, increases [9–10] owing to the accumulation of the space charge. The observed decreasing of the dielectric permittivity when the frequency increases can be explained by the fact that, at high frequencies, the charged states defining the barrier capacitance do not have enough time to recharge. At high frequencies, the capacitance of the system is defined by the intergrain capacitance of the silicon particles.

Thus, the analysis of the obtained results allows one to state that, in the studied composites, the resistivity strongly diminishes, though the dielectric permittivity increases when the duration of the electric discharge increases.

REFERENCES

1. Souza, F.L., Gomes, J.W., Bueno, P.R., et al., *Mater. Chem. Phys.*, 2003, vol. 80, pp. 512–516.
2. Hashimov, A.M., Hasanli, Sh.M., Mehtizadeh, R.N., Bayramov, Kh.B., and Azizova Sh.M., *Phys. Stat. Sol. (C)*, 2006, no. 8, pp. 2871–2875.
3. Bagirov, M.A., and Malin, V.P., *Elektricheskoe starenie polimernykh dielektrikov* (Electrical Ageing of Polymer Dielectrics), Baku: Azerb. Gos. Izdat., 1987.
4. Dzhuvarly, Ch.M., Veghaizer, G.V., and Leonov, P.V., *Elektron. Tekhn.,* 1977, p. 6.
5. Hasanli, Sh.M., Mehtizadeh, R.N., Imanova, A.Y., and Nuriyev, M.A., Features of Elecrtophysical Characteristics of Composite Varistors Based on Semiconductor (GaAs and InAs) and Polymer, *5th Int. Conf. Techn. Phys. Probl. Power Eng.*, 2009, Univ. Bilbao, pp. 210–213.
6. Abramov, R.Kh., Bagirov, M.A., and Malin, V.P., *Elektron. Obrab. Mater.*, 1990, no. 2, pp. 51–53.
7. Dzhuvarly, Ch.M, Veghaizer, G.V., and Leonov, P.V., *Elektricheskii razryad v gazovykh vklyucheniyakh vysokovol'tnoi izolyatsii* (Electric Discharge in Gas Inclusions of High-Voltage Isolation), Baku: Elm, 1983.

8. Gasanli, Sh.M., Guseinli, A.Ya., Abdullaev, M.I., and Abdullaev, A.P., Electrophysical Characteristics of Composite Nonlinear Resistors on the Basis of Polypropylene and Silicon, *VI Natsional'naya konferentsiya po primeneniyu rentgenovskogo, sinkhrotronnogo izluchenia, neitronov i elektronov dlya issledovaniya materialov, RSNE-2007*, (VI Nation. Conf. Application of X-Ray, Synchrotron Radiation, Neutr. Electron. Investig. Mater.), Moscow, 2007, p. 257.

9. Bidadi, H., Hasanli, Sh.M., Imanova, A.Y., and Mamedova, S.I., Electrophysical Characteristics of Composit Varistors Based on Semiconductor (GaAs and InAs) and Polymer, *7th Int. Conf. Composite Sci. and Technol.* (ICCST/7), 2009, pp. 150–155.

10. Pikulev, A.A., and Tzvetkov, V.M., Simulation of the Discharge Process in a Barrier Discharge Cell Based on a Three-Parameter Model, *Techn. Phys.*, 2007, vol. 52, no. 9, pp. 1121–1126.

ISSN 1068-3755, Surface Engineering and Applied Electrochemistry, 2010, Vol. 46, No. 2, pp. 169–172. © Allerton Press, Inc., 2010.
Original Russian Text © A.M. Magerramov, M.A. Nuriev, I.A. Veliev, S.I. Safarova, 2010, published in Elektronnaya Obrabotka Materialov, 2010, No. 2, pp. 92–95.

EQUIPMENT AND INSTALLATIONS

Coronoelectrets Based on Polypropylene Composites Dispersed by a $TlIn_xCe_{1-x}Se_2$ Semiconductor Filler

A. M. Magerramov, M. A. Nuriev, I. A. Veliev, and S. I. Safarova

Institute of Radiation Research, Academy of Science of Azerbaijan, ul. F. Agaeva 9, Baku, AZ-1143 Azerbaidjan

e-mail: musa_nuriev@mail.ru

Received December 11, 2009

Abstract—The electret properties in the heterogeneous polymer–semiconductor system have been investigated by the method of the electret–thermal analysis (ETA) of the PP composites with $TlInSe_2$ and $TlIn_xCe_{1-x}Se_2$ semiconductor fillers. It is shown that a small change in the filler structure causes a significant alteration of the spectrum of the thermostimulated depolarization currents. As the investigation shows, the $TlInSe_2$ and $TlIn_xCe_{1-x}Se_2$ fillers having the p-type conductivity play the role of the structure-forming agent in the polypropylene matrix changing the structure of the polymer and the near-boundary layer of the polymer and the filler.

DOI: 10.3103/S106837551002016X

Electrets are materials capable of retaining a long electrolyzed state after the external polarizing voltage is turned off. Recently, these materials have found application in many fields of engineering. Electrets, being sensitive elements of electroacoustic converters, air cleaners, and electric transducers [1], find use in medicine [2]. The electrets of polymer films have been studied rather well [3, 4]. In this connection, it is of great interest to create electret materials on the basis of polymer mixtures and polymer composites dispersed by various inorganic fillers, including semiconductor fillers [5–8].

In this work, the $TlIn_xCe_{1-x}Se_2$ semiconductor filler used possesses photo and strain sensitivity, as well as changing-over properties with memory [9]. The composites with semiconductor fillers also have good electret features [8]. Some aspects of the electrophysical properties of these materials have been considered in [10]. However, their physicomechanical characteristics and charge state are insufficiently studied. The investigation of these problems should help to produce new electroactive composite materials with controlled properties.

The aim of this work is the study of the charge state and the peculiarities of the interphase phenomena in the heterogeneous polymer–semiconductor system by the method of the electret–thermal analysis (ETA) of the compositions on the basis of the isotactic PP with the $TlIn_xCe_{1-x}Se_2$ semiconductor filler and their electret properties.

EXPERIMENT

The specimens are produced by hot molding from a mixture of powders of the polymer and the $TlIn_xCe_{1-x}Se_2$ filler with fineness $d \le 50$ μm. The mixing of the powders of the polymer and the filler is carried out in the sampler pulverizer at room temperature. Then, from these mixtures, there are produced the specimens through hot molding between two *Al* foils under a pressure of 10^7 Pa and a temperature of 473 K with the following hardening at 273 K. The thickness of the specimen is ~140 ± 10 μm.

The electret–thermal analysis was conducted by the conventional method [4], when the composite is placed between two electrodes and short-circuited through an electrometric voltmeter (V7-42) in a heated measuring cell. The recording of the TSD current spectra in the range from 293 to 523 K is carried out at the linear rise of the specimen's temperature with a rate of $\beta \sim 5$ K/min.

RESULTS AND DISCUSSION

The electret state of the investigated composites is the result of the change of the charge state and the polarization processes occurring in the filler near-boundary interphase layer of the polymer matrix. The dependence of the stabilized surface charge on the filler content for the PP/$TlInSe_2$ composites (1) and the PP/$TlIn_xCe_{1-x}Se_2$ composites (2) is presented in Fig. 1.

It is seen that, for both composites, the dependence between the surface charge and the filler content has an extreme character being the result of the extreme change of the efficient surface of the filler with the growth of its content in the polymer matrix. In the next two figures, there are presented the TSD current spectra for the initial polypropylene (Fig. 2, curve *1*), for the PP/$TlInSe_2$ composites (Fig. 2, curves *2*, *3*),

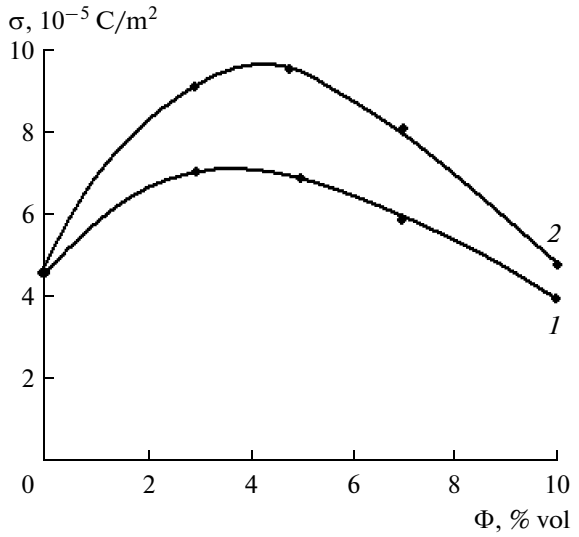

Fig. 1. The stabilized surface charge σ versus the filler content Φ characteristic. *1*—PP/$TlInSe_2$; *2*—PP/$TlIn_xCe_{1-x}Se_2$.

and the PP/$TlIn_xCe_{1-x}Se_2$ composite with different fillers contents (Fig. 3, curves *1–3*).

It is seen from the TSD current spectra that the accumulated charge for the polypropylene has two peaks situated on the opposite sides relative to the temperature axis, thus pointing to two kinds of heteropolar charges accumulated in different traps.

The relaxation of the charges from the low energy surface traps is the cause of the relatively low temperature peak in the spectrum, and the relaxation of the charges from the deep volume traps connected with the polymer crystallinity degree results in the appearance of the high temperature peak with the opposite sign. Judging about the charge value from the area of the first and the second peaks, it can be seen that the difference is negligible. This cannot be said about the TSD spectra for the composites. It is seen with the unaided eye that the area of the high temperature peak, which is connected with the charge accumulation at the interphase boundary, is much greater than the area of the low temperature one. Thus, the filler content increase results in the growth of this difference in spite of the peak temperature decrease by 8–10 K relative to the initial polymer.

The comparison of the TSD current spectra for the composite PP/$TlIn_xCe_{1-x}Se_2$ with the previously presented spectra for the PP/$TlInSe_2$ supports the above mentioned assumption. It is seen that an insignificant change in the filler structure results in substantial changes in the TSD current spectra (Fig. 3). Firstly, unlike the composite with $TlInSe_2$, in the PP/$TlIn_xCe_{1-x}Se_2$ composite, there are observed two high temperature peaks that shift towards low temperatures with the change of the filler content. We think that the second peak is identical to the high temperature peak of the PP/$TlInSe_2$ composite. In our opinion, the appearance of the first peak is associated with the change of the filler composition. The substitution of the indium atoms in the filler composition partly by cerium atoms results in the additional defect formation in the filler structure and the occurrence of new trapping centers, which are indicated in the TSD current spectra of the PP/$TlIn_xCe_{1-x}Se_2$ composites. As is seen, the high temperature peaks of the spectra for the PP/$TlIn_xCe_{1-x}Se_2$ embrace a relatively wide temperature range, which is conditioned by the high concentration and the wide energy dispersion of the trapping centers with the temperature peak reducing with the filler content decreasing and, at 10%, nearly disappearing. We think that all the observed processes are the result of the electro-ion and polarization processes occurring in the near-boundary layer of the polymer

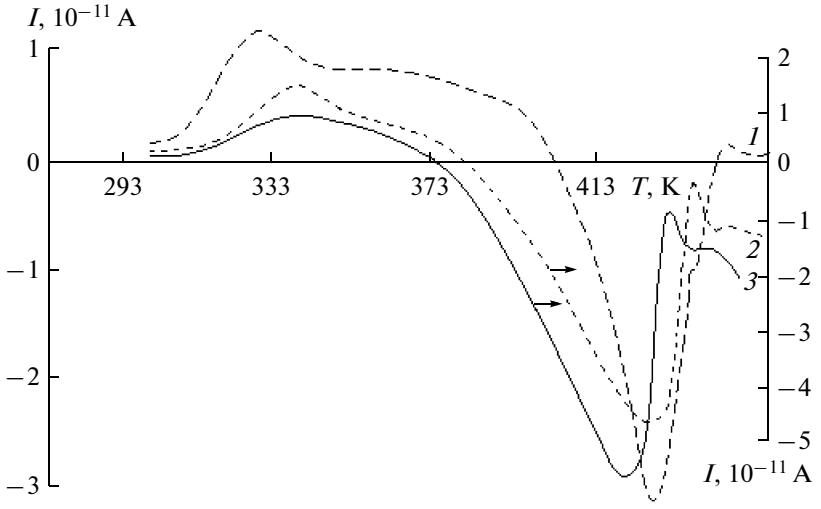

Fig. 2. The TSD current spectra for the initial polypropylene and the PP/$TlInSe_2$ composite. *1*—PP/$TlInSe_2$, *2*—PP/3% of $TlInSe_2$, *3*—PP/5% of $TlInSe_2$. Curve *1* refers to the left ordinate axis and curve *2* and *3* refers to the right ordinate axis.

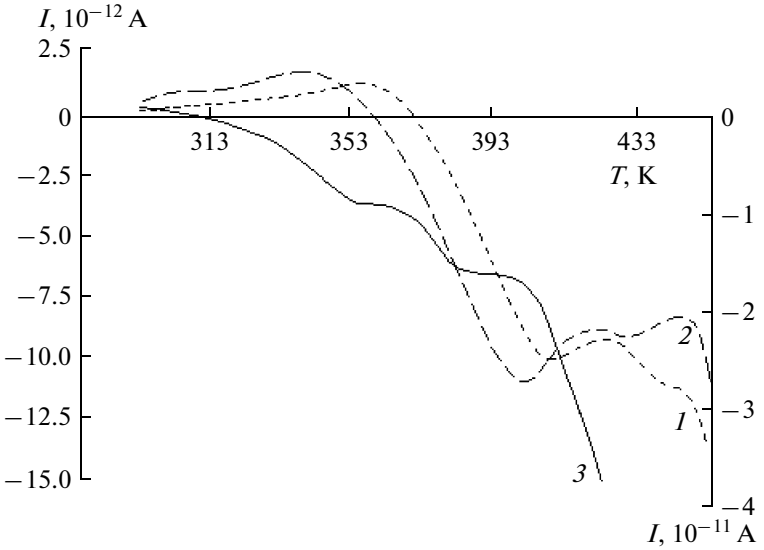

Fig. 3. TSD current spectra for the composite PP/TlIn$_x$Ce$_{1-x}$Se$_2$. *1*—PP/3% of PP/TlIn$_x$Ce$_{1-x}$Se$_2$, *2*—PP/5% of PP/TlIn$_x$Ce$_{1-x}$Se$_2$, *3*—PP/10% of PP/TlIn$_x$Ce$_{1-x}$Se$_2$. Curve *1* and *2* refer to the left ordinate axis and curve *3* refers to the right ordinate axis.

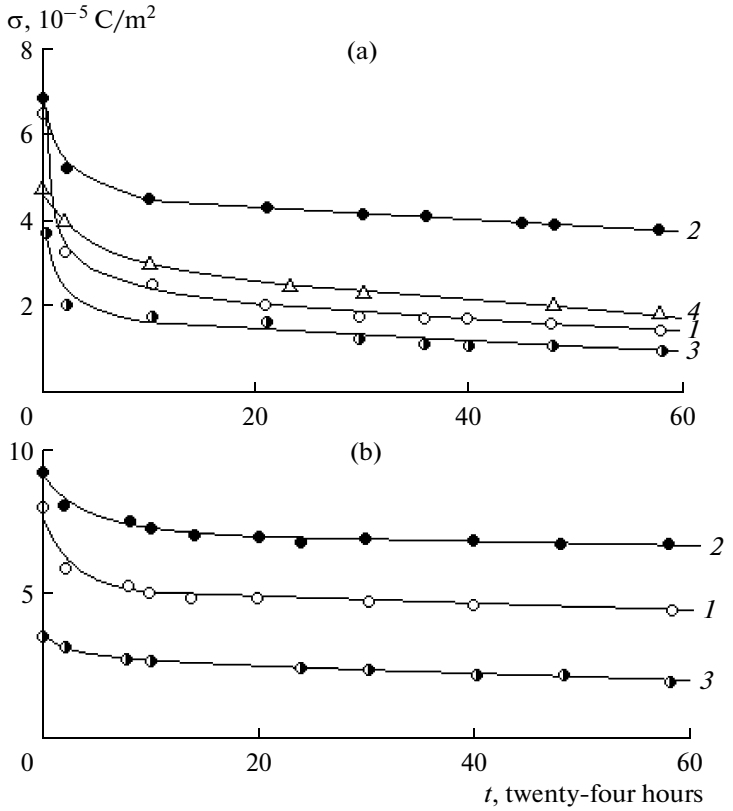

Fig. 4. The electret charge surface density σ versus the storage time t_{st} characteristic. (a) PP/TlInSe$_2$; (b) PP/TlIn$_x$Ce$_{1-x}$Se$_2$; *1*—3%, *2*—5%, *3*—10%, *4*—the initial PP.

matrix and the semiconductor filler. This assumption proves the time dependence of the surface charge density of the electrets on the basis of the PP/TlInSe$_2$ (Fig. 4a) and PP/TlIn$_x$Ce$_{1-x}$Se$_2$ composites (Fig. 4b).

It is seen from these curves that the both composites at 3% and 5% of the filler content have relatively stable characteristics compared with the initial polymer. However, if the results for the stabilized value are

compared, it will be seen that the composites with the $TlIn_xCe_{1-x}Se_2$ filler have a relatively higher value of the charge than the composites with the $TlInSe_2$, thus confirming the obtained results on the electret–thermal analysis.

In conclusion, it may be said that the $TlInSe_2$ and $TlIn_xCe_{1-x}Se_2$ fillers, having the p-type conduction, play the role of the structure-forming agent in the polypropylene matrix, changing the crystallinity and supermolecular structure of the polymer and the near-boundary layer between the polymer and the filler. The alterations of the charge state of the $PP/TlIn_xCe_{1-x}Se_2$ polymer composites are caused by the change of the efficient surface of the interphase boundary of the polymer with the filler, resulting in the growth of the concentration of the charge trapping levels.

REFERENCES

1. Goel, M., Elecret Sensors, Filters and MEMS Devices: New Challenges in Materials Research, *Curr. Science*, 2003, v. 85, no. 4, pp. 443–543.
2. Electret Polymer Curing Film (Applicator) "POLIMEDEL". Registration Certificate no. FS 01011993/3169-06, 2006.
3. Electrets, Sesler, G., Ed., Moscow: Mir, 1983, p. 487.
4. Lushcheikin, G.A., *Polimernye elektrety* (Polymer Electrets), Moscow: Khimiya, 1984, p. 184.
5. Galikhanov, M.F., Muzibullin, M.N., and Deberdeev, R.Ya, Study of Coronoelectrets on the Basis of Mixtures of Polyethylene with Polyvinylchloride, *Plast. Massy*, 2005, no. 3, pp. 8–10.
6. Galikhanov, M.F., Eremeev, D.A., and Deberdeev, R.Ya., Influence of Carbon Black on the Elecret Effect in Polystyrene, *Plast. Massy*, 2003, no. 10, pp. 46–48.
7. Magerramov, A.M., *Strukturnoe i radiatsionnoe modifitsirovanie elektretnykh, p'ezoelektricheskikh svoistv polimernykh kompozitov* (Structural and Radioactive Modification of Electret, Piezoelectric Properties of Polymer Composites), Baku: Elm, 2001, p. 327.
8. Godzhaev, E.M., Magerramov, A.M., Osmanova, S.S., Nuriev, M.A., and Allakhyarov, E.A., Charge State of Composites on the Basis of Polyethylene with $TeInSe_2$ Semiconductor Filler, *Electr. Obrab. Mater.*, 2007, no. 2, pp. 84–88.
9. Godzhaev, E.M., Ragimov, R.S., and Rustamov, V.D., Optic Switchers on the Basis of $TlInSe_2$ Single Crystals, *Trudy XVIII mezhdunarodnoi nauchno-tekhnicheskoi konferentsii po fotoelektronike i priboram nochnogo videniya* (Proc. XVIII Int. Conf. on Photoelectronics and Night Vision Devices), Moscow, 2004, pp. 110–111.
10. Godzhaev, E.M., Magerramov, A.M., Nuriev, M.A., and Safarova, S.I., Dielectric Properties of Polymer Composites with $TlInSe_2$ Semiconductor Filler, *Electr. Obrab. Mater.*, 2008, no. 6, pp. 66–70.

ISSN 1068-3755, Surface Engineering and Applied Electrochemistry, 2010, Vol. 46, No. 2, pp. 173–177. © Allerton Press, Inc., 2010.
Original Russian Text © N.S. Dimitraki, S.N. Dimitraki, 2010, published in Elektronnaya Obrabotka Materialov, 2010, No. 2, pp. 96–101.

OPERATING EXPERIENCE

Measuring the Resistance of Resistors in the Winding Process with Insulated Wire

N. S. Dimitraki and S. N. Dimitraki

Technical University of Moldova, ul. Stefan chel Mare 168, Chisinau, MD-2004 Republic Moldova

e-mail: sdimitraki@mail.ru

Received October 15, 2009

Abstract—A method for measuring the resistance of resistors and dividers in the process of their winding using an insulated wire, along with their resistance distribution onto a frame according to a preset law, is proposed. The theory, error analysis, and possibilities of the method are studied.

DOI: 10.3103/S1068375510020171

The maximum accuracy of high voltage measurements at a constant current is found to be achieved using high voltage resistive dividers of the voltage in their simplest case comprising two series-connected resistors R_1 and R_2 [1].

The measured high voltage being applied to such a divider is determined by the expression

$$U_1 = \left(1 + \frac{R_2}{R_1}\right) U_2 = (1 + K) U_2, \qquad (1)$$

where K is the coefficient of the scale point of the divider, and U_2 denotes the measured R_2 voltage.

It follows from the Eq. (1) that the accuracy of voltagt measurement is determined by the accuracy and stability of coefficient K.

When discussing the measurement precision of high voltages at an alternate current using resistive dividers, one should note that, along with the K coefficient's accuracy, the exactness of its reactances ratio must be ensured. The resistive dividers consist of a microwire. Further, the wires are to be characterized by only their capacitive reactance, because the reactance of the inductive character is negligibly small in comparison with its resistive resistance [2]. The capacitive reactance of such dividers is determined by the type of the wire frame winding, by its resistance per unit of length, and by the uniformity of the wire's distribution with respect to the resistance in the winding. The resistors having a layer-winding* (the wire is placed only in one direction at a step of more (or less) than the diameter of the insulated wire or equal to it) and a uniform distribution of the wire in the winding with respect to the resistance have the minimal capacitive reactance.

With account for the peculiarities of the cast microwire, the continuous measuring of the resistance of the wire placed on the frame and the resistance of the length of the frame the wire is placed on is to be performed for achieving the uniform distribution (with regard to the resistance) of the cast microwave in the winding layer. Their percent ratio should be incessantly compared.

The known measuring methods insufficiently meet the above requirements, in particular, in the winding process of high-ohmic resistors and resistance dividers [3–5, 6–9].

The method discussed in this paper makes it possible to manufacture mean-ohmic resistors with a resistance error of no more than 1–2% at a uniform distribution of the resistance in the winding with the wire quantity required for the winding of ($l_w < 3/\sqrt{r\omega c}$) and at a particularly high accuracy when the wire quantity l_s in the recoil spool has the length

$$\left(l_w + \frac{3}{\sqrt{r\omega c}}\right) < l_s > l_w, \qquad (2)$$

which is the most often used length for the winding of high megohmic resistors.

The principle of the method is explained by the scheme shown in Fig. 1. A spool with a metal-frame-wound resistive wire (of the layer-winding type) can be represented at a sufficient approximation as a structure of R–C–O type with distributed electric parameters [6] or a double-wire line with distributed electric parameters.

One wire is a metal spool whose resistance is of a negligibly small value in comparison with this wire's resistance [7]. The equivalent electric resistance of such a line at its bipolar mode in the electric circuit is

$$Z_s = \sqrt{\frac{r}{j\omega c}} \operatorname{cth} \sqrt{r\omega c} l, \qquad (3)$$

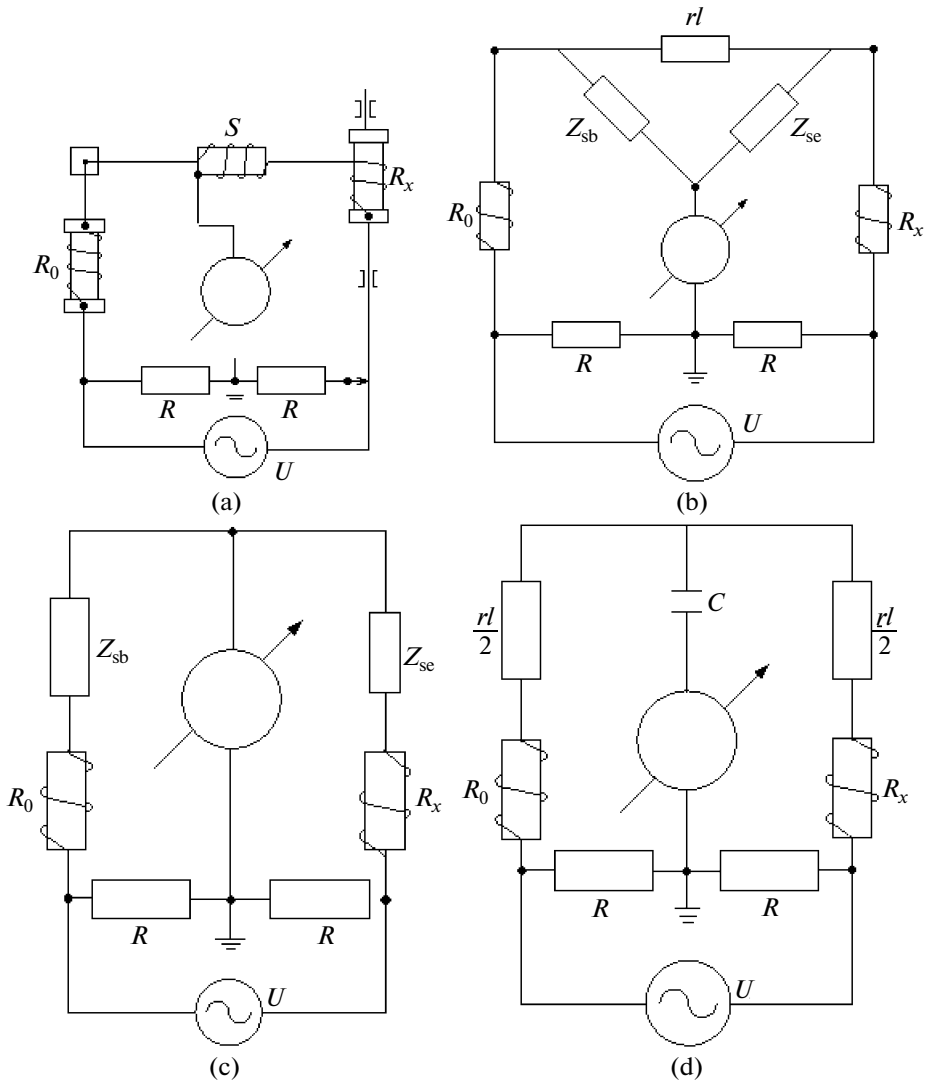

Fig. 1.

when $l < 3/\sqrt{r\omega c}$, u,

$$Z_s = \sqrt{\frac{r}{j\omega c}}, \tag{4}$$

when $l > 3/\sqrt{r\omega c}$, where r and C denote the resistance per unit of length of the wire itself and, correspondingly, its capacity per unit of length with respect to the metal frame.

In the above methods [3–5, 9], at the resistance measurement of the resistors in the winding process, the recoil spool with a wire enters the electric circuit as an electric bipolar unit and, along with the measured resistor, it may [9] or may not be a measured object. At $l_\delta < 3/\sqrt{r\omega c}$, it has a negative effect on the accuracy of the resistor's resistance measurement, thus increasing the manufacturing error of the resistor with respect to the resistance up to tens of percents.

This paper offers a tripolar mode of the spool in the electric circuit (Fig. 1a) and a bridge system for the resistor's resistance measurement (Fig. 1b). The resistance winding error of the resistor resulting from the finite value of the equivalent resistance of the spool with a wire can be substantially decreased and, in some cases, entirely removed.

Indeed, at $l_\delta > 3/\sqrt{r\omega c}$, $rl_\delta \gg Z_{sb}$, $rl_\delta \gg Z_{se}$, the scheme in Fig. 1c is simplified and takes the form of Fig. 1c, and the bridge balance takes place at the equality of

$$R_0 + \mathrm{Re}Z_{sb} = \mathrm{R}_x + \mathrm{Re}Z_{se}. \tag{5}$$

Here, two cases may occur:

(a) $\mathrm{Re}Z_{sb} = \mathrm{Re}Z_{se}$, and then

$$R_x = R_0; \tag{6}$$

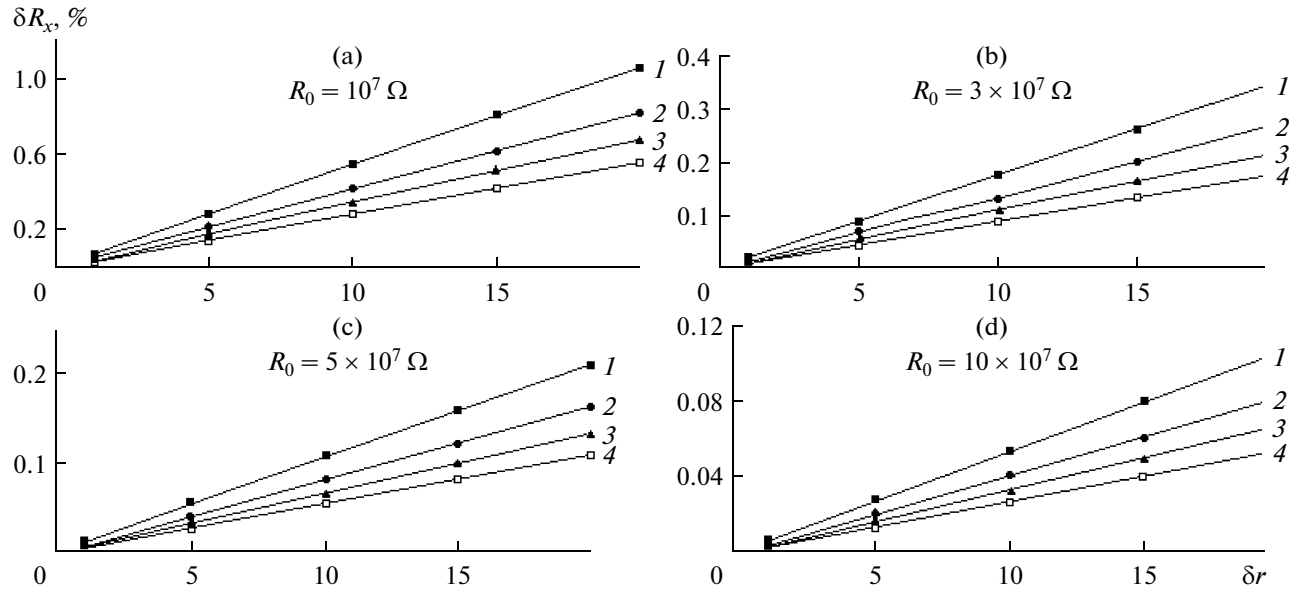

Fig. 2. r, kOhm/m: *1*—150, *2*—90, *3*—60, *4*—40; $r = (r_w - r_k)/r_k$, %.

(b) $RZ_{sb} \neq RZ_{se}$, and then

$$R_x = R_0 + \mathrm{Re}Z_{sb} - \mathrm{Re}Z_{se}. \quad (7)$$

Hence, the relative error in the resistor's manufacturing with respect to the resistance will be the following:

$$\delta R = \frac{R_0 - R_x}{R_0} = \frac{\mathrm{Re}Z_{sb} - \mathrm{Re}Z_{se}}{R_0} = \frac{1}{R_0}\frac{\sqrt{r_B} - \sqrt{r_E}}{\sqrt{2\omega C}}. \quad (8)$$

The values r_B and r_E denote the resistance per unit of length of the wire, correspondingly, of the beginning and of the end of the winding averaged over the length of $l = 3/\sqrt{r\omega c}$. In Figs. 2 and 3, some graphs of the probable resistance errors in the manufacturing of the resistors are shown when the averaged resistance per unit of length of the wire end differs from the averaged resistance per unit of length of its beginning; i.e., $r_B \neq r_E$.

At $l_\delta < 3/\sqrt{r\omega c}$; $rl_\delta < Z_{sb}$; $rl_\delta < Z_{se}$ (Fig. 1 d), the condition of the bridge's balance has the form

$$R_0 + \frac{rl}{2} = R_x + \frac{rl}{2}, \quad (9)$$

hence,

$$R_x = R_0. \quad (10)$$

The resistance in this case is averaged over the length of $3/\sqrt{r\omega c}$ both from the side of the spool's beginning and from the side of its ending.

It follows from the latter that, with account for the quantity of wire left on the spool ($l_\delta > 3/\sqrt{r\omega c}$), the resistance error of the resistor's winding is determined only by the error of the method and is independent of the value of the equivalent electric resistance either of the beginning of the spool (Z_{sb}) or of its end (Z_{se}).

As practice shows, considering the modern measuring methods of the wire's resistance per unit of length during the wire's casting and the casting control methods, the inhomogeneity of the wire's resistance per unit of length does not exceed 10–15% [8].

The scheme shown in Fig. 4 explains the principal of the uniform distribution of the wire on the layer-winding resistor. A uniform distribution of the wire's resistance in the winding decreases its capacitive reactance, which makes it possible to use microwire resistors in alternating current circuits. For the uniform distribution of the wire's resistance in the resistor winding, according to the method proposed in this paper, the R_0 of the sample resistor and the operating length L of the frame of the resistor being wound are divided into N sections with the R_0/N and L/N values, correspondingly. Each of the sections with the R_0/N resistance of the sample resistor has a terminal that is galvanically connected with the N fixed contact of the S switch. The variable resistor VR with the R_0/N resistance (that operates in the rheostatic control mode) is connected in series with the sample resistor through the movable contact of the switch S. The above variable and sample resistors form a sample arm of the measuring bridge. The axis of the VR resistor is kinematically connected with the G_{LD} guide of a wire lay-down device WLD. The above connection is selected so that a full rotation of the VR resistor moving cursor (0–360°) is relevant to the displacement of the guide of the wire lay-down device along the resistor frame axis for the L/N length, and the resistance of the VR resistor introduced into the sample arm increases from 0 to R_0/N. Proportionally to the resistance growth law

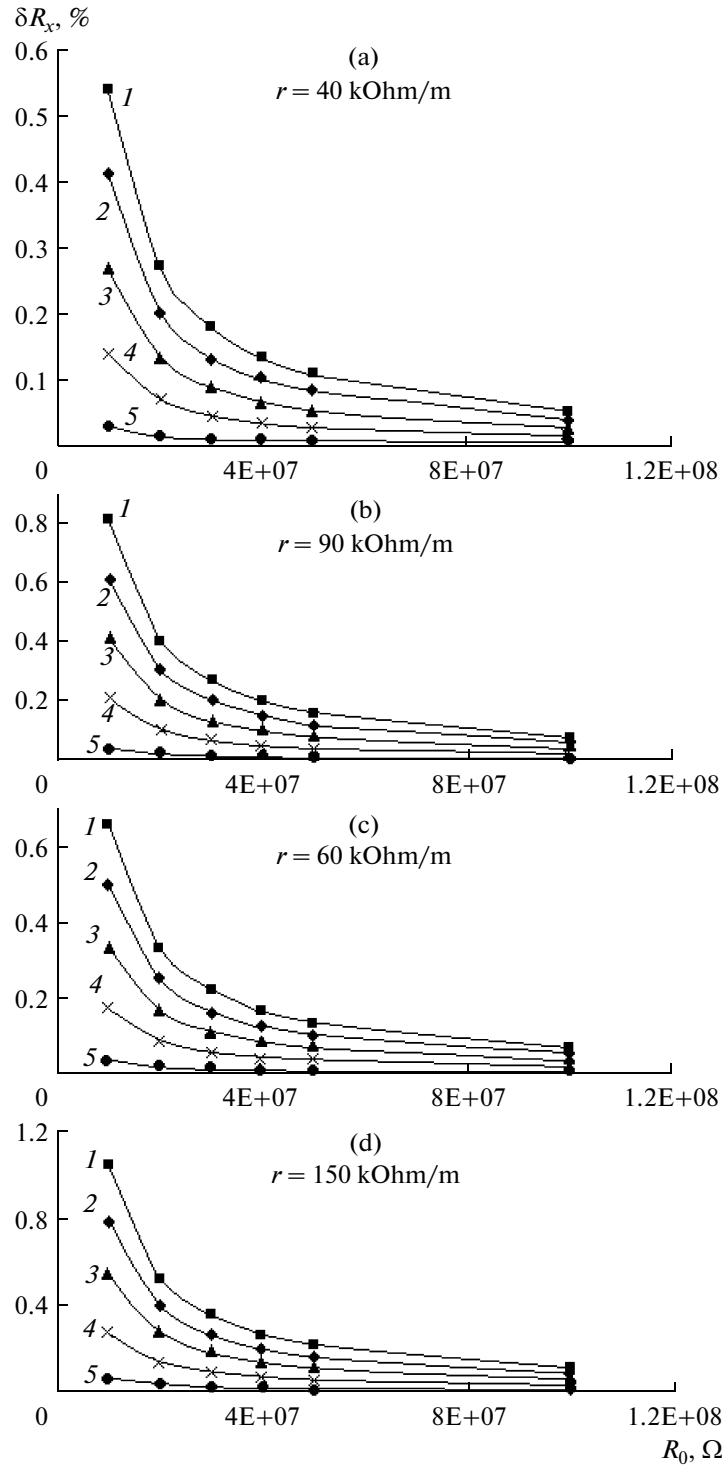

Fig. 3. δr, %: *1*—20; *2*—15; *3*—10; *4*—5; *5*—1.

of the *VR* resistor introduced into the sample bridge arm, the resistance of the wire wound on the resistor frame also increases, forming the bridge arm being measured. Using the winding rate control, the quantity of the resistance of the wire placed onto the frame is maintained equal to the resistance quantity of the *VR* resistor introduced into the sample arm. Maintaining the equality of these resistances in the winding pro-

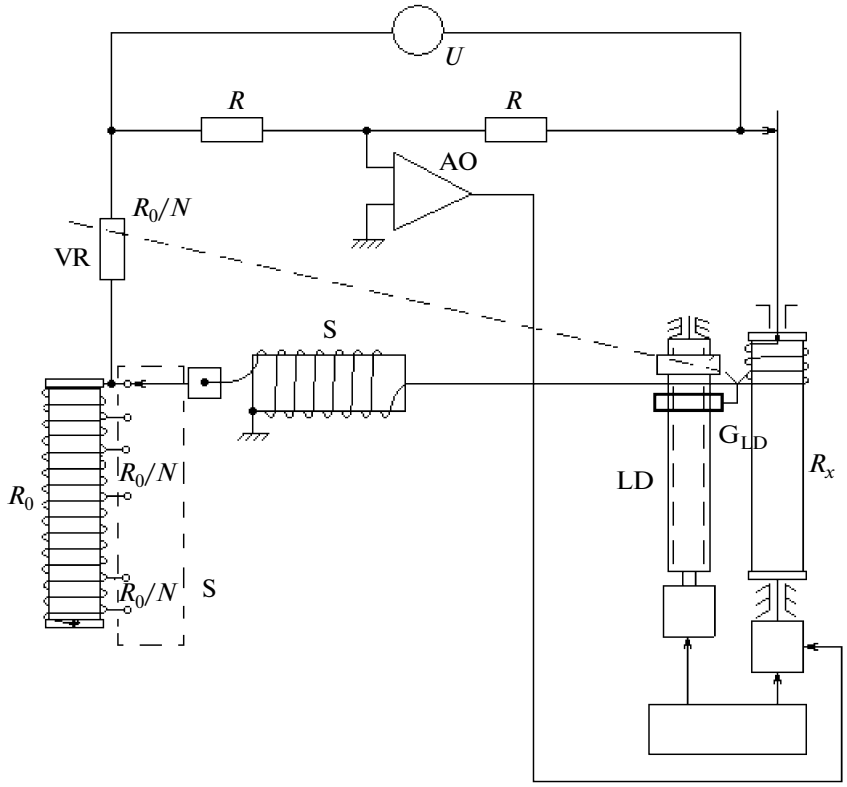

Fig. 4.

cess provides for the resistance of the frame-wound wire to be distributed according to the law of variation of the variable resistor's resistance in time.

After the *VR* resistor's first rotation, its moving cursor returns to the zero initial position (0`), and the first section of the sample resistor with the R_0/N resistance is introduced into the sample bridge arm instead of the resistor of the alternative resistance. The cycle is repeated until the $(N-1)$ sections of the resistance of the sample resistor are introduced into the sample bridge arm, the wire with the resistance of $R_x = R_0$ is wound on the frame of the manufactured resistor, and the guide of the wire lay-down device covers the length *L*. This is where the resistor winding process finishes.

REFERENCES

1. Shvab. A., *Izmeritel'nye pribory i sposob izmereniya* (Measuring Instruments and a Measuring Method), Moscow: Energoatomizdat, 1983, pp. 59–68.
2. Degtyar', L.E. and Zelitovskii, Z.I., *Mikroprovod i pribory soprotivleniya* (Microwire and the Instruments of Resistance), Chisinau: Shtiintsa, 1962.
3. Dimitraki, S.N., *Metody nekontaktnogo izmereniya izolirovannogo soprotivleniya* (Methods of Noncontact Measurement of the Insulated Resistance), Chisinau: Shtiintsa, 1978.
4. Feigel's, V.Z., The Methods and Facilities for the Noncontact Measurement of the Resistance of a Moving Insulated Wire, *Abstract Doct. Sci. (Tech.) Disser.*, Leningrad: 1963.
5. Luchkin, A.M. and Davydov, L.N., USSR Inventor's Certificate no. 222555, *Byull. Izobret.*, 1968.
6. Kaizer, Kastro, and Nikhols, Schemes with the Constants Distributed over Thin Films *Zarubezhnaya Radioelektronika*, 1963, no. 4, pp. 112–123.
7. Dimitraki, S.N., Methods and Instruments for the Measurement and Reproduction of a Microwire and the Microwire Items in the Production Process, *Doct. Sci. (Tech.) Dissertation*, Moldova Tech. Univer., 1986.
8. Dimitraki, S., Dimitraki, N., and Nicolu, D., MD Brevet de inventie no. 3329, *BOPI*, 2007.
9. Bolbochan, V.F., Drabenko, I. F., and Koditsa, V.M., *Mikroprovod i pribory soprotivleniya* (Microwire and Instruments of Resistance), Chisinau: Kartya Moldovenyaske, 1972.

ISSN 1068-3755, Surface Engineering and Applied Electrochemistry, 2010, Vol. 46, No. 2, pp. 178–191. © Allerton Press, Inc., 2010.
Original Russian Text © B.I. Stavitskii, 2010, published in Elektronnaya Obrabotka Materialov, 2010, No. 1, pp. 97–109.

INFORMATION

November 11, 2010, marks the centenary of Boris Romanovich Lazarenko. We have started publishing a series of papers entitled Glimpses of the History of Electrospark Machining of Materials written by B.I. Stavitskii, a Lenin Prize laureate and the chief designer of electrospark equipment for the electronic industry of the Soviet Union, who dedicated more than 50 years to this domain of science and technology.

Glimpses of the History of Electrospark Machining of Materials

B. I. Stavitskii

DOI: 10.3103/S1068375510020183

"The centuries-long reign of the mechanical method of metal machining... comes to an end. Its place is being taken by a higher organized process when a metal is treated by electrical forces. There can be no reasons that would have stopped the development of this revolutionary process breaking the present-day conceptions of the machining of materials. It will govern in the future; moreover, in the nearest future."

B.R. Lazarenko, 1947

When the present-day generation of young engineers is looking at the current leadership in the domain of designing electrospark equipment of such companies as AGIE, Charmilles, FINE Sodick, and Mitsubishi Electric, they can hardly believe that this technology originated in the former Soviet Union. Moreover, it was Soviet scientists and engineers who were really "in front of the entire planet" for the first 20–30 years of the existence of electrospark machining. During the first decades of the development of electrospark technology, almost all the current world leaders in this domain were concerned only with studying the Soviet achievements and trying to reproduce them in their plants. Now the time is ripe for answering the question why has the Soviet Union lost the leadership in the electrospark technology? Boris Romanovich Lazarenko, in one of his letters to the authorities dated April 27, 1948, cautioned the probability of this situation.

Among the outstanding discoveries of the 20th century, there is an invention of Soviet scientists—the spouses Boris Romanovich and Nataliya Ioasafovna Lazarenko—that is a crucially new technique for machining of metals, alloys, and other conductive materials, i.e., electrospark machining based on the use of high-concentration electric discharges for material removal from a workpiece under machining or for material deposition on it.

This method has opened a new era in the development of metal machining by allowing using electric energy directly for shaping workpieces of any conductor and semiconductor materials irrespective of their physicochemical and mechanical properties as well as for hardening and alloying their surfaces.

Invented in 1938, the electrospark method of material machining opened infinite possibilities for improving various industries. The invention of this crucially new technique of machining by the Soviet scientists B.R. and N.I. Lazarenko is confirmed by inventor's certificate no. 70010 dated April 3, 1943, and by the patents of other countries: France, no. 525414 dated June 18, 1946; the United Kingdom, no. 285822 dated September 24, 1946; the United States, no. 6992718 dated August 23, 1946; Switzerland, no. 8177 dated July 14, 1946; and Swe-

den, no. 9992/46 dated November 1, 1946, as well as by many publications.

For the discovery and development of this method, the spouses B.R. and N.I. Lazarenko were awarded the Stalin Prize in 1946; as per the decision of the State Commission for Academic Degrees and Titles dated June 26, 1949, B.R. Lazarenko was conferred the degree of Doctor of Engineering.

However, the appearance of the electrospark technology in the early 1940s was somewhat anticipatory, because the level of development of some branches of engineering at that date (as well as two or three decades later) did not allow using its capabilities to the full extent.

On the one hand, the traditional methods of metal machining applied at that time fully met the needs of industry, and major users of the electrospark technique only started appearing. On the other hand, at that moment, there was lack of devices that were designed as early as the late 20th century and that allow making the most efficient use of the advantages of electrospark machining: 32-bit CNC; linear actuators providing servo-feed rates up to 600 mm/s with a maximum acceleration up to 2G with extremely low inertia, the absence of backlashes and pitch error, minimum friction, and with an increment up to 0.1 μm; high-response switching devices; high-precision linear displacement transducers and measuring scales with an increment up to 0.1 μm; and constructions of functional assemblies of machine modules (including those made of advanced ceramics).

The advances in engineering with the appearance of new materials, facilities, and devices, particularly with increasing capabilities and the enhanced reliability of the controlling microcomputers, gave rise to the design of high-efficiency and high-precision electrospark processing systems, to the significant enlargement of the application domain of this method of material machining, and to an enhancement of the efficiency of its use in industry. This is the explanation for the continuous updating of the method and its infinite possibilities.

In the long-term competition with other techniques of metal machining, the electrospark method proved its suitability for use, its particular operability, low power consumption, and almost unbounded domain of application. The popularity of this technique is proved by the fact that Japan, which today is the worldwide leader in the production of electrospark equipment, in the mid-1990s produced more than 6000 of these installations annually; the gain in their production amounted to 30–35% per annum. One of the leading companies (24% of the world market) in the production of EDM systems with CNC generators (32-bit multiprocessor systems) is the FINE Sodick Co. (Japan). In January 2005, it produced its 10000th electrospark machine with linear drives; it took little more than 6 years.

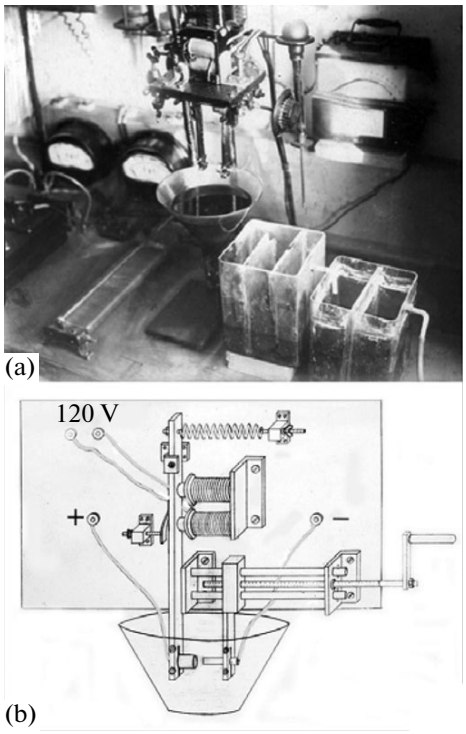

Fig. 1. First electrospark installation for preparation of powders ("feeder") that was used to prove the possibility of using the electrospark method for machining of metals for the first time in the world.

FIRST STAGE

Taming of the Spark Discharges

The first stage (from 1938 to the late 1940s) comprised the invention of the electrospark method and the experimental proof of the fact that its technological capabilities exceed the metal machining by mechanical cutting. This was demonstrated in 1943–1946.

After the inventors of the method had studied the mechanisms that govern the damage of electric contacts on an experimental installation (Fig. 1), had found the possibility of obtaining powders by electric spark discharges (Fig. 2), and had made the first holes in metals (Figs. 3–5), they predicted that there are no and cannot be any conductor materials that cannot be treated with electric discharges.

Seventy years have passed since then; however, we do not know for a fact if somebody has found at least one exception to this rule. After the inventors had found the inversion of electrical erosion from the arc mode of discharge into the spark one, they came to the conclusion that only the latter is applicable for the sizing of materials (Figs. 6–8). As soon as a discharge

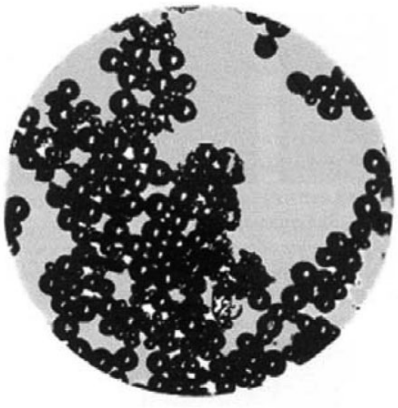

Fig. 2. Electrode material crushed by electric discharges.

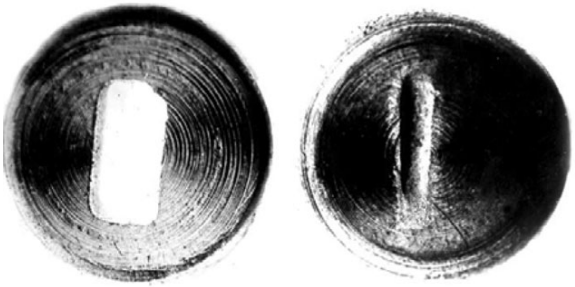

Fig. 3. Physical configuration of the electrodes that were used to prove the possibility of sizing conductor materials by spark pulses of electric current for the first time (1943).

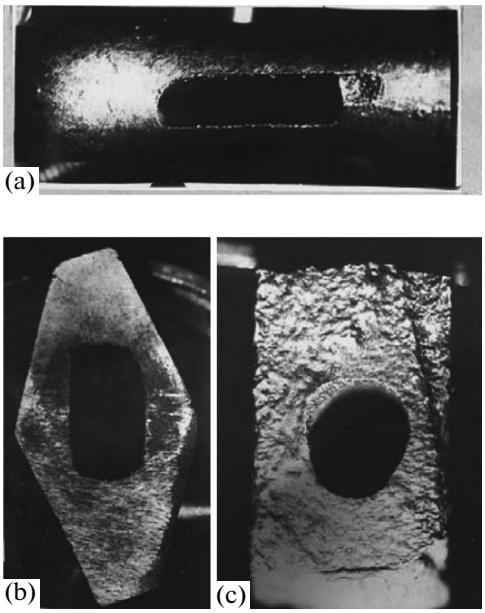

Fig. 4. First holes made by the electrospark method using a copper tool in (a) tungsten, (b) a hard alloy, and (c) a magnetic alloy (1943).

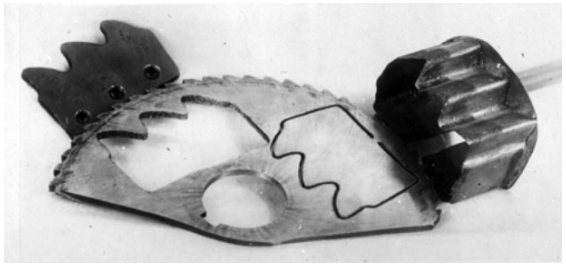

Fig. 5. Carving of a saw element by trepanning.

transits into the region of an arc pulse, it starts "creeping" over the anode surface. The action of ionic processes causes the strong heating of the electrode surface up to its partial melting. This is clearly seen in Fig. 8 (the left-hand side of the image), where the hole obtained by means of an eight-faced electrode roughly resembles an octahedron. The metal surface is hard-burned and melted. However, the time spent for the preparation of this hole is several times more than the time taken for making a hole by spark discharges (the right-hand side). In this case, there are no traces of heating of the surface and the hole has a considerably sharp outline.

B.R. and N.I. Lazarenko made an emphasis on that it is the spark discharge where it is the most appropriate to concentrate the electric energy in time and space. They formulated the features of this process:

(i) the ease of obtaining of the spark discharge mode;

(ii) the particular ease of the control of the machining process's intensity, which makes it possible either to "direct" flows of powerful discharges at the place under machining, which roughly tear metal portions along strictly specified directions, or to make a spark perform "delicate" work.

Nevertheless, despite the fact that the authors showed the possibility of applying the method for precise fabrication operations, at first it was used mainly for auxiliary and preparatory works, such as powdering of metals (required for metal-ceramics, explosives, chemical production, etc.), the removal of parts of broken instruments (drills, taps, etc.) from workpieces, sharpening of tools equipped with carbide blades, hardening and alloying of metal-cutting tools, and cutting of rough pieces of alloyed metals. This was the main trend of the respective research and engineering developments.

Meanwhile, the industrial application of the electrospark method had begun before its official registration. It was used in the early years of the Great Patriotic War in the Urals in the production of projectiles for the legendary Katyusha missile launchers. A device for removal of broken instruments from the shells of

Katyusha projectiles designed in the Uralmash and one of the experimental installations with a vibrator are depicted in Fig. 9; Fig. 10 shows the contact action machine of the early 1940s.

The inscription *Nauchis' delat' chernuyu rabotu v nauke!* (Learn to do the dirty work in science!) in Fig. 11 is made by the electrospark method on glass; Fig. 12 depicts a portrait of V.I. Lenin made by electrospark deposition of silver on a surface of blue steel. For these operations, a special apparatus for electrospark carving and painting was developed (Fig. 13).

Based on studies of the behavior of the electrode material under the action of various modes of discharge (irrespective of the techniques used for increasing the electric field intensity), the authors made the following generalizations:

(i) Each mode of self-maintained discharge exhibits its electrode erosion polarity inherent in it.

(ii) The spark mode of discharge is accompanied by a predominant decrease in the anode.

(iii) The transition of the spark mode of electric discharge into the arc one (and vice versa) is accompanied by the inversion of the electrical erosion.

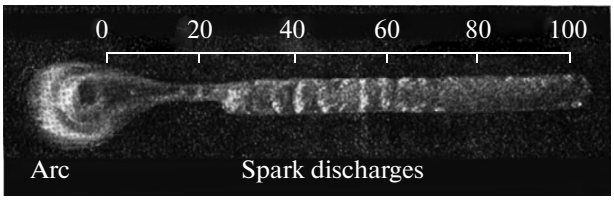

Fig. 6. Erosion diagram of the arc and spark modes of discharge.

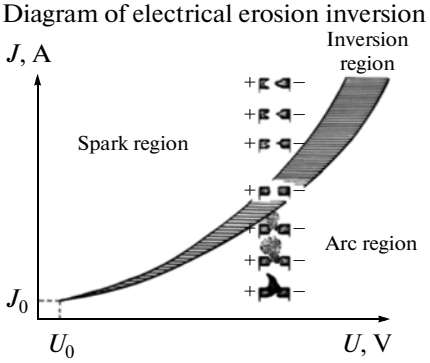

Fig. 7. Diagram of electrical erosion inversion.

SECOND STAGE

Maximum Production, Minimum Quality

The second stage (from the late 1940s to the mid-1950s) of the development of the technique of electrospark machining involved the foundation of research laboratories, the beginning of training of highly skilled specialists in the domain of electrospark machining of materials, the design of the first in the world industrial types of electrospark installations, and the first commercial production of them.

In the mid-1940s, on the initiative of B.R. Lazarenko, in the Moscow Aviation Technology Institute (MATI), whose director at that time was Mikhail Andreevich Popov, the laboratory of electrospark machining of metals was organized (Figs. 14–15).

The laboratory was equipped with different purpose installations for metal cutting with a rotating disc with a thickness up to one millimeter, for making holes of any shape, for cylindrical grinding, etc., which were constructed mainly on the basis of cylindrical grinding and drilling metal-cutting machines.

In March 1949, the Scientific and technical conference of students was held at the MATI; it was dedicated to the XI Congress of the All-Union Leninist Young Communist League (Fig. 16). In the section of electrospark machining headed by Stalin Prize winner B.R. Lazarenko, diploma students made four reports on electrospark machining of metals. Summing up the work of the section and estimating the reports of students, Lazarenko emphasized the importance of the

Fig. 8. Eight-faced holes made in a steel milling cutter by arc and spark electric discharges.

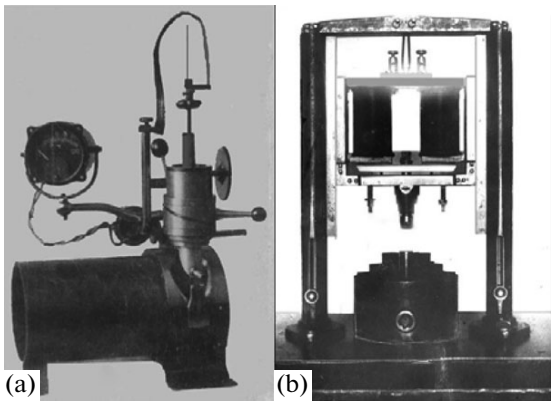

Fig. 9. Device (a) for the removal of broken instruments from the shells of Katyusha projectiles and one of the first installations with a vibrator (b).

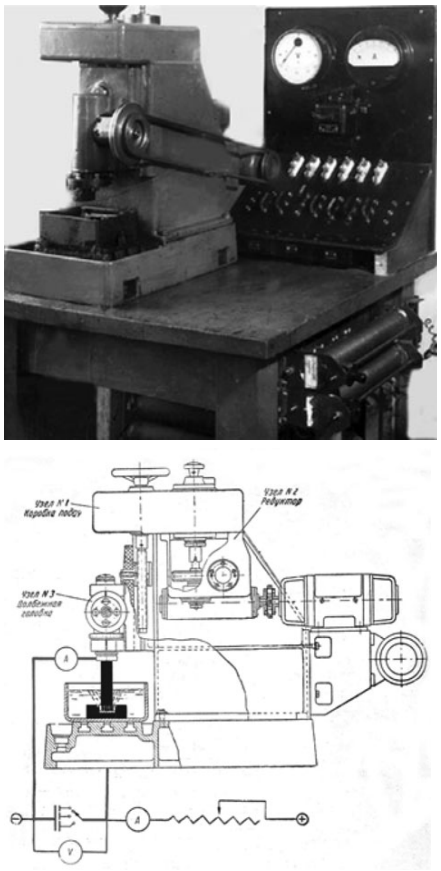

Fig. 10. EPS-KMP electrospark contact action machine (1944).

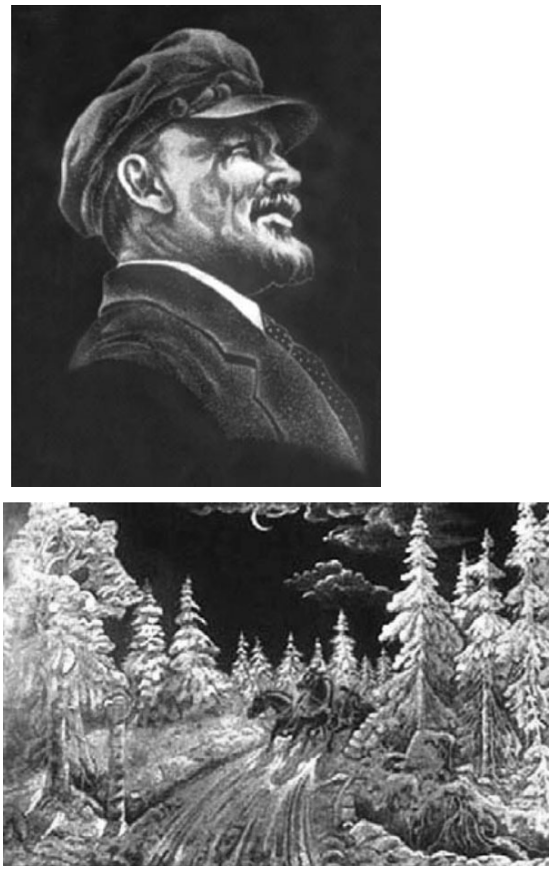

Fig. 12. Portrait of V.I. Lenin and the picture "Troika" made by electrospark painting of silver on plates of blue steel (1947).

Fig. 11. The inscription "Nauchis' delat' chernuyu rabotu v nauke!" (Learn to do the dirty work in science!) made by the electrospark method on glass.

initiated training of engineers in electrospark machining of metals. He drew particular attention to the advantages and future development of this new method in comparison with mechanical and other methods of metal machining and stressed the importance of expanding the research in this extremely promising branch of engineering.

However, a short time later, an unexpected thing happened. Boris Romanovich, who had not got the support of the new authorities of the MATI concerning training of highly skilled specialists with a degree in "Electrospark machining of materials in the aircraft engineering", had to cease his cooperation with the Institute, and the electrospark laboratory, which was situated in the building of the MATI at Petrovka at that date, ceased to be by 1950. Therefore, my diploma work dedicated to electrospark polishing of cast magnetic alloys of the ALNIKO type started by me under the supervision of B.R. Lazarenko was under threat. I had to carry out all my experiments in one of the laboratories of TsNIL-Elektrom, which was situated near Krasnye Vorota at Khoromnyi pereulok 4.

For the implementation of various technological processes by the electrospark method, various constructions of installations had already been designed in the TsNIL-Electrom: for cutting rough pieces of various shapes, grinding, making various holes, and hardening and alloying metal-cutting tools and machine components, as well as devices for electrospark carving and painting.

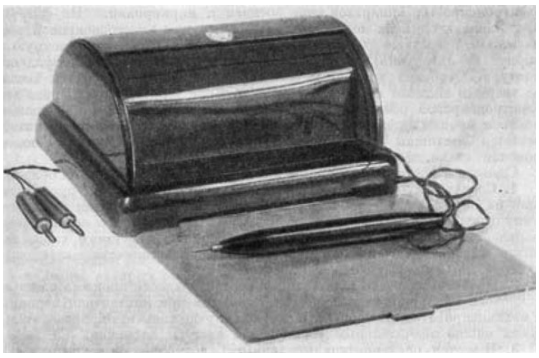

Fig. 13. Apparatus for electrospark carving and painting (1957).

Fig. 14. B.R. Lazarenko (at the center) among researchers of the Laboratory of electrospark machining of materials of the MATI. From the left to right: T.I. Makeeva, D.Z. Mityashkin, A.M. Belov, and B.N. Lyamin (1948).

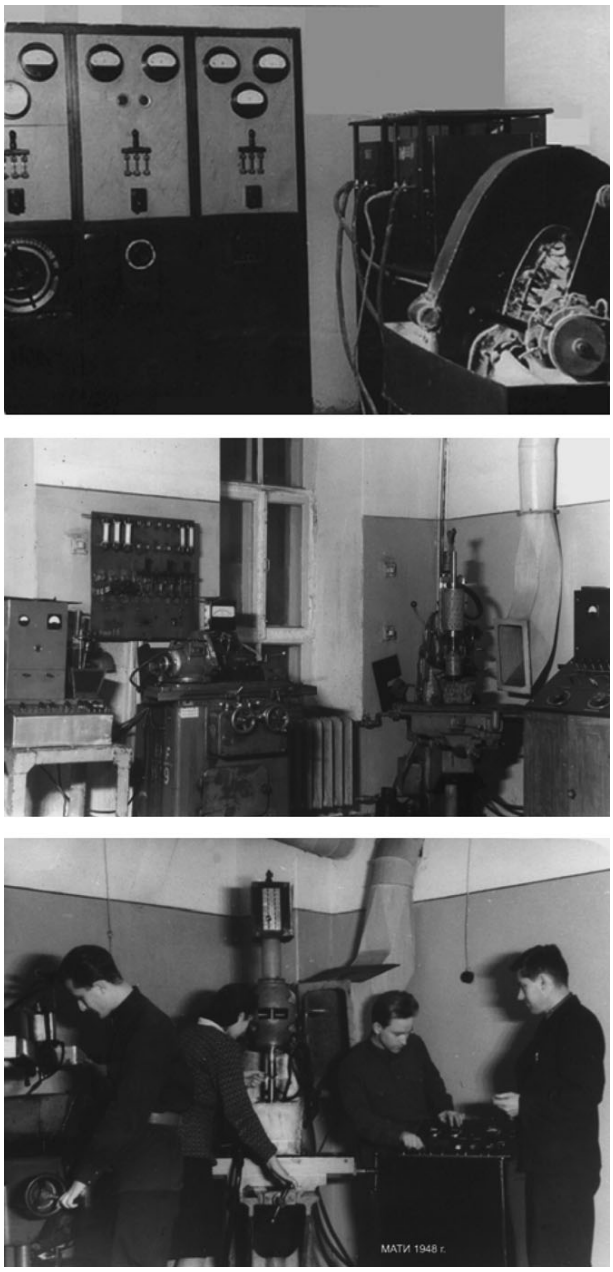

Fig. 15. In the Laboratory of electrospark machining of materials of the MATI (1948).

However, in a short time, namely on June 16, 1948, according to a decree of the government of the Soviet Union signed by I.V. Stalin, the Central Research Laboratory of Electric Machining of Materials (TsNIL-Elektrom) was founded; B.R. Lazarenko was assigned to be its head. At the early stages, it was a part of the NII-627 of the Ministry of the Electrotechnical Industry of the Soviet Union. Therefore, through the late 1940s to the early 1950s, the TsNIL-Elektrom headed by Lazarenko became not only a base for training of highly skilled specialists but also a source of manpower that yielded first the Soviet scientists who were electrospark specialists (Fig. 17).

In those years, in the TsNIL-Elektrom (in the laboratory headed by B.N. Zolotykh), basic research in the field of the principal physics of electrospark machining of metals was carried out. Unfortunately, the attention was focused mainly on the study of electrical erosion of electrodes in a spark discharge with the pulse stored energy within a range from tenths of joule to a few joules, which is suitable only for crude and preliminary treatment. The erosion of electrodes at pulse energies of less than thousandths of a joule was not studied. It is this energy range that is characteristic of electrospark precision working of metals. In addition, the technique applied was time and labor-intensive; it could not fully represent the processes occurring on the electrodes and give an objective picture of the spark discharge impact on the anode and the cathode.

Meanwhile, for the implementation of various electrospark processes, respective constructions of

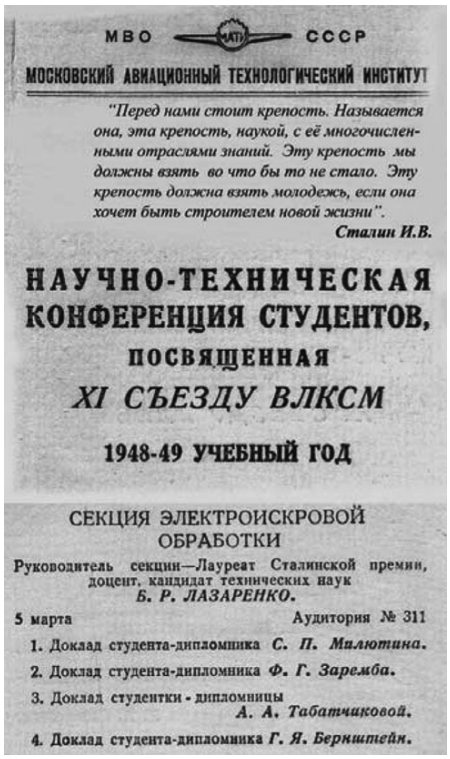
МВО МАТИ СССР

МОСКОВСКИЙ АВИАЦИОННЫЙ ТЕХНОЛОГИЧЕСКИЙ ИНСТИТУТ

"Перед нами стоит крепость. Называется она, эта крепость, наукой, с её многочисленными отраслями знаний. Эту крепость мы должны взять во что бы то не стало. Эту крепость должна взять молодежь, если она хочет быть строителем новой жизни".

Сталин И.В.

НАУЧНО-ТЕХНИЧЕСКАЯ КОНФЕРЕНЦИЯ СТУДЕНТОВ,

ПОСВЯЩЕННАЯ

XI СЪЕЗДУ ВЛКСМ

1948-49 УЧЕБНЫЙ ГОД

СЕКЦИЯ ЭЛЕКТРОИСКРОВОЙ ОБРАБОТКИ

Руководитель секции—Лауреат Сталинской премии, доцент, кандидат технических наук *Б. Р. ЛАЗАРЕНКО.*

5 марта Аудитория № 311

1. Доклад студента-дипломника *С. П. Малютина.*
2. Доклад студента-дипломника *Ф. Г. Заремба.*
3. Доклад студентки - дипломницы *А. А. Табатчиковой.*
4. Доклад студента-дипломника *Г. Я. Бернштейн.*

Fig. 16. A part of the program of the Scientific and technical conference of students (1949).

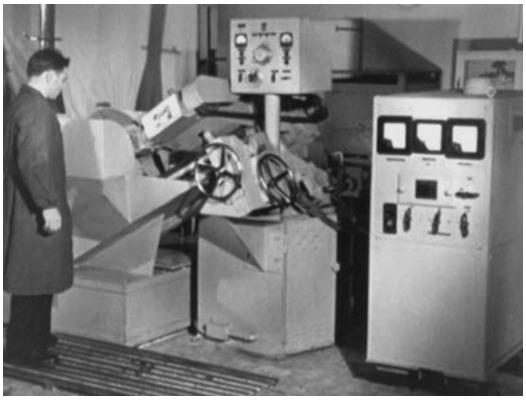

Fig. 18. Experimental electrospark installation for cutting various materials by a moving tape tool.

Fig. 17. B.R. Lazarenko among young scientists of the TsNIL-Elektrom. From the left to right: B.R. Lazarenko, V.K. Nevezhin, B.N. Zolotykh, and E.A. Deev (1950).

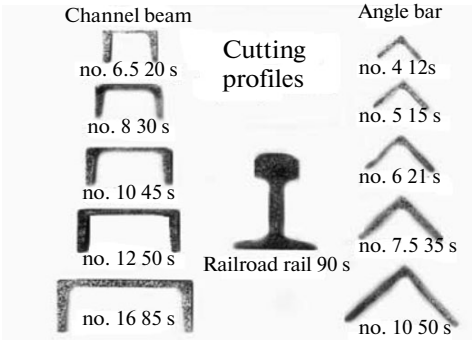

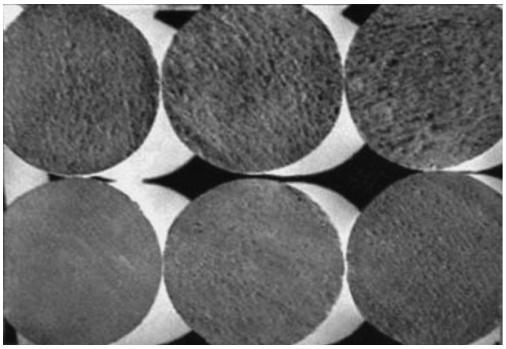

Fig. 19. Examples of electrospark cutting of profiles by a circular saw blade where a disc of roof steel was used as the tool electrode.

installations were designed: for making various holes, cutting rough pieces, grinding, sharpening, hardening, and alloying various metal-cutting tools.

Figure 18 shows one of the experimental electrospark installations for cutting various materials by a moving tape tool designed in the TsNIL-Elekrom. As the interelectrode medium, an aqueous suspension of kaolin, which provides the highest processing rate, was used.

Figure 19 depicts examples of electrospark cutting of profiles by a circular saw blade where the tool electrode was a disc of roof steel. Channel beams with a size from no. 6 to no. 16 were cut within 20–84 s; angle bars from no. 4 to no. 10, within 10–50 s; a railroad rail, within 90 s. The bottom of the figure shows rough pieces of chromium steel with a diameter of 50 mm cut in five different modes both rough and finishing. Figure 20 shows a cut rail against the background of a disc-electrode.

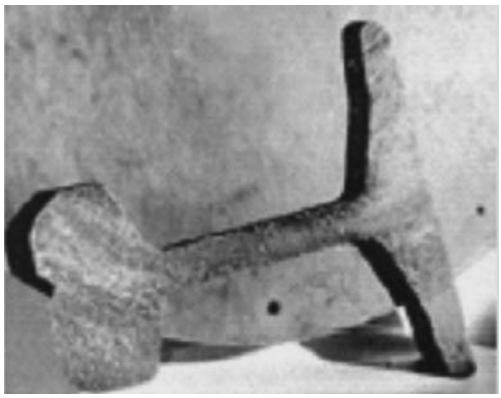

Fig. 20. Cut rail against the background of a disc-electrode of roof steel.

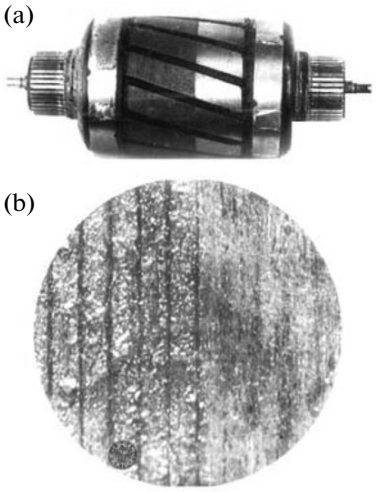

Fig. 21. Electric-motor rotor after grinding (a) by an abrasive material (the left side of the rotor) and (b) the same blown up.

The grinding of layered magnetic conductors composed of separate metal plates insulated from one another and which are intended for reducing magnetic losses in transformers, throttles, armatures, and stators of electric machines is representative. However, the rough edges that appear upon abrasive grinding of these magnetic conductors connect separate plates; as a result, closed loops are formed and, as a consequence, the magnetic losses increase sharply. The electrospark grinding is not accompanied by the formation of rough edges; therefore, it is highly desirable for grinding magnetic conductors. Figure 21 shows an electric-motor rotor whose right side was ground with an abrasive disc and the left side, by the electrospark method. Figure 22 illustrates the electrospark cylindrical grinding of a magnetic alloy and the diagram of a modernized grinding head with spindle insulation and a collector with a current lead through copper–graphite brushes. The grinding is exercised at a voltage of 24 V from a unit of selenium rectifiers.

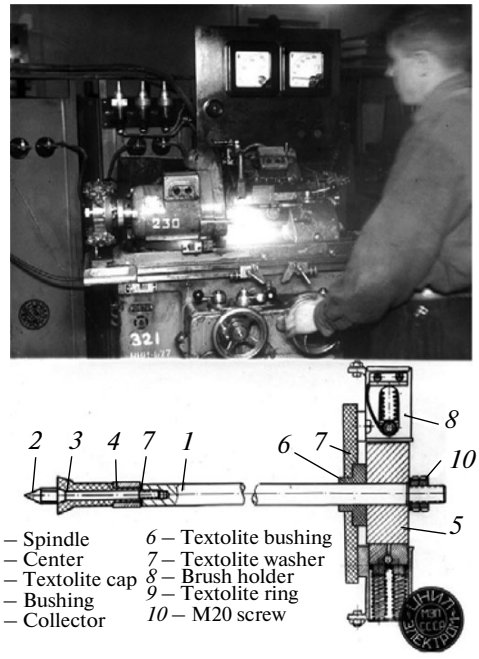

Fig. 22. Electrospark cylindrical grinding of a magnetic alloy and the diagram of a grinding head with spindle insulation and a collector with a current lead through copper–graphite brushes.

An interesting variant of the use of the electrospark method was breaking-in of milling rolls with a diameter of 250 mm in exhaust aircraft oil or in a mixture of 2/3 machine oil and 1/3 spindle oil (Fig. 23). As is known, the grinding of corn into flour requires mill rolls to exhibit high mechanical durability and a certain degree of roughness necessary for grasping the corn. Abrasive grinding of rolls made of chilled cast iron was ineffective and required a heavy consumption of abrasive materials and electric power. In the electrospark process, mill rolls grind each other. In this case, there is no product electrode or tool electrode. The polarity of the electrodes (two rolls) is reversed at regular intervals. Thus, in the course of the electrospark machining, the mill rolls as though grind one another. The studies carried out by B.M. Gorbunov showed the undeniable advantages of electrospark grinding over the abrasive one. The machining time and the power consumption decreased by a factor of 4. In addition, in a production environment, an increase in performance of the mill units by 20% was found for the rolls machined by the electrospark method.

Electrospark grinding differs from the process of mechanical abrasive grinding by the following features:

(1) It is exercised with no pressure on the tool and the product.

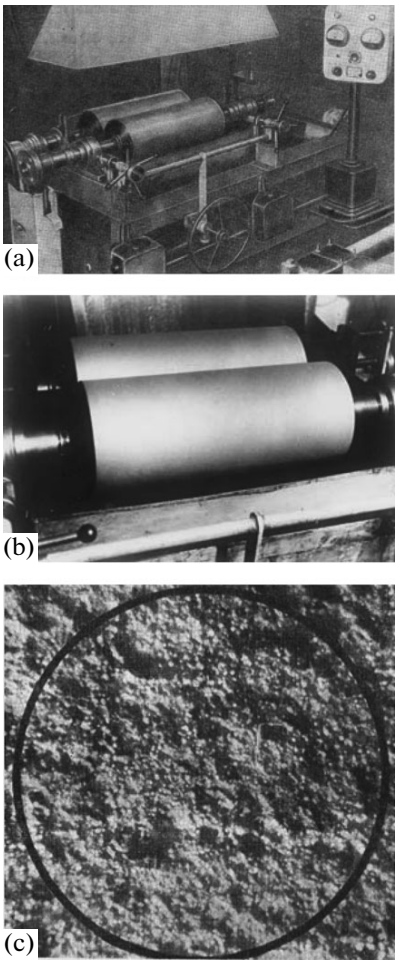

Fig. 23. Installation for electrospark breaking in of milling rolls (a), their view (b), and a microphotograph of their surface (c). $R_a = 20–25$ μm (1960).

(2) The tool–electrode in the form of a disc is made of customary gray cast iron; no abrasive material is required.

(3) One and the same disc may be used for stepless grinding of the product from a rough surface to the cleanest one with one positioning of the product while varying only the parameters of the electric circuit.

(4) Since the particles removed from a metal are separated normal to the surface, the rubbing action of the disc is absent, thereby all the surface defects (e.g., microcracks) can be easily found.

(5) It is possible to use one and the same disc for grinding materials of any hardness, including highly viscous ones.

(6) The grinding process can be combined with the simultaneous hardening of the machined surface by its alloying in the course of treatment with various chemical elements from the interelectrode medium.

If we compare the metal samples, one of which is made by any of the methods of mechanical machining and the others by the electrospark method, then it is clear that they are far different, even in physical configuration.

After a mechanical treatment, the surface is covered with more or less deep grooves being tracks of the impact of cutting elements of the tool. In addition, the surface metal layer undergoes a mechanical shift in one direction. Therefore, with respect to both the physical configuration and the internal state, the metal is inhomogeneous in different directions. After the electrospark machining, the entire surface is covered with overlapping dimples and it makes the impression of a surface treated with fine shot. In the course of electrospark alloying, the metal ejected from the anode reaches the cathode (the surface under alloying) and precipitates on it, having the appearance as if a handful of liquid clay is thrown on a smooth surface. In the two latter cases, the surface properties are identical in all the directions.

The electrospark process makes it possible to change the physical and chemical properties of products significantly. That is why, as late as 1960, N.I. Lazarenko turned her attention to the terminology in this domain: *First of all, we must specify that the electrospark method is divided into two main technological procedures: the treatment in a liquid medium and the treatment in a gaseous environment, which are variously termed in practice depending on the result. It is called electrospark hardening, coating, improvement, carbonization, deposition welding, etc. Such a variety of names cannot be considered valid; it causes confusion in the implementation of this new method. Therefore, it would be more correct to assign a name to the process of changing the initial properties of metal surfaces by electric pulses in a gaseous environment that defines it in full, namely, electrospark alloying of metal surfaces.*

It was found that even a simple "exposure" of the sample surface to spark discharges leads to an increase in the abrasion hardness of the product. In addition, its corrosion resistance increases. As early as the late 1940s to the early 1950s, electrospark alloying, i.e., cutting tool hardening, became in common use. The study of this process was the subject of many dissertations. Figure 24 depicts the UPR-1 electrospark installation for surface alloying and painting of metal surfaces, which was developed in the TsNIL-Elektrom NII-627 of the Ministry of the Electrotechnical Industry of the Soviet Union. The installation's vibrator has a potentiometer-type connection to the ballast resistance; thereby, its rate of operation increases with decreasing capacitance. This leads to the fact that the rate of the coating deposition does not decrease in passing to softer modes. The vibrator weight is only 120 g. The vibration system is situated in its housing. In addition, the installation is equipped with an electric pen for application of painting on any metal.

Fig. 24. KEI-1 device for electrospark alloying and the assembly workshop of the Leningrad plant KINAP (1949).

Many enterprises of various branches of industry situated in Berdyansk, Voronezh, Leningrad, Komsomolsk-on-Amur, Kuibyshev, Novosibirsk, Omsk, Kharkov, etc., having no possibility to obtain electrospark equipment on request, were forced to design and prepare the equipment by their own efforts.

Fig. 25. Electrospark installation for alloying metal surfaces of the Kharkov tractor plant.

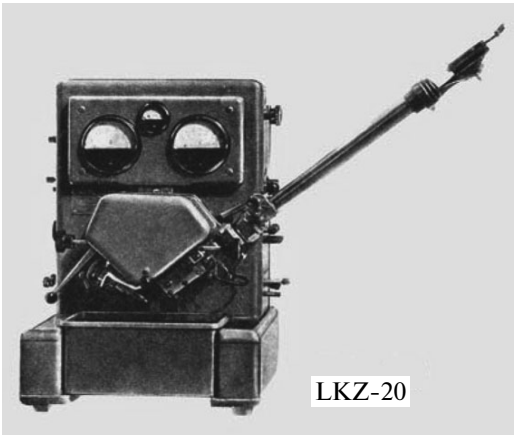

Fig. 26. LKZ-20 electrospark installation for making holes with a diameter of $\varnothing 0.15^{+0.01}$ mm in sprayers of diesel pump–injector units (1957).

The Leningrad Plant of Cinematographic Instrumentation (KINAP) assimilated series production of KEI-1 electrospark installations for alloying metal surfaces (Fig. 25). The installation contains a double-wave rectifier based on VG-129 gas-filled rectifier diodes feeding the circuit of a spark discharge. The Kharkov tractor plant also produced electrospark installations for alloying metals of domestic construction (Fig. 26). In the late 1940s, electrospark alloying of various cutting tools of high-speed steels and blanking dies was widely used. Thus, in the Elektrosila plant named after S.M. Kirov, 20% of all the types of tools and up to 70% of the dies were subjected to electrospark alloying. In this plant, packaged and grooving tools, twist drills; cylindrical, side-milling, and end-milling cutters; Heller saw blades; countersink bits; and rasps produced by the tool workshop underwent electrospark alloying. This machining increased their lifetime by five- to sixfold.

Of all the industrial electrospark installations manufactured in the Soviet Union in those years, the installations of the Leningrad carburetor plant named

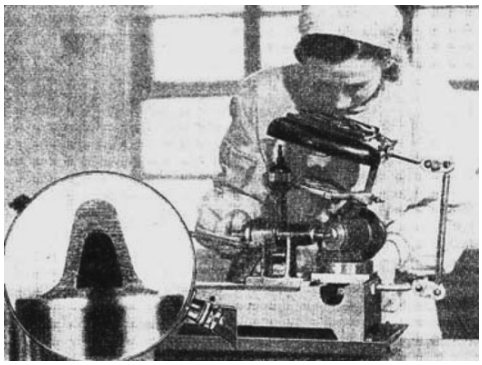

Fig. 27. Drilling holes with a diameter of ∅0.15 mm in sprayers of pump–injector units by a high-speed drilling machine with a pneumatic drive.

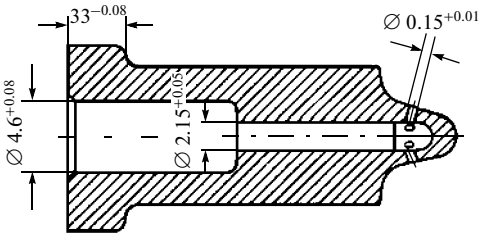

Fig. 28. Sprayer of the pump–injector unit.

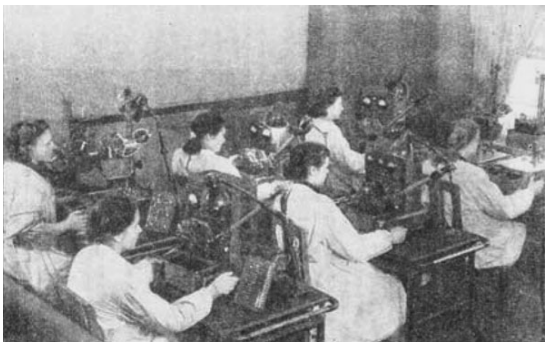

Fig. 29. Section of the workshop of the LKZ for making holes in fuel sprayers by the electrospark method.

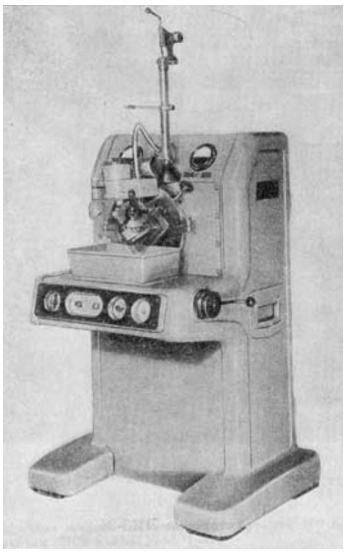

Fig. 30. LKZ-34 electrospark special-purpose installation for machining of mass-produced workpieces (with one standard size).

after V.V. Kuibyshev (LKZ) deserve the closest attention; in fact, this plant was a principal supplier of electrospark equipment for home industry and for some foreign countries for many years. This was possible owning to E.M. Levonson, a gifted engineer, who made an invaluable contribution to the development of the electrospark method of metal machining.

Of many processes of the electrospark technology in the Soviet Union, the process of making holes in components of fuel equipment completely replaced the procedure of the mechanical drilling of these holes. It was found by experiments that the process of making holes with a diameter of 0.35 mm in steels is limiting when the efficiency of electrospark and mechanical treatment of a metal subjected to cutting is approximately the same. As the diameter of the holes decreases, difficulties of their drilling increase sharply, while the electrospark machining efficiency is almost of the same level (even with the use of an RC generator and kerosene as an interelectrode medium). One of the first attempts to use electrospark machining in production work was made in 1948; it consisted in the passing to electrospark making of holes with a diameter of 0.15 mm in components of diesel fuel equipment. The subject of machining was a sprayer of relatively hard steel 50KhFA; it was necessary to drill six nozzle holes with a diameter of 0.15 + 0.01 mm in its spout (Fig. 27). The production of domestic pump–injector units started in 1947; the assimilated American technology of drilling holes by special machines (Fig. 28) with a horizontal arrangement of the spindle at a rate of its rotation of 60000 rpm did not satisfy the growth rate of their production.

In 1947–1948, in the making of holes with a diameter of $\varnothing 0.15^{+0.01}$ mm in mass-produced workpieces (sprayers of diesel fuel equipment), the electrospark method completely replaced the procedure of mechanical drilling. Figure 29 shows the LKZ-20 electrospark installation of the LKZ for making holes in sprayers of diesel pump–injector units. Even in the beginning, i.e., with no elements of automation, the efficiency increased sixfold and the faulty production

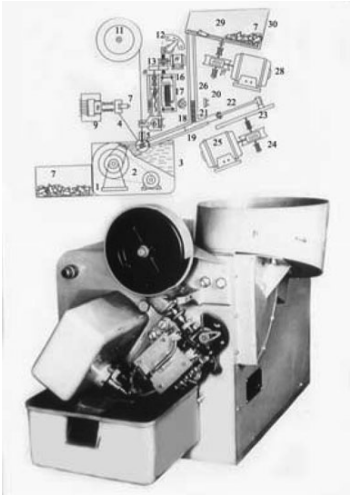

Fig. 31. Automatic machine for electrospark machining of holes with a diameter of 0.15 mm.

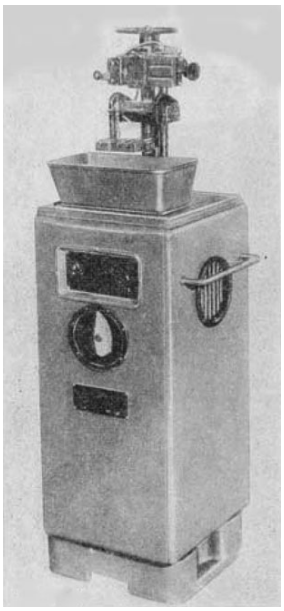

Fig. 32. LKZ-57 installation for production of fine blanking dies, profiled dies, and drawing dies.

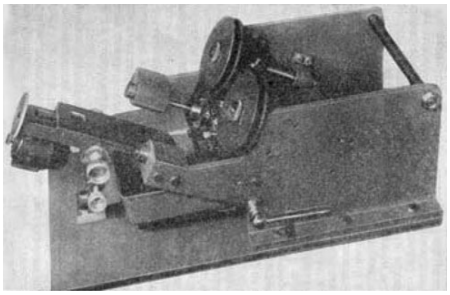

Fig. 33. LKZ-49 installation for cutting narrow slits by a brass or copper tape tool.

decreased to 0.5%. Later, in the site of electrospark machining of holes equipped with semiautomatic installations, the efficiency increased 300-fold. Figure 30 depicts the section of the workshop of the LKZ for making holes with a diameter of 0.15 + 0.01 mm in components of fuel equipment (in fuel sprayers), the cross sectional area of which is much less than 1 mm^2 by the electrospark method. Figure 31 shows the LKZ-34 electrospark special-purpose installation for machining of mass-produced workpieces (with one standard size). It is used for machining of diesel pump–injector units; six holes with a diameter of ∅0.15 + 0.01 mm are made in them simultaneously. The efficiency of machining of the sprayers with six holes in each is 900 pieces in 8 h.

The final stage of automation of the electrospark machining of nozzle holes in sprayers in the LKZ is the design of an automatic machine that does not require human intervention in the process of machining (Fig. 32). In it, sprayers *7* are filled in hopper *30* with rotating disc *29*. The hopper is filled for 8–10 h of continuous operation of the automatic machine. One worker can service a large park of such machines. Since the passing from mechanical drilling to electrospark machining, the efficiency increased 300-fold!

By 1949, the LKZ had produced more than 1000 electrospark installations of 48 models and modifications. Among them, there were not only installations for machining of mass-produced workpieces, i.e., sprayers of diesel pump–injector units for injection of fuel, in which holes with a diameter of 0.15 + 0.01 mm are made, but also installations for instrument production:

(i) LKZ-57 for production of fine blanking dies and profiled dies of hard alloys and steels (Fig. 33);

(ii) LKZ-49 for cutting narrow slits by a brass or copper tape tool in workpieces of hard alloys, steels, and nonferrous metals (Fig. 34);

(iii) LKZ-55 with a thin rotating disc for cutting hard-alloy workpieces and for pattern cutting hard-alloy plates as well as for cutting slits in collet groups and bushings (Fig. 35);

(iv) for electrospark sharpening of tools and grinding of workpieces of various materials;

(v) for making cavities of large forging dies.

In 1951, the publishing house of Mashgiz issued the monograph of E.M. Levinson and E.I. Vladimirov *Elektroiskrovye ustanovki* (Electrospark Installations); many foreign electrospark installations were designed after the type of constructions of the LENKARZ plant.

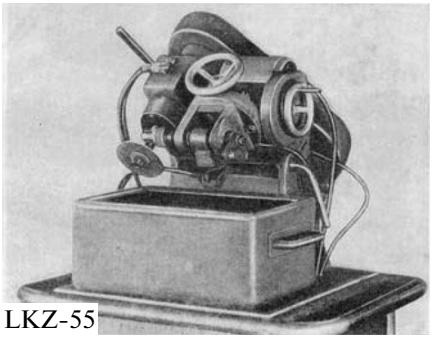

Fig. 34. LKZ-55 installation for cutting with a thin rotating disc.

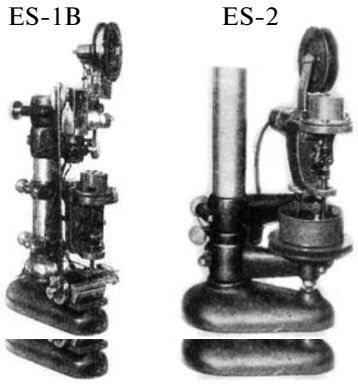

Fig. 35. ES-1B and ES-2 installations for making grids with round pin holes.

Fig. 36. Eight-spindle electrospark machine for grinding the housing of the fuel pump sprayer of a DT-54 tractor.

A significant contribution to the development of electrospark technologies and automation of the processes was made by B.G. Gutkin (Leningrad branch of the VPTI MTrM). He designed a series of semiautomatic installations for making holes with a diameter of ∅0.15–0.3 mm with an accuracy of 0.006 to 0.02 mm in sprayers and for grinding of their working cone as well as for fabricating grids with round pin holes. His experience in this domain was described in the book *Avtomatizatsiya elektroiskrovykh i anodno-mekhanicheskikh stankov* (Automation of Electrospark and Anode-Mechanical Machines) (Mashgiz, 1952) and in the paper "Electrospark Semiautomates for Machining of Pin Holes" (in the book *Novye metody elektricheskoi obrabotki metallov* (New Methods for Electric Machining of Metals), Moscow–Leningrad, 1955).

On May 16, 1956, it was written in no. 46 of the Promyshlenno-ekonomicheskaya newspaper that the electrospark laboratory and the production department of the Kharkov Tractor Plant named after Sergo Ordzhonikidze had designed and constructed an 8-spindle electrospark machine for grinding the housing of the fuel pump sprayer of a DT-54 tractor (Fig. 36). Eight workpieces may be machined by it simultaneously. The machine capacity is up to 1000 workpieces per shift. The machine is serviced by one worker. The photo shows engineer V. Polovnev inspecting the workpieces machined by L. Natorova by this machine.

The range of the use of electrospark installations started extending to the machining of both workpieces whose sizes were measured in microns and large products whose weight amounted to a few tons.

However, the analysis of the development of the electrospark method in that period shows that the main efforts of researchers were focused on increasing the efficiency of the process due to increasing the power and discharge duration up to a few joules and hundreds or thousands of microseconds, respectively. The desire to obtain the maximum intensity of the metal removal in a unit time, i.e., in a single spark discharge, was dominant. However, it led to a significant decrease in the machining accuracy, to degradation of the machined surface quality, to problems with removal of eroded material from the machining zone, and to structural changes in the surface layer of the material. The accuracy of the fabrication of workpieces was determined by hundredths or even tenths of millimeters; the roughness of the machined surface is not less than 5–10 μm R_a.

In the mid-1950s, there was an opinion that the electrospark technology had achieved its saturation point, particularly with regard to accuracy and the minimum roughness, and that this method cannot be used for finishing operations. **Some researchers even**

insisted that low energies and short pulse durations will not allow removing material.

Finally, such a unidirectional line of work resulted in the significant arrest of the development of such a promising trend as electrospark precision machining in the Soviet Union.

The processes of machining with the maximum sustainable yield in the Soviet Union at that time were developed in the Experimental Research Institute of Metal-Cutting Equipment (ENIMS) and the Special Design Bureau of Spark-Erosion Equipment of the Ministry of the Machine-Building and Toolmaking Industry. They designed a number of machines (4V721, 4B722, 4723, 4A724, etc.) in which the accuracy of the machining of workpieces did not exceed 0.02–0.07 mm; the lowest roughness of the machined surface ranged within 10–25 μm.

At the same time, in the early 1950s, some companies dealing with the development of electrospark equipment were organized abroad.

Among them, there were the Swiss companies AGIE and Charmilles. In 1953, Kiyoshi Inoue registered Japax, which was first company for production of electrospark machines in Japan and one of the first in the world. Since 1949, works on electrospark machining in Japan were carried out in the research firm the Japanese Institute of Electrospark Machining of Metals. The name of the company JAPAX is composed of Japan + X (movement in the future, unknown).

To be continued.

ISSN 1068-3755, Surface Engineering and Applied Electrochemistry, 2010, Vol. 46, No. 2, pp. 192–199. © Allerton Press, Inc., 2010.
Original Russian Text © B.I. Stavitskii, 2010, published in Elektronnaya Obrabotka Materialov, 2010, No. 2, pp. 102–109.

INFORMATION

Glimpses of the History of Electrospark Machining of Materials (Continuation)

B. I. Stavitskii

Candidate of Engineering, Senior Researcher, Lenin Prize Laureate,
Chief Designer of Electrospark Equipment for the Electronic Industry
Fryazino, Russia

DOI: 10.3103/S1068375510020195

TATE-OF-THE-ART OF THE ELECTROSPARK MACHINING OF METALS ABROAD[1]

In 1957, B.R. Lazarenko wrote in the first issue of the Proceedings of the Academy of Sciences of the Soviet Union that the remarkable properties of the electrospark method of metal machining cannot fail to be noticed by researchers and manufacturers from foreign countries.[2] After all, the possibilities to machine conductor materials with any physicochemical properties not involving any cutting tools offered new; simpler; far less energy-intensive; and, therefore, more cost-efficient operating procedures. Since the first publications of Lazarenko on the discovery of the electrospark method of metal machining and up to the present moment, the number of works concerned with the study of this process and its practical use is increasing rapidly.[3]

Let us quote some typical pronouncements in the foreign technical press.

"Within the last few years, there appeared a new method of metal machining called "electrospark", which is referred to as something mystical like flying saucers and which is even considered mock-scientific. However, the phenomenon of electric erosion underlying the electrospark method of machining was observed and described in the 18th century by the English scientist Priestley; that is, it has been known for more than 200 years. How did it happen that engineers and the manufacturers took no notice of this phenomenon for almost two hundred years and did not try to derive benefit from it? The answer to this question would be incomplete without taking into account the psychological human qualities that compel us to consider new things ones that we have seen at least once with our own eyes.

As to the phenomenon of electroerosion, which leads to the collision of electricity and the matter, it cannot be attributed to any classical and general notion of machining of materials.

Electrospark machining makes no improvements to the present-day technique of metal machining; it is an entirely new method based on other principles; it opens such ample opportunities that the word "impossible" must completely disappear from the vocabulary of mechanics. Along with the development of this new technology—electrospark machining—will introduce drastic changes in the way of thinking of engineers, designers, and shop mechanics. Some components of machines and engines will be redesigned with the view to taking advantage of electrospark machining; moreover, the design as such of mechanical systems (i.e., machinery and motors) will be revised in order to maximize the use of hard alloys and even metal carbides, which are considered to be not susceptible to mechanical treatment.

Taking into account the gain in sales of these alloys, the manufacturers will start producing various alloys with more valuable mechanical properties, which, in turn, must have a convincing effect on the "laggards" and compel them to recognize the advantages of electrospark machining. This interdependence of interests and their distribution over the entire front of the machine-building industry carry the embryo of a chain reaction characteristic of the industrial revolutions."[4]

"The interest in techniques that replace metal cutting has increased particularly strongly due to the development of rocketry using heat-resistant materials

[1] In the first decade after the discovery of the method.

[2] Lazarenko, B.R., State-of-the-Art of the Electrospark Machining of Metals Abroad, in *Elektroisrovaya obrabotka metallov* (Electrospark Machining of Metals), Trudy TSNIL-Elektrom, Moscow: Akad. Nauk SSSR, 1957, no. 1, pp. 176–225.)

[3] Lazarenko, B.R. and Lazarenko, N.I., USSR Inventor's certificate no. 70010, *Byull. Izobret.*, 1943; Resolution of Sovnarkom (Council of People's Commissars) for patenting of the method abroad dated June 18, 1946; Patent priority of the Soviet Union in: Switzerland, no. 18177 dated December 14, 1945; France, no. 525414 dated June 18, 1946; the United States, no. 692718 dated August 13, 1946; the United Kingdom, no. 285822 dated September 24, 1946; and Sweden, no. 9992/46 dated November 14, 1946.)

[4] A series of papers concerned with electrospark machining in *Machine moderne*, 1954, December.

that earlier were considered machinable only by diamond wheels. It has been estimated that if we as a nation in the case of a blitzkrieg faced the necessity of mass production, then the entire world production of industrial diamonds would be insufficient for our needs. This circumstance, coupled with the unreliability of the transoceanic transportation of diamonds in the conditions of a war, will become a national problem."[5]

"Although the electrospark method of machining of metals is still very young, nevertheless, now it is quite clear that this method has met the interests of the manufacturers that brought it about in recent years."[6]

"A tame electron can just as well process metals as it transmits sounds and images. Electrospark machining is a method that is becoming common in industry and is developing rapidly. Now, we are talking about industrial implementation of full-scale production of electrospark action installations."[7]

The new nature of metal removal has forced researchers to formulate the requirements for modern electrospark installations.[8, 9, 10]

(1) Any electrospark action installation that is designed for sizing products consists of the following components:

(a) a generator of ***unipolar*** *pulses of electric current;*

(b) a bed on which a tank with a workpiece and with a tool electrode is mounted;

(c) a servo system that automatically maintains the continuous machining;

(d) a hydraulic system with circulation and filtration of the liquid.

(2) You cannot design electrospark installations by modernizing the existing types of metal-cutting equipment, because, in this case, it is impossible to use the electrospark process with maximum efficiency. It is necessary to design special electrospark installations. Any attempts to implement the electrospark processes by means of any auxiliary devices are doomed to failure.

Some designs of electrospark installations developed by different companies in the first ten years after Lazarenko discovered the method are of interest.

The French company Qualitex produced the "Uzimyu" electrospark installation.

Boris Romanovich and Nataliya Iosafovna Lazarenko in the Laboratory of Alloying of the TsNIL-Elektrom of the Academy of Sciences of the Soviet Union in 1960.

Figure 37 depicts the physical configuration and circuit schematic of the output stage of this installation.

It is equipped with a generator of electric current pulses with a pulsing transformer equipped with a core of "ferroxcube" with two three-leg packets assembled of inverted-L-shaped plates. The purpose of the charge is to operate the electronic device. The ready-assembled core weighs 15 kg. The secondary winding of the transformer is a tube through which oil circulates and cools the tube.

The generator consists of the following components: (i) a driver stage consisting of a frequency-controlled multivibrator, a pulse-shaping stage, a stage of automatic width correction, and an output stage for swinging of an output tube; (ii) an output stage consisting of a tube of the Philips QB-5-1670 type and an output transformer with a ferroxcube core and a controlled secondary winding impedance; and (iii) a rectifier stage for feeding the anodes of the output tubes consisting of two mercury high-vacuum rectifiers.

The installation allows making holes of any shape and plane grinding of surfaces. It is claimed that the rate of grinding by the electrospark method is significantly higher than using a diamond wheel. In grinding of a hard alloy by a diamond wheel, a layer with a thickness of no more than 0.02 mm is removed in one pass, whereas the electrospark method allows removing a layer with a thickness of 0.06 mm, i.e., four times as much.

The American Company Method X has developed and produces industrial electrospark installations of various types and various powers. The circuit designs of these systems differ from the conventional relaxation circuits (Fig. 38) up to and including current pulse sensors.

It is reported that Method X has developed and produces an industrial electrospark installation in

[5] Alden, C.R., Electrospark Machining, *Mech. Eng.*, 1953, vol. 75, no. 9, pp. 701–706.

[6] Porterfield, C. Paul, Electrospark Machining, *Steel Process.*, 1954, vol. 40, no. 7, pp. 443–446.

[7] Martin, A., L'usinage par etincelles, *Electronique Industrielle*, 1955, Nov.–Dec., pp. 171–176.

[8] Bruma, M., Aspects scientifiquis de L'usinage par etincelles, *Revue Universelle des Mines*, 9 Serie, vol. 11, no. 11.

[9] Glasny, H., Die derseitigen elektroerosiven Bearbeitungsmaschinen, *Deutsche Elektrotechnik*, 1956, Mai, Heft 5, 10 Jg.

[10] Adcock, J.Z., Electro-Erosien, *Machinery* (London), 1955, vol. 83, no. 2127, pp. 355–356.

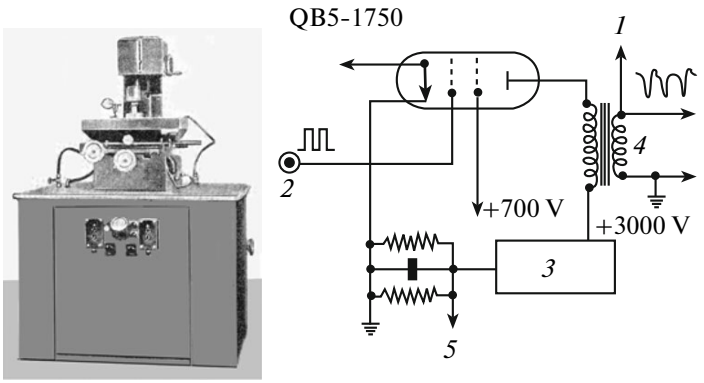

Fig. 37. Physical configuration of the Uzimyu electrospark installation (Qualitex, France) and the circuit of the output stage of its generator: (*1*) to an oscillograph, (*2*) to the driving stage, (*3*) to a high-voltage rectifier, (*4*) to a winding circuit, and (*5*) to the automated control of the driving stage.

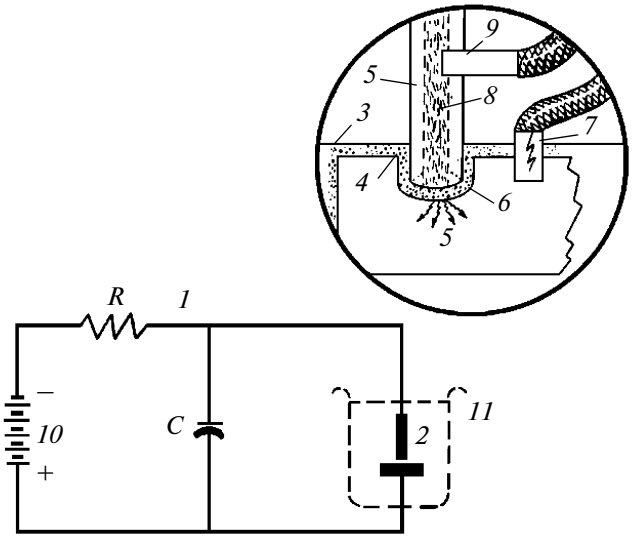

Fig. 38. Basic circuit of electrospark machining by Lazarenko and Tiebner: (*1*) circuit schematic; (*2*) electrode; (*3*) oil surface; (*4*) ejected particles; (*5*) workpiece; (*6*) spark gap; (*7*) positive lead; (*8*) dielectric liquid; (*9*) negative lead; (*10*) dc power supply; (*11*) bath with a dielectric medium.

which the electric requirements for that sort of installations are adhered to the maximum.[11] The circuit contains a three-phase bridge rectifier that applies a voltage of 10 kV to the primary winding of the pulsing transformer through a rotating spark breaker. The spark breaker commutes the electric circuit with a power of 10 kW with a frequency of 2880 Hz. The pulsing transformer with forced oil cooling has a transformation ratio of 100 : 1.

To minimize the inductance, the entire wiring of the spark-forming circuit is made of coaxial cable. To reduce the value of the back voltage, which destroys the tool electrode, a special damping system of vacuum devices and resistors is used. The optimal distance between the electrodes is estimated to be about 0.012 mm; therefore, severe requirements are imposed on the design and operation of the servo mechanism. The control signal is the voltage across the working clearance. It is applied to the amplidyne with an amplification gain factor of 3000–10000, which controls the toll electrode drive.

The installation has the following characteristics: a pulse duration of 0.2–50 μs, a pulse repetition rate of 20000 Hz, a mean power of 15 kW, a pulse current of 3000 A, and a peak pulse power of 50000 kW.

The new design "Cybernetron" was produced in France; it was an automated electrospark installation.[12] Its physical configuration is shown in Fig. 39.

The degree of finish by this installation can be seen in the right-hand photo, which shows (highly blown-up) two types of surface finish: the left one is obtained by grinding by an abrasive material; the right one, by electrospark machining where the surface quality is higher.

The English company Wickman-Erodomatic produced several designs of different-purpose electrospark installations. In the 2-kVA W/SM installation, the electric, hydraulic, and mechanical portions are connected into an integral unit (Fig. 40). It is specifically designed to solve problems that may arise in both tool and machining workshops of general purpose. In its development, particular attention was given to the simple construction of control elements and the ease of assembling. As a result, the installation is controlled

[11]Williams, E.M. and Woodford, J., Electronic Considerations in the Theory and Design of Electric Spark Machine Tools, *IRE Trans., Ind. Electron., FGIE*, 1955, March.

[12]"Cybernetron". La machine Cybernetique de "cerveau-usinage" par etincelleelectrique, *Machine moderne*, 1954, vol. 48, no. 539, Avril, pp. 49–50.

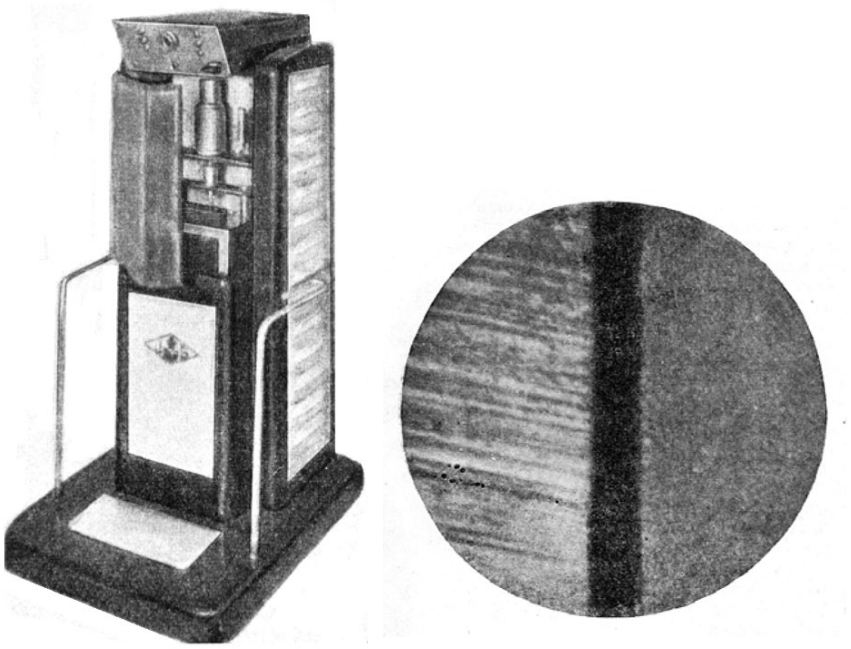

Fig. 39. Physical configuration of the Cybernetron automated electrospark installation and the comparison of the quality of the surfaces obtained by abrasive grinding and by this installation.

by means of two buttons ("start" and "stop"), a rotary switch for setting the desired accuracy of the finish, and a pivoted lever with three positions for the dielectric liquid. The head carrying the tool electrode is mounted on a steel tubular column; it contains a motor of automatic control of operation of the installation and gear wheels for moving the spindle. The friction gearing eliminates any risk of damage to the mechanism, even in the case of long electrode feeds. The head may be displaced both vertically and horizontally. The basic tank with the dielectric liquid is at the bottom of the casing. The operating bath is integral with the upper part of the installation casing; a table with gutters is situated inside the bath.

In the cable manufacturing plant in Kopenick (German Democratic Republic), a special type of electrospark installation was designed for machining of draw dies and drawing nozzles. Figure 41 depicts the physi-

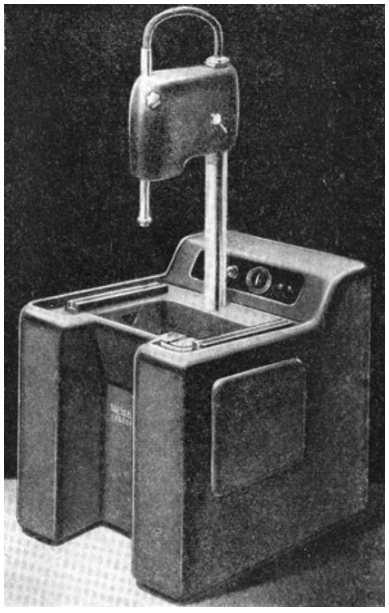

Fig. 40. Physical configuration of an electrospark installation of the W/SM type (Wickman–Erodomatic).

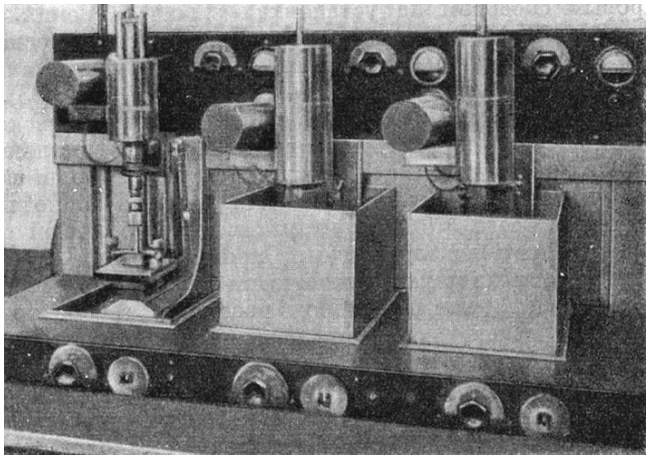

Fig. 41. Physical configuration of the triple-spindle electrospark installation of the cable manufacturing plant in Kopenick (German Democratic Republic).

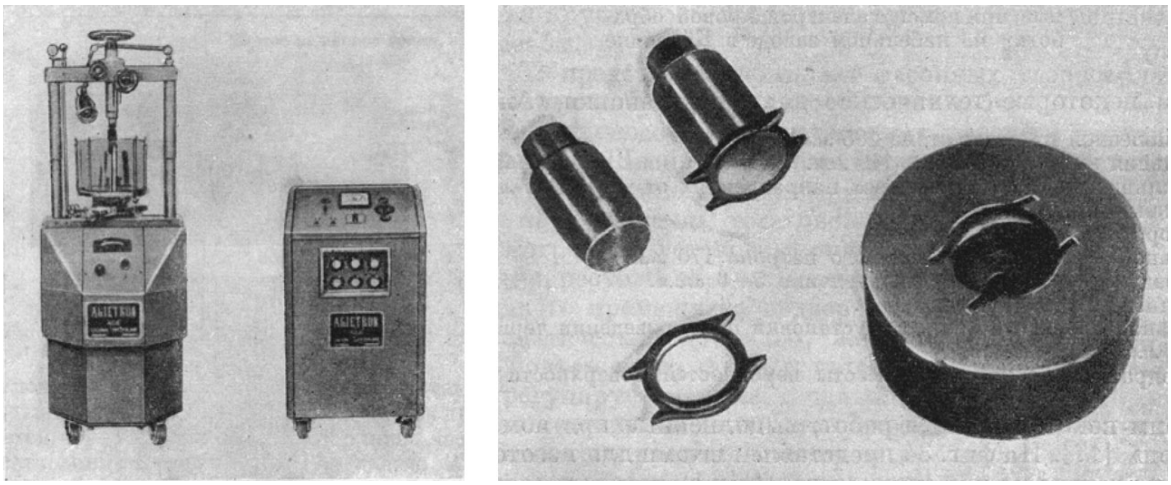

Fig. 42. Physical configuration of the Agietron electrospark installation; the die for a watchcase made by this installation and the electrodes used for its preparation.

cal configuration of this installation. The installation is triple-spindle; it has three independent generators assembled by a capacitor circuit.

It is reported that, until recently, for economic reasons, the obtaining of shaped dies of a desired profile did not seem possible. At present, using the electrospark method, we can obtain any profiles in a hard alloy. This means that presintering, which was usually used to obtain the most common hard-alloy dies, is no longer an efficient method of their production.

The electrospark method offers particular opportunities for the cable-manufacturing industry, because the reduction in the wire diameters makes it possible to lower the costs of production considerably.

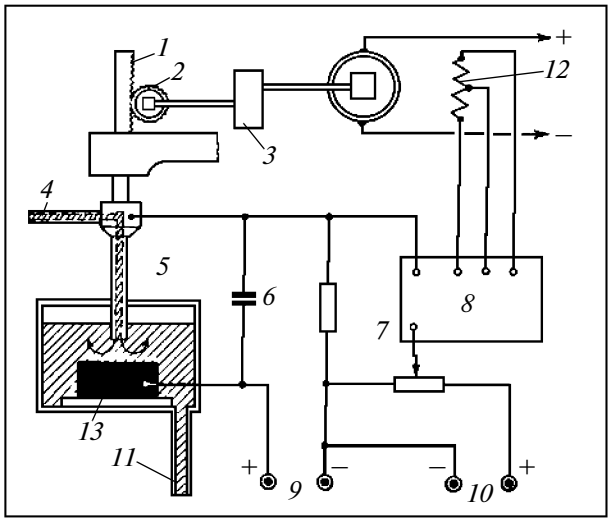

Fig. 43. Electrokinematic circuit schematic of the Sparkatron electrospark installation.

Using simple facilities for this installation, we can easily make a thread in hard-alloy rough pieces and perform similar procedures.

The Swiss company AGIE has developed and produces several types of electrospark installations with some ingenious units. Figure 42 shows one of these installations (Agietron), a die for watchcase, and the electrodes used for its preparation.

The installation consists of two electrically connected devices, i.e., an installation proper and a benchboard; a pulse generator is located in the latter. The machine casing contains a reservoir with a dielectric liquid and a pump that provides its circulation from the reservoir in a removable bath, in which a work table with the workpiece under treatment is placed.

In England and Northern Ireland, Burton, Griffiths, and Co., Ltd. has produced the electrospark installation Sparkatron.[13] The most interesting feature of this design is the servo mechanism that allows maintaining the value of the spark gap within the limits of 0.013–0.025 mm. The servo mechanism is an electronic circuit connected with the spark discharge loop; it is automatically actuated depending on the intensity of the current in the discharge loop. The control voltage proportional to the discharge current is compared with the reference voltage value, which is chosen so that, at a specified size of the interelectrode gap, the two voltages are equal to zero.

Figure 43 shows the electric circuit of a Sparkatron installation.

The electrics (transformers, rectifiers, capacitors, etc.) appear as a separate installation electrically connected with the kinematic component.

Electrospark installations were developed and produced in some plants in the Czechoslovak Socialist

[13] Spark Machining, *Mech. World*, 1954, August.

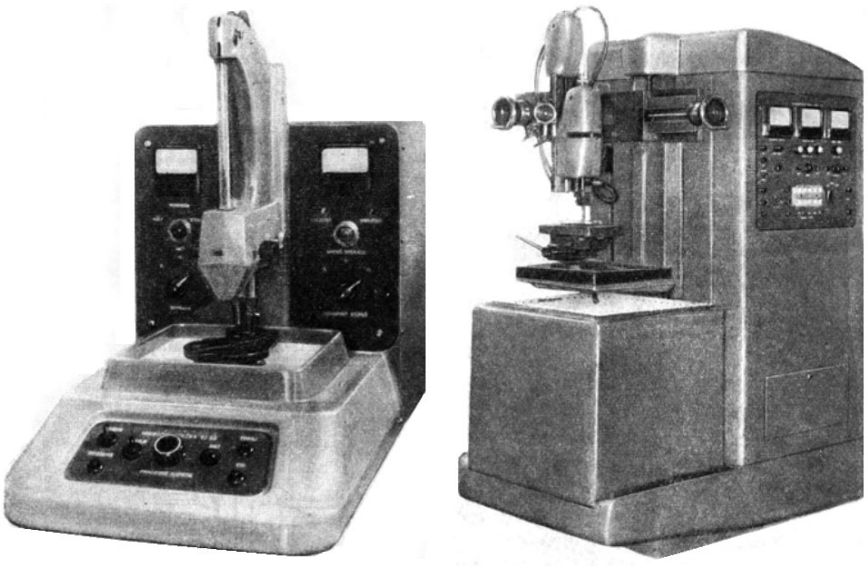

Fig. 44. Physical configuration of the electrospark installation for making holes with small diameters (to the left) and an installation for making large workpieces (Czechoslovak Republic).

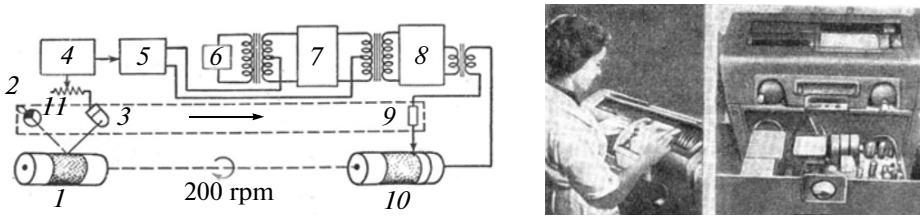

Fig. 45. Block schematic diagram of a Roneo electrospark photoengraving installation and its physical configuration: (*1*) original; (*2*) light source; (*3*) photomultiplier; (*4*) linear approximation unit; (*5*) inverted circuit; (*6*) heterodyne oscillator; (*7*) ring modulator; (*8*) push–pull amplifier (two stages); (*9*) electrode of tungsten wire; (*10*) stencil; (*11*) lens.

Republic. Figure 44 depicts the physical configuration of two electrospark installations.

The left-hand photo shows a machine for making holes of small diameters (up to 0.5 mm); the right-hand photo illustrates the more powerful installation (7 kVA) for making holes. As the previous design, it has a capacitor feed circuit and a servo mechanism. It allows making machine pieces by trepanning as well as drawing dies for drills and grooving in magnetic plates.

In addition, in the Czechoslovak Republic, some electrospark devices for auxiliary works (e.g., for removal of broken instruments and fastening members from products) were produced. Such a device is fixed in the chuck of a metal-cutting machine, and it is fed by a special electrical panel.

The Japanese company Ikegai has developed and produces a number of electric-action installations. For example, the D-5 installation is designed for making holes with a diameter of 0.5–150 mm with a depth of 10–100 mm. The maximum spindle stroke is 500 mm. The maximum rate of machining of steel is 1.5 g/min. The more powerful installation S-12 is designed for making dies, including carbide ones.

We pay particular attention to a new use of spark electric discharges because it means the origin of a new important domain of electrical engineering that can be rightfully referred to as electric photography.

The English company Roneo produced an electronic photoengraving machine designed for making stencils used for typographic printing of continuous tone originals by the electrospark method.[14] A block schematic diagram of this machine and its physical configuration are shown in Fig. 45.

It follows from the figure that, for obtaining a typographic stencil by the electrospark method, an original

[14]Photoelectric Printing and Engraving Machines, *Electron.*, 1953, vol. 26, no. 5, pp. 138–140.

Fig. 46. Physical configuration of the Stenofax electrospark photoengraving installation.

and a special stencil sheet with a conductor coating are fixed on the two drums assembled rigidly along the same axis. The read-out of the original is carried out using a photomultiplier mounted in a moveable carriage. The same carriage contains a spark replicating mechanism that forms a printing screen; it is controlled by the photomultiplier, which reads the image through electronics. For the stencil to accurately reproduce the tone value of the replicated image on paper, the number of fixed-dimension holes made by the electrospark replicating mechanism in the stencil sheet in a unit of time must be proportional to the current density coefficient of the replicated image. Since the value of the photocurrent induced by the photomultiplier of the replicating carriage is inversely proportional to the current density at a given point of the replicated image, it cannot be directly used to control the spark replicating mechanism. Special electronic devices approximate the relationship between the values of the current, its density, and the photocurrent and invert the outgoing signals.

The corrected and converted photocurrent fluctuations are fed to a ring modulator, where they are superimposed on the carrier frequency (20 kHz), amplitude modulated, amplified, and fed to the electrode of the spark replicating mechanism. Thus, the number of holes made in a stencil varies from one hole per second for a white picture to up to 12000 holes per second for the continuous black surface of the original, where the stencil must let pass the maximum paint.[15]

Spark pulses cause wear of the electrode tip made of tungsten (which is a considerably erosion-resistant material) in the form of a thin tungsten wire, which is fed through a guide capillary by a special electrical device while wearing.

Here are some characteristics of the installation: *the rate of rotation of the drums is 200 rpm; the carriage displacement rate is 64 mm/min; the sweep time of the original with a width of 20 cm is 20 min; the screen line number is 200 lines/cm.*

The electrospark method of reproduction of continuous tone originals by means of this installation has the following advantages over the hand or photochemical method.

(1) A stencil is made directly from the original not involving intermediate photocopying.

(2) The electrospark method takes significantly less time for making stencils than other known methods.

(3) The quality of the photoprints is so high that often they are no worse than the original.

(4) The cost of production of such stencils does not depend on the complexity of the original image; therefore, the making of stencils by the electrospark method is often cheaper than by other methods.

The Stenofax electrospark photoengraving machine made by the Times Facsimile Corporation is also designed for making stencils used for reproduction of continuous tone originals. The principle of operation of this machine is generally similar to that of a Roneo machine. However, the design data of this machine are somewhat simpler: it exhibits a screen line number of 55 lines/cm; therefore, the stencils made by a Stenofax machine provide a fairly good reproduction of continuous tone illustrations rich in contrast. The physical configuration of a Stenofax machine is shown in Fig. 46.

The time of production of one stencil does not exceed 6 min. The auxiliary time (the time for placement of a new original and a new stencil sheet and for the removal of a finished stencil) in total does not exceed 1 min. Note the following two statements. First, the stencils are made of sheets of special vinyl plastics covered with a current-conducting powder. Each such stencil allows producing 1000 high-quality prints while working with standard equipment. Second, if we need only one print of the original, special paper is used instead of a plastic sheet; a high-quality duplicate is obtained within 3 min.

The rapid propagation of electrospark machining abroad is due to the fact that many specialists in diverse areas of expertise work in this domain, as well due to the fact that a variety of companies have developed and produce a large amount of electrospark equipment. For the scientific development of this method, special institutions (such as the Japanese Institute of Research of the Methods of Electric Discharge Machining of Metals) and special companies that develop and produce electrospark installations in lots have been organized.

[15]Since the making of holes in a stencil requires that the holes must not run into one line, i.e., a partition must remain between individual holes, the carrier frequency must be (and it was selected so) approximately half as much as the maximum rate of operation of the discharge circuit. It is clear that the size of the resultant holes is the same in all the cases.

The information presented in this section is far from complete; it only partially characterizes the state-of-the-art of electrospark machining of materials abroad in the first decade after the discovery of the method. It is obvious even from the given data that the electrospark machining of metals as a new electrical process has started forming as an independent extremely large and cutting-edge domain of electrical engineering.

Let us conclude this small section with the idea expressed by the Wickman engineer J.Z. Adcock in his paper "Electro-Erosion Machining" in the *Machining* journal in July 1955:

"Among those who are working on the further improvement of the electrospark method of metal machining, an opinion of the enormous potential of this process is generally held. The electrospark method opens the way for more flexible and unusual approaches to the design of machine parts and tools, thereby eliminating the great difficulties in production occurring at the present day. Moreover, calculations show that, by using this method over the next 10 years, it is possible to achieve an increase in the metal-removal rate in comparison with the other most sophisticated methods of metal machining."

To be continued.